DRAFT
CMS Paper

The content of this note is intended for CMS internal use and distribution only

2024/05/24
Archive Hash: dd7a76f-D
Archive Date: 2024/05/23

Stairway to discovery: a report on the CMS programme of cross section measurements from millibarns to femtobarns

The CMS Collaboration

Abstract

The Large Hadron Collider at CERN, delivering proton-proton collisions at much higher energies and far higher luminosities than previous machines, has enabled a comprehensive programme of measurements of the standard model (SM) processes by the CMS experiment. These unprecedented capabilities facilitate precise measurements of the properties of a wide array of processes, the most fundamental being cross sections. The discovery of the Higgs boson and the measurement of its mass became the keystone of the SM. Knowledge of the mass of the Higgs boson allows precision comparisons of the predictions of the SM with the corresponding measurements. These measurements span the range from one of the most copious SM processes, the total inelastic cross section for proton-proton interactions, to the rarest ones, such as Higgs boson pair production. They cover the production of Higgs bosons, top quarks, single and multibosons, and hadronic jets. Associated parameters, such as coupling constants, are also measured. These cross section measurements can be pictured as a descending stairway, on which the lowest steps represent the rarest processes allowed by the SM, some never seen before.

To be submitted to Physics Reports

Dedication: We dedicate this work to the memory of Prof. Peter Ware Higgs, whose transformative and groundbreaking ideas laid the foundation for the physics of the standard model and of the Higgs particle, which are the subjects of this Report.

This box is only visible in draft mode. Please make sure the values below make sense.

PDFAuthor:	CMS Collaboration
PDFTitle:	Stairway to discovery: a report on the CMS programme of cross section measurements from millibarns to femtobarns
PDFSubject:	CMS
PDFKeywords:	top quark,Higgs boson,cross section,standard model,electroweak,QCD

Please also verify that the abstract does not use any user defined symbols

DRAFT

Contents

1 Introduction

The Large Hadron Collider (LHC) at CERN, colliding protons at much higher energies and delivering far higher luminosities than previous machines, has enabled comprehensive measurements of the standard model (SM) of particle physics by the general-purpose experiments, CMS and ATLAS. The Higgs boson plays a special role in the SM, being the particle predicted by the Brout–Englert–Higgs (BEH) spontaneous electroweak (EW) symmetry-breaking mechanism. The discovery of the Higgs boson and the measurement of its mass became the keystone

DRAFT

of the SM. This allowed significantly tightening the constraints on the theory and facilitated precision comparison of predictions with the corresponding measurements.

The unprecedented capabilities of the LHC detectors have enabled precise measurements of the properties of a wide array of processes. The most fundamental of the properties is the cross section, which quantifies the probability of two particles interacting and producing a particular final state. Figure 1 shows the cross sections of selected high-energy processes measured by the CMS experiment spanning some fourteen orders of magnitude, stepping from the total inelastic proton-proton (pp) cross section to the production of hadronic jets, single and multibosons, top quarks, Higgs bosons, down to the rarest processes, such as vector boson scattering of Z boson pairs, production of Higgs boson pairs or four top quarks, the most massive of the SM particles. Since the start of operation, the LHC has operated at several increasing energies allowing the experiments to map the change of cross sections with energy. The agreement in Fig. 1 between the SM predictions and the measurements is remarkable.

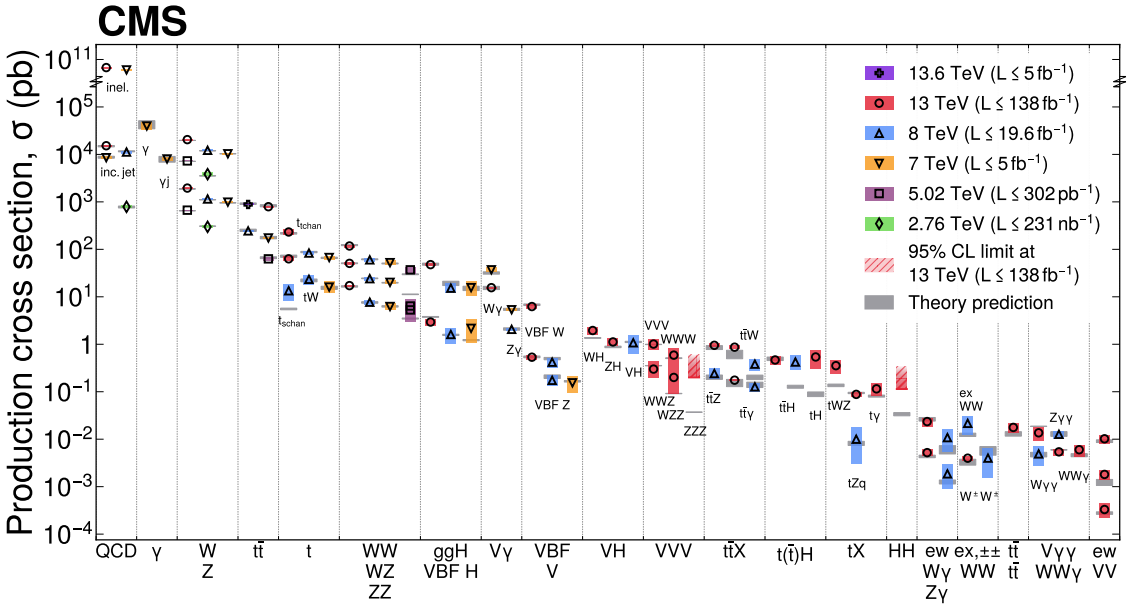

Figure 1: Cross sections of selected high-energy processes measured by the CMS experiment. Measurements performed at different LHC pp collision energies are marked by unique symbols and the coloured bands indicate the combined statistical and systematic uncertainty of the measurement. Grey bands indicate the uncertainty of the corresponding SM theory predictions. Shaded hashed bars indicate the excluded cross section region for a production process with the measured 95% CL upper limit on the process indicated by the solid line of the same colour.

In this Report, we exemplify the full spread of the CMS experimental programme in measuring cross sections involving high-energy quantum chromodynamics (QCD) and EW processes, including those involving the top quark and those involving the Higgs boson. We point out the fundamental aspects of the SM elucidated by these cross section measurements, highlighting their importance. Accurate measurements of fundamental parameters, such as the Higgs boson mass, top quark mass, their production cross sections, along with the strong coupling constant and other SM parameters, play a pivotal role in refining the SM. They also contribute significantly to shaping a more accurate and comprehensive model of the origin of matter and of cosmology, e.g. by understanding the features that affect the early universe and its eventual

fate: the shape of the BEH vacuum potential and the EW vacuum stability, respectively.

The construction and operation of the LHC and the CMS and ATLAS detectors are a product of the accumulated experience of the high-energy physics community. The instantaneous luminosity provided by the LHC exceeds that of the most recent previous hadron collider, the Fermilab Tevatron, by nearly two orders of magnitude. The higher pp collision energy significantly increases all production cross sections. This enables, for many processes, the collection of data sets, sometimes in only days, that match those of the entire experimental programme of previous experiments. For example, the precise measurement of the W and Z boson production cross sections can be performed in CMS with data collected in one day of LHC operation with a precision similar to that obtained during several years of operation of the UA1 and UA2 experiments that discovered the W and Z bosons.

The CMS detector at the LHC has performed both as a discovery instrument, observing a new particle—the Higgs boson—and new production processes, such vector boson scattering and $t\bar{t}t\bar{t}$ production, and as a cross section measuring device with the precision substantially exceeding that of previous experiments for a wide variety of final states. The CMS detector has a larger angular acceptance than the previous generation of hadron collider experiments. It measures physics objects, electrons, muons, tau leptons, photons, and jets, with higher efficiency, better precision, better purity, and fewer gaps in geometric coverage. These capabilities both expand the CMS potential and enable cross section measurements with high precision. The ability to measure new states in the SM allows CMS to study new aspects of the gauge structure of the theory, processes involving the top quark, explore the mechanism of EW symmetry breaking, and to search for beyond-the-SM (BSM) physics. The Higgs sector, currently only accessible at the LHC, is an ideal place to study the SM and to simultaneously look for signs of BSM physics signalled by deviations from the predictions of the SM.

For a given process, with a particular final state, the number of events produced, n, is given by the product of the instantaneous luminosity, $\mathcal{L}$, and the cross section, σ, integrated over the time during which the events are recorded, i.e. $n = \int \mathcal{L}\sigma \mathrm{d}t$. The instantaneous luminosity, which is expressed as an inverse cross section per unit of time, t, depends on the number of protons in the colliding bunches, the frequency with which the bunches collide, and the lateral size and overlap of the bunches. The unit of cross section used in particle physics is the barn, where the barn is defined as 10^{-24} cm^2. Cross sections of production processes involving heavy SM particles are typically of the order of nanobarns (nb), picobarns (pb), or femtobarns (fb).

Not all events produced are observed due to limitations in the acceptance and efficiency of the detectors. The acceptance, A, is the fraction of events in which the kinematics of the final state particles are such that they traverse, or impact, a detector with the capability to measure them. The efficiency, ϵ, is the fraction of events within the acceptance that are detected. Thus if N signal events are observed σ is given by:

$$\sigma = N / \int (\mathcal{L} A \epsilon) \mathrm{d}t.$$

We frequently measure a "fiducial" cross section, that is the part of the cross section that corresponds to a defined set of kinematic requirements on the final-state particles for which the acceptance is high. Measuring fiducial cross sections eliminates theoretical uncertainties related to the extrapolation from the fiducial phase space to the full phase space.

In the following sections, we first describe the LHC operation and the CMS detector; discuss the simulations and calculations used to predict cross sections; and then report cross sections, fiducial cross sections, and selected differential cross sections (cross sections as functions of

DRAFT

kinematic variables) covering high-energy QCD and EW processes, including processes involving the top quark and the Higgs boson. Finally, we include projections for High-Luminosity LHC and conclude with a brief summary of the results.

2 The LHC and CMS

2.1 LHC operations, energies, and luminosities

The LHC has operated providing collisions to feed its physics programme over three runs, with long shutdowns in between for collider and detector maintenance, and upgrades. In Run 1 from 2010 to 2012, the LHC operated at 7 TeV (2010–2011) and 8 TeV (2012)providing 6.1 fb^{-1} and 23.3 fb^{-1} of pp collision data, respectively, to the CMS experiment. In Run 2 from 2015 to 2018, the LHC increased the collision energy to 13 TeV and eventually more than doubled the peak luminosity providing 163.6 fb^{-1} of pp collision data to the CMS experiment. In Run 3, currently in progress (since 2022), the LHC has increased the collision energy to 13.6 TeV and also increased the peak luminosity. The Run 3 results presented in this Report use data collected during the first year of Run 3 operation. Only a subset of Run 3 data has been analyzed and used in this Report.

The CMS experiment typically operates and records data for over 90% of the LHC operational time, with the detector working at peak performance suitable for physics analysis 88% of the LHC operational time. The LHC has additionally operated for short periods taking pp collision data at collision energies of 2.76 TeV and 5.02 TeV as reference for heavy ion collision runs having those collision energies per nucleon pair.

CMS integrated luminosity: The integrated luminosities collected by the CMS experiment for each LHC running period are listed in Table 1. The integrated luminosity for 2016–2018 Run 2 period was reevaluated, achieving a lower uncertainty and an increase in the evaluated value from 137 to 138 fb^{-1}. The total integrated luminosity of Run 2 is known with a better relative uncertainty than that of subperiods of data taking within Run 2. The integrated luminosities for the years 2015–2018 of LHC Run 2 data taking have individual uncertainties between 1.2 and 2.5% [1–3], and the overall uncertainty for the 2016–2018 period used in most of the analyses included in this Report is 1.6%. The Run 1 absolute integrated luminosity of the pp collisions at 7 and 8 TeV has been determined with a relative precision of 2.2% and 2.6%, respectively [4, 5]. The Run 3 integrated luminosity is measured using the techniques from the 2015–2016 Run 2 luminosity determination [1] and is estimated to be 2.1% [6].

Some measurements were performed using short runs of pp collision data with features such as low instantaneous luminosity. These measurements use luminosity determinations specific to those runs with the uncertainties described with each corresponding analysis.

2.2 The CMS detector

The central feature of the CMS apparatus is a superconducting solenoid of 6 m internal diameter, providing a magnetic field of 3.8 T. The large size of the solenoid allows the inner tracker and almost all the calorimetry to be installed inside the solenoid. Thus, within the magnetic volume are a silicon pixel and strip tracker, a lead tungstate crystal electromagnetic calorimeter (ECAL), and a brass and scintillator hadron calorimeter (HCAL), each composed of a barrel and two endcap sections. The geometric coverage of the ECAL and HCAL goes down to an angle of about 6° from the beamline, i.e. at a pseudorapidity $|\eta|$ of about 3. The hadron forward (HF) calorimeter extends the η coverage, using steel as an absorber with quartz fibres embedded in

DRAFT

Table 1: Integrated pp collision luminosity $\mathcal{L}$, analyzed by the CMS experiment during LHC Runs 1, 2 and 3, as well as during pp reference runs for the heavy ion physics programme at 2.76 and 5.02 TeV.

Run	Energy (TeV)	$\mathcal{L}$ (fb^{-1})	Uncertainty
1	7	5.0	2.2%
1	8	19.6	2.6%
2	13	138	1.6%
3	13.6	5.0	2.1%
1	2.76	2.31×10^{-4}	3.7%
2	5.02	0.302	1.9%

a matrix arrangement as the sensitive material. The two halves of the HF are located 11.2 m from the interaction region, one at each end, and together they provide coverage in the range $3.0 < |\eta| < 5.2$. They also serve as luminosity monitors. The very forward angles are covered at one end of CMS ($-6.6 < \eta < -5.2$) by the CASTOR calorimeter [7]. Muons are measured in gas-ionization detectors embedded in the steel flux-return yoke outside the solenoid. The precision proton spectrometer [8] (PPS) is a system of near-beam tracking and timing detectors, located in Roman pots (RPs) at about 200 m from the CMS interaction point.

A detailed description of the CMS detector, together with a definition of the coordinate system used and the relevant kinematic variables, is given in Ref. [9]. The upgraded configuration of the detector for the LHC Run 3 is given in Ref. [10]. The CMS detector as it was configured during 2017–2018 is shown in Fig. 2.

Calibration of the calorimeters and alignment of the tracking systems have played an important role in both maintaining and improving the performance of the detector as refined techniques are developed. The calorimeter calibration includes both relative calibration of the detector elements, in particular following changes in response (typically those resulting from radiation-induced effects on the scintillating materials), and also absolute calibration of the physics objects, electrons, photons, and jets, using, e.g. the mass of the Z boson as a reference. Alignment of the tracker uses tracks of charged particles to improve upon the original information about the relative positions of the various detector modules and from the laser alignment system.

As described in Section 2.1 there have been three periods of LHC operation: Runs 1-3. The Run 3 analyses covered in this Report typically rely on the methods developed for Run 2. In the description of the CMS event selection and reconstruction below, substantial differences in the CMS operation and methodology between these operational periods are noted.

Trigger: Events of interest are selected using a two-tiered trigger system. The first level, composed of custom hardware processors, uses information from the calorimeters and muon detectors to select events at a rate of around 100 kHz within a fixed latency of about 4 μs [11]. The second level, known as the high-level trigger, consists of a farm of processors running a version of the full event reconstruction software optimized for fast processing, and reduces the rate of selected events to around 1 kHz before data storage [12].

Particle-flow: The global event reconstruction (also called particle-flow event reconstruction [13]) aims at reconstructing and identifying each individual particle in an event, with an optimized combination of all subdetector information. In this process, the identification of the particle type (photon, electron, muon, charged or neutral hadron) plays an important role in the determination of the particle direction and energy. Photons, both prompt, produced in parton-parton collisions, and nonprompt, e.g. from π^0 decays or electron bremsstrahlung, are iden-

DRAFT

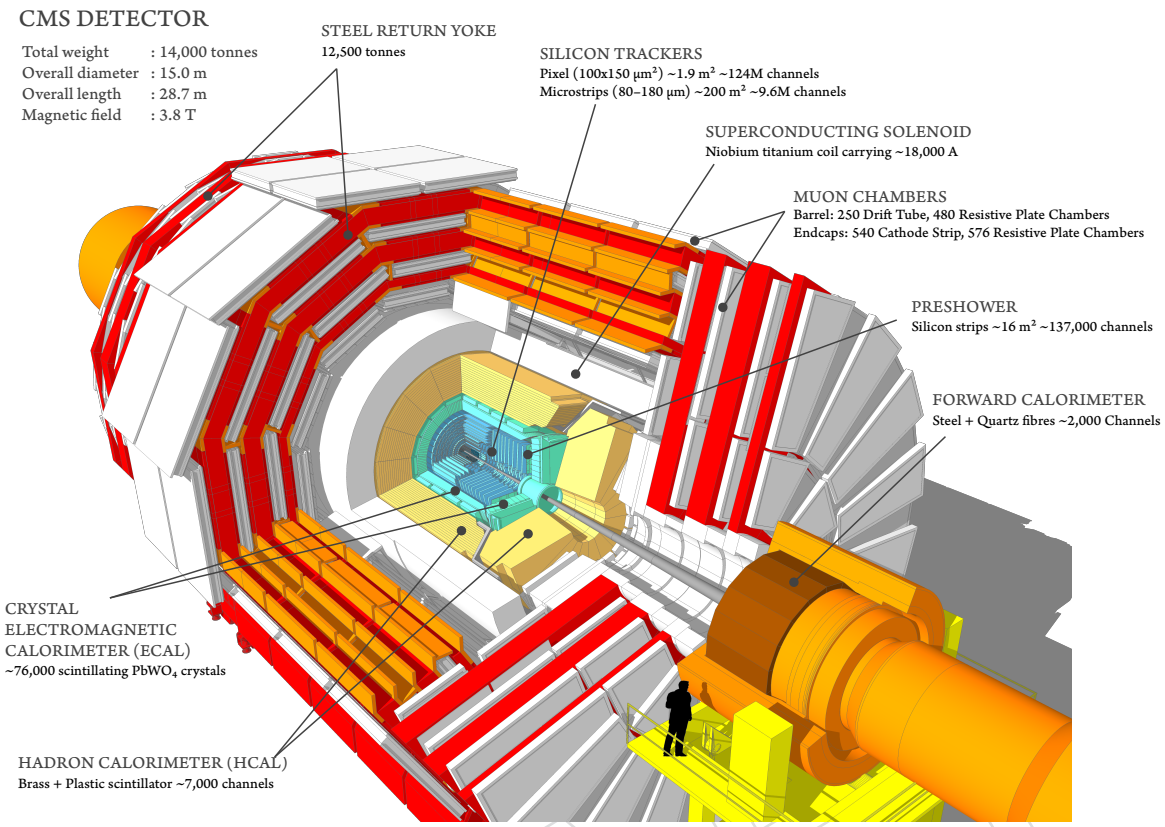

Figure 2: The CMS detector for the data-taking period 2017–2018.

tified as ECAL energy clusters not linked to the extrapolation of any charged-particle trajectory into the ECAL. Prompt electrons and nonprompt electrons, which come from photon conversions in the tracker material or b hadron semileptonic decays, are identified as a primary charged-particle track with potentially more than one ECAL energy cluster, corresponding to the track, as extrapolated to the ECAL and possible bremsstrahlung photons emitted by the electron as it traverses the tracker material. Prompt muons and nonprompt muons, which come from b hadron semileptonic decays, are identified as tracks in the central tracker consistent with either a track or several hits in the muon system, and associated with energy deposits in the calorimeter compatible with the muon hypothesis. Charged hadrons are identified as charged-particle tracks neither identified as electrons, nor as muons. Finally, neutral hadrons are identified as HCAL energy clusters not linked to any charged-hadron trajectory, or as a combined ECAL and HCAL energy excess with respect to an expected charged-hadron energy deposit.

The energy of photons is obtained from the ECAL measurement. The energy of electrons is determined from a combination of the track momentum at the main interaction vertex, the corresponding ECAL cluster energy, and the energy sum of all bremsstrahlung photons assigned to the track. The energy of muons is obtained from the corresponding track curvature. The energy of charged hadrons is determined from a combination of the track momentum and the corresponding ECAL and HCAL energies, corrected for the response function of the calorimeters to hadronic showers. Finally, the energy of neutral hadrons is obtained from the corresponding corrected ECAL and HCAL energies. The reconstruction of each of these individual physics objects is described below.

Electrons: Electrons are identified and measured in the range $|\eta| < 2.5$. The momentum res-

olution for electrons with transverse momentum $p_T \approx 45\,\text{GeV}$ from $Z \to ee$ decays ranges 1.6–5.0% in Run 2, and 1.7–4.5% in Run 1. The resolution is better in the barrel region than in the endcaps, and also depends on the bremsstrahlung energy emitted by the electron as it traverses the material in front of the ECAL [14–16].

The dielectron mass resolution for $Z \to ee$ decays is in the ranges 1.2–2.0% (1.9% in Run 1) when both electrons are in the ECAL barrel, and 2.2–3.2 (2.9% in Run 1) otherwise, the exact values depending on the bremsstrahlung energy emitted by the electrons and the data-taking year [14, 16].

Photons: Photons are identified and measured in the range $|\eta| < 2.5$. In the barrel section of the ECAL, an energy resolution of about 1% is achieved for unconverted or late-converting photons in the tens of GeV energy range. The energy resolution of the remaining barrel photons is about 1.3% up to $|\eta| = 1$, worsening to about 2.5% by $|\eta| = 1.4$. In the endcaps, the energy resolution is about 2.5% for unconverted or late converting photons, and 3–4% for the rest [17].

The diphoton mass resolution, as measured in $H \to \gamma\gamma$ decays, is typically in the 1–2% range, depending on the topology of the photons [18].

Muons: Muons are identified and measured in the range $|\eta| < 2.4$, with detection planes made using three technologies: drift tubes, cathode strip chambers, and resistive-plate chambers. The single-muon trigger efficiency exceeds 90% over the full η range, and the efficiency to reconstruct and identify muons is greater than 96%. Matching muons identified in the muon detection system to tracks measured in the silicon tracker results in a p_T resolution, for muons with p_T up to 100 GeV, of 1% (1.3–2.0% in Run 1) in the barrel and 3% (6% in Run 1) in the endcaps. For muons with p_T up to 1 TeV, the p_T resolution in the barrel is better than 7% (10% in Run 1) [19, 20].

Taus: Hadronic τ decays (τ_h) are reconstructed from jets, using the hadrons-plus-strips algorithm [21], which combines one or three tracks with energy deposits in the calorimeters, to identify the tau lepton hadronic decay modes. Neutral pions are reconstructed as strips with a dynamic size in η–ϕ (where ϕ is the azimuthal angle about the beam axis, measured in radians) from reconstructed electrons and photons, where the strip size varies as a function of the p_T of the electron or photon candidate.

To distinguish τ_h decays from jets originating from the hadronization of quarks or gluons, and from electrons or muons, the DEEPTAU algorithm is used [22]. Information from all individual reconstructed particles near the (τ_h) axis is combined with properties of the (τ_h) candidate and the event. The rate of a jet to be misidentified as τ_h by the DEEPTAU algorithm depends on the p_T and quark flavour of the jet. Based on simulated events from W boson production in association with jets, the misidentification rate has been estimated to be 0.43% for an identification efficiency for genuine τ_h of 70%. The misidentification rate for electrons (muons) is 2.60 (0.03)% for a genuine τ_h identification efficiency of 80 (>99)%.

Primary vertex: In Run 2, the primary vertex (PV) is taken to be the vertex corresponding to the hardest, i.e. highest p_T, scattering in the event. The vertex position is evaluated from tracking information alone, using a vertex fit procedure on a collection of charged-particle tracks that are compatible with originating from the same interaction, as described in Section 9.4.1 of Ref. [23]. In Run 1, the reconstructed vertex with the largest value of summed charged-particle track p_T^2 was taken to be the PV.

Jets: Using the particle-flow global event reconstruction, hadronic jets are clustered from the reconstructed particles, using the infrared- and collinear-safe anti-k_T algorithm [24, 25]. Typi-

DRAFT

cally, a distance parameter that measures the angular separation between constituents in the jet and is defined as $\Delta R = \sqrt{(\Delta y)^2 + (\Delta \phi)^2}$ of 0.4 is used ($\Delta R = 0.5$ in Run 1), but also $\Delta R = 0.8$ is used to identify merged jets from hadronic decays of Lorentz-boosted particles, e.g. the W boson. Jet momentum is determined as the vectorial sum of all particle momenta in the jet, and is found from simulation to be, on average, within 5–10% of the true momentum over the entire p_{T} spectrum and detector acceptance.

Additional tracks and calorimetric energy depositions resulting from particles produced in additional pp interactions within the same or nearby bunch crossings (pileup) can add to the jet momentum. To mitigate this effect, charged particles identified as originating from pileup vertices are discarded and an offset correction is applied to correct for remaining contributions. Jet energy corrections are derived from simulation to bring the measured response of jets on average to that of jets constructed directly from the simulated particles. In situ measurements of the momentum balance in dijet, $\gamma +$ jet, $\mathrm{Z} +$ jet, and multijet events are used to correct any residual differences in the jet energy scale (JES) between data and simulation [26]. Additional selection criteria [27] are applied to each jet to remove jets that are potentially affected by anomalous contributions or reconstruction failures.

In many cases, the pileup-per-particle identification (PUPPI) algorithm [28, 29] is used to mitigate the effect of pileup, utilizing local shape information, event pileup properties, and tracking information. A local shape variable distinguishes between collinear particles originating from the hard scatter and the (on average) softer diffuse particles originating from the additional pp interactions. Charged particles identified as originating from pileup vertices are discarded. For each neutral particle, a local shape variable is computed using the surrounding charged particles compatible with the PV within the tracker acceptance ($|\eta| < 2.5$), and using both charged and neutral particles in the region outside of the tracker coverage. The momenta of the neutral particles are then rescaled according to the probability that they originated from the PV deduced from the local shape variable, superseding the need for jet-based pileup corrections [28].

In a few early Run 1 analyses, prior to the full deployment of the particle-flow global event reconstruction methodology, hadronic jets were reconstructed from the energy deposits in the calorimeter, clustered using the anti-k_{T} algorithm with a distance parameter of $\Delta R = 0.5$.

Missing transverse momentum: The missing p_{T} vector $\vec{p}_{\mathrm{T}}^{\,\mathrm{miss}}$ is computed as the negative vector sum of the transverse momenta of all the particle-flow candidates in an event, and its magnitude is denoted as $p_{\mathrm{T}}^{\mathrm{miss}}$ [30]. The $\vec{p}_{\mathrm{T}}^{\,\mathrm{miss}}$ is modified to account for corrections to the energy scale of the reconstructed jets in the event. In some cases, the PUPPI algorithm is applied to reduce the pileup dependence of the $\vec{p}_{\mathrm{T}}^{\,\mathrm{miss}}$ observable. The $\vec{p}_{\mathrm{T}}^{\,\mathrm{miss}}$ is computed from the particle-flow candidates weighted by their probability to originate from the PV [30]. Several early analyses used a $\vec{p}_{\mathrm{T}}^{\,\mathrm{miss}}$ calculated from the calorimeter information alone, using calorimeter towers.

Heavy-flavour identification: A variety of algorithms are used to identify jets that originate from heavy-flavour b and c quarks. The algorithms may incorporate primary and secondary vertex information; track kinematics, impact parameter and quality information; decay product information that is indicative of a heavy-flavour hadron decay, such as the presence of charged leptons with high impact parameter; or partial or full reconstruction of heavy-flavour hadrons; and various combinations of these ingredients.

The heavy-flavour jet identification algorithms used in the analyses presented in this Report are listed below. Typically these algorithms are applied to the constituents of a particle-flow jet and produce an estimator for the probability of the jet to originate from a b or c quark.

- SSV, cimple secondary vertex algorithm [31]: SSV uses the significance of the dis-

DRAFT

placement from the PV of a reconstructed secondary vertex (the ratio of the displacement to its estimated uncertainty) as the discriminating variable.

- IVF, inclusive vertex finder [32, 33]: IVF identifies vertices with high diaplcement significance independently of jet reconstruction, by examining vertices around seed tracks with high impact parameter significance S_{IP} (the ratio of the track impact parameter to its estimated uncertainty).
- CSV, combined secondary vertex algorithm for 7 TeV [31] and 8 TeV [34]: CSV uses secondary vertex information as in SSV, "pseudo vertices" formed from tracks with high S_{IP}, in addition to directly using the track S_{IP} information to form a likelihood-based discriminator.
- CSVv2, combined secondary vertex algorithm for 13 TeV [35]: CSVv2 is based on CSV and combines the information of displaced tracks with the information on secondary vertices associated with the jet using a multivariate technique.
- DEEPCSV [35]: A deep machine-learning-based secondary vertex algorithm using IVF vertices and tracks as input. Probability outputs are provided for bottom-, charm- and light-flavoured or gluon jets and can be combined to form the bottom or charm jet discriminants.
- DEEPJET [35, 36]: A deep neural network algorithm based on the properties of charged and neutral particle-flow jet constituents, as well as 12 properties of secondary vertices associated with the jet.
- D hadron tag: Identifies a fully reconstructed D hadron within a jet based on the secondary vertex and mass reconstruction of the decay products.
- μ tag: Identifies a muon found in the candidate jet with large S_{IP} and representing a significant portion of the total jet momentum.

Jet substructure: Finally, massive particles such as top quarks, Higgs bosons, and W and Z bosons that decay to jets can be identified in boosted topologies using algorithms that make use of jet substructure, based on jets reconstructed with a distance parameter of 0.8. These algorithms are described where the specific analyses that use them are discussed.

Intact scattered protons: The PPS makes it possible to measure the four-momentum of scattered protons, along with their time-of-flight from the interaction point (IP). The proton momenta are measured by the two tracking stations in each arm of the spectrometer.

3 Event simulation and cross section calculation

The measurement of cross sections and their comparison with the predictions of the SM requires precise calculation of cross sections and the production of simulated events using Monte Carlo (MC) techniques. Monte Carlo simulation of signal and background events involves a sequence of distinct operations. First, occurrences of the hard scattering process are generated modelling the full distribution of the possible kinematics of the partons (quarks and gluons) and other elementary particles (leptons and gauge bosons) in the process of interest. This can be achieved either by attaching a weight corresponding to the probability of the kinematic state generated or by producing the states according to their kinematic probability. The calculations are performed by factorization of the problem into a perturbatively calculable parton scattering process, and generalized functions that are obtained semi-empirically with fits to data. The most essential of these functions, used in every calculation, are the parton distribution functions (PDFs), which describe the momentum distribution of the partons within the collid-

DRAFT

ing protons. They represent the probability densities to find a parton carrying a momentum fraction x at a given energy scale (expressed as the squared momentum transfer Q^2), and are derived from fits to a large number of cross section measurements, generally measurements made by many experiments, over a large range of Q^2 and x values. The hard scattering is modelled by first sampling the probability distribution of the PDFs to take account of the kinematics of the incoming partons in the proton. The final-state partons produced by the hard scattering are evolved down to some energy scale limit in a "parton shower" (PS) process that simulates the radiation of additional quarks and gluons, using leading logarithmic approximations. The resulting partons are then hadronized—assembled into hadrons—producing jets of final-state particles. This full process is known as hadronization. Short-lived particles are decayed. An "underlying event" (UE), including, e.g. multiparton interactions (MPI), is added simulating the production of particles from the partons in the colliding protons that were not directly involved in the hard scattering process (and properly accounting for the kinematics of the initial state partons of the process). The UE parameters in event generators are tuned so that observed features of data particularly sensitive to the contribution of the underlying event, such as charged-particle multiplicity and transverse momentum densities, match those in simulated events, as described, e.g. in Ref. [37]. Finally, the particles are tracked through the detector, modelling their interactions with the detector elements, followed by simulation of the generation of electrical signals and their digitization to form a recorded event.

Table 2 lists the MC simulation programs used for analyses included in this Report. General-purpose MC event generators, such as PYTHIA, which aim to describe all final state particles emerging from a pp collision, usually rely on only the Born matrix element for the perturbative calculation of the hard scattering. Increased precision may be achieved by using dedicated MC programmes that aim to better model some subset of hard scattering processes, or some aspect of a process, usually by using an improved level of approximation in QCD perturbative expansion: next-to-leading order (NLO), next-to-next-to-leading order (NNLO), or even N^{3}LO (i.e. adding another "next-to"). These generators modelling higher-order Feynman diagrams are thus usually called matrix element (ME) generators. When dedicated generators are used, the hadronization, and provision of the UE must be accomplished by a more general event-generator program, such as PYTHIA or HERWIG, that can model the hadronization, particle decay, final-state radiation, and UE, in addition to the hard-scattering process. Simulation of the interactions of the particles with the detector is performed by GEANT4, using a detailed geometrical model of the CMS detector, whereas the simulation of signal generation and digitization is handled by the CMS software.

A list of the sets of PDFs used for analyses included in this Report is shown in Table 3, categorized by the collaboration that produced them.

4 Measurements of quantum chromodynamics

The strong interaction between quarks is mediated by the gluons and is described by QCD, which is a quantum gauge theory based on a non-Abelian $SU(3)_C$ symmetry group, operating with three colour charges. Quarks and gluons are the fundamental constituents of the proton, which makes QCD physics ubiquitous at a hadron collider. The non-Abelian nature of QCD, which leads to a self-coupling of the massless gluon, results in a renormalization scale dependence (running) of strong coupling, the leading of the two major properties of the strong interaction. On the one hand, the asymptotic freedom at large scales (or small distances) allows for a perturbative description of quasi-free quarks. On the other hand, at small scales (large distances), the coupling becomes too large for perturbative calculations to be applied.

DRAFT

Table 2: Monte Carlo programs used by analyses included in this Report.

Cross section calculation	
DYTURBO	[38]
FEWZ	[39–41]
γ + jet	[42, 43]
HELAC-ONIA	[44, 45]
MATRIX	[46]
NLLJET	[47]
NLOJET++ (with FASTNLO)	[48, 49] ([50, 51])
NNLOJET (with FASTNLO)	[52–54] ([50, 51])
OPENLOOPS	[55]
Hard-scattering process generation	
BLACKHAT	[56]
COMPHEP	[57]
HJ-MINLO	[58–60]
JHUGEN	[61–65]
MCFM	[66, 67]
MADGRAPH 5, MADGRAPH5_AMC@NLO	[68–70]
NNLOPS	[71–73]
OPENLOOPS	[74–77]
PHOTOS	[78]
POWHEG, POWHEG BPX	[79–81]
VBFNL0, VBFNL0 2.7	[82–84]
Full particle event generation	
CASCADE 3	[85]
HERWIG 7, HERWIG++	[86, 87]
PHOJET	[88]
PYTHIA 6, PYTHIA 8	[89–91]
SHERPA 1, SHERPA 2	[92–96]
Particle transport and detector interaction	
GEANT4	[97]

DRAFT

Table 3: Sets of PDFs used for analyses included in this Report.

ABKM/ABM/ABMP Collaboration	
ABKM09	[98]
ABM11	[99]
ABMP16	[100, 101]
CTEQ-Jefferson Lab Collaboration	
CJ15	[102]
CTEQ-TEA Collaboration	
CT10	[103, 104]
CT14	[105]
CT18	[106]
HERAPDF Collaboration	
HERAPDF1, 1.5	[107]
HERAPDF2.0	[108]
MSTW/MMHT/MSHT Collaboration	
MSTW 2008 NLO, NNLO	[109]
MMHT2014	[110]
MSHT2020 NLO, NNLO	[111]
MSHT20an3lo	[112]
NNPDF Collaboration	
NNPDF 2.0	[113]
NNPDF 2.1	[114]
NNPDF 2.3	[115]
NNPDF 3.0	[116]
NNPDF 3.1	[117]
NNPDF 3.1luxQED	[118]
NNPDF 4.0	[119]
Transverse momentum dependent PDFs	
PB-TMD PDFs	[120–122]

DRAFT

This large-α_S region of the confinement can be only described phenomenologically. In many cases of interest at the LHC, the interactions involve large momentum transfers, where the theory is perturbative. However, the nonperturbative aspects of QCD are still relevant for the understanding of large momentum transfer physics.

This section presents a selection of measurements essential for probing QCD in nonperturbative and perturbative regimes. The measurements include PDF constraints, determinations of the strong coupling constant α_S, multiple-parton interaction (MPI) effective cross sections, and the total inelastic cross section. High-p_T measurements span total, inclusive differential, and exclusive differential measurements of jet production cross sections. In differential measurements regions of phase space can be chosen, typically involving high jet multiplicities, to test the predictions of recent higher-order QCD calculations. Also, the high-p_T jet data collected by the CMS experiment offer sensitivity to deviations from the SM predictions that may occur in a diverse set of BSM scenarios involving heavy new particles or new forces. Measurements of the QCD jet production in association with heavy objects, such as vector bosons (as discussed in Sections 5.1.4, 5.1.5), top quarks (Section 6.6), and Higgs bosons (Section 7.2) are detailed in the respective sections on those topics.

4.1 Total inelastic cross sections

The total pp cross section includes elastic- and inelastic-scattering components. In elastic scattering, the protons scatter via QCD or quantum electrodynamics (QED) processes without the proton dissociating (breaking up) or producing any additional particles. Inelastic scattering includes diffractive and nondiffractive interactions. In the diffractive events, the protons may emerge intact, excited, or dissociate into low-mass states, and these interactions are mediated by the exchange of colour-singlet objects such as the Pomeron (for QCD-induced) or a photon (for QED-induced) processes [123] (see section 20). In the nondiffractive case, the partons in the colliding protons interact with sufficient momentum transfer to break up the protons. Processes included in the inelastic component of the total pp cross section are the primary subject of this Report. They encompass interactions with large momentum transfer (Q), and most cases where heavier SM particles and possibly BSM particles may be produced. The total cross section and its components are not analytically calculable and instead fit from lower-energy data, and extrapolated to the LHC energies. The components of the total pp collision cross section can be described by nonperturbative phenomenological models based on unitarity and analyticity principles [124]. These models have large uncertainties when extrapolating to TeV-scale collision energies and the measurement of these cross sections at new energies is an essential input to improving the reliability of the predictions. The measurement of the inelastic pp interactions is necessary to address many issues essential for measuring cross sections. For example, the inelastic cross section determines probability and properties of additional inelastic collisions in the same or adjacent bunch crossings, referred to as pileup, which is necessary for interpreting the performance of nearly all physics object reconstruction at hadron colliders. Similarly, it enhances our understanding of the hadronic recoil from hard interactions, which is essential in modelling the p_T distributions of massive SM particles. Finally, understanding the inelastic cross section is necessary for the estimation of the pp collision luminosity, a critical component in the cross section measurements.

The CMS experiment has measured the inelastic component of the total pp cross section in 7 [125] and 13 TeV [126] pp collisions. The measurements were done for events with the dissociation system masses exceeding 15.7 GeV using the 7 TeV data. In the 13 TeV analysis, the thresholds were above 4.1 GeV and 13 GeV for dissociation masses at negative and positive pseudorapidities, respectively. The extension of the 13 TeV analysis phase space to include

DRAFT

very low dissociated masses was enabled by utilizing the CMS CASTOR forward calorimeter. The measurements reported here are for a common phase space delineated by the requirement that the longitudinal momentum loss fraction from one proton, ξ, exceeds 5×10^{-6}. This corresponds to the mass of the larger disassociated proton system, m_X, being greater than 16 GeV, such that $\xi = m_X/\sqrt{s} > 5 \times 10^{-6}$. At 7 TeV, the CMS Collaboration measured $\sigma_{in} = 60.2 \pm 0.2\,(\text{stat}) \pm 1.1\,(\text{syst}) \pm 2.4\,(\text{lumi})$ mb and at 13 TeV $\sigma_{in} = 67.5 \pm 0.8\,(\text{syst}) \pm 1.6\,(\text{lumi})$ mb with a negligible statistical uncertainty. These measurements are compared with predictions of general-purpose MC generators PYTHIA 6.4 [89], 8 [90, 91] for a variety of generator parameter tunes; generators specific to large rapidity gap physics PHOJET [88]; and generators used in cosmic ray physics QGSJET-II [127, 128], SIBYLL [129], and EPOS [130]. The agreement of the theory predictions with the data is good for almost all the generators at 7 TeV, whereas at 13 TeV most generators overestimate the cross section by about 10%, which is attributed to the mismodelling of the low-mass diffractive processes. The results are consistent with those measured by the TOTEM Collaboration in the same fiducial phase space [131–134]. Fits to lower-energy cross section data performed before the start of the LHC operations [135] by the COMPETE Collaboration [136], which predicted the total hadronic cross sections from GeV energies to the 57 TeV energy measured by the Pierre Auger Collaboration [137], are in agreement with these measurements. The CMS measurements of fiducial inelastic production cross sections are shown in Fig. 1 together with total or fiducial cross sections of all other processes covered in this Report.

4.2 Jet production cross section measurements

Jet production measurements at the LHC test QCD over a large range of energies. The statistical power of the data allows for comparison of QCD predictions to precise total, differential, and multidifferential measurements. State-of-the-art calculations in QCD jet physics extend to NNLO QCD and NLO EW accuracy in the perturbative expansion and may include additional final-state partons in the ME predictions at a given order.

4.2.1 Inclusive fiducial jet production cross section measurements

Inclusive jet production cross sections have been measured as functions of basic kinematic distributions at 2.76 [138, 139], 5.02 [140], 7 [139, 141–144], 8 [139], and 13 [145, 146] TeV. The measurements typically present the inclusive jet production cross section as a function of p_T in intervals of rapidity y. The measurement is inclusive in that each jet that meets the rapidity and p_T criteria contributes to the cross section of the corresponding bin. The events including those jets may contain any number of additional jets or other final-state particles. Multiple jets in a collision event may contribute to the cross section according to their transverse momenta and rapidity. These measurements have been used to test NLO and NNLO QCD predictions.

The conceptually simplest possible observable in high-p_T QCD physics is a fiducial inclusive cross section for the total production of all jets above a given p_T threshold and within a given rapidity range. The jet cross sections at 2.76 [138], 7 [142], 8 [139], and 13 [146] TeV for inclusive production of jets that satisfy $p_T > 133$ GeV and $|y| < 2.0$ are reported in Table 4. Jets are clustered from particle-flow objects using the anti-k_T algorithm with a distance parameter of $\Delta R = 0.7$. These cross sections are calculated by integrating the differential measurements presented in the original publications, taking into account the correlation of systematic uncertainties between the bins when calculating the total systematic uncertainty. These results are compared with NNLO QCD predictions calculated using the NNLOJET programme [52–54] with FASTNLO [50, 51] and the CT18 [106] PDF set, with nonperturbative (NP) corrections applied based on MC generators, such as PYTHIA 6, PYTHIA 8, or HERWIG++ [86, 87] using

the state-of-the-art UE generator parameter sets (so called "tunes") derived at the time of each publication. These generators simulate UE and hadronization effects. Several MC generators are used in each publication to derive NP corrections and associated uncertainties. Finally, the QCD predictions are corrected for the EW effects [147]. These predictions in a single phase space region have improved statistical and systematic precision compared to what is achievable in more restricted phase space regions or differential measurements.

Table 4: The measured inclusive fiducial jet production cross sections for four pp collision energies for inclusive production of anti-k_T $R = 0.7$ jets satisfying $p_T > 133\,\text{GeV}$ and $|y| < 2.0$. Results are compared with predictions at NNLO QCD and NLO EW precision. The statistical uncertainty of the theory predictions is negligible.

$\sqrt{s}$ (TeV)	σ(jet) (pb)	σ^{SM}(jet) (pb)
2.76 [138]	$787 \pm 7\,(\text{stat}) \pm 49\,(\text{syst})$	$777\,^{+40}_{-33}\,(\text{syst})$
7 [142]	$8520 \pm 90\,(\text{stat}) \pm 610\,(\text{syst})$	$8760\,^{+390}_{-440}\,(\text{syst})$
8 [139]	$11\,220 \pm 40\,(\text{stat})\,^{+610}_{-600}\,(\text{syst})$	$11\,650\,^{+270}_{-330}\,(\text{syst})$
13 [146]	$15\,230 \pm 70\,(\text{stat}) \pm 700\,(\text{syst})$	$14\,980\,^{+420}_{-570}\,(\text{syst})$

4.2.2 Inclusive differential jet production cross section measurements

The analysis of inclusive jet production at 13 TeV [146] includes comparisons to several perturbative QCD (pQCD) predictions. The NLO prediction using NLOJET++ [48, 49] and FASTNLO [50, 51] is further complemented by next-to-leading logarithmic (NLL) calculations using logarithmic resummation techniques. Two classes of logarithmic terms are relevant to jet physics are resummed using the NLLJET programme [47]; those that depend on the jet radius and the so-called threshold logarithms. The latter involve logarithmic terms created when a jet just fails to pass the threshold to be considered as a jet. In addition, these cross section measurements are compared with the NNLO predictions obtained using the NNLOJET programme. This is the first analysis of jet production in pp collisions that is compared to NNLO predictions. These QCD predictions at NLO+NLL and NNLO accuracy are computed by using different available PDF sets, e.g. CT14 [105], NNPDF3.1 [117], MMHT2014 [110], ABMP16 [100, 101], and HERAPDF2.0 [108], evaluated at NLO or NNLO, respectively. The pQCD predictions are augmented with the EW corrections [147]. Finally, the predictions are corrected for NP effects using a correction derived from the average of the HERWIG++ (EE5C tune [148]) and PYTHIA 8 (CP1 tune [37]) simulations. The NP factors correct for the hadronization and UE effects that are not included in the pQCD predictions. The inclusive jet production cross section at 13 TeV, measured as a function of p_T in four bins of rapidity, is shown in Fig. 3. The agreement seen in the figure is excellent in all rapidity regions and spans nine orders of magnitude in cross section.

4.2.3 Exclusive differential measurements of jet production cross sections

The CMS experiment has performed a wide array of differential cross section measurements of jet production at all the collision energies at which the LHC operated. Of particular interest are measurements that isolate areas of phase space where current cross section calculations and MC simulations do not model the data well. For instance, let's consider a case of high-p_T

DRAFT

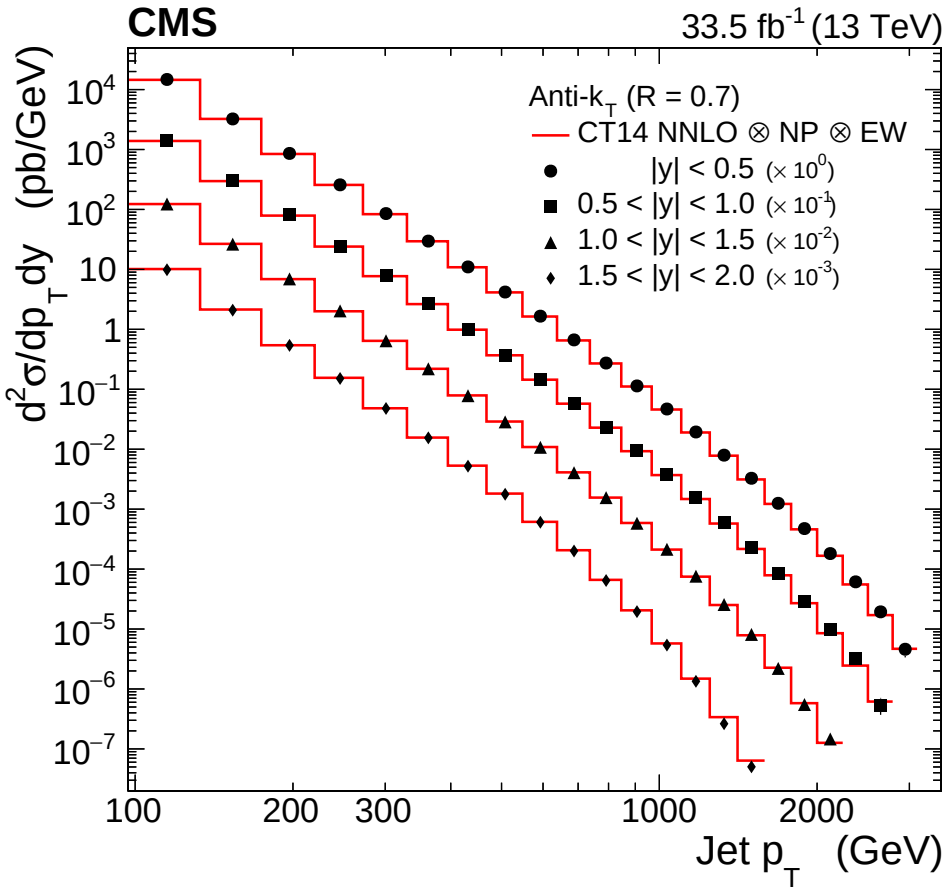

Figure 3: The inclusive jet production cross sections as functions of the jet transverse momentum p_{T} measured in intervals of the absolute rapidity $|y|$. The cross section obtained for jets clustered using the anti-k_{T} algorithm with $\Delta R = 0.4$ is shown. The results in different $|y|$ intervals are scaled by constant factors for presentation purposes. The data in different $|y|$ intervals are shown by markers of different styles. The statistical uncertainties are too small to be visible; the systematic uncertainties are not shown. The measurements are compared with NNLO QCD predictions (solid line) using the CT14nnlo PDF set and corrected for EW and NP effects. Figure and caption taken from Ref. [146].

jets where the two highest p_T jets are not back-to-back because of multiple additional jet emissions. In this topology, no single MC prediction can model the jet multiplicity distribution for all ranges of azimuthal angle between the two highest p_T jets [149] (as shown in Fig. 4). The predictions shown in the figure use NLO MCs and matched PS generators at NLO including dijet predictions from MADGRAPH5_aMC@NLO: MG5_aMC+Py8 (jj) and MG5_aMC+CA3 (jj), as well as the NLO three-jet prediction of MG5_aMC+CA3 (jjj). The NLO prediction includes MEs with one additional real emission of a parton at LO accuracy, effectively generating events with up to three or four hard partons. Parton showering is performed with PYTHIA 8 (Py8) and CASCADE3 [85] (CA3). The CA3 prediction uses transverse momentum dependent (TMD) PDFs [120] based on the parton-branching method (PB-TMD PDFs)[121, 122] in the PS model. In this analysis initial-state p_T is generated and PB-TMD PDF-dependent PS is performed using the CASCADE 3 MC simulation [85] and compared with predictions using standard PS simulations. The TMD PDFs assess the p_T of hard-scattering system as it recoils against the UE physics involving the rest of the partons. These TMD PDFs implemented in the CA3 PS describe the data as well as do the standard PS methods, but without the need for tunable parameters. In general, the MC predictions fail to model the data for events with the jet multiplicity greater than the number of hard partons generated in the ME predictions. Extending calculations and simulations to NNLO with matched NNLO PS generation and/or a larger number of partons simulated at the ME level would be expected to improve the agreement of the prediction with the data in high jet multiplicity topologies. Improved agreement with the predictions would increase the sensitivity of BSM physics searches using final states with high jet multiplicities. However, improvements in methods of NNLO calculation for processes with high jet multiplicity are necessary to make them widely available for all pp collision processes.

4.2.4 Additional differential measurements of jet production cross sections

The full array of differential measurements performed by the CMS experiment is too extensive to report here. Only selected examples were discussed above. In addition, many measurements have been done that investigate lower-p_T QCD physics and flavour physics. Other differential measurements of high-p_T jet production cross sections performed by CMS not already discussed are listed below. Each analysis includes a rich set of comparisons to state-of-the-art QCD predictions

- Differential dijet production *vs.* dijet invariant mass and jet rapidity at 7 TeV [150]
- Dijet azimuthal decorrelations at 7 [151], 8 [152], and 13 TeV [153].
- Ratio of two- to three-jet cross sections as a function of the total jet transverse momentum at 7 TeV [154].
- Shape, transverse size, and charged-hadron multiplicity of jets at 7 TeV [155]
- Jet mass in dijet and W/Z+jet (7 TeV only) events, 7 [156] and 13 [157] TeV.
- Azimuthal separation between the second- and third-leading jets in nearly back-to-back topologies at 7 TeV [158].
- Study of hadronic event-shape variables, 7 [159] and 13 [160] TeV.
- Topological observable in inclusive three- and four-jet events at 7 TeV [161].
- Jet charge at 8 TeV [162].
- Azimuthal separation between the leading and second-leading jets in nearly back-to-back jet topologies in inclusive two- and three-jet events at 13 TeV [163].
- Dependence of inclusive jet production on the anti-k_T distance parameter at 13 TeV [164].
- Study of quark and gluon jet substructure in Z+jet and dijet events at 13 TeV [165].

DRAFT

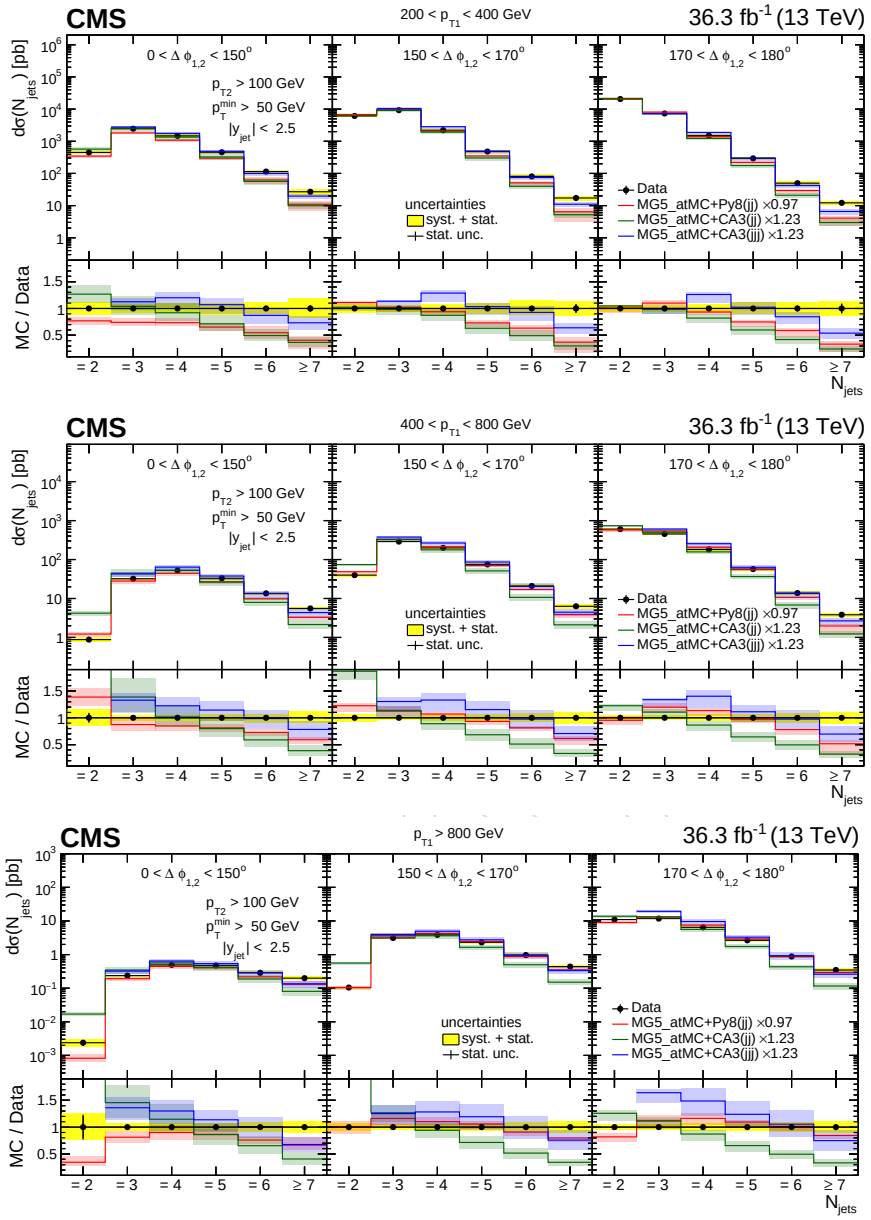

Figure 4: Differential cross section of jet production as a function of the exclusive jet multiplicity (inclusive for 7 jets) in bins of p_{T} and $\Delta\phi_{12}$. The data are compared with the NLO dijet predictions from MADGRAPH5_aMC@NLO: MG5_aMC+Py8 (jj) and MG5_aMC+CA3 (jj), as well as the NLO three-jet prediction of MG5_aMC+CA3 (jjj), where parton showering is performed by PYTHIA 8 (Py8) and CASCADE3 [85] (CA3). The vertical error bars correspond to the statistical uncertainty, the yellow band shows the total experimental uncertainty. The shaded bands show the uncertainty from a variation of the normalization and factorization scales. The predictions are normalized to the measured inclusive dijet cross section using the scaling factors shown in the legend. Figure taken from Ref. [149].

4.3 Proton PDFs

Description of the proton structure, expressed in terms of PDFs, plays a central role in the interpretation of all the processes in pp collisions at the LHC. Protons are composite particles consisting of valence up- and down-flavoured quarks, gluons, and contributions from other quarks and antiquarks collectively known as the sea quarks. High-energy pp collisions probe the structure of the proton at small distance scales. Proton-proton collisions at high energies are described by the QCD factorization theorem [166]. At a certain factorization scale, the pp cross section may be represented as a convolution of a (hard) partonic process, where individual, asymptotically-free partons from both colliding protons interact, with the parton distributions. The parton (quark and gluon) distributions, are functions of the fraction x of the proton momentum carried by the parton involved in the interaction, and the factorisation scale. The scale dependence is encoded in the Dokshitzer–Gribov–Lipatov–Altarelli–Parisi (DGLAP) [167–174] evolution equations, which are known up to N^3LO. The dependence of PDFs on x needs to be extracted from the experimental data. Most of the information on the PDFs is provided by measurements in deep-inelastic scattering experiments data from either HERA-I [107] or the combined HERA-I and HERA-II data [108]. Production of jets, top quarks, and weak bosons at the LHC provides additional sensitivity to the PDFs. Using corresponding cross section measurements, the PDFs and the strong coupling constant α_S can be extracted with improved precision. PDFs have been extracted at LO, NLO, NNLO, and even at approximate N^3LO, as well as in more complex systems, such as nuclei.

In practice, the PDFs are obtained in a course of a QCD analysis, assuming a certain x-dependence of the PDFs at a starting evolution scale. In such a QCD fit, the measurements are confronted with the corresponding pQCD predictions at highest available order and the parameters driving the x behaviour of each PDF are obtained. Besides a comprehensive QCD analysis where the PDFs are fitted, sometimes it is useful to investigate a possible impact of a new measurement on an uncertainty in already existing PDF without the re-evaluating PDF . This is done by performing a so-called profiling analysis. In the CMS experiment, the open-source QCD analysis framework xFitter (former HERAFitter) [175, 176] are used for PDF fits and profiling. In a full PDF fit, together with the PDFs, further QCD or EW parameters such as quark masses, strong coupling or EW mixing angle, can be obtained and the correlations of these parameters with the PDFs are mitigated. Furthermore, once contributions of new physics are included (e.g. via methods of effective field theory) in addition to the SM the cross section prediction, their couplings can be constrained together with the PDFs and SM parameters.

4.3.1 Overview of CMS constraints on PDFs

The CMS Collaboration has explored the sensitivity of different processes to the PDFs and SM parameters. The CMS Drell–Yan measurements have improved constraints on the valence quark distributions, while production of $t\bar{t}$ and (multi)jets is particularly sensitive to the mass of the top quark, the gluon distribution, and the α_S. The associated production of W boson with a charm quark (W+c) is the only process at a hadron collider directly probing the strange content of the proton quark sea. The CMS experiment has pioneered the measurement of W+c production at a hadron collider and its interpretation in terms of the strangeness distribution. A list of CMS analyses used to constrain PDFs is given in Table 5. For each analysis the QCD order of the analysis and a PDF distribution of interest that is constrained by the inclusion of CMS data is listed. To date, the majority of these measurements are used by the global PDF fit collaborations. Finally, comparisons of cross section measurements with the predictions employing various PDFs are discussed in the relevant sections.

DRAFT

Table 5: The CMS analyses where PDF fits were performed. The table lists the final state and distributions considered, the pp collision energy, the HERA data set used or global PDF provided, the QCD perturbative order of the fit, and the most constrained PDFs. Whenever data from multiple analyses are used, the first analysis listed contains the PDF extraction. In the 13 TeV analysis the inclusive jet data are used in an NNLO PDF fit, whereas the inclusive jet and $t\bar{t}$ data are used in an NLO PDF fit.

Analysis	$\sqrt{s}$ (TeV)	HERA Data or PDF	QCD order	Best PDF constraint
W charge asym. [177], W+c [178]	7	HERA-I	NLO	u, d, s
Inclusive jet [144]	7	HERA-I	NLO	gluon
W charge asym. [179]	8	HERA-I + II	NLO	u and d
Inclusive jet [139]	8	HERA-I + II	NLO	gluon
3D dijet [180]	8	HERA-I + II	NLO	gluon
Inclusive jet [146], $t\bar{t}$ [181]	13	HERA-I + II, CT14nnlo	NNLO,NLO	gluon
Dijet mass [182]	13	HERA-I + II	NNLO	gluon

4.3.2 The PDF constraints from jet production measurements

CMS measurements of multi-differential inclusive jet and dijet cross sections at different centre-of-mass energies were extensively used to constrain the PDFs and the value of α_S (presented in Section 4.4). They include double-differential inclusive jet analysis at 7 [144], 8 [139], and 13 TeV [146]; triple-differential dijet analysis at 8 TeV [180]; and an analysis of dijet mass at 13 TeV [182]. These data were included in comprehensive QCD analyses together with the measurements of the DIS cross sections, available at the date of each analysis. Since the NNLO predictions in a form suitable for the PDF fit became available only recently, the fits to 7 and 8 TeV measurements were performed only at NLO QCD, while the QCD analysis of 13 TeV data were performed at NNLO. The CMS inclusive jet and dijet measurements provide a substantial additional constraint on the gluon PDF at all values of x, as illustrated in Fig. 5 taken as an example from the results obtained with inclusive jet cross sections at 13 TeV. In the same analysis, the value of α_S was extracted simultaneously with the PDFs. That paper also presents an analysis including 13 TeV $t\bar{t}$ data was performed at NLO.

4.4 The strong coupling constant, α_S, and its running

Important tests of QCD are the precise extraction of the value of α_S at the scale of the Z boson mass, $\alpha_S(m_Z)$, and the illustration of the running α_S as a function of the renormalization scale Q, usually taken as p_T of the jet in proton collision, or momentum transfer in DIS. The scale dependence is encoded in the renormalization group equation (RGE) of QCD and represents a basic demonstration of our understanding of the dynamics of the strong interaction [183].

Jet production is an ideal instrument for determination of α_S, since its cross section is proportional to α_S already at LO QCD. The first CMS determination of α_S was performed by investigating the ratio of jet cross sections in three- and 2-jet topologies R_{32} [184], which is linearly proportional to the value of α_S. In high-p_T collisions involving the production of jets, α_S is

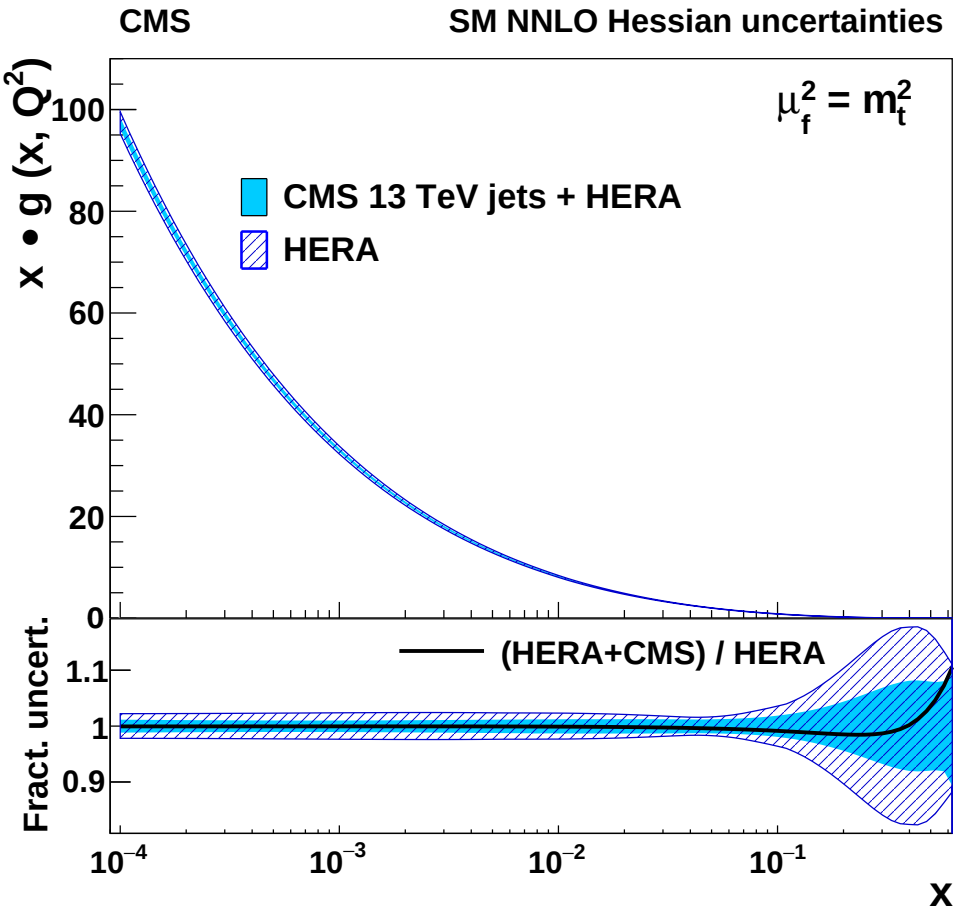

Figure 5: The gluon distribution, shown as a function of x for the factorization scale $\mu_f = m_t$. The filled (hatched) band represents the results of the NNLO fit using HERA DIS and the CMS inclusive jet cross section at $\sqrt{s} = 13$ TeV (using the HERA DIS data only). The PDFs are shown with their total uncertainty. In the lower panel, the comparison of the relative PDF uncertainties is shown for each distribution. The solid line corresponds to the ratio of the central PDF values of the two variants of the fit. Figure and caption taken from Ref. [146].

typically of order 0.1–0.2, which, as calculated using pQCD, corresponds to a probability for additional jet emissions in any pp hard-collision event of the same order. Two-jet and multijet events with three or more jets are common, allowing for statistically precise determinations of α_S. The R_{32} analysis used events with jets with p_T in the range 0.42 to 1.39 TeV and conducted the first determination of α_S at TeV scale energies. Simultaneous extraction of α_S together with PDFs was performed using inclusive jet and di-jet measurements and exploring the jet substructure. The uncertainties in α_S extracted using jet production at hadron colliders is dominated by missing higher-order pQCD calculations, usually estimated by varying the renormalization and factorization scales by a factor of 2. Most of the aforementioned measurements were performed at NLO and suffer from a large theory uncertainty. Simultaneously CMS has pioneered extraction of α_S using $t\bar{t}$ production cross section measurements, which resulted in higher precision than jet-based extractions, due to availability of NNLO calculations for $t\bar{t}$ production cross section. In addition, other physics processes such as weak boson production have been used to make precise determinations of α_S. Since the NNLO calculation for jet production in pp collisions have become available, the theory uncertainty in α_S extraction using jet production is significantly reduced. The most precise measurement of $\alpha_S(m_Z)$ to date of $\alpha_S(m_Z) = 0.1166 \pm 0.0014\,(\text{fit}) \pm 0.0007\,(\text{model}) \pm 0.0004\,(\text{scale}) \pm 0.0001\,(\text{param}) = 0.1166 \pm 0.017\,(\text{tot})$ is obtained using in a simultaneous fit of PDF and α_S at NNLO using double-differential inclusive jet production data at 13 TeV [146]. The most recent CMS determination of α_S uses jet substructure[185], performed by comparing with NLO plus approximate next-to-next-to-leading-logarithmic (aNNLL) [186–188] predictions of two- and three-point energy correlators inside jets. The most precise value of $\alpha_S(m_Z)$ in substructure measurements is achieved and the running of as is probed.

The CMS extractions of α_S are listed in Table 6 and displayed in Fig. 6. For comparison, the results are presented by extrapolating α_S to the energy scale of the Z boson mass, $\alpha_S(m_Z)$. Uncertainties are grouped together by type and further descriptions of the uncertainty types are reported in the glossary of terms in Appendix A.

A summary of the running of α_S, probed by several measurements shown in Fig. 7 including CMS, ATLAS [194, 195], and earlier determinations by the D0 [196, 197], H1 [198], and ZEUS [199] Collaborations. For the CMS measurements α_S is determined in dijet p_T (R_{32} [184]), 3-jet mass [189], and jet p_T (inclusive jets 7 TeV [144], inclusive jets 8 TeV [139], and $R_{\Delta\phi}$ [193]) regions based on the average Q of events in those regions. The QCD RGEs, encoding the running of α_S, are obtained using NLOJET++ implemented in the FASTNLO framework evolved from 2023 world-average value of $\alpha_S(m_Z) = 0.1180 \pm 0.0009$ [123]. The CMS determinations of α_S agree well with the world-average and with the RGE at NLO predictions.

4.5 Double-parton scattering

Double-parton scattering (DPS) is a process in which two parton-parton scattering interactions occur in a single hadron-hadron collision. The study of DPS is a test of our knowledge of the structure of the proton. For instance, DPS provides information on the energy evolution of the p_T profile of the partons in the proton, which is information that cannot be accessed in single-parton scattering (SPS) events. Thus, where SPS interactions are widely used to measure the longitudinal PDFs of the partons in the proton, DPS events can measure the transverse PDFs. Also, since multiple partons in each proton are colliding, DPS can be used to study the correlations between quantum numbers of the constituents of the proton. For instance, the spin of two partons in a single proton will be correlated and will have effects on the kinematics of a DPS collision.

DRAFT

Table 6: Overview of $\alpha_S(m_Z)$ from CMS analyses. Results where α_S is determined by profiling a global PDF set, list the set used. The other results were obtained using a combined PDF and α_S fit of the CMS and HERA data as described in the text. The 2D inclusive jet [144] analysis only uses the HERA-I data, whereas the other combined PDF and α_S fits use the combined HERA-I and HERA-II data. The QCD perturbative order(pQCD order) of the determination is also given. For publications where more than one value is extracted, only one is reported. Whenever data from other analyses are used in the α_S determination, the first analysis listed documents the α_S extraction.

Analysis	$\sqrt{s}$ (TeV)	$\alpha_S(m_Z)$	fit unc.	PDF unc.	scale unc.	other unc.	PDF	pQCD order
R_{32} [184]	7	0.1148	±0.0014	±0.0018	±0.0050 theo incl. scale		NNPDF2.1	NLO
2D inclusive jet [144] [142]	7	0.1185	±0.0019	±0.0028	$^{+0.0053}_{-0.0024}$	±0.0004 NP	—	NLO
Inclusive 3-jet mass [189]	7	0.1171	±0.0013	±0.0024	$^{+0.0069}_{-0.0040}$	±0.0008 NP	CT10	NLO
$t\bar{t}$ cross section [190]	7	0.1151	$^{+0.0017}_{-0.0018}$	$^{+0.0013}_{-0.0011}$	$^{+0.0009}_{-0.0008}$	$\underbrace{\pm0.0013}_{m_t}$ $\underbrace{\pm0.0008}_{\sqrt{s}}$	NNPDF2.3	NNLO
2D inclusive jet [139]	8	0.1185	$^{+0.0019}_{-0.0021}$	$\underbrace{^{+0.0002}_{-0.0015}}_{\text{model}}$ $\underbrace{^{+0.0000}_{-0.0004}}_{\text{param}}$	$^{+0.0022}_{-0.0018}$		—	NLO
3D dijet mass [180]	8	0.1199	±0.0015	$\underbrace{\pm0.0002}_{\text{model}}$ $\underbrace{^{+0.0002}_{-0.0004}}_{\text{param}}$	$^{+0.0026}_{-0.0016}$		—	NLO
W, Z cross section [191]	7, 8	0.1163	$\underbrace{\pm0.0007}_{\text{stat}}$ $\underbrace{\pm0.0010}_{\text{syst}}$	$^{+0.0016}_{-0.0022}$	±0.0009	$\underbrace{\pm0.0013}_{\text{lumi}}$ $\underbrace{\pm0.0006}_{\text{num}}$	CT14	NNLO
$t\bar{t}$ (dilepton) [192]	13	0.1151	±0.0035 fit + PDF		$^{+0.0020}_{-0.0002}$		MMHT14	NNLO
Normalized $t\bar{t}$ [181]	13	0.1135	±0.0016	$\underbrace{^{+0.0002}_{-0.0004}}_{\text{model}}$ $\underbrace{^{+0.0008}_{-0.0001}}_{\text{param}}$	$^{+0.0011}_{-0.0005}$		—	NLO
2D inclusive jet [146]	13	0.1166	±0.0014	$\underbrace{\pm0.0007}_{\text{model}}$ $\underbrace{\pm0.0001}_{\text{param}}$	±0.0004		—	NNLO
2D & 3D dijet mass [182]	13	0.1181	±0.0013	$\underbrace{\pm0.0006}_{\text{model}}$ $\underbrace{\pm0.0002}_{\text{param}}$	±0.0009		—	NNLO
$R_{\Delta\phi}$ [193]	13	0.1177	±0.0013	$\underbrace{\pm0.0010}_{\text{NNPDF3.1}}$ $\underbrace{\pm0.0020}_{\text{choice}}$	$^{+0.0114}_{-0.0068}$	$\underbrace{\pm0.0011}_{\text{NP}}$ $\underbrace{\pm0.0003}_{\text{EW}}$	NNPDF3.1	NLO
Energy correlators in jets [185]	13	0.1229	$\underbrace{^{+0.0014}_{-0.0012}}_{\text{stat}}$ $\underbrace{^{+0.0023}_{-0.0036}}_{\text{syst}}$		$^{+0.0030}_{-0.0033}$		—	aNNLL

DRAFT

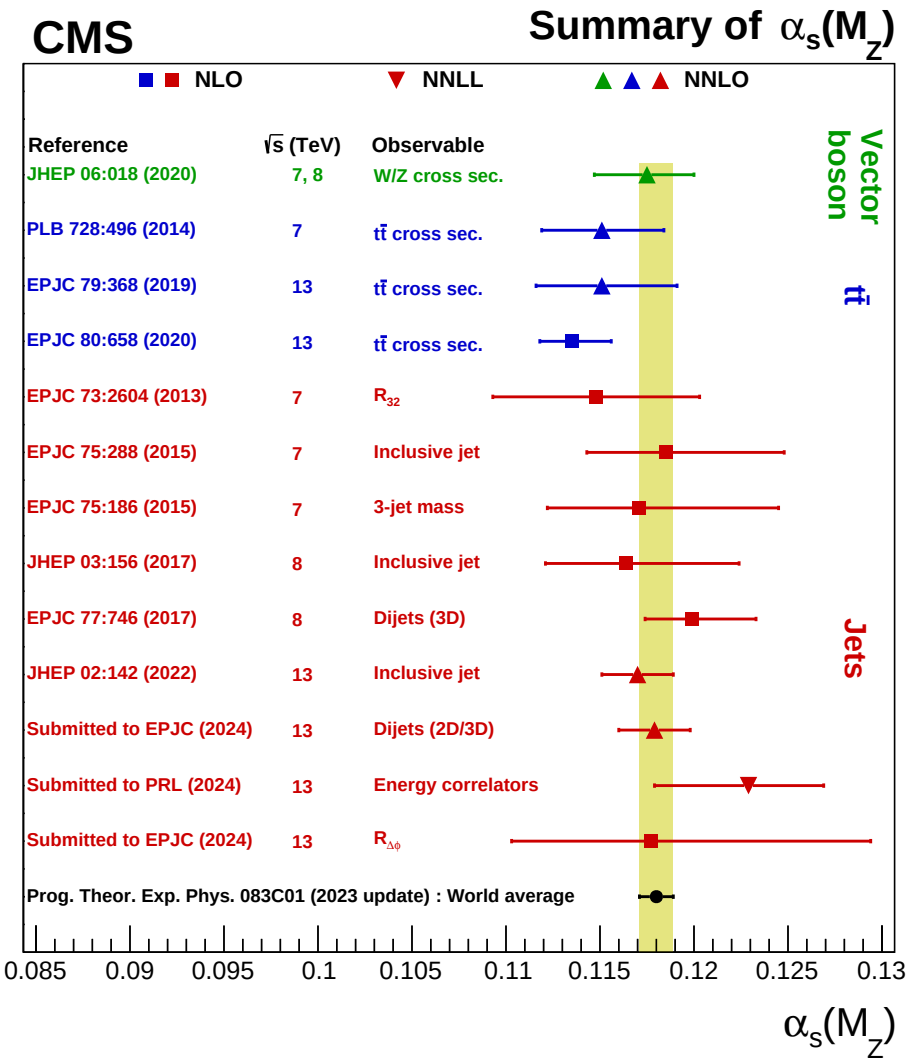

Figure 6: A summary of $\alpha_S(m_Z)$ extractions from the CMS experiment compared with the 2023 PDG world-average. For each measurement, pp collision energy and the QCD perturbative order of the $\alpha_S(m_Z)$ extraction are listed. Results are grouped by the type of the final state used: vector boson, $t\bar{t}$, and jets.

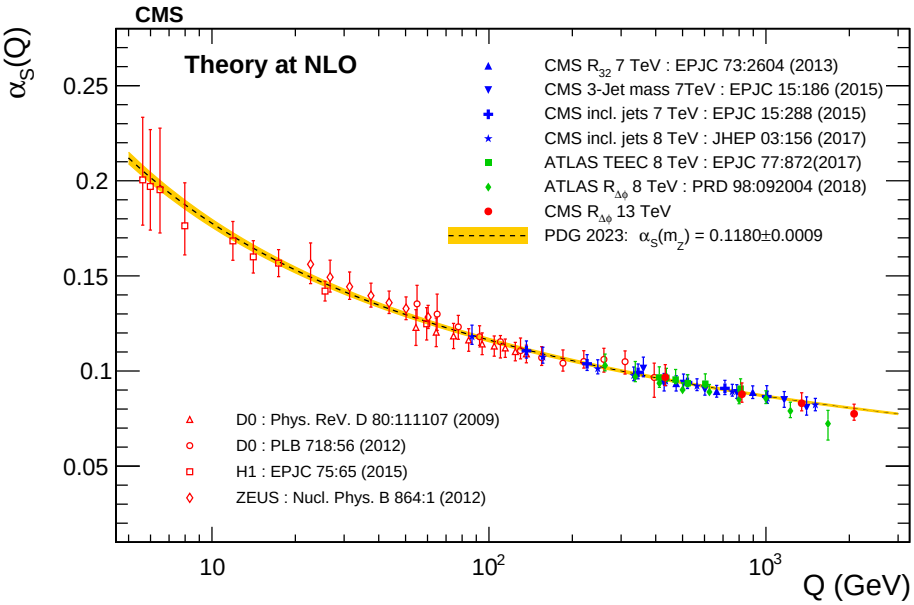

Figure 7: Running of the strong coupling as a function of momentum transfer, $\alpha_S(Q)$ (dashed line), evolved using the 2023 world-average value, $\alpha_S(m_Z) = 0.1179 \pm 0.0009$, together with its associated total uncertainty (yellow band). The CMS extractions, which extend above 2 TeV, are compared with results from the H1, ZEUS, D0, and ATLAS experiments. The vertical error bars indicate the total uncertainty (experimental and theoretical). All the experimental results shown in this figure are based on predictions at NLO accuracy in perturbative QCD. Figure from Ref. [193].

The cross sections of DPS interactions are typically modelled as the product of the two independent SPS cross sections divided by an effective cross section, σ_{eff}, as shown in Eq. (1). The ratio is multiplied by a combinatorial factor, m, that is equal to 2 when processes A and B are different and 1 when they are the identical. This effective cross section can be interpreted as the square of the average transverse distance between the interacting partons.

$$\sigma^{\text{DPS}}_{\text{A,B}} = \frac{m}{2}\frac{\sigma_{\text{A}}\sigma_{\text{B}}}{\sigma_{\text{eff}}} \tag{1}$$

The DPS has been extensively studied at the Tevatron by the CDF [200] and D0 [201–204] experiments and at the LHC by the CMS [205–208] and ATLAS experiments. Figure 8 shows the effective cross section values for DPS processes from the Tevatron and LHC experiments determined from measurements with quarkonium final states and from processes with jets, photons, and W bosons. The expected relationships between the SPS, DPS and triple-parton scattering (TPS) cross sections from HELAC-ONIA [44, 45] are used to extract σ_{eff} for DPS from the CMS measurement of triple-J/ψ production [205]. Distributions sensitive to DPS based on the MADGRAPH5_aMC@NLO and PYTHIA 6 simulation of DPS physics are used to extract σ_{eff} in W plus 2 jet events, whereas multivariate classifiers based on PYTHIA 8 simulation with the CP5 and CUETP8M1 tunes of MPI parameters [37] are used to extract σ_{eff} in $\text{W}^{\pm}\text{W}^{\mp}$ and $\text{W}^{\pm}\text{W}^{\pm}$ events. The effective cross sections obtained from quarkonium measurements favour values below 10 mb, as compared with effective cross sections derived from final states with harder scales, which favour values above 10 mb. Such apparent process-dependent σ_{eff} values are suggestive of different parton transverse PDFs and/or correlations probed inside the proton at varying fractional momenta.

DRAFT

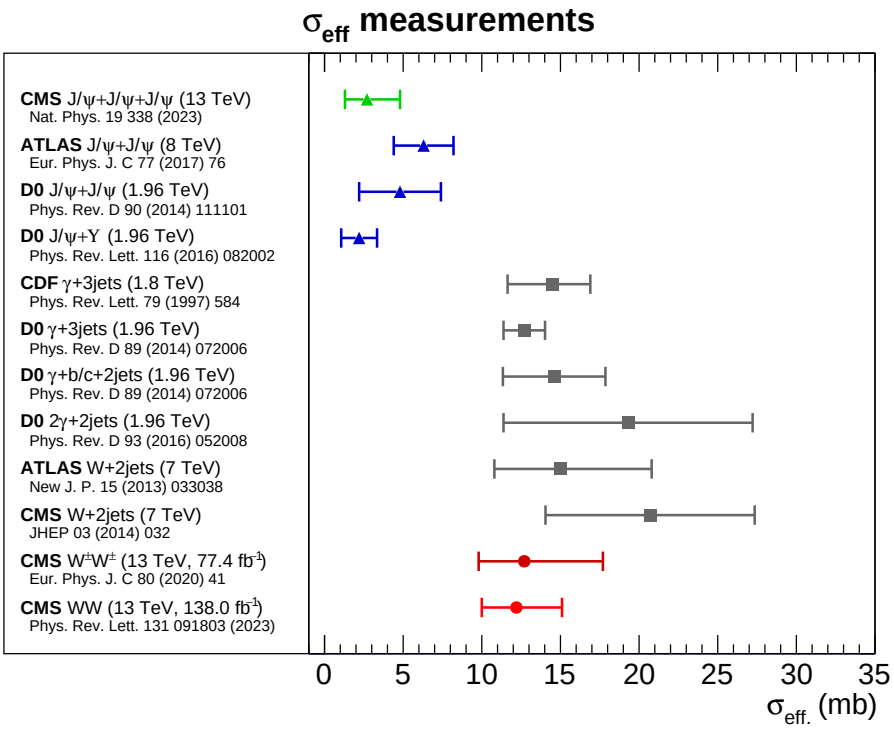

Figure 8: Selected measurements of the effective DPS cross section in pp collisions at the LHC by the CMS and ATLAS experiments, and in $p\overline{p}$ collisions at the Tevatron by the CDF and D0 experiments. The horizontal bars indicate the combined statistical and systematic uncertainty for each measurement. Figure taken from Ref. [205].

4.6 Summary of QCD measurements

The CMS Collaboration has conducted a broad array of QCD measurements across a large range of energies. The PDF measurements substantially constrain the gluon, valence quark, and sea quark (collectively and individually such as constraints on the s quark) PDFs. The $\alpha_S(m_Z)$ extractions are competitive and agree with those of other experiments and measure the running of $\alpha_S(m_Z)$ up to TeV energy scales. Together these measurements constrain important aspects of QCD that are essential for making predictions of high-p_T interactions at the LHC. Inclusive and multidifferential jet production measurements have been performed, testing the limits of the current generation of NNLO QCD and NLO EW perturbative predictions. In general, given the high probability of additional jet production in high-energy pp collisions, the detailed QCD analyses produced by the LHC experiments and their comparisons with the most sophisticated theory predictions are essential for expanding our understanding of all aspects of high-p_T SM physics.

5 Measurements in the electroweak sector of the standard model

The EW sector involves the EW gauge bosons (the photon, and the W and Z bosons) and their interactions with other SM particles. The EW sector of the SM combines a $\mathcal{U}(1)_Y$ and a non-Abelian $\mathcal{SU}(2)_L$ gauge symmetries, with associated weak hypercharge and weak isospin charges, respectively. The electromagnetic force is based on a $\mathcal{U}(1)_{EM}$ symmetry, with electric charge, and the associated massless photon resulting from a linear combination of the B and W_3 fields of the $\mathcal{U}(1)_Y$ and $\mathcal{SU}(2)_L$ gauge symmetries after the EW symmetry breaking. Similarly, the weak force, weak charges, and W and Z bosons result from linear combinations of the W_1 and W_2 fields of the $\mathcal{SU}(2)_L$ symmetry and a linear combination of the B and W_3 fields, respectively. The combination of these gauge symmetries and the EW symmetry-breaking mechanism forms a unified EW theory. Electroweak physics measurements at the LHC test many aspects of the SM. These include the complex interactions between multiple EW gauge bosons predicted by the non-Abelian $\mathcal{SU}(2)_L$ portion of the EW gauge structure and the nature of EW symmetry breaking via the Brout–Englert–Higgs mechanism, which generates masses of the W and Z bosons. The small values of the EW couplings imply that most EW processes at the LHC can be calculated perturbatively with good precision. The EW bosons are copiously produced at the LHC and can be measured with high precision by the LHC detectors.

For EW physics, the number of accessible final states at the LHC is without precedent. They include states with single, double, or triple gauge bosons. Production of EW gauge bosons can occur via radiation from quarks, multi-gauge-boson interactions, such as vector boson scattering (VBS) and vector boson fusion (VBF), and from the decay of heavier particles, such as the Higgs boson and top quark. Many processes have only been observed at the LHC, which is the first collider that allows access to processes such as VBS. In each subsection total and fiducial cross sections, cross sections including production of additional jets, and differential measurements are presented. At the end of the section we briefly summarize the results.

Analysis of the EW physics at the CMS experiment is primarily conducted using physics objects, such as jets, photons, electrons, or muons. Neutrinos are inferred from the $\vec{p}_T^{\,miss}$ in the vector sum of objects reconstructed as originating from the PV. Jets are typically required to have $p_T > 30\,GeV$. Photons are required to satisfy $p_T > 25\,GeV$ to remove lower-p_T photons originating from the decay of neutral pions. Electrons and muons are used to identify events with W or Z bosons. In EW analyses described in this Report, W (W^+ or W^-) and Z bosons are efficiently reconstructed via their leptonic decays, $W^+ \to \ell^+\nu_\ell$ (charge conjugate states are

implied) and $Z \to \ell^+\ell^-$, where $\ell = \mu$ or e. Backgrounds to $Z \to \ell^+\ell^-$ decays are very low. Muons and electrons with $p_T > 20\,\text{GeV}$ are used in analysis with a single W boson. Analyses with Z bosons or multiple bosons often use thresholds as low as $p_T > 10\,\text{GeV}$ for a second lepton and $p_T > 5\,\text{GeV}$ for additional leptons. The W bosons are also selected by identifying events with $\vec{p}_T^{\,\text{miss}}$ or selecting events with large transverse mass calculated using a lepton momentum and $\vec{p}_T^{\,\text{miss}}$. The selection listed above is typical of CMS analyses, but higher thresholds are used in some cases to reject backgrounds, or lower thresholds to increase the acceptance. Generally, events using reconstructed W and Z candidates have low background caused by misidentified prompt leptons. The largest backgrounds (the so-called "physics" backgrounds) come from events with identical final-state particles. Flavour-tagging algorithms are used to identify bottom and charm jets. Reconstruction algorithms and identification criteria are described in Section 2.1.

5.1 Vector boson production

Measurements of the production of single EW bosons are the simplest test of EW theory predictions. However, the prediction of the corresponding cross sections at a hadron collider is complicated by the necessity to understand the radiation of QCD jets and the PDFs of the proton, which describe the structure of the proton and predict the partonic luminosities of the colliding partons. Despite these complications, measurements of EW production cross sections can still be made with percent-level precision. This makes physics involving single bosons both a precision test of EW theory and, in either inclusive production or production of vector bosons with jets, of perturbative QCD predictions. The low backgrounds when identifying vector bosons in the $W^+ \to \ell^+\nu_\ell$ and especially $Z \to \ell^+\ell^-$ decay modes and the size of the LHC data sets allows theoretical and experimental comparisons of total, differential, and often multidifferential distributions with good precision over wide ranges of energy, angle, and jet multiplicity. Together these processes provide a stringent test of SM predictions over a broad array of final states and kinematic configurations.

Measurements of single-boson production constitute an essential test of our ability to predict SM parton-parton interaction cross sections using perturbative techniques. Single photons are radiated off charged objects. Single weak boson production proceeds primarily through the Drell–Yan (DY) quark-antiquark annihilation process [209], as shown in Fig. 9. The production of Z bosons is sensitive to the sum of the u and d and the sum of the $\overline{\text{u}}$ and $\overline{\text{d}}$ PDFs and also the EW mixing angle θ_W. The W^+ and W^- boson production has sensitivity to the ratios of u to d and $\overline{\text{u}}$ to $\overline{\text{d}}$ contributions, especially when considering the charge asymmetry of the leptons from the W boson decays as a function of their pseudorapidity. The DY process has been predicted at N^3LO accuracy in perturbative QCD using matching N^3LO PDF sets. The PDF uncertainties, and higher-order QCD and EW radiative corrections limit the precision of current predictions. Other sensitive comparisons are made using N^3LO or NNLO predictions of ratios of production cross sections or in two-dimensional planes depicting pairs of the Z, W^+, and W^- boson cross sections.

5.1.1 Single photon production

The photon is the longest known and most extensively studied vector boson. In high-energy pp collisions the photon is observed as a promptly produced particle in a large number of SM processes and may also be produced in BSM topologies. Examples are Higgs boson decay to two photons [210] and monophoton searches for new physics, such as dark matter [211]. Photons are also produced in neutral pion decays and are radiated from final-state particles, leading to backgrounds in the study of prompt high-energy photons. The simplest measurement of

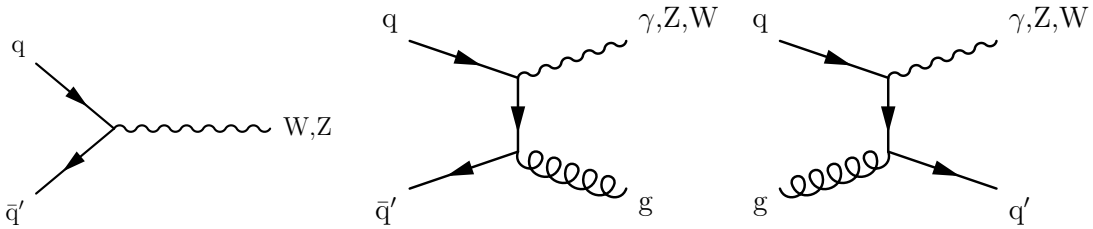

Figure 9: The Feynman diagram for Drell–Yan production of W and Z bosons (left). The Z boson production process involves annihilation of quark-antiquark pairs of same flavour. The W boson production process requires different-flavour quarks, such as $u\bar{d}$ or $\bar{u}d$ pairs. The NLO diagrams with real emission of a jet for the production of single vector bosons and one jet with a final-state gluon jet (middle) or quark jet (right).

photon production uses events with one or more prompt isolated photons above a given p_T threshold that are produced in the hard interaction. Unlike the situation with massive vector bosons, it is necessary to define a minimum momentum threshold, because singularities in the perturbative calculation of cross sections near zero momentum are not well defined. Also, experimental constraints make it impossible to measure the lowest energy portion of photon production due to overwhelming backgrounds. A minimum threshold is required to reject both instrumental and physics backgrounds. In 7 TeV collision data the CMS experiment finds a production cross section of $39.6 \pm 0.7\,(\text{stat}) \pm 6.9\,(\text{syst})$ nb for photons with $p_T > 25$ GeV [212]. This cross section was calculated by integrating the differential cross section for photon production presented in that paper.

Inclusive photon production cross sections have been measured differentially as functions of basic kinematic variables at 7 [212, 213] and 13 [214] TeV. As with jet production, the results are reported as functions of the photon E_T in several intervals of rapidity. An example from the 13 TeV analysis of single-photon data is shown in Fig. 10. The measurements of differential and inclusive photon production cross sections are compared with the NLO calculations from JETPHOX [215] using the BFG [216] fragmentation functions for quarks and gluons into photons, and found to be well modelled.

5.1.2 Single weak boson production

The cross sections of single prompt massive vector bosons inclusively produced with any number of final-state quarks or gluons are among the most precisely measured at hadron colliders. The CMS experiment has measured single inclusive W and Z boson production in events where the boson decays to an electron or a muon and the corresponding antineutrinos, and e^+e^- or $\mu^+\mu^-$ pairs, respectively. Inclusive cross section measurements have been made with 2% precision primarily limited by the uncertainty in the integrated luminosity. This precision has been achieved because of several factors. The large data sets of W and Z bosons result in small to negligible statistical uncertainty in the measurements. Small systematic uncertainty is achieved due to large data sets for evaluating in granular detail the efficiency of lepton (electron and muon) detection; accurate MC simulations for estimating the acceptance for prompt leptons from W and Z boson decays, and predicting physics backgrounds involving prompt leptons from other sources; and low backgrounds and reliable methods to predict the rates of hadrons and leptons in jets being misidentified as prompt leptons based on control samples in data. The limiting integrated luminosity uncertainty has been extensively studied and minimized using techniques described in the references given in Section 2.1.

These measurements have been made in fiducial phase spaces and extrapolated to the full pro-

DRAFT

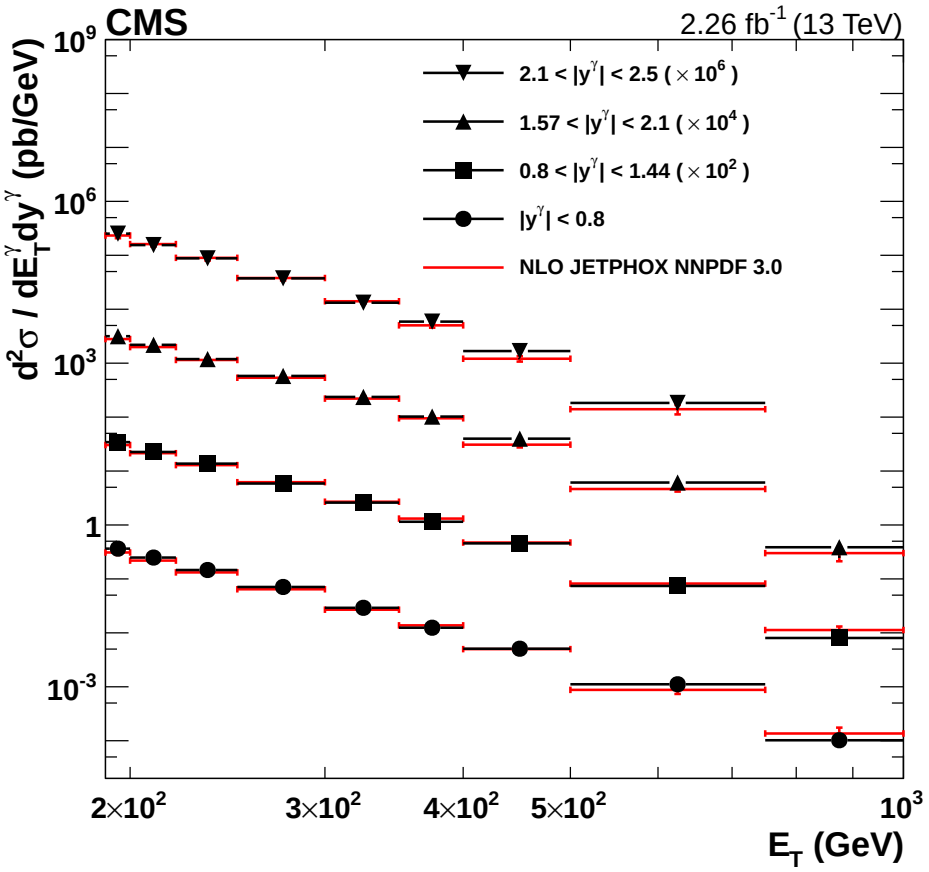

Figure 10: Differential cross sections for isolated-photon production in four photon rapidity intervals. The points show the measured values and their total uncertainties; the lines represent the NLO JETPHOX predictions with the NNPDF3.0 PDF set. Figure and caption taken from Ref. [214].

duction cross sections for both the W and Z bosons at each energy at which the LHC has operated. Shown in Fig. 11 is a comparison of the CMS measurements of the full production cross section of W and Z bosons in leptonic decay channels at 2.76 TeV [217, 218] (W and Z bosons, respectively), 5.02 [219], 7 [220, 221], 8 [222, 223], and 13 [219] compared with the predictions at N^3LO [224] in QCD using the MSHT20aN^3LO [112] PDF set. The measurement of the Z boson cross section at 2.76 TeV uses the differential measurement versus rapidity presented in Ref. [218] integrating the results over the measured rapidity range and extrapolating to the full one using DYTURBO [38] at N^3LO. The measurements at 2.76 and 5.02 TeV are based on the pp collision reference data for the heavy ion physics programme. The N^3LO cross section predictions are the most accurate currently available and Fig. 11 illustrates the ability to make precise comparisons of cross sections between experimental measurements and theoretical prediction at a hadron collider. Figure 12 presents the CMS W and Z cross section measurements along with cross section measurements from previous $p\overline{p}$ colliders including the UA1 [225] and UA2 [226] experiments at the CERN $Sp\overline{p}S$, where the W and Z bosons were first discovered, and the CDF [227] and D0 [228] experiments at the Tevatron. The results are compared with the NNLO predictions computed using DYTURBO and the NNPDF4.0 PDF, which yields the smallest cross section uncertainties for weak boson production of the currently available global PDF sets. The CMS results are also presented in the full cross section summary Fig. 1. The theoretical predictions for total, fiducial, and ratio measurements presented in the following tables are computed at NNLO using, for the 5 and 13 TeV predictions, DYTURBO with the NNPDF3.1 PDF set; and, for 7 TeV, using FEWZ with the NNPDF2.1 PDF set. The theoretical predictions for the 8 TeV ratio of cross sections are computed at NNLO using FEWZ with the MSTW2008 PDF set.

Table 7 presents the inclusive cross section for Z production in pp collisions at various energies. The largest source of uncertainty in the measurements is the integrated luminosity. The most precise cross section measurements have been made with low-pileup data sets collected in short time periods that allow a more precise determination of the luminosity.

Table 7: Measured inclusive cross sections for Z boson production at pp collision energies from 2.76 to 13.0 TeV. Total uncertainties in the experimental measurements are given in pb and as a percentage. Separate components of the experimental statistical and systematic uncertainties other than the dominant integrated luminosity uncertainty were not published for the 2.76 TeV cross section measurement. The statistical uncertainties of the 7 and 8 TeV measurements are smaller than 1 pb and are not shown. The measurements are compared with theoretical predictions obtained at N^3LO in QCD using the MSHT20aN^3LO PDF set. The theoretical uncertainty is from normalization and factorization scale variations.

$\sqrt{s}$ (TeV)	$\sigma(Z)$ (pb)	(tot) exp. unc. (%)	$\sigma^{SM}(Z)$ (pb)
2.76 [218]	$298 \pm 10\,(stat) \pm (syst) \pm 11\,(lumi)$	5.0%	313^{+1}_{-2}
5.02 [219]	$669 \pm 2\,(stat) \pm 6\,(syst) \pm 13\,(lumi)$	2.2%	$674.7^{+7.1}_{-7.4}$
7 [221]	$986 \pm 22\,(syst) \pm 22\,(lumi)$	3.1%	968^{+6}_{-7}
8 [223]	$1138 \pm 26\,(syst) \pm 30\,(lumi)$	3.5%	1124^{+7}_{-2}
13 [219]	$1952 \pm 4\,(stat) \pm 18\,(syst) \pm 45\,(lumi)$	2.5%	1940^{+15}_{-21}

DRAFT

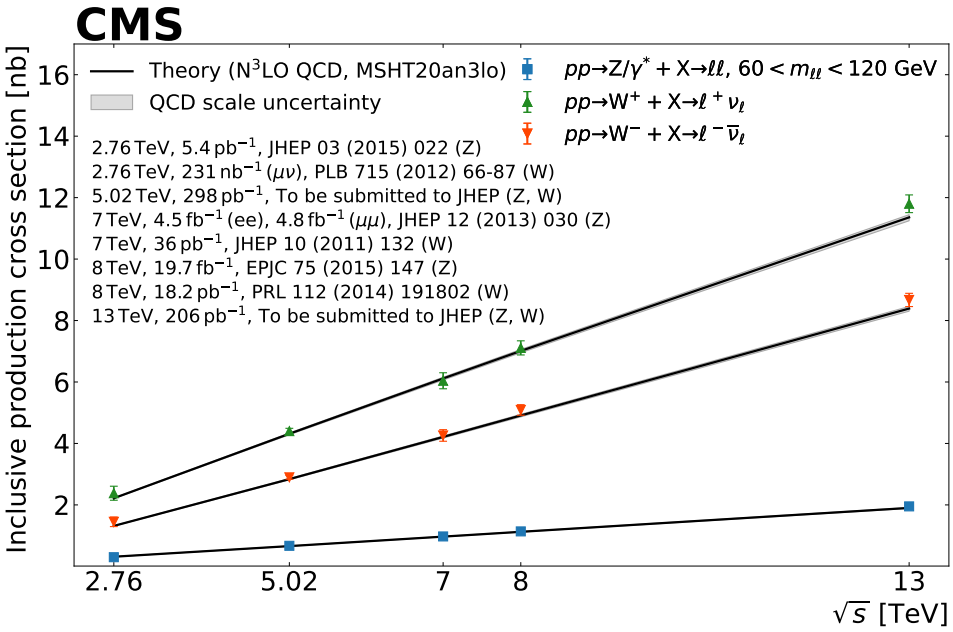

Figure 11: Summary of the production cross section of weak gauge bosons, measured by CMS, plotted against the pp centre-of-mass energy ranging from 2.76 to 13 TeV. The error bars around the experimental data points represent the total uncertainty of the measurement. The measurements are compared with theoretical predictions (black lines) obtained at N^3LO in QCD using the MSHT20aN^3LO PDF set. The grey band shows the envelope from normalization and factorization scale variations.

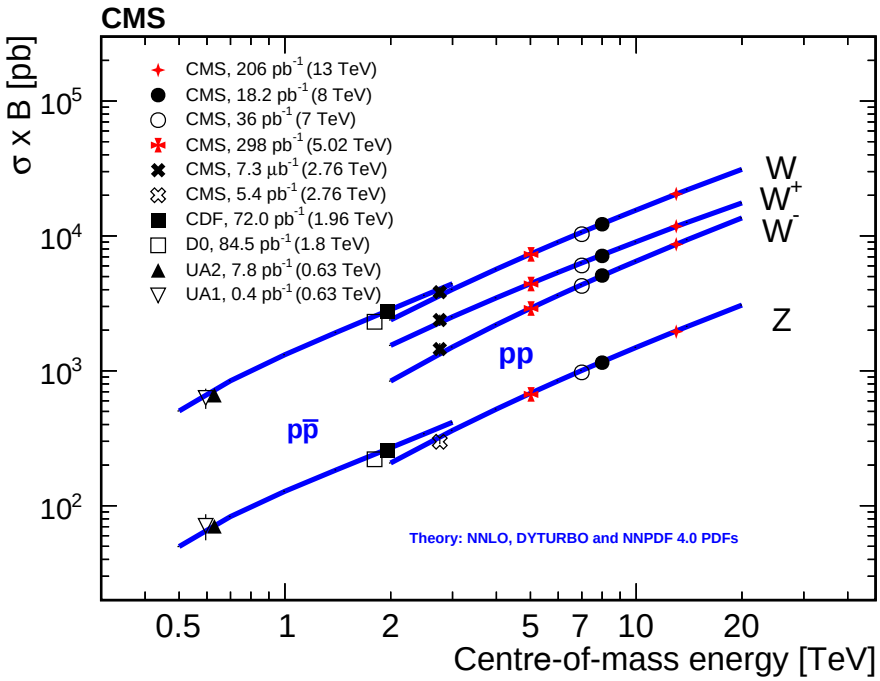

Figure 12: Summary of the production cross section of weak gauge bosons in pp collisions, measured by CMS, and in $p\bar{p}$ collisions, by the UA1, UA2, CDF, and D0 experiments, plotted against the pp or $p\bar{p}$ centre-of-mass energy ranging from 0.63 to 13.0 TeV. The measurements are compared with theoretical predictions (blue lines) obtained at NNLO in QCD by using DYTURBO and the NNPDF4.0 PDF set. Figure taken from Ref. [219].

Measuring the cross section in a fiducial phase space reduces the total systematic uncertainty by removing or minimizing the additional uncertainty from the extrapolation of the cross section from the fiducial phase space region where it is measured to the full production phase space. Fiducial measurements of the Z cross section are presented in Table 8. The 8 TeV fiducial cross section measurement is from Ref. [222].

Table 8: Measured fiducial cross sections for Z boson production and decay to electrons and muons in pp collisions at energies from 5.02 to 13 TeV. Total uncertainties in the experimental measurements are given in pb and as a percentage. The measurements are compared with theoretical predictions at NNLO in QCD described in the references above. In each case, the uncertainty in the CMS measurement of the fiducial Z boson cross section is reduced compared with the inclusive measurement and the integrated luminosity uncertainty dominates the overall uncertainty of the measurements.

$\sqrt{s}$ (TeV)	$\sigma_{\text{fid.}}(\text{Z})$ (pb)	(tot) exp. unc. (%)	$\sigma^{\text{SM}}_{\text{fid.}}(\text{Z})$ (pb)
5.02 [222]	$319.8 \pm 0.9\,(\text{stat}) \pm 1.2\,(\text{syst}) \pm 6.2\,(\text{lumi})$	2.0%	319.5 ± 3.7
7 [221]	$524.7 \pm 0.4\,(\text{stat}) \pm 5.2\,(\text{syst}) \pm 11.5\,(\text{lumi})$	2.4%	525 ± 6
8 [222]	$410.0 \pm 10.0\,(\text{stat}) \pm 10.0\,(\text{syst}) \pm 10.0\,(\text{lumi})$	4.2%	400 ± 10
13 [222]	$754 \pm 2\,(\text{stat}) \pm 3\,(\text{syst}) \pm 17\,(\text{lumi})$	2.3%	743 ± 18

Table 9 lists the measurements of ratios of the inclusive W and Z cross sections, and Table 10 lists the measurement of the ratios of fiducial cross sections. The measurements of the ratios of W to Z boson cross sections remove the dependence on the integrated luminosity determination and that of any other efficiencies or factors that apply to both measurements identically, substantially reducing the systematic uncertainty. For this reason, cross section ratios are among the most precise measurements performed by the CMS experiment.

The recent cross section results at 5.02 TeV are the most precise because they feature an improved integrated luminosity uncertainty of 1.9%. Comparisons of theoretical predictions to the total, fiducial, and the ratios of the measured 5.02 and 13 TeV W to Z cross sections are reported in Ref. [219], computed at NNLO in QCD using DYTURBO [38, 229, 230] and the NNPDF3.1 NNLO PDF set. These predictions were improved to next-to-next-to-leading-logarithmic (NNLL) accuracy using resummation [231, 232], which better models the p_{T} distribution of the Z bosons at low p_{T} values. This reduces systematic uncertainties associated with the extrapolation from the measurement in the fiducial region to the total cross section. For instance, in 5.02 TeV pp collisions the Z and W boson cross sections with a subsequent decay to leptons were measured in a fiducial phase space as: $\sigma(\text{Z}) = 319.8 \pm 0.9\,(\text{stat}) \pm 1.2\,(\text{syst}) \pm 6.2\,(\text{lumi})$ (2.0% total uncertainty), and $\sigma(\text{W}) = 4000 \pm 3\,(\text{stat}) \pm 11\,(\text{syst}) \pm 76\,(\text{lumi})$ pb (1.9% total uncertainty), which are the most precise single cross section measurements performed by the CMS experiment. Ratios of cross sections can be measured with better than 0.5% precision in fiducial phase space, since the dependence of the measurement on the integrated luminosity and the understanding of some reconstruction efficiencies is removed by forming a ratio of cross sections of similar production processes. For 13 TeV pp collisions the same analysis measured $\sigma(\text{W}^+)/\sigma(\text{W}^-) = 1.3159 \pm 0.0017\,(\text{stat}) \pm 0.0053\,(\text{syst})$ (0.43% total uncertainty), and $\sigma(\text{W})/\sigma(\text{Z}) = 12.078 \pm 0.028\,(\text{stat}) \pm 0.032\,(\text{syst})$ (0.35% total uncertainty). The effort by the LHC experiments to make precise measurements has been matched by progress in theory

DRAFT

Table 9: Measured ratios, R_{exp}, of inclusive cross sections for W and Z boson production times the branching fractions $\mathcal{B}(W \to \ell\nu)$ and $\mathcal{B}(Z \to \ell^+\ell^-)$ (with the dilepton mass between 60 and 120 GeV), respectively. Ratios $R_{W^+/W^-} = \sigma(W^+)\mathcal{B}(W^+ \to \ell^+\nu)/\sigma(W^-)\mathcal{B}(W^- \to \ell^-\overline{\nu})$ and $R_{W/Z} = \sigma(W)\mathcal{B}(W \to \ell\nu)/\sigma(Z)\mathcal{B}(Z \to \ell^+\ell^-)$ are shown for pp collision energies from 5.02 to 13 TeV. The total uncertainty in the experimental measurement is shown in the standard and percentage forms. The measurements are compared with theoretical predictions, R_{SM}, obtained at NNLO in QCD. The theoretical uncertainties, expressed as percentages, are from renormalization and factorization scale variations, α_S, and the PDF uncertainty.

$\sqrt{s}$ (TeV)	Ratio	R_{exp}	Total exp. unc.	R_{SM}
5.02 [219]	R_{W^+/W^-}	1.519 ± 0.002 (stat) ± 0.010 (syst)	0.67%	$1.5240^{+0.33\%}_{-0.31\%}$
7 [220]	R_{W^+/W^-}	1.421 ± 0.006 (stat) ± 0.032 (syst)	1.8%	$1.43 \pm 0.7\%$
8 [222]	R_{W^+/W^-}	1.39 ± 0.01 (stat) ± 0.02 (syst)	1.6%	$1.41 \pm 0.7\%$
13 [219]	R_{W^+/W^-}	1.3615 ± 0.0018 (stat) ± 0.0094 (syst)	0.70%	$1.3536^{+0.37\%}_{-0.33\%}$
5.02 [219]	$R_{W/Z}$	10.905 ± 0.032 (stat) ± 0.054 (syst)	0.58%	$10.777^{+0.33\%}_{-0.34\%}$
7 [220]	$R_{W/Z}$	10.54 ± 0.07 (stat) ± 0.18 (syst)	2.3%	$10.74 \pm 0.4\%$
8 [222]	$R_{W/Z}$	10.63 ± 0.11 (stat) ± 0.25 (syst)	2.6%	$10.74 \pm 0.4\%$
13 [219]	$R_{W/Z}$	10.491 ± 0.024 (stat) ± 0.083 (syst)	0.82%	$10.341^{+0.41\%}_{-0.38\%}$

Table 10: Measured ratios, R_{exp}, of fiducial cross sections for W and Z boson production times the branching fractions $\mathcal{B}(W \to \ell\nu)$ and $\mathcal{B}(Z \to \ell^+\ell^-)$, respectively. Ratios $R_{W^+/W^-} = \sigma(W^+)\mathcal{B}(W^+ \to \ell^+\nu)/\sigma(W^-)\mathcal{B}(W^- \to \ell^-\overline{\nu})$ and $R_{W/Z} = \sigma(W)\mathcal{B}(W \to \ell\nu)/\sigma(Z)\mathcal{B}(Z \to \ell^+\ell^-)$ are shown for at pp collision energies from 5.02 to 13 TeV. The total uncertainty in the experimental measurement is shown in the standard and percentage forms. The measurements are compared with theoretical predictions, R_{SM}, obtained at NNLO in QCD. The theoretical uncertainties, expressed as percentages, are from normalization and factorization scale variations, α_S, and PDF uncertainty.

$\sqrt{s}$ (TeV)	Ratio	R_{exp}	tot. exp. unc.	R_{SM}
5.02 [219]	R_{W^+/W^-}	1.6232 ± 0.0026 (stat) ± 0.0065 (syst)	0.43%	$1.631 \pm 0.98\%$
8 [222]	R_{W^+/W^-}	1.40 ± 0.01 (stat) ± 0.02 (syst)	1.6%	$1.42 \pm 1.4\%$
13 [219]	R_{W^+/W^-}	1.3159 ± 0.0017 (stat) ± 0.0053 (syst)	0.43%	$1.307 \pm 1.3\%$
5.02 [219]	$R_{W/Z}$	12.505 ± 0.037 (stat) ± 0.032 (syst)	0.39%	$12.51 \pm 0.96\%$
8 [222]	$R_{W/Z}$	13.26 ± 0.15 (stat) ± 0.21 (syst)	1.9%	$13.49 \pm 2.1\%$
13 [219]	$R_{W/Z}$	12.078 ± 0.028 (stat) ± 0.032 (syst)	0.35%	$12.02 \pm 2.3\%$

DRAFT

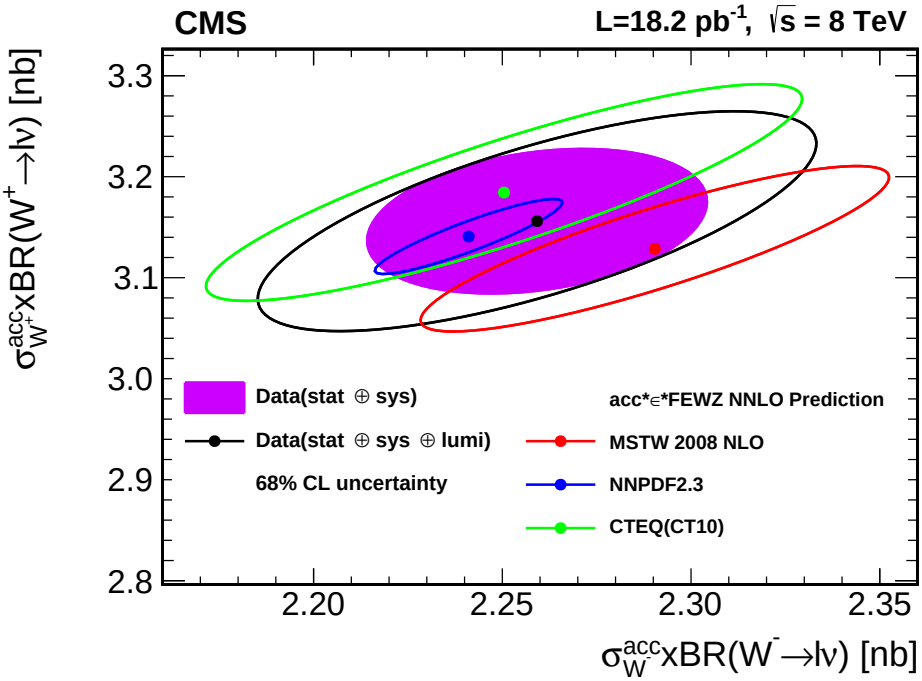

Figure 13: Measured and predicted W^+ versus W^- production fiducial cross sections times branching fractions. The ellipses illustrate the 68% CL coverage for total uncertainties (open) and excluding the integrated luminosity uncertainty (filled). The uncertainties in the theoretical predictions correspond to the PDF uncertainty components only and are evaluated for three PDF sets: NNPDF2.3, CTEQ CT10, and MSTW 2008 NLO. Figure taken from Ref. [222].

in producing higher QCD and EW perturbative order predictions, and improving our understanding of PDFs and other relevant theoretical issues. As with the experimental measurements precise predictions can be made of ratios of production cross sessions. For comparison theoretical prediction of $\sigma(W^+)/\sigma(W^-)$ at 13 TeV, computed at NNLO, has a precision 0.35% for the ratio of total cross sections and 1.3% for the ratio of fiducial cross sections (using one PDF set) due to larger renormalization and factorization scale uncertainties when computing the ratio in a restricted phase space. These ratios are sensitive to the quark content of the protons as described above and, in general, vector boson production measurements are a strong input to determining the proton PDFs.

In Fig. 13 a 2D comparison of the W^+ and W^- boson cross sections in 8 TeV pp collisions is shown, illustrating the improved precision of ratios of both the experimental measurements [222] and theoretical predictions calculated at NNLO in QCD using FEWZ [39, 40]. The large integrated luminosity uncertainty and its cancellation in the ratio are clearly seen in the shape of the uncertainty ellipse.

5.1.3 Differential measurements of vector boson production

The CMS experiment has measured the differential cross sections of photons, and W and Z bosons *vs.* a variety of kinematic variables considered in up to three dimensions. Of particular interest are analyses that differentially measure the rapidity or other angular variables of the weak bosons or their leptonic decays. In W boson decays, these measurements have direct sensitivity to the PDFs of the quarks in the proton of the same charge sign as the W boson. The DY production of $\ell^+\ell^-$ pairs, when considering a wider range of masses around the Z boson peak, has the sensitivity to the EW mixing angle θ_W. The measurements are often reported as

asymmetries comparing the positive and negative W boson or lepton distributions as a function of rapidity in W boson production or as a forward-backward asymmetry of the negative lepton direction in DY production of $\ell^+\ell^-$ pairs.

The W production charge asymmetry can be measured as:

$$\mathcal{A}(|y_W|) = \frac{d\sigma/d|y_W|(W^+ \to \ell^+\nu) - d\sigma/d|y_W|(W^- \to \ell^-\overline{\nu})}{d\sigma/d|y_W|(W^+ \to \ell^+\nu) + d\sigma/d|y_W|(W^- \to \ell^-\overline{\nu})}, \quad (2)$$

where $d\sigma/d|y_W|$ is the differential cross section for the absolute value of the W boson production rapidity in the laboratory frame.

The charge asymmetry in leptonic W boson decays has been measured in pp collisions at 7 [177, 233, 234], 8 [179], and 13 [235] TeV, where the charge asymmetry was also separately reported for the left- and right-handed W boson helicity states. The W boson charge asymmetry as a function of the absolute value of the W boson rapidity is shown in Fig. 14. Comparisons are made to MADGRAPH5_aMC@NLO NLO simulation (denoted MC@NLO) interfaced with PYTHIA for PS and QED lepton FSR and normalized to NNLO calculations using FEWZ 2.0 [41] with two PDF sets. For the NLO comparison, the p_T distribution of the generated W boson is reweighted based on comparisons between the p_T distribution of Z boson data and MADGRAPH5_aMC@NLO simulation. Also, the QED lepton FSR distribution is corrected to that of PHOTOS [78]. All predictions agree well with the data, except at high rapidity where some fluctuations are visible in the measurements relative to all three predictions. The PDF fits performed using the 7 and 8 TeV data were reported in Section 4.3.

For DY production of $\ell^+\ell^-$ pairs, the forward-backward asymmetry, A_{FB}, is computed in several regions of lepton pair mass as:

$$A_{FB} = \frac{\sigma_F - \sigma_B}{\sigma_F + \sigma_B}, \quad (3)$$

where σ_F (σ_B) is the total cross section for the forward (backward) events, defined by $\cos\theta^* > 0$ ($\cos\theta^* < 0$), where $\cos\theta^*$ is the angle between the negatively charged lepton and the Z boson momentum vector direction (in the laboratory frame) measured in the lepton pair centre-of-mass frame. The A_{FB} depends on $m(\ell^+\ell^-)$, quark flavour, and the EW mixing angle θ_W. Near the Z boson mass peak, the A_{FB} is close to zero because of the small value of the charged-lepton vector coupling to Z bosons. Due to weak-electromagnetic interference, A_{FB} is large and negative for m below the Z boson peak ($m < 80$ GeV) and large and positive above the Z boson peak ($m > 110$ GeV).

The DY A_{FB} measurements are reported for pp collision data at 7 [236, 237] and 8 [238, 239] TeV. In Ref. [239], using A_{FB} around the Z boson peak, as modelled for different $\sin^2\theta^{eff}_{lept}$ values using POWHEG v2 and the NNPDF3.0 PDF set, the effective leptonic EW mixing angle was extracted as $\sin^2\theta^{eff}_{lept} = 0.23101 \pm 0.00036\,(stat) \pm 0.00018\,(syst) \pm 0.00016\,(theo) \pm 0.00031\,(PDF) = 0.23101 \pm 0.00053$.

5.1.4 Measurements of vector boson production in association with jets

Many vector boson analyses also consider associated jet production. As with pure QCD jet analysis, the production of vector bosons in association with jets is an excellent test of perturbative QCD predictions. Production of W and Z in association with jets, followed by the $W^+ \to \ell^+\nu_\ell$ and $Z \to \ell^+\ell^-$ decays, respectively, allows for some of the most stringent perturbative QCD tests. Figure 9 shows Feynman diagrams for the radiation of a photon, Z boson, or W boson from a quark where the boson is produced in association with one jet. These NLO

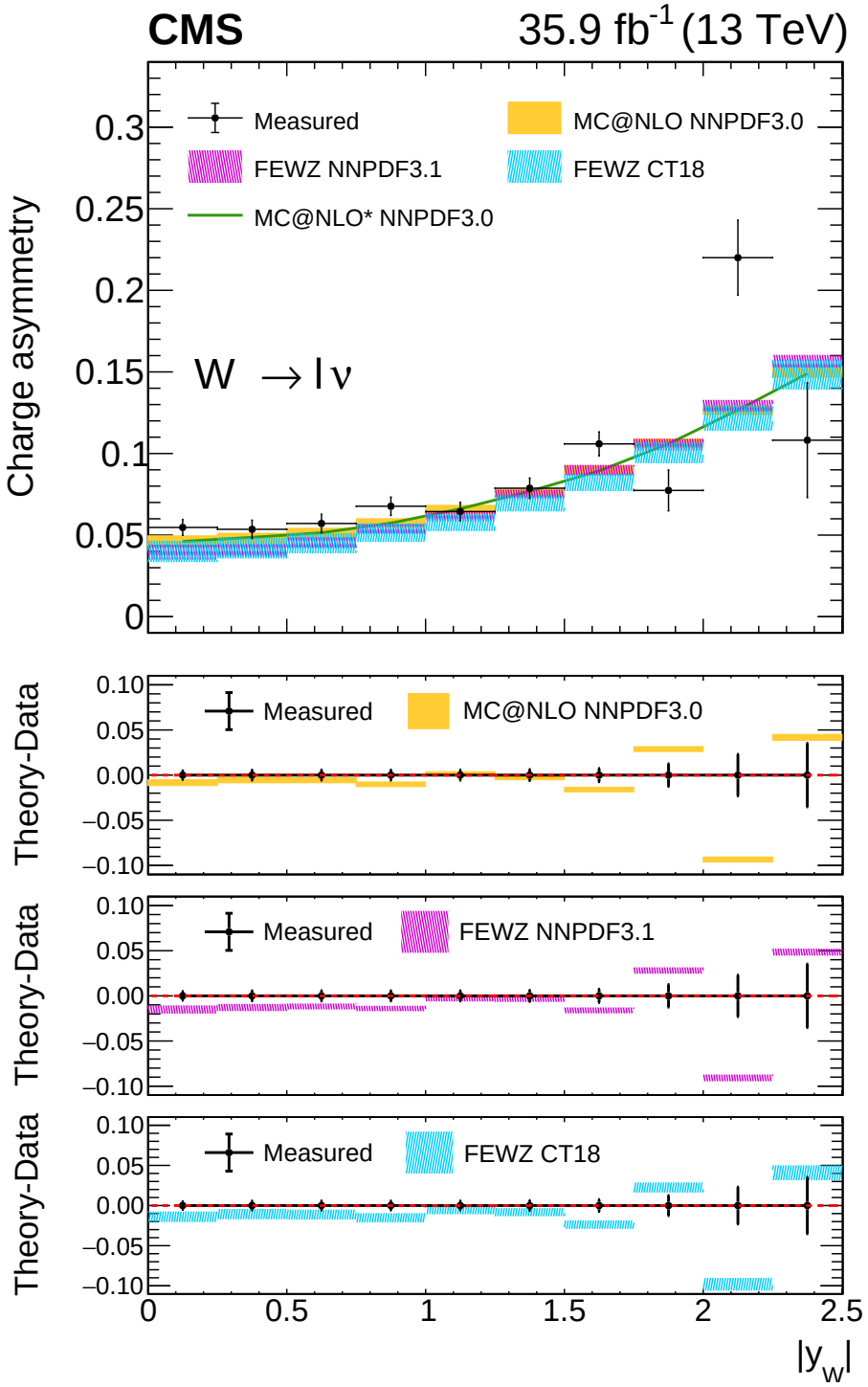

Figure 14: Measured W boson charge asymmetry as a function of $|y_W|$ from the combination of the electron and muon channels (black dots), compared with different theoretical predictions. The vertical errors bars around the experimental data points show the total uncertainty of the measurements. The yellow band represents the default generator used in this analysis, MG5_aMC with the NNPDF3.0 PDF set, the pink band represents the FEWZ generator with the NNPDF3.1 PDF set, and the cyan band represents the FEWZ generator with the CT18 PDF set. The uncertainty bands of the prediction include the PDF uncertainties only, which are dominant with respect to α_S, or renormalization and factorization scale variations for this quantity. Figure taken from Ref. [235].

QCD diagrams for vector boson production can either involve a gluon in the initial state or the radiation of a gluon in the final state. The addition of new initial states, in this case involving a gluon, means that NLO production almost always increases the expected inclusive cross section and including NLO diagrams is always necessary to get reasonably accurate cross section predictions. Topologies with up to 8 jets have been analyzed and compared with MC generators at LO, NLO, and NNLO accuracy.

The most recent 13 TeV Z+jets measurement [240] is shown in Fig. 15 with comparisons to three fixed-order MC generator predictions. Fixed-order predictions generate at a given level of perturbative accuracy all tree-level production diagrams for the selected process and all diagrams with additional partons up to a given number. In the analysis, jets are required to have $p_T > 30\,\text{GeV}$ and $|y| < 2.4$. The first comparison is to MADGRAPH5_aMC@NLO generated with $\leq$4 partons at LO accuracy interfaced with PYTHIA 8 for PS using the MLM [241, 242] ME-PS jet merging scheme. The second comparison is to MADGRAPH5_aMC@NLO generated with $\leq$2 partons at NLO accuracy interfaced with PYTHIA 8 for PS using the FxFx [243] ME-PS jet merging scheme. As an NLO QCD prediction, one-loop diagrams are included, as well as diagrams with real emission of an additional parton at LO accuracy. The samples are normalized to NLO cross section predictions produced using MCFM. The final comparison is to the GENEVA [244, 245] MC which combines an NNLO ME calculation with an NNLL accuracy resummation of the zero-jettiness τ variable, also known as the beam thrust [246]. The NNLO matrix elements include the real emission of two additional partons. Thus the MADGRAPH5_aMC@NLO prediction effectively includes three-jet topologies at LO accuracy, and the GENEVA NNLO prediction effectively includes one-jet topology at NLO accuracy and two-jet topology at LO accuracy. The results show that modelling additional jets using ME calculations produces the best agreement with predictions at higher jet multiplicities. In fact, the MADGRAPH5_aMC@NLO (NLO) and GENEVA (NNLO) predictions exhibit disagreement for all jet multiplicities that exceed the number of jets included in the ME calculations. The MADGRAPH5_aMC@NLO L0 generator, with up to 4 partons in the ME calculations, models the entire distribution well. In this analysis, PYTHIA 8uses the CUETP8M1 [148] tune of UE physics based on the MONASH [247] tune, which was trained to improve modelling of a wide variety of data sets including DY production at lower LHC energies.

A complete set of cross section measurements for W and Z production in association with jets is displayed in Fig. 63. The analyses, and the MC generators and configurations used to evaluate the theory comparisons shown in the plot are given in Table 11. The figure includes cross section measurements for topologies with vector bosons, multiple vector bosons, Higgs bosons, and top quark production in association with jets. The 8 TeV Z+jets results [248] are summed as necessary over the exclusive results per number of jets with uncertainties computed accounting for correlations of systematic sources.

Differential properties of vector boson production in association with jets are a complex and stringent test of our understanding of perturbative QCD physics. An illustrative example is shown in Fig. 16 of the jet rapidity of the 4^{th} jet from the 8 TeV analysis of Z+jets data [248]. This 8 TeV Z+jets measurement includes comparisons to three MC generators. The first comparison is to MADGRAPH 5 generated with $\leq$4 partons with LO accuracy interfaced to PYTHIA 6 for PS (denoted MG5 + PY6). The parameters of PYTHIA 6 are set to the Z2* tune [254], which are designed to reproduce lower collision energy LHC data, and are found to model DY data well [148]. The MADGRAPH 5 prediction is normalized to the FEWZ NNLO cross section. The second comparison is to MADGRAPH5_aMC@NLO (denoted MG5_aMC) generated with $\leq$3 partons, at NLO accuracy for events with $\leq$2 partons and LO accuracy for 3 partons. The MADGRAPH5_aMC@NLO generator is interfaced with PYTHIA 8 for PS using the FxFx ME-PS

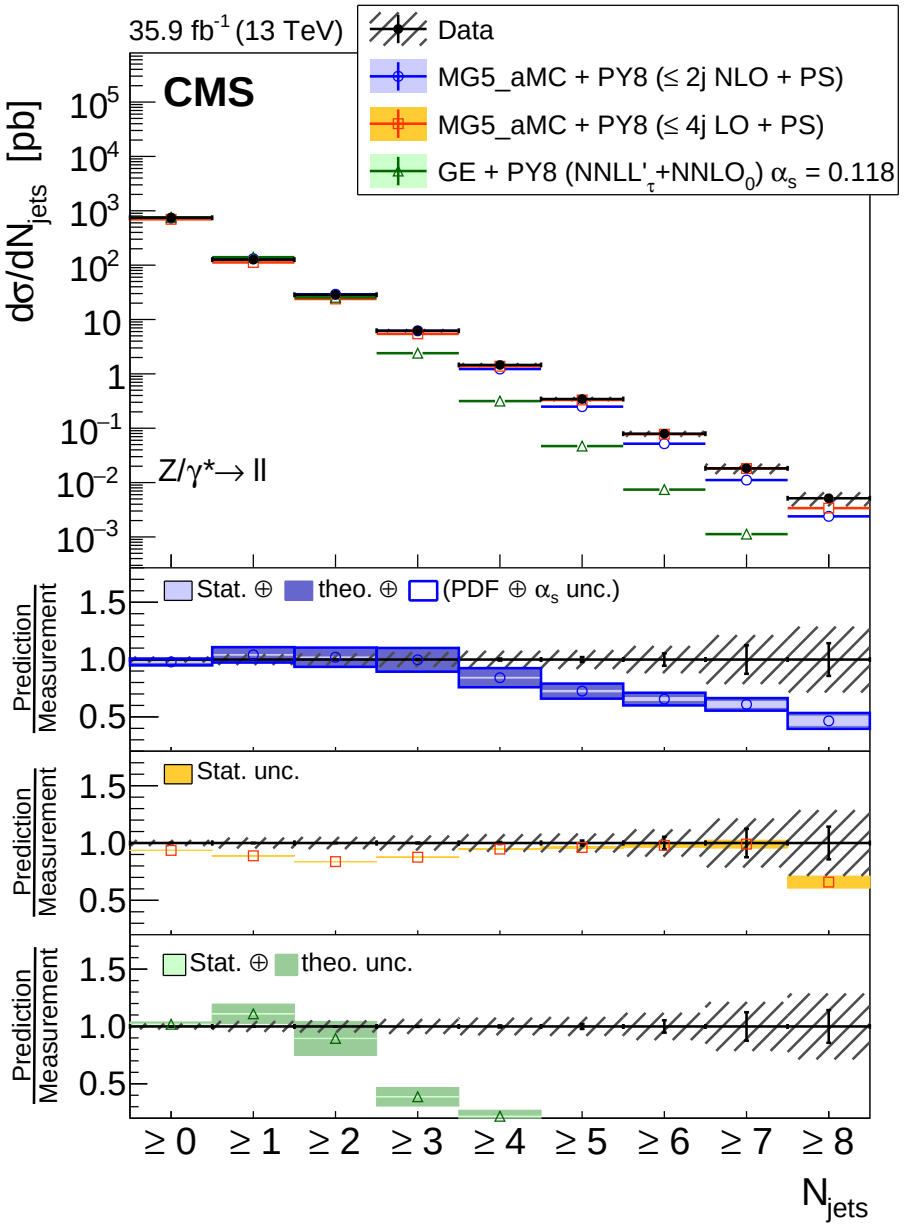

Figure 15: The differential cross section of $Z \to \ell^+\ell^-$+jets production as a function of inclusive jet multiplicity, compared with the predictions calculated with MADGRAPH5_aMC@NLO (LO) + PYTHIA 8, MADGRAPH5_aMC@NLO (NLO) + PYTHIA 8, and GENEVA. The lower panels show the ratios of the theoretical predictions to the measurements. The measurement statistical (systematic) uncertainties are presented with vertical error bars (hashed areas). The boxes around the MADGRAPH5_aMC@NLO (NLO) + PYTHIA 8 to measurement ratio represent the uncertainty in the prediction as listed in the legend. Figure taken from Ref. [240].

Table 11: Measurements of W and Z boson production in association with jets and the MC generators used for comparison to the measured cross sections. All measurements are inclusive cross sections for the vector boson produced in association with the listed or higher number of jets. For each measurement, the pp collision energy, ME generator, largest number of hard partons generated, largest number of hard partons generated at NLO accuracy, PS generator, and the ME-PS matching scheme are given. Events generated with greater than the number of NLO partons have LO accuracy. If no matching scheme is listed the comparison was done directly to the parton-level cross section predictions after applying a correction for NP effects. For the 7 and 8 TeV results the SHERPA with BLACKHAT (SHERPA 1/2, BH) NLO comparison was done only for lower parton multiplicities. The MADGRAPH 5 or MADGRAPH5_aMC@NLO (denoted MG5_aMC) comparisons are shown for higher jet multiplicities.

Boson # Jets	$\sqrt{s}$ (TeV)	Generator	partons total	partons NLO	PS	ME-PS scheme
W 1–5j [249]	7	SHERPA 1,BH	5	5	—	—
W 6j [249]	7	MADGRAPH 5	4	—	Py6	CKKW [241]
W 1–4j [250]	8	SHERPA 2,BH	4	4	—	—
W 5,6j [250]	8	MG5_aMC	3	2	Py8	FxFx
W 1–6j [251]	13	MG5_aMC	4	2	Py8	FxFx
Z 1–6j [252]	7	SHERPA 1,BH	4	1	CS	MEPS@NLO
Z 1–7j [248]	8	SHERPA 2,BH	4	2	CS	MEPS@NLO
Z 1–6j [253]	13	MG5_aMC	4	2	Py8	FxFx

DRAFT

merging scheme. The final comparison is to SHERPA 2 with BLACKHAT [56, 255] generated with $\leq$4 partons, with NLO accuracy for events with $\leq$2 partons and LO accuracy for 3 and 4 partons, PS using CSSHOWER PS [94] based on Catani–Seymour dipole factorization, interfaced with NLO accuracy using the MEPS@NLO [256] ME-PS merging scheme (the combination of which is denoted Sherpa 2). The NLO predictions are not normalized. In this measurement, an analysis of the rapidity of each jet, where the jets are ordered in p_{T}, is performed. The selected plot corresponds to the fourth p_{T}-ordered jet, which is the highest jet multiplicity for which the statistical power is sufficient for a precise comparison of the rapidity distribution with the simulation. As shown above, LO predictions do well with more inclusive properties, such as the simple production of a given number of jets. However, they do not perfectly model many kinematic features of the production of jets. Higher-order generators can capture more of the details of the production kinematics. In this analysis, the LO predictions of the rapidity distribution of jets disagree for the lower-p_{T} jets in Z boson + multijet events with high multiplicities of jets. The best agreement is seen with the SHERPA 2 predictions, which include LO MEs for four-jet production and NLO generation for lower numbers of jets. Differential analyses of complex final states are essential in pushing our understanding of QCD and combined EW and QCD physics. These are the types of analyses that most directly reveal the shortcomings in our ability to model complex physics interactions and show the need for higher perturbative order predictions of parton-parton interactions.

Associated production of a photon and a jet has been measured triple-differentially at 7 [257], 8 [258] and 13 [214] TeV as a function of photon E_{T}, photon rapidity, and jet rapidity. The results are compared with the NLO calculations from JETPHOX [215] (7 and 13 TeV) and NLL calculations using γ + jet [42, 43] and the CJ15 PDF set [102] (8 TeV). Both calculations use the BFG [216] fragmentation functions for quarks and gluons. The measurements are in good agreement with the predictions. In the same analysis, the inclusive production cross section of events with at least one photon and one jet has been measured. With a requirement of $p_{\mathrm{T}} >$ 40 GeV for both objects, a cross section of $8.01 \pm 0.11\,(\mathrm{stat}) \pm 0.74\,(\mathrm{syst})$ nb [257] is measured consistent with theory predictions. This result was obtained by integrating over the differential η and p_{T} cross sections presented in Ref. [257], accounting for correlations between systematic uncertainty sources.

Although the CMS experiment has not generally performed simple γ+jets counting analyses as in the W+jets and Z+jets cases, it has performed an array of differential analyses of γ+jets production. Among the most interesting of these analyses are comparisons between γ+jets and Z+jets production, where the Z bosons decay to muons which is the lowest background decay mode. These allow us to study the similarities between these final states, which are leveraged in SM cross section analysis and BSM physics searches involving photons, by using our extensive understanding of low-background events with Z bosons to better describe topologies involving a photon. The γ+jets and Z+jets comparisons have been performed at 7 [259], 8 [260], and 13 [261] TeV. Comparisons are made to MC simulations of the kinematic distributions of the bosons and the jets as functions of the number and type (light or b-flavoured) of jets. Cross section distributions are shown separately for events with Z bosons and photons, and as ratios. Figure 17 shows a comparison from the 13 TeV analysis [261] of the ratio of Z+jets and γ+jets production in events with at least one jet compared with NLO QCD with NLO EW theoretical predictions. Two fixed-order NLO MC generator comparisons are shown. The MADGRAPH5_aMC@NLO comparison (denoted MG5_aMC) of Z production includes topologies with up to 3 hard partons and events with $\leq$2 partons have NLO QCD accuracy, whereas events with 3 partons have LO accuracy. The MADGRAPH5_aMC@NLO γ+jets production is generated with up to one parton at NLO QCD accuracy. Matrix element to PS matching is

DRAFT

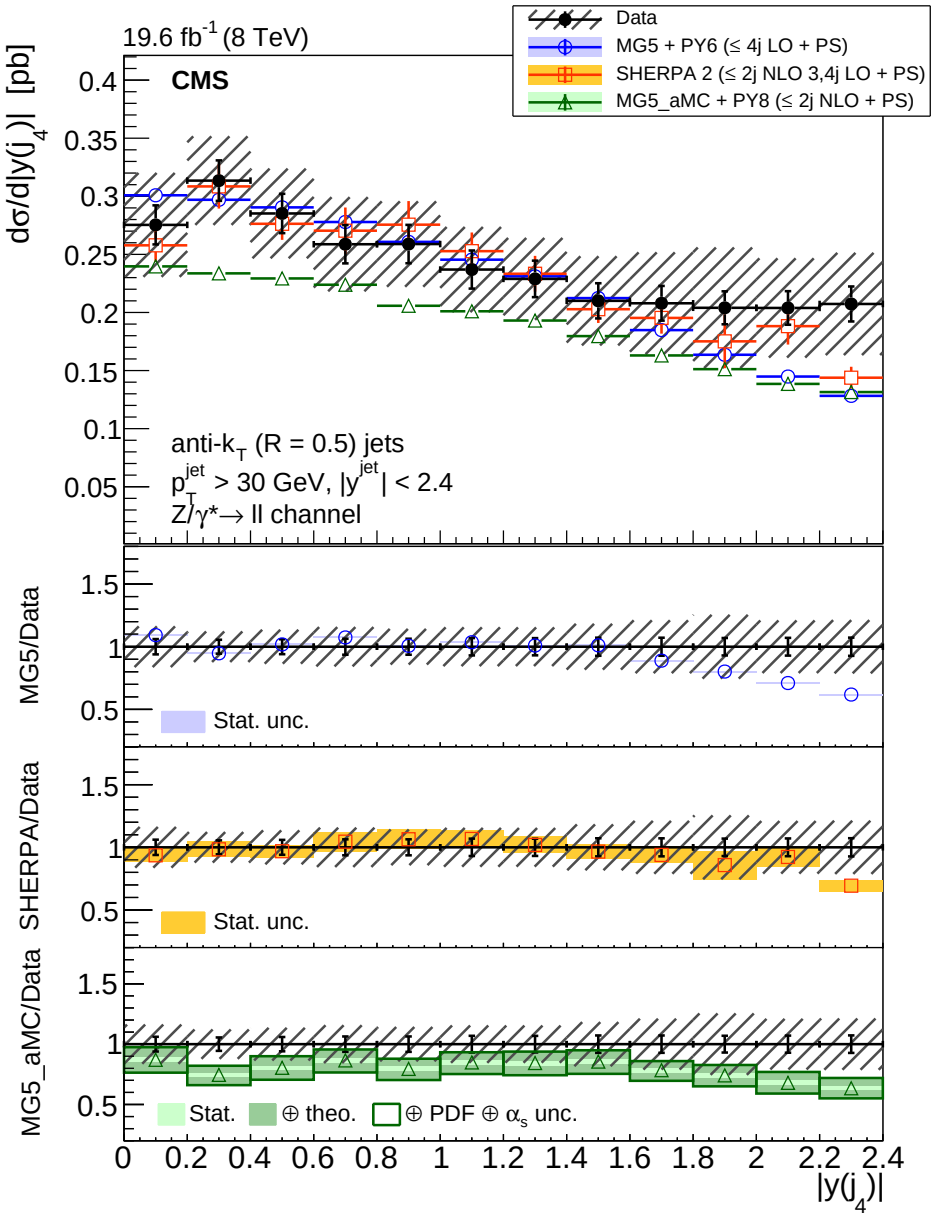

Figure 16: The differential cross section for Z $\rightarrow \ell^+\ell^-$+ jets production as a function of the absolute value of the 4th jet's rapidity compared with the predictions calculated with MADGRAPH 5+PYTHIA 6, SHERPA 2, and MG5_aMC +PYTHIA 8. The lower panels show the ratios of the theoretical predictions to the measurements. Error bars around the experimental points show the statistical uncertainty and the cross-hatched bands indicate the statistical and systematic uncertainties added in quadrature. The boxes around the MG5_aMC + PYTHIA 8 to measurement ratio represent the uncertainty in the prediction, including statistical, theoretical (from scale variations), and PDF uncertainties. The dark green area represents the statistical and theoretical uncertainties only and the light green area represents the statistical uncertainty alone. Figure taken from Ref. [248].

performed using the FxFx prescription [243]. The cross section of the generated Z boson sample is normalized to the value of an NNLO prediction computed with FEWZ. The SHERPA + OPENLOOPS [55, 96] samples of Z and γ production are generated with $\leq$4 partons, with NLO QCD accuracy for events with $\leq$2 partons and LO accuracy for events with 3 and 4 partons. Approximate EW corrections are applied to these samples using the COMIX [93] and OPENLOOPS [74–77] ME generators. Parton showering is performed using CSSHOWER [94] and ME-PS jets matching is performed using the MC@NLO method [262, 263]. As the branching fraction of the Z boson to muons is 3.4%, Fig. 17 is an illustration of EW unification at high energy, since the ratio of production cross sections and thus the coupling constants for the Z bosons and photons is of order one and independent of energy above several times the Z boson mass.

5.1.5 Measurements of vector boson production in association with heavy-flavour jets

The CMS experiment has performed many analyses of vector boson production in association with bottom- and charm-flavoured jets. Representative Feynman diagrams are shown in Fig. 18. Advancements in machine-learning techniques have resulted in the creation of highly efficient jet taggers for bottom and charm jets, demonstrating high accuracy and minimal backgrounds from light-flavour quark and gluon jets. Other effective techniques of identifying heavy-flavour jets include the reconstruction of exclusive final states for charm tagging. The measurement of W + charm jet events provides a direct probe of the strange quark content of the proton. The CMS PDF constraints from W + charm measurements are competitive with those from the neutrino scattering and global PDF fits. The study of W and Z boson production with charm jets may eventually contribute to the endeavour to measure the second-generation quark Yukawa coupling to the Higgs boson using associated VH production with the Higgs boson decaying to charm quarks. The study of Z + charm jets could contribute to studies of the intrinsic charm component of the proton PDF, where it would contribute to additional Z + charm jet events at high p_{T}. Consequently, the CMS Z + charm analyses measure the differential distribution of charm jet production *vs.* jet p_{T}. The V+b or multiple b jets production, where V is a W or Z boson, contains events sensitive to the b quark content in the proton or gluon splitting to b jets. The CMS experiment has also studied WZ and ZZ production, with one Z boson decaying to two b jets [264], yielding the V+2 b jets signature, constitutes the dominant irreducible background to associated Higgs boson production (WH and ZH), and provides important input to that study.

A complete set of cross section measurements for vector boson with heavy-flavour jet production is shown in Fig. 63. One of the most critical components of each analysis is the heavy-flavour jet tagging method. Table 12 lists the production cross sections measured, the pp collision energy, the heavy-flavour tagging technique, and the source of theory cross section calculation used for comparison of the vector boson with heavy-flavour jet production measurements. The heavy-flavour tagging techniques were explained in Section 2.2. In addition, the table lists for each analysis other results produced, such as differential distributions and PDF constraints. As the measurement of the Z + charm jet cross section at 8 TeV is performed in a fiducial region, the cross section is multiplied by the acceptance for leptonic Z boson decays taken from the same Ref. [265] to calculate the total cross section for comparison to the other results. The measurement and prediction of cross sections with jets have long been difficult at high-energy colliders with many discrepancies between data that were identified and later resolved with a better understanding of both detector calibration of quark and gluon jet momentum and the theoretical modelling of such processes. The good agreement between the experimental measurements and predictions for a high multiplicity of jets, including the production of heavy-flavour jets, is an important achievement of the LHC physics programme that

DRAFT

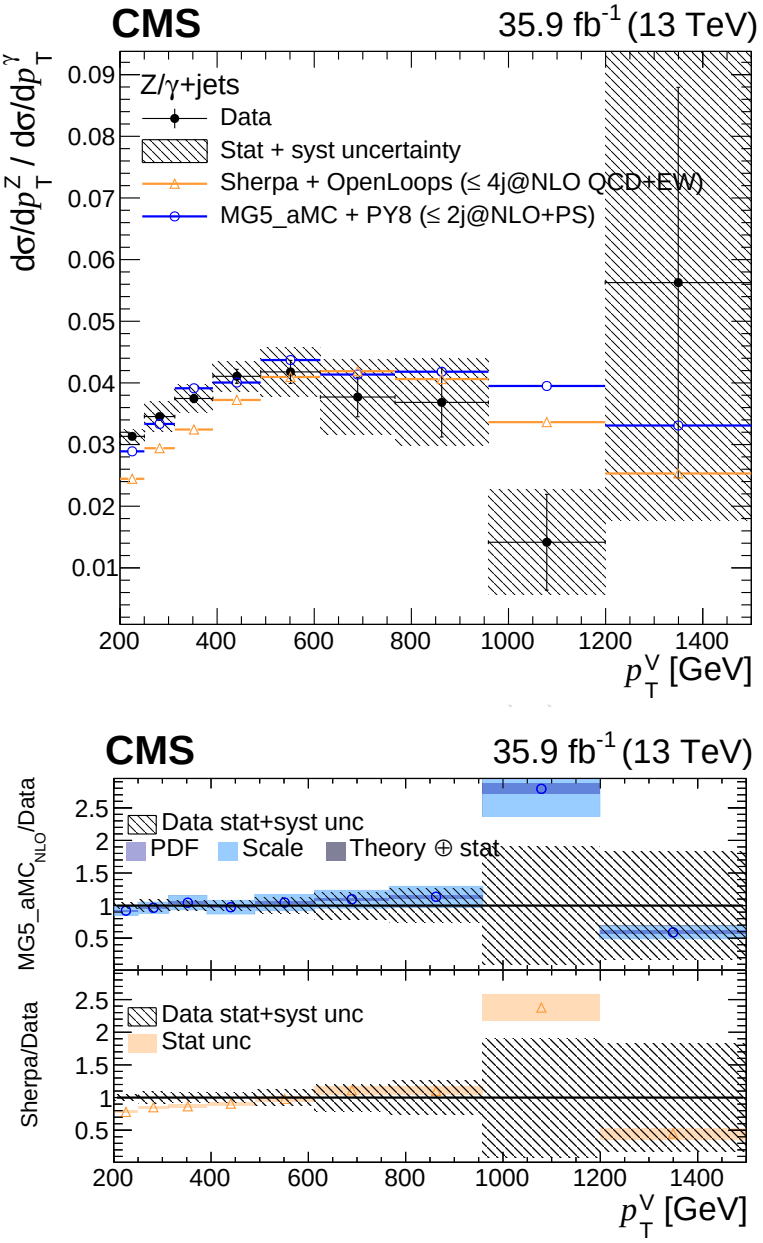

Figure 17: Differential cross section ratio of Z+jets to γ+jets as a function of the vector boson (V) transverse momentum compared with the theoretical prediction from MADGRAPH5_aMC@NLO and SHERPA + OPENLOOPS. Only bosons produced centrally, with $|y| < 1.4$, in association with one or more jets are considered. The panel shows the ratio of the theoretical prediction to the unfolded data. The vertical errors bars around the experimental data points show the statistical uncertainties of the measurements. The hatched band is the sum in quadrature of the statistical and systematic uncertainty components in the measurement. The dark (light) shaded band on the NLO prediction from MADGRAPH5_aMC@NLO represents the PDF (scale) uncertainties, which are treated as uncorrelated between Z+jets and γ+jets, whereas the statistical uncertainties are barely visible. The shaded band on the SHERPA + OPENLOOPS calculation is the statistical uncertainty. Figure taken from Ref. [261].

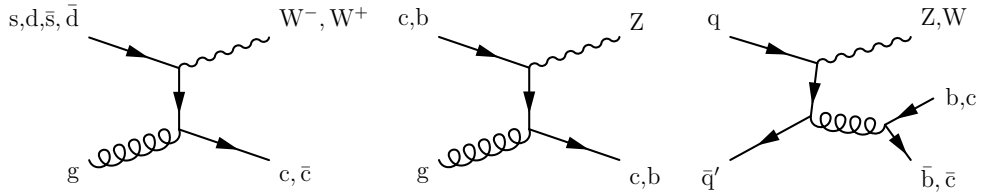

Figure 18: Production of W or Z bosons with heavy-flavour quarks. Examples of lowest order Feynman diagrams include W + charm (left), Z + charm or bottom (middle), W or Z production with two heavy-flavour quarks (right).

found use in the discovery of the Higgs boson and in the searches for BSM physics.

5.2 Inclusive multiboson production and interactions

Multiboson production is typically categorized into inclusive production that is dominated by the radiation of vector bosons from initial-state quarks in the proton, and EW production in which the radiation of bosons is followed by pure EW interactions among the vector (and Higgs) bosons via scattering or fusion. These interactions are classified into the subsets of diboson production, triboson production, VBF, and VBS. Studying multiboson production provides a test of the gauge structure of the SM that uniquely predicts how the gauge bosons interact with each other by directly measuring triple gauge boson couplings (TGCs) and eventually quartic gauge boson couplings (QGCs). Studying VBS and the polarization of the bosons gives sensitivity to the features of EW symmetry breaking, which has been exclusively studied at the LHC and can provide a platform to search for BSM anomalous quartic gauge boson couplings (aQGCs). In addition, ratios of production rates have sensitivity to PDFs. Measurements are typically made either inclusively of a diboson signature, including the EW processes, or of only the EW component, as described in Section 5.3. In principle, every multi-gauge-boson process in the SM with up to three gauge bosons can be observed at the LHC experiments. Several multiboson states can be observed in such pure samples for which cross section measurements are approaching the 3% total uncertainty level, and they may eventually be measured with the accuracy approaching that of single vector boson production. Currently, only the rarest of the multivector boson processes, such as ZZ VBS production (which has been detected with 4σ significance [277]), have not been observed by the CMS experiment. Representative LO Feynman diagrams for WZ production are shown in Fig. 19 including both radiative production, where the bosons are radiated off a quark, and TGC production, where $q\overline{q}$ annihilation results in an off-shell W boson, which splits into the W and Z bosons. The interference of the amplitudes of these two processes dominates the production cross section for inclusive WZ production.

5.2.1 Diboson production

The diboson production cross sections are among the most precisely measured by the CMS experiment. The combination of pure $W^+ \to \ell^+\nu_\ell$ and $Z \to \ell^+\ell^-$ samples and the large integrated luminosity delivered by the LHC and collected by the CMS experiment provide a precision rarely achieved previously by hadron collider experiments. An understanding of diboson production is essential for the studies of the Higgs boson and searches for new physics where diboson production is often a significant SM background. Diboson production also has an indirect sensitivity to new physics that may occur in loop diagrams often characterised as anomalous additions to the SM TGC and QGC multiboson couplings. The Feynman diagram shown in Fig. 19 (right) illustrates how WZ production has sensitivity to measure the SM WWZ TGCs or anomalous TGCs (aTGCs) that could modify those couplings due to BSM physics contributions.

Table 12: Table of measurements of W and Z boson production in association with heavy-flavour quarks. The table lists the measured production cross sections, pp collision energy, heavy-flavour tagging technique, source of theory cross section calculation used for comparison, and other results of interest produced by the analysis. In several cases, ratios of production cross sections are measured including $R_{W^+\bar{c}/W^-c} = \sigma(W^+\bar{c})/\sigma(W^-c)$, $R_{Wc/Zb} = \sigma(Wc)/\sigma(Zb)$, $R_{Zb/Zq} = \sigma(Zb)/\sigma(Zq)$ and $R_{Z\geq 2b/Z\geq 1b} = \sigma(Z \geq 2b)/\sigma(Z \geq 1b)$. Parton-level MCFM NLO and NNLO predictions are corrected for NP effects. All predictions are computed at NLO QCD accuracy except for the W+c 13 TeV analysis, where the prediction is done at NNLO QCD and NLO EW accuracy [266, 267].

Boson # Jets	$\sqrt{s}$ (TeV)	Heavy flavour tagging	Theory calculation	Other results
W+1c [178]	7	D meson	MCFM	$R_{W^+\bar{c}/W^-c}$, $p_T(\mu)$
W+1c [268]	8	μ, SSV, IVF	MCFM	$R_{W^+\bar{c}/W^-c}$, $p_T(\mu)$, $\eta(\ell)$, s PDF
W+1c [269]	13	D meson	MCFM	$R_{W^+\bar{c}/W^-c}$, $\eta(\mu)$, s PDF
W+1c [270]	13	SV tag: SSV IVF	NNLO	$R_{W^+\bar{c}/W^-c}$, $p_T(\mu)$, $\eta(\mu)$
W+2b [271]	7	CSV	MCFM	
W+2b [272]	8	CSV	MCFM	
Z+1c [265]	8	μ+SV: SSV IVF, D	MCFM	$R_{Wc/Zb}$, $p_T(Z)$, $p_T(c)$
Z+1c [273]	13	DEEPCSV+m_{SV}	MG5_aMC	$p_T(Z)$, $p_T(c)$
Z+1,2b [274]	7	SSV	MCFM	$R_{Zb/Zq}$
Z+1,2b [275]	8	CSV	MG5_aMC	$R_{Z\geq 2b/Z\geq 1b}$, m_{bb}, 20 dist.
Z+1,2b [276]	13	DEEPCSV	MG5_aMC	$R_{Z\geq 2b/Z\geq 1b}$, m_{bb}, 15 dist.

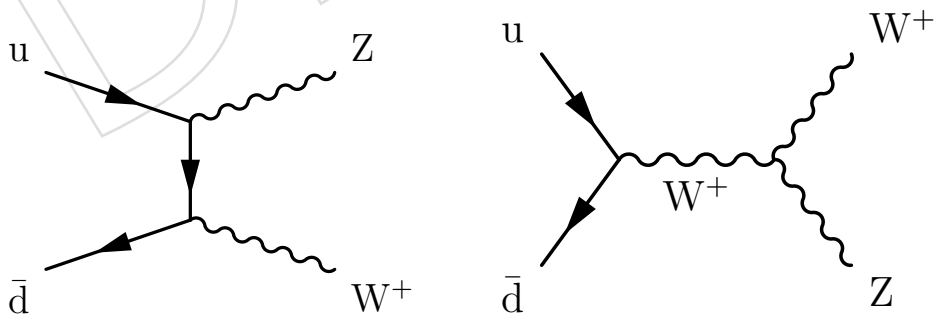

Figure 19: Feynman diagrams for WZ diboson production. Shown are radiative production (left), where the vector bosons are radiated off a quark, and a TGC production (right), where a W boson is created by $q\bar{q}$ annihilation and splits into W and Z bosons. These diagrams are representative of all diboson production mechanisms that involve radiative or TGC processes. In the case of neutral final states TGCs are forbidden in the SM and only anomalous coupling due to new physics could lead to contributions from that type of diagram.

DRAFT

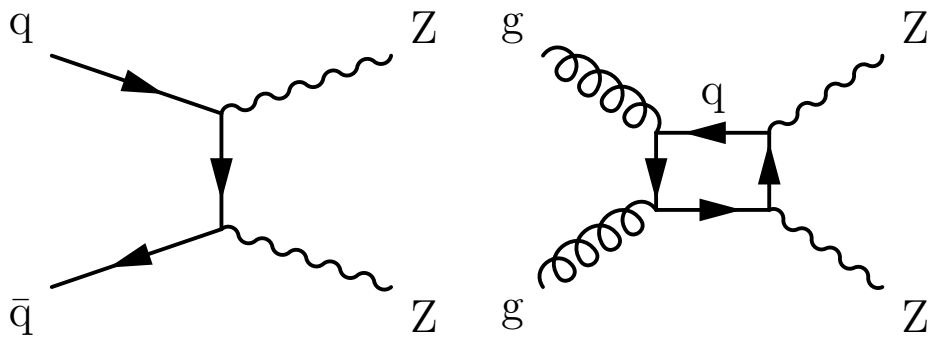

Figure 20: Feynman diagrams for ZZ diboson production including radiative production (left) and NNLO production via a gluon-gluon initial state (right), which increases the total production cross section significantly.

In the first LHC 7 TeV run all the diboson states seen by previous experiments were observed, including $\gamma\gamma$ [278], Wγ and Zγ [279], opposite-sign $W^{\pm}W^{\mp}$ [280], WZ [281], and ZZ [282] signatures. The cross sections for diboson production have been measured at 5.02, 7, 8, and 13 TeV in Run 1 and Run 2 of the LHC. The diboson production processes measured at CMS are listed in Table 13. Included is information on pp collision energy, theory calculations used for comparison in Fig. 21, and other results of interest. For comparison NNLO QCD predictions are necessary to predict the cross sections and distributions of these processes with sufficient accuracy. This is both because NNLO production can introduce new initial states, such as the gluon-gluon initial state for ZZ (and $W^{\pm}W^{\mp}$) production, shown along with the radiative production Feynman diagram in Fig. 20, and because the precision of the experimental diboson production measurement in many final states is at the several percent level, which requires NNLO QCD computations to achieve equivalent accuracy. These factors have pushed extensive developments in the theory to accurately predict these states and match the precision of the experimental measurements. The theoretical cross section for comparison to the measured $\gamma\gamma$ production rate is calculated using the 2γNNLO [283] programme. Comparisons to theoretical cross section predictions for the 7 TeV Wγ and Zγ production are calculated using parton-level MCFM NLO predictions corrected for NP effects. The 8 TeV Z γ result is compared with the NNLO prediction from Ref. [284]. The MATRIX predictions have NNLO QCD and NLO EW precision for $q\bar{q}$ processes, and NLO QCD accuracy for the gg initial state processes that contribute to $W^{\pm}W^{\mp}$ and ZZ production. Same-sign (SS) $W^{\pm}W^{\pm}$ production has been measured as well and is discussed in Section 5.3.

These measurements are summarized in Fig. 21. The figure shows that both experimental measurements and theory, typically at the level of NNLO QCD, agree over all of the diboson production states with percent-level precision. In papers with total and fiducial measurements (13 TeV $W^{\pm}W^{\mp}$, WZ and ZZ), the fiducial cross section measurements have better precision and are used in the figure.

A plot focused on VV production, where V = W or Z, is shown in Fig. 22 for four energies measured by the CMS experiment. The measured total cross sections of pairs of weak bosons agree with the theoretical predictions [287]. Also shown are results from the ATLAS experiment [293–301], and from the Tevatron CDF [302, 303] and D0 [304–306] experiments where the production of pairs of weak bosons in hadron collisions was first observed. The figure presents the inclusive total cross sections for weak boson pair production and, where necessary, results reported as production cross section times branching fraction to lepton final states have been scaled by the inverse of the appropriate branching fraction. Extrapolation from the fiducial

DRAFT

Table 13: Table of diboson production cross section measurements. Listed in the table are the final states studied, pp collision energy, theory cross section calculation used for comparison, and selected additional results of interest from each paper.

Process	$\sqrt{s}$ (TeV)	Theory calculation	Other results
$\gamma\gamma$ [278]	7	2γNNLO	$m_{\gamma\gamma}$, 4 dist.
Wγ [279]	7	MCFM NLO	aTGC, $p_{\mathrm{T}}(\gamma)$
Wγ [285]	13	MG5_aMC 1p NLO	aTGC
Zγ [279]	7	MCFM NLO	aTGC, $p_{\mathrm{T}}(\gamma)$
Zγ [286]	8	NNLO	aTGC, $p_{\mathrm{T}}(\gamma)$
$\mathrm{W}^{\pm}\mathrm{W}^{\mp}$ [287]	5.02	MATRIX	
$\mathrm{W}^{\pm}\mathrm{W}^{\mp}$ [280]	7	MATRIX	aTGC
$\mathrm{W}^{\pm}\mathrm{W}^{\mp}$ [288]	8	MATRIX	aTGC, σ: with jet veto, 4 dist.
$\mathrm{W}^{\pm}\mathrm{W}^{\mp}$ [289]	13	MATRIX	aTGC, σ: with jet veto
WZ [287]	5.02	MATRIX	
WZ [281]	7	MATRIX	
WZ [281]	8	MATRIX	aTGC, $p_{\mathrm{T}}(\mathrm{Z})$, $p_{\mathrm{T}}(\mathrm{jet})$
WZ [290]	13	MATRIX	aTGC, boson polarization, 9 dist.
ZZ [287]	5.02	MATRIX	
ZZ [282]	7	MATRIX	aTGC
ZZ [291]	8	MATRIX	aTGC, $m_{4\ell}$, 7 dist.
ZZ [292]	13	MATRIX	aTGC, 6 dist.

DRAFT

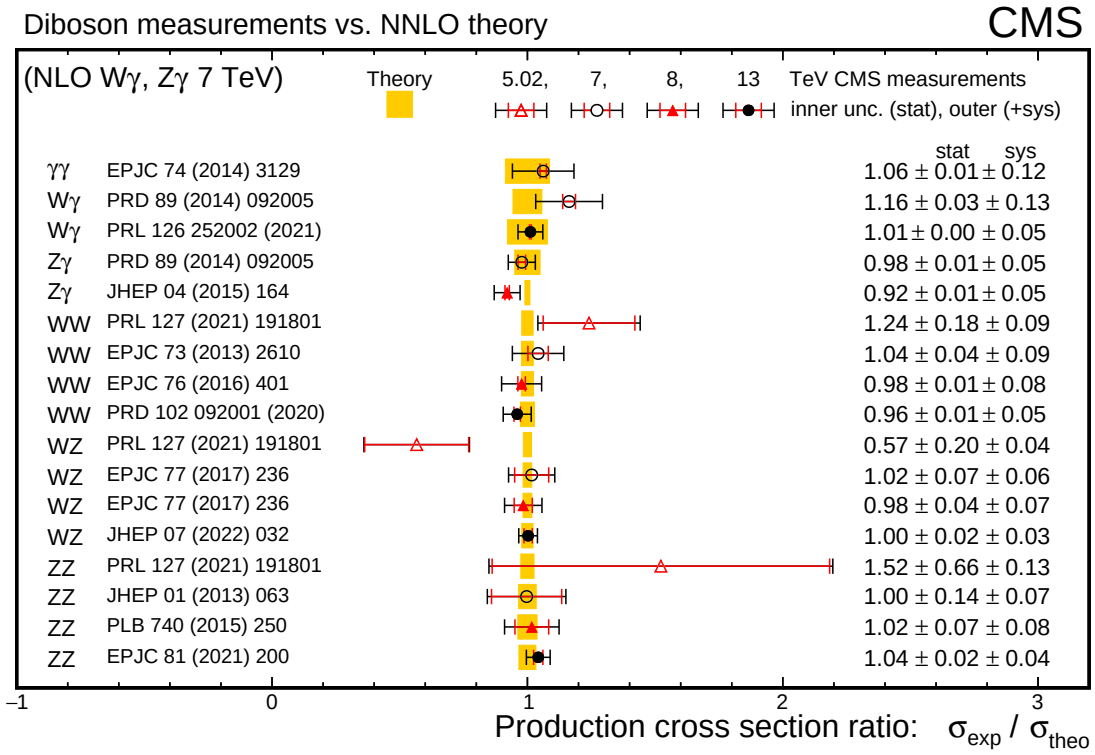

Figure 21: Summary of cross section measurements for diboson production shown as a ratio over the NNLO or NLO QCD predictions. The yellow bands indicate the uncertainties in the theoretical predictions and the error bars on the points are the statistical uncertainties, whereas the outer bars are the combined statistical and systematic uncertainties.

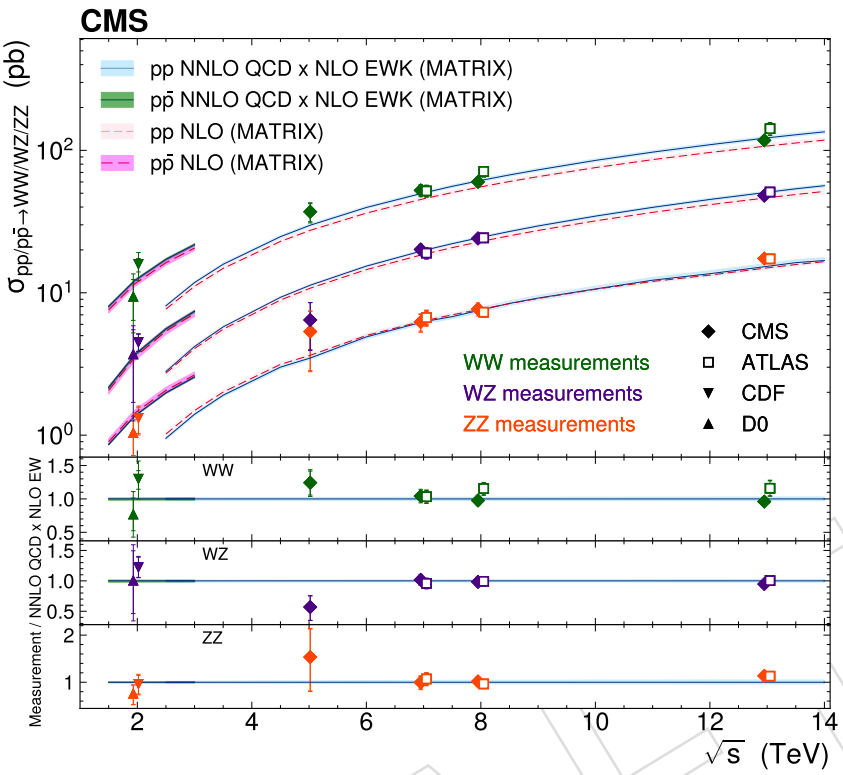

Figure 22: The total $W^{\pm}W^{\mp}$, WZ and ZZ cross sections as functions of the pp centre-of-mass energy. Results from the CMS and ATLAS experiments for pp collisions are compared with the predictions from MATRIX at NNLO in QCD and NLO in EW, and at NLO in QCD. Also shown are results from $p\bar{p}$ collisions at the CDF and D0 experiments compared with MATRIX predictions as above. The inner vertical errors bars around the experimental data points show the statistical uncertainties of the measurements, whereas the outer bars show the total uncertainties. Measurements at the same centre-of-mass energy are shifted slightly along the horizontal axis for clarity. Figure taken from Ref. [287].

measurement regions for the states involving $Z \to \ell^+\ell^-$ to total cross sections was done in mass ranges of 66–116 GeV and 60–120 GeV for ATLAS and CMS, respectively, leading to a 1.6% (0.8%) difference in the total cross sections calculated by ATLAS *vs.* CMS and the MATRIX predictions for ZZ (WZ) production. This effect is not corrected for in the plot and is not visible given the logarithmic scale. Diboson production cross sections are also summarized with other cross sections measured by CMS in Fig. 1 where, as above, the diboson results are presented as total cross sections.

The most precisely measured diboson cross sections at the CMS experiment are WZ and ZZ production. In the WZ case the high precision is possible because of the low background for Z decays to electrons or muons and the higher branching fraction for leptonic W decay. The WZ cross section in 13 TeV pp collisions [290] is measured as $\sigma_{\text{tot}}(\text{pp} \to \text{WZ}) = 50.6 \pm 0.8\,(\text{stat}) \pm 1.5\,(\text{syst}) \pm 1.1\,(\text{lumi}) \pm 0.5\,(\text{theo})\,\text{pb} = 50.6 \pm 1.9\,\text{pb}$. The overall 3.7% accuracy is dominated by the systematic and integrated luminosity uncertainties. The cross section is also measured in a fiducial phase space, which reduces the extrapolation uncertainty to the full phase space, where a 3.4% precision is achieved. At the time, the precision exceeded that of the single bo-

son cross section measurements from the CMS. Despite having the lowest statistical precision of any diboson production process, the cross section for ZZ production is the next most accurately measured. The precision of the measurement is driven by the very low background to two fully reconstructed Z boson decays to electrons and muons. The ZZ cross section for 13 TeV pp collisions [292] is measured as $\sigma_{\text{tot}}(\text{pp} \to \text{ZZ}) = 17.2 \pm 0.3\,(\text{stat}) \pm 0.5\,(\text{syst}) \pm 0.4\,(\text{theo}) \pm 0.3\,(\text{lumi})$ pb. The combined overall uncertainty is 4.3%. The cross section measured in a fiducial phase space has 3.7% precision.

The importance of NNLO QCD calculations is shown in Fig. 23 taken from Ref. [292], where the measured ZZ cross sections are shown compared with two calculations. The first calculation is performed with MCFM [66] at NLO in QCD for $\text{q}\bar{\text{q}}$ processes and LO QCD accuracy for gg initial-state processes (denoted MCFM qqNLO+ggLO). The second calculation is performed using MATRIX [46], which includes both NNLO QCD and NLO EW contributions for $\text{q}\bar{\text{q}}$ processes and NLO QCD accuracy for gg initial-state processes [307] (denoted MATRIX qq[NNLOxNLOEW]+ggNLO). The predictions use NNPDF31_nnlo_as_0118_luxqed and NNPDF3.0 PDF sets, respectively, and fixed factorization and renormalization scales $\mu_{\text{F}} = \mu_{\text{R}} = m_{\text{Z}}$. The CMS and ATLAS [299–301] measurements are compared with the theoretical predictions. The ATLAS measurements were performed with a Z boson mass window of 66–116 GeV, instead of 60–120 GeV used by CMS, and are corrected for the resulting 1.6% difference in acceptance. Contributions from NLO and NNLO QCD diagrams substantially enhance the cross section of diboson production and are necessary to show agreement with the experimental data with measured total cross sections.

Differential measurements have been made for all the diboson final states. A variety of distributions have been measured focusing on: basic kinematics, such as the p_{T} of leptons in leptonic vector boson decays and the p_{T} of the bosons; measurements of jets, including the number and p_{T} of associated jets; and quantities with sensitivity to possible BSM physics, such as the invariant mass of the diboson system or other quantities that assess the energy of the vector boson system. In differential measurements, areas of phase space can be identified that are particularly sensitive to higher-order QCD and EW perturbative predictions. For instance, variables that assess the energy of the diboson system, such as the diboson invariant mass, show large enhancements due to NLO and NNLO QCD effects at high mass. The NLO EW contributions tend to reduce the cross sections in the high-energy part of the distributions. As an illustration, Fig. 24 shows the $m_{4\ell}$ distribution from Ref. [308]. Comparisons are made to four MC generator predictions. The first prediction is from MADGRAPH5_aMC@NLO for $\text{q}\bar{\text{q}} \to \text{ZZ}$ at NLO QCD, POWHEG $\text{H} \to \text{ZZ}$ at NLO QCD, and MCFM $\text{gg} \to \text{ZZ}$ at LO QCD (denoted MG5_aMC@NLO). The second prediction is from POWHEG at NLO in QCD. The final two comparisons are calculated using nNNLO simulation, which performs NNLO QCD calculations matched to PS using the MiNNLO method [309] (denoted nNNLO+PS). This simulation includes EW corrections that were applied as a multiplicative K-factor as a function of $m_{4\ell}$. The best agreement with data is seen with the nNNLO+PS with EW corrections applied, which are necessary to achieve better agreement at high $m_{4\ell}$.

An essential test of the EW interactions and the nature of the W and Z bosons is a measurement of their polarization. Through the EW symmetry-breaking Brout–Englert–Higgs mechanism, the W and Z bosons acquire longitudinal polarization and hence mass. The SM fractions of bosons produced in specific polarization states in pp collisions in both single and multiboson production are predicted by the EW theory. These fractions can be extracted from the angular distributions of the decay products of W and Z bosons. In cases with decays to charged leptons, the CMS experiment makes very accurate measurements of the angular distributions of the emitted leptons. The lepton emission angles in the boson rest frame relative to the bo-

DRAFT

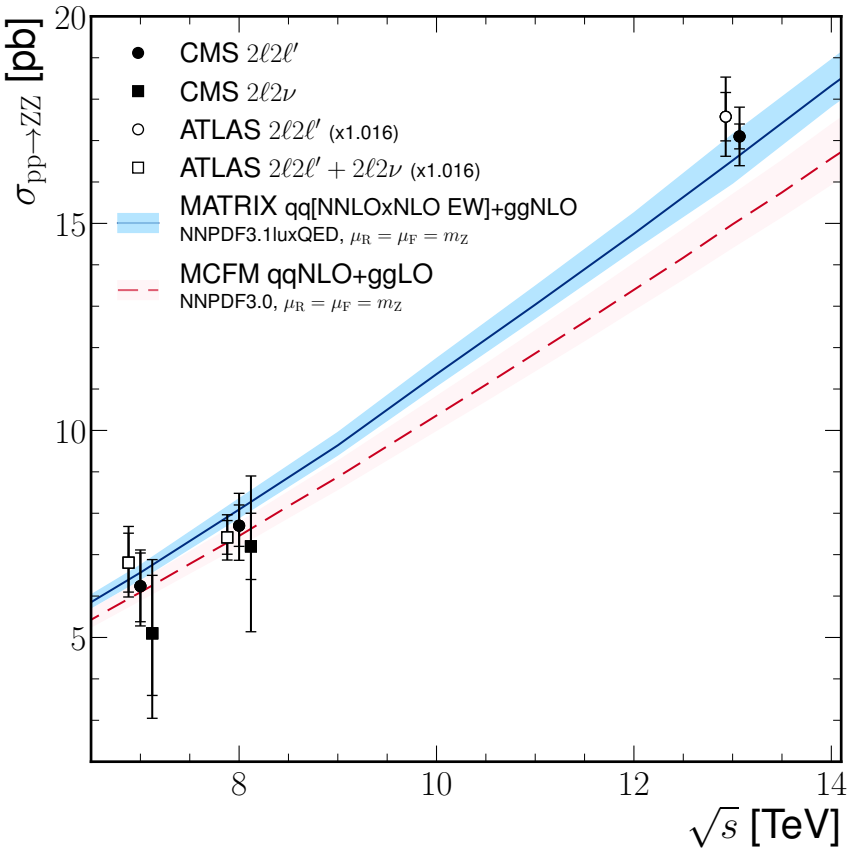

Figure 23: The total ZZ cross section as a function of the pp centre-of-mass energy. Results from the CMS and ATLAS [299–301] experiments are compared with the predictions from MATRIX and MCFM, as described in the text. The ATLAS measurements were performed with a Z boson mass window of 66–116 GeV, instead of 60–120 GeV used by CMS, and are corrected for the resulting 1.6% difference in acceptance. The inner vertical errors bars around the experimental data points show the statistical uncertainties of the measurements, whereas the outer bars show the total uncertainties. Measurements at the same centre-of-mass energy are shifted slightly along the horizontal axis for clarity. Figure taken from Ref. [292].

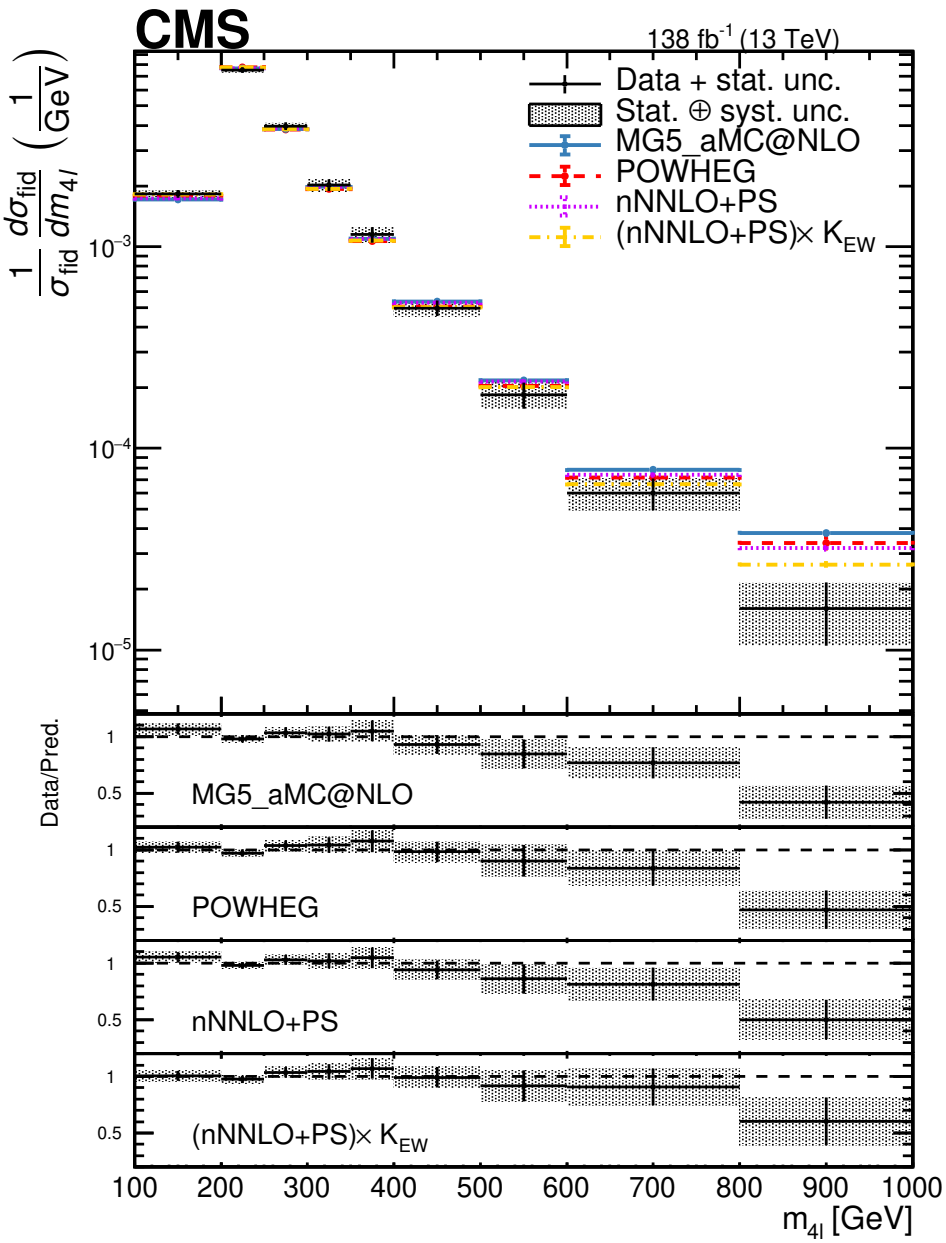

Figure 24: Differential cross section normalized to the fiducial cross section as a function of $m_{4\ell}$. The on-shell Z requirement $60 < m_Z < 120\,\text{GeV}$ is applied for both Z boson candidates. Points represent the unfolded data, the solid lines the (MADGRAPH5_aMC@NLO $q\bar{q} \to ZZ$) + (MCFM $gg \to ZZ$) + (POWHEG $H \to ZZ$) predictions, and red dashed lines the (POWHEG $q\bar{q} \to ZZ$) + (MCFM $gg \to ZZ$) +(POWHEG $H \to ZZ$) predictions. The MADGRAPH5_aMC@NLO EW ZZ predictions are included. The purple dashed lines represent the nNNLO+PS predictions, and the yellow dashed lines represent the nNNLO+PS prediction with EW corrections applied. Vertical bars on the MC predictions represent the statistical uncertainties. The lower panels show the ratio of the measured to the predicted cross sections. The shaded areas represent the full uncertainties calculated as the sum in quadrature of the statistical and systematic uncertainties and the vertical bars around the data points represent the statistical uncertainties only. The overflow events are included in the last bin of the distributions. Figure and caption taken from Ref. [308].

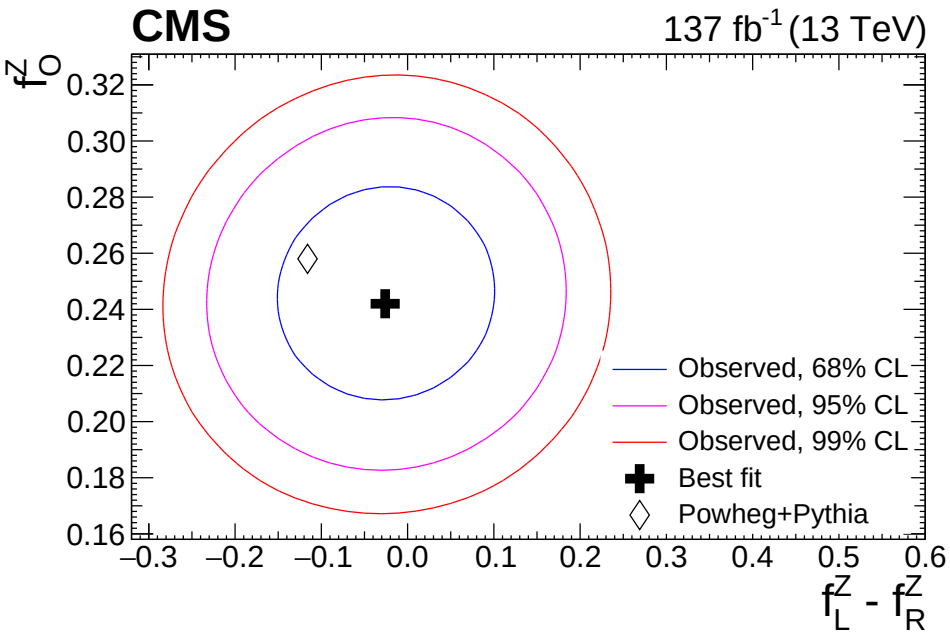

Figure 25: Confidence regions in the $f_{\mathrm{L}}^{\mathrm{Z}}$ *vs.* $f_{\mathrm{R}}^{\mathrm{Z}}$-$f_{0}^{\mathrm{Z}}$ parameter plane for the Z boson polarization. The results are obtained with no additional requirement for the charge of the W boson. The blue, magenta, and red contours present the 68, 95, and 99% confidence levels, respectively. Figure from Ref. [290]. The cross indicates the best fit to the observed data and the diamond shows the result of the POWHEG +PYTHIA simulation.

son momentum direction in the laboratory frame, which are approximately expected to have simple trigonometric probability distributions based on first- and second-order sine and cosine functions for each polarization state, can be precisely reconstructed and the polarization fractions extracted by fitting the expected distributions for the fraction of each polarization. In events with neutrinos, partial reconstruction of the full angular information can be used. The CMS experiment has measured boson polarization in the $\mathrm{W}^{\pm}\mathrm{W}^{\pm}$ (discussed in Section 5.3) and WZ production [290]. In the latter case, polarized production was observed. The fitted longitudinal polarization fraction versus the difference of left and right polarization fractions for Z bosons in WZ production is shown in Fig. 25 demonstrating the ability of the measurement to distinguish the polarization states.

A test of perturbative QCD in a more complex signature involving EW vector bosons is the measurement of differential cross sections of diboson production versus the number of observed jets. Accurate predictions of these types of final states are essential for performing studies of diboson production through VBS, which is observed in the diboson + 2 jets final state; in Higgs physics where many signatures involve multiple vector bosons; and in searches for BSM physics involving multiple vector bosons. Previously, this type of analysis had only been performed by the CDF experiment, which observed $\mathrm{W}^{\pm}\mathrm{W}^{\mp}$+jets production and measured the cross section for final states up to 2 jets [310]. The CMS experiment has measured $\mathrm{W}\gamma$ [311] and $\mathrm{Z}\gamma$ [312] with two jets production in 13 TeV collisions; $\mathrm{W}^{\pm}\mathrm{W}^{\mp}$+jets up to two jets at 13 TeV [289]; WZ+jets up to three jets in 8 TeV collisions [281]; and ZZ+jets up to three jets at 8 and 13 TeV [313]. Details of the cross sections measured and generators used for comparison are given in Table 14. In the last case, a subsequent reanalysis of the 13 TeV ZZ+jets data [308] with larger data samples showed that a more advanced nNNLO+PS simulation achieves better agreement at high jet multiplicities (as shown in Fig. 26). The full description of the predictions

in Fig. 26 is presented above in the discussion of the $m_{4\ell}$ distribution from the same analysis. The improved modelling of the data seen with the new nNNLO+PS simulation demonstrates the importance of continued development of advanced NNLO computations.

Table 14: Summary of measurements of diboson production in association with jets. Listed are the diboson state, number of jets measured, generator(s) used with perturbative QCD order and K-factors used to scale the result to a higher order, total number of additional partons generated, number of partons generated at NLO, parton shower MC, and ME-PS jet merging scheme. The total number of partons includes additional real-emission partons generated by NLO or NNLO QCD matrix element calculations. The highest bin in the jet multiplicity includes events with a higher number of jets as well.

Diboson State	N_{jets}	$\sqrt{s}$ (TeV)	Generator	Partons total	Partons NLO	PS	ME-PS scheme
Wγ [311]	2	13	MG5_aMC (NLO)	2	1	Py8	FxFx
Zγ [312]	2	13	MG5_aMC (NL0)	2	1	Py8	FxFx
W^+W^- [289]	0–2	13	(POWHEG (NLO) + MCFM (LO)) * K_{NNLO} [314]	1	0	Py8	—
WZ [281]	0–2	8	(MADGRAPH 5 (LO) + MCFM (LO)) * K_{NLO} MCFM	0	—	Py6	—
ZZ [313]	0–3	8	(MG5_aMC (NLO)+ MCFM (LO)) * K_{NLO} MCFM	2	1	Py8	CKKW
ZZ [315]	0–3	8	nNNLO + MCFM (NLO)	2	1	$\text{MiNNLO}_{\text{PS}}$	—

The results for diboson production in association with jets are summarized in Fig. 63 where they are presented as fiducial cross sections for leptonic final states. In the case of the WZ+jets at 8 TeV [281], the result was multiplied by the leptonic branching fractions for easier comparison.

5.2.2 Triboson production

The high centre-of-mass collision energy and the large integrated luminosity produced by the LHC have made it possible to observe triboson production for the first time. The most challenging measurements are those of the production of three massive vector bosons. The Feynman diagrams for WZZ production are shown in Fig. 27 including radiative production of three vector bosons and diagrams involving TGCs and QGCs. The sensitivity of triple gauge boson production to measure TGCs is weaker than that of diboson production because of the small production cross section, but the quartic coupling diagram gives this type of process direct sensitivity to QGCs. In a comprehensive analysis, CMS measured all possible massive triboson states simultaneously, categorizing them into all the possible final states involving electrons and muons, according to type and charge, and pairs of jets from hadronic boson decay. This analysis achieved collective observation of WWW, WWZ, WZZ, and ZZZ, and individual evidence for WWW and WWZ production at 3.3 and 3.4 standard deviations, respectively [316]. Figure 28 depicts all of the analysis categories clearly showing the observed signal for all of the final states. The triboson production processes measured at CMS are listed in Table 15. Included in the table is information on pp collision energy, theory calculations used for comparison in Fig. 21, and other results of interest in the paper.

5.3 Electroweak single-boson and multiboson production

Pure EW production of single and multiple vector bosons with jets in collision events where bosons are radiated off incoming quarks and either fuse to a single boson (VBF) or scatter to

DRAFT

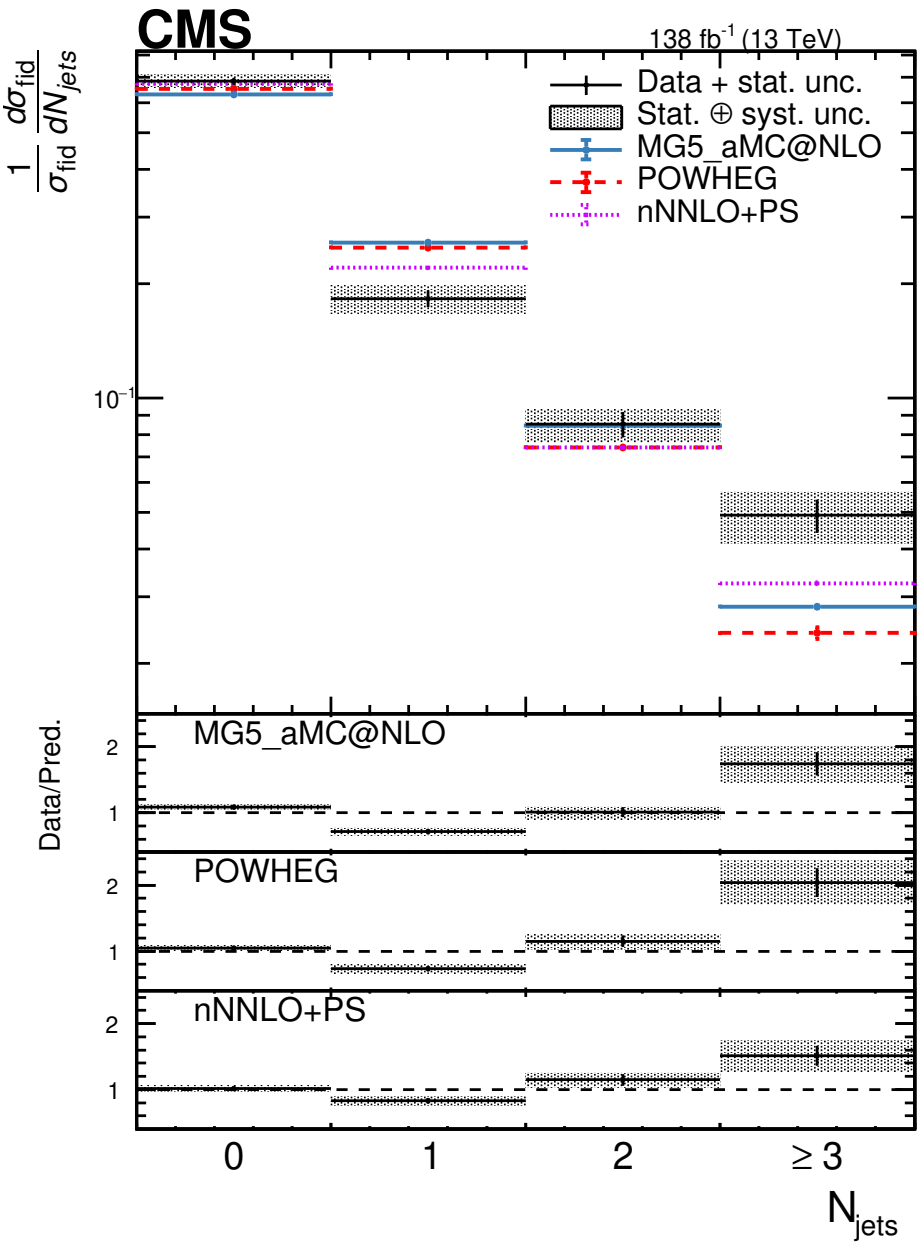

Figure 26: The differential cross section normalized to the fiducial cross section as a function of the number of jets. The on-shell Z requirement $60 < m_Z < 120\,\text{GeV}$ is applied for both Z boson candidates. Points represent the unfolded data, the solid lines the (MADGRAPH5_aMC@NLO $q\bar{q} \to ZZ$) + (MCFM $gg \to ZZ$) + (POWHEG $H \to ZZ$) predictions, and red dashed lines the (POWHEG $q\bar{q} \to ZZ$)) + (MCFM $gg \to ZZ$) + (POWHEG $H \to ZZ$) predictions. The MADGRAPH5_aMC@NLO EW ZZ predictions are included. The purple dashed lines represent the nNNLO+PS predictions. Vertical bars on the MC predictions represent the statistical uncertainties. The lower panels show the ratio of the measured to the predicted cross sections. The shaded areas represent the full uncertainties calculated as the sum in quadrature of the statistical and systematic uncertainties and the vertical bars around the data points represent the statistical uncertainties only. The overflow events are included in the last bin of the distributions. Figure and caption taken from Ref. [308].

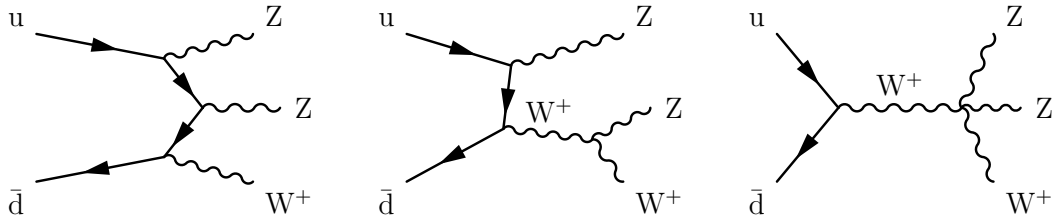

Figure 27: Triboson WZZ production via diagrams involving radiative production (left), TGCs (centre), and QGCs (right). This set of triboson Feynman diagrams is representative of most triboson signatures, with the caveat that neutral TGCs and some QGC combinations are not allowed in the SM.

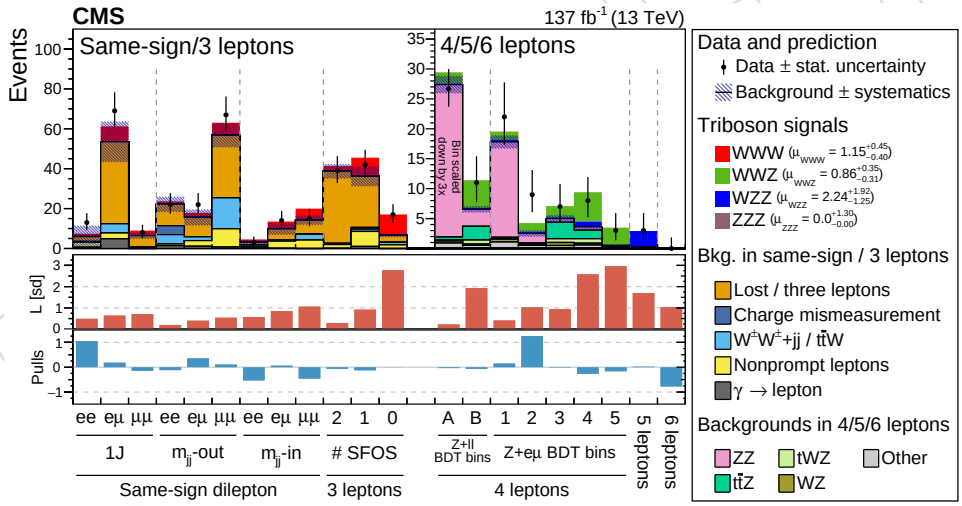

Figure 28: Comparison of the observed numbers of events to the predicted yields. For the WWW and WWZ channels, the results from boosted decision tree (BDT)based selections are used. For the other results different categorizations based on the number of jets, whether dijet masses are inside or outside a selection window used to identify the boson, and specific lepton combinations or the number of same-flavour, opposite-sign (SFOS) leptons are shown. The VVV signal is shown stacked on top of the total background. The points represent the data and the error bars show the statistical uncertainties. The expected significance L in the middle panel represents the number of standard deviations (sd) with which the null hypothesis (no signal) is rejected. The lower panel shows the pulls for the fit result. Figure taken from Ref. [316].

Table 15: Table of triboson production cross section measurements. Listed in the table are signatures studied, pp collision energy, theory cross section calculation used for comparison, and selected additional results of interest from each measurement.

Process	Energy (TeV)	Theory calculation	Other results
W$\gamma\gamma$ [317]	8	MG5_aMC Py6 NLO	aQGC
W$\gamma\gamma$ [318]	13	MG5_aMC Py8 NLO	aQGC
Z$\gamma\gamma$ [317]	8	MG5_aMC Py6 NLO	aQGC
Z$\gamma\gamma$ [318]	13	MG5_aMC Py8 NLO	aQGC
WVγ [319]	8	MG5_aMC Py8 NLO	aQGC
WWγ [320]	13	MG5_aMC Py8 NLO	aQGC, Hγ search
VVV [316]	13	NLO [321–323]	VH production
WWW [316]	13	NLO [321–323]	VH production
WWZ [316]	13	NLO [321–323]	VH production
WZZ [316]	13	NLO [321–323]	VH production
ZZZ [316]	13	NLO [321–323]	VH production

DRAFT

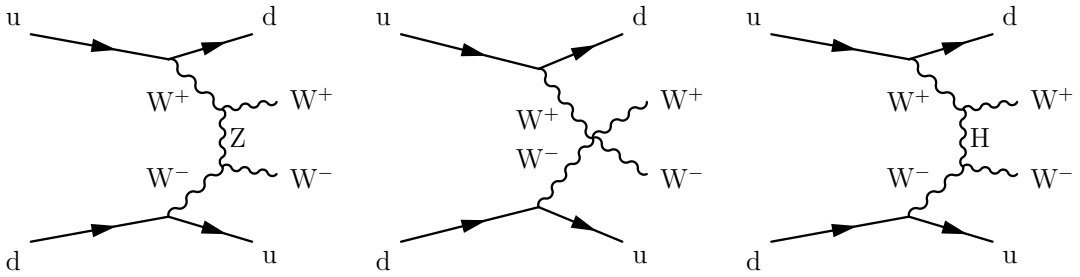

Figure 29: Production of oppositely charged W bosons via vector boson scattering. Example Feynman diagrams include: scattering via Z boson and two TGC vertices (left), a QGC vertex (middle), and scattering via a Higgs boson in *t*-channel (right).

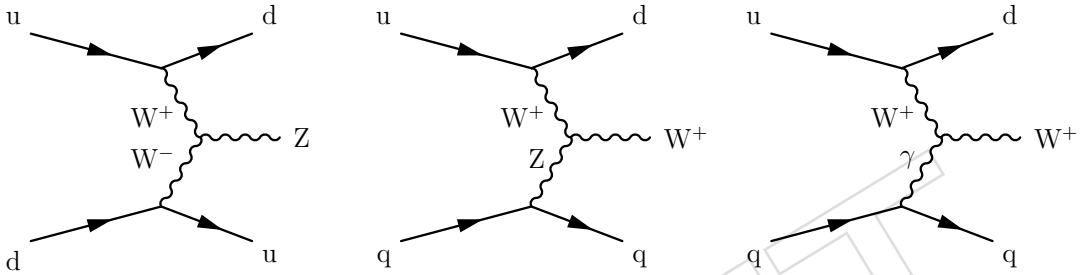

Figure 30: Feynman diagrams for vector boson fusion production of Z (left) and W bosons (middle) via the WWZ TGC vertex and W via the WWγ TGC vertex (right).

pairs of bosons (VBS) is an essential test of the EW sector of the SM. Vector boson fusion directly measures the TGCs of the SM. Vector boson scattering events can occur via the combination of double TGC interactions, in *t*- or *s*-channel; quartic coupling of bosons; or scattering via a Higgs boson, in *t*- or *s*-channel. The theoretical investigation of the Higgs boson scattering process was an important early component in understanding the essential role of the Higgs boson in the SM. The calculation of longitudinalVBS without the Higgs boson would predict an infinite cross section at high energy. Shown in Fig. 29 are representative VBS Feynman diagrams for $W^{\pm}W^{\mp}$ scattering. The features of these types of interactions are two scattered jets with large rapidity separation and one or two bosons produced centrally. The expected kinematic distributions from the different amplitudes contributing to VBS and their interference can be used to study the scattering kinematics and assess the polarization of the scattered bosons

The CMS experiment has measured VBF of single W or Z bosons in 7 (Z only) [324], 8 [325, 326], and 13 [327, 328] TeV pp interactions. The Feynman diagram for VBF production of a Z boson is depicted in Fig. 30 showing direct sensitivity to the WWZ TGC. The extraction of the signal from a very large background of standard single boson + jets production requires the use of a multivariate discriminant. An example BDT distribution from the measurement of EW Z production at 13 TeV is shown in Fig. 31 demonstrating the performance of machine- learning techniques to separate the signal over an overwhelming Z+jets background with the same final state but slightly different kinematics [328]. These analyses have been used to set stringent limits on deviations from the expected SM TGC values.

The EW production processes measured at CMS are listed in Table 16. Included is information on pp collision energy, theory calculations used for comparison in Fig. 32, and other results of interest. Good agreement with theoretical calculations is observed for all of these purely EW production processes.

The first observed VBS process was $W^{\pm}W^{\pm}$. The distinctive same-sign signature and signifi-

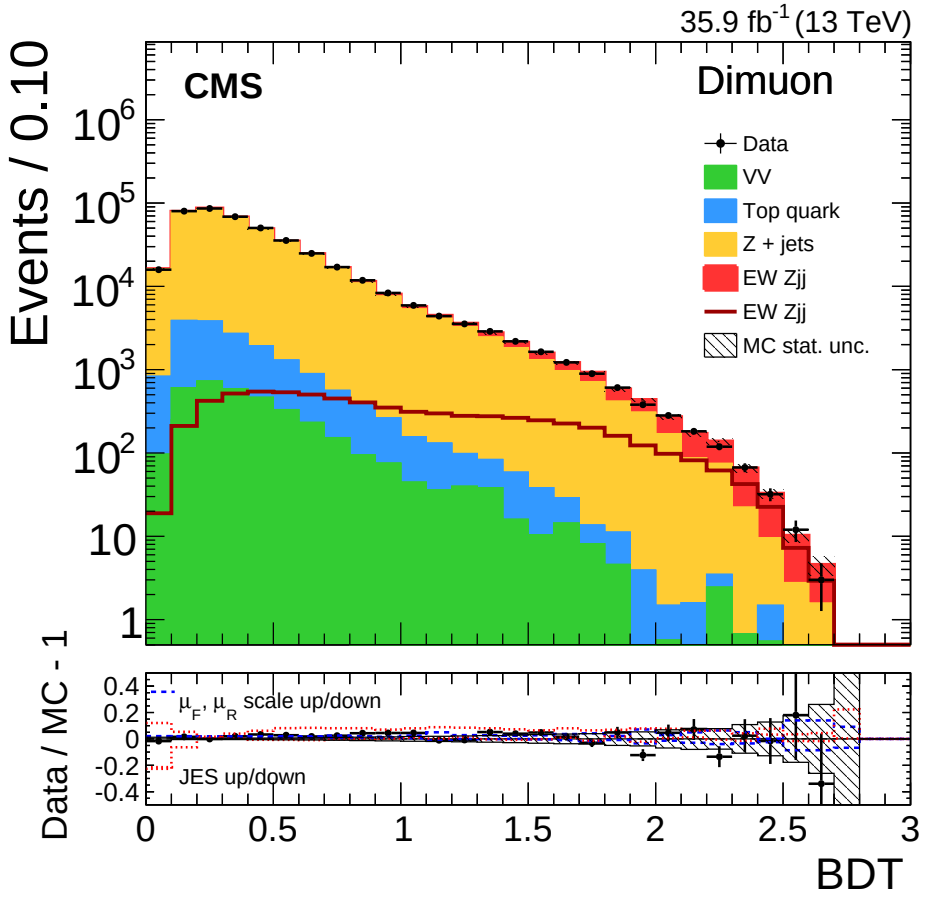

Figure 31: Distribution for a BDT discriminant used to select VBF Z events in dimuon events. The contributions from the different background sources and the signal are shown stacked, with data points superimposed. The vertical errors bars around the experimental data points show the total uncertainties. The expected signal-only contribution is also shown as an open histogram. The lower panel shows the relative difference between the data and expectations, as well as the uncertainty envelopes for the jet energy scale, and renormalization and factorization scale uncertainties. Figure taken from Ref. [328].

Table 16: Purely EW production cross section measurements. Listed in the table are signatures studied, pp collision energy, theory cross section calculation used for comparison, and selected additional results of interest from each paper.

Process	Energy (TeV)	Theory calculation	Other results
VBF W [325]	8	MG5_aMC Py6 LO	—
VBF W [327]	13	MG5_aMC Py8 LO	aQGC
VBF Z [324]	7	VBFNL0 NLO	central hadronic activity
VBF Z [326]	8	MG5_aMC Py6 LO	jet activity
VBF Z [328]	13	MG5_aMC Py8 LO	aQGC, jet, central hadronic activity
EW $W^{\pm}W^{\mp}$,WZ [329]	13	MG5_aMC Py8 LO	aQGC
$\gamma\gamma \to W^{\pm}W^{\pm}$ [330]	13	MADGRAPH 5 LO rescaled	aQGC
EW Wγ [331]	8	MADGRAPH 5 Py6 VBFNL0 NLO	aQGC
EW Wγ [311]	13	MG5_aMC Py8 LO	aQGC, m_{jj}, 6 dist.
EW Zγ [332]	8	MADGRAPH 5 Py6 LO	aQGC
EW Zγ [312]	13	MG5_aMC Py8 LO	aQGC, $m_{jj} x \Delta\eta(jj)$ + 3 1D dist.
EW $W^{\pm}$ $W^{\pm}$ [333]	8	MADGRAPH 5 Py6 VBFNL0 2.7 NLO	aQGC
EW $W^{\pm}$ $W^{\pm}$ [334]	13	MG5_aMC Py8 corr NLO QCD and EW [335, 336]	aQGC, m_{jj}, 3 dist.
EW W^{+} W^{-} [337]	13	MG5_aMC Py8 LO	—
EW WZ [338]	13	MG5_aMC Py8 corr NLO QCD and EW [339]	aQGC, m_{jj}
EW ZZ [277]	13	POWHEG BPX NLO [340]	aQGC

DRAFT

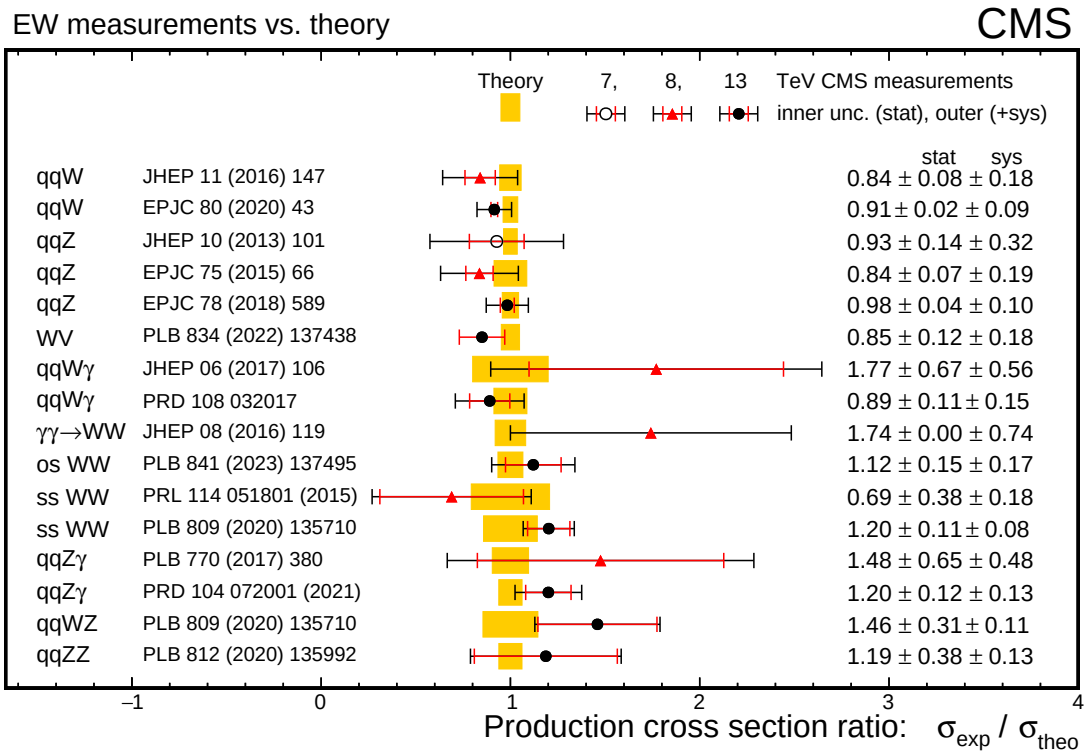

Figure 32: Summary of cross section measurements of EW single or diboson production processes including vector boson fusion, vector boson scattering, and scattering via exclusive processes. Production of pairs of W bosons can occur in same-sign (ss) $W^{\pm}W^{\pm}$, opposite-sign (os), $W^{\pm}W^{\mp}$, or exclusive production where photons are radiated from the incoming protons and form $W^{\pm}W^{\mp}$ pairs via EW scattering. Results are displayed as a ratio of the experimental measurement over the SM prediction. The yellow bands indicate the uncertainties in the theoretical predictions and the error bars on the points are the experimental uncertainties, with the outer bar being the combined statistical and systematic uncertainty.

cant $p_{\mathrm{T}}^{\mathrm{miss}}$ in leptonic decays of the W bosons, as well as the smaller cross section for the QCD-induced $\mathrm{W}^{\pm}\mathrm{W}^{\pm}$ process, where the W bosons are radiated off incoming quarks that scatter via a gluon, made it possible to observe this process in the initial year of LHC Run 2 at 13 TeV. Similarly, these characteristics made this mode the first place where polarized vector boson production in VBS could be studied [341]. The observation of the scattering of longitudinal vector bosons would be a clear sign of the presence of the Higgs boson scattering interaction as a component of VBS and is considered one of the essential tests of the EW symmetry-breaking mechanism. A first measurement has been made of longitudinal VBS in this mode using 13 TeV collision data where a 2.3 standard deviation signal consistent with the SM expectation was measured. A summary of all the measured EW production cross sections presented as a ratio to the SM prediction is shown in Fig. 32 showing the ability of the CMS experiment to see clear, well-measured signals in never before observed VBS production modes.

Among the listed results is the purely EW process of exclusive scattering to W boson pairs, $\gamma\gamma \to \mathrm{W}^{\pm}\mathrm{W}^{\mp}$, for which evidence is reported using 8 TeV collision data [330]. The calculation of the expected theory cross section for exclusive $\gamma\gamma \to \mathrm{W}^{\pm}\mathrm{W}^{\pm}$ is performed using MADGRAPH 5 using the equivalent photon approximation [342] and rescaled to account for proton dissociation, as studied in the same analysis using a comparison of $\gamma\gamma \to \mu^{+}\mu^{-}$ to a MC sample generated using LPAIR [343, 344]. The CMS experiment has also searched for the high-mass exclusive scattering of $\gamma\gamma \to \mathrm{W}^{\pm}\mathrm{W}^{\pm}$ and $\gamma\gamma \to \mathrm{ZZ}$ using intact forward proton reconstruction in the precision proton spectrometer and set limits on these processes [345].

A combination of production mechanisms is necessary to unitarize the cross section of the overall VBS processes. Contributions from new scalar or vector particles could cause large deviations in the cross section, especially at the highest energies where the unitarization of the divergent contributions to the cross section would be modified. In CMS, analyses of most VBS modes have used that sensitivity to search for anomalous couplings and differential measurements have been made of related kinematic distributions.

5.4 Summary of EW measurements

The CMS Collaboration has carried out a broad array of QCD EW measurements. The precision of some measurements has reached the percent level and $\mathrm{N^3LO}$ perturbative QCD theory computations are necessary to test the measurements at a similar level of precision. Differential measurements are also testing our ability to model SM processes and NNLO QCD, NLO EW, and integrated PDF and parton shower computations at the same perturbative order are necessary to model the data. In general, SM predictions model the data well. At the level of both inclusive and fiducial cross sections, all the measurements are well modelled, within statistical expectations, across a large number of signatures involving single or multiple vector bosons and up to two jets, as would be expected with correct modelling of the physics using computations of at least NLO accuracy. Also, the modelling of differential distributions is generally good with discrepancies observed only in complex final states involving larger numbers of additional jets. The theory community is actively engaged in confronting the LHC data, and in many cases, new computations have improved the modelling of the data where previously there was disagreement. Measurements with percent-level accuracy and studies of complex final states along with improved theoretical modelling are constantly extending our ability to further investigate the complexities of the SM and search for BSM physics indirectly and in complex final states. A visual summary of the results of the standard model QCD, EW, top quark, and Higgs boson measurements of individual cross sections and cross sections of processes including jets is presented in Figs. 63, and 1, respectively.

DRAFT

6 Top quark measurements

The large mass of the top quark, $m_t = 172.5\,\text{GeV}$ [346], and, as a consequence, its short lifetime of about $0.5 \times 10^{-24}\,\text{s}$, drive the phenomenology associated with this particle. Its properties make the top quark stand out amongst all the elementary fermions. The top quark lifetime is so short that it decays before hadronizing [347], making it the only quark whose physical properties can be studied as if it were "bare", which, in turn, makes it a unique probe for constraining several extensions of the SM. Its mass attracts particular attention also from a BSM physics perspective, for two main reasons: because it is the largest known for an elementary particle, by orders of magnitude with respect to any other elementary fermion; and because its Yukawa coupling to the Higgs boson (y_t) is remarkably close to unity. These two facts have inspired a very rich theoretical literature, in which the top quark is surmised to hold the key to the spontaneous EW symmetry breaking of the SM [348–350], and, in general, to be a promising window on BSM physics, contributing to the EW oblique parameters [351] and, potentially, coupling to new physics with a rich phenomenology, as discussed in a recent review [352]. The top quark is also a privileged probe of the proton PDFs, since, due to its large mass, its production is very sensitive to the gluon density at high values of x. Moreover, the relatively abundant production rates, the variety of final states, and the large kinetic energy of its decay products, make top quark processes a significant background for several other studies at particle colliders. The measurements of the production cross sections, its decay parameters, and the properties of the top quark are key areas of study at the LHC and have been explored by the CMS Collaboration since the beginning of Run 1.

At the LHC, the top quark is predominantly produced in top quark-antiquark pairs ($\mathrm{t\bar{t}}$) through the strong interaction, with a relatively large cross section that translates to a rate of about 8 Hz at an instantaneous luminosity of $10^{34}\,\text{cm}^{-2}\,\text{s}^{-1}$ at 13 TeV. Other production modes include mixed EW and QCD, or pure EW vertices, which yield either single top quarks, or top quarks produced in association with other particles, such as vector bosons, Higgs bosons, or additional quarks.

The top quark decays through an EW process, and hence its natural width is primarily determined by m_t, m_W, and the Fermi constant (G_F), receiving relatively small higher-order corrections from α_S [123]. The $t \to Wb$ decay channel dominates, since the value of the V_{tb} element of the Cabibbo–Kobayashi–Maskawa (CKM) matrix is very close to unity, and thus $|V_{tb}| \gg |V_{td}|, |V_{ts}|$. As a result, top quark events are characterized by final states with b jets and the decay products of the W bosons, i.e. charged leptons and neutrinos, or light-quark jets. Additional jets, stemming from gluon radiation, may also be present in the events, and add to the complexity of the event signature.

Experimentally, the kinematics of the parent top quark are reconstructed using dedicated algorithms. Challenges arise from the presence of neutrinos originating in the decays of the W bosons, as well as from combinatorial ambiguities in associating hadronic jets and charged leptons to form top quark or antiquark candidates; both difficulties are typically addressed by exploiting mass constraints. The CMS Collaboration has explored different techniques in fully hadronic [353, 354], single leptonic [355, 356], and dileptonic [181, 357, 358] final states, and in boosted topologies [359, 360], or in associated production with bosons [361]. Top quark cross section measurements at the LHC are often presented as differential cross sections, obtained using an unfolding procedure [362–364] in which corrections for detector resolutions and efficiencies, as well as PS and hadronization effects are applied, to obtain a measurement at the level of stable particles or at parton level. At the particle level, so-called pseudotops [365] have been defined, which are reconstructed from generator-level final-state particles with a lifetime

DRAFT

greater than 0.3×10^{-10} s. The particle level simplifies the definition of detector-independent cross section acceptances and minimizes the impact of theory assumptions. Parton-level measurements of top quark cross sections and properties, although affected by uncertainties stemming from nonperturbative models and PS uncertainties, are crucial inputs for comparison of the data with fixed-order calculations and the extraction of fundamental theoretical parameters, such as α_S or m_t^{pole}, the top quark pole mass [366]. CMS has often made measurements at both particle and parton level. Conceptual definitions and technical details for both these approaches are described in Refs. [365, 367].

The following subsections focus on cross section measurements performed by CMS using pp collisions at centre-of-mass energies ranging from 5.02 to 13.6 TeV. The first cross section measurements with proton-lead (pPb) and lead nuclei (PbPb) collisions are also described. A detailed report of top quark mass measurements in CMS has recently been published in Ref. [366].

An overview of the measurements of inclusive single top quark and $t\bar{t}$ production is presented in Sections 6.1 and 6.2. In Section 6.3, a few examples of differential $t\bar{t}$ cross sections are presented. The first measurements of top quarks in heavy ion collisions are described in Section 6.4. The processes of top quark production in association with vector bosons or with additional jets are reviewed in Sections 6.5 and 6.6, and the four top quark production process is presented in Section 6.7. Finally, the extraction of fundamental SM parameters from inclusive top quark cross sections is briefly discussed in Section 6.8. A summary of the quark cross section measurements spanning several orders of magnitude (10 fb to 1 nb) is presented in Section 6.9.

6.1 Electroweak top quark production

The production and decay of single top quark events occur through the EW tWq vertex. Figure 33 represents the dominant Feynman diagrams for single top quark production in the SM. In single top quark measurements, the properties of the tWq vertex, marked in Fig. 33 as a purple dot, are probed, including its magnitude, the CKM matrix elements (V_{tq}), and the polarization of the top quark. As a result of the V–A coupling structure of the EW interaction, the top quarks are expected to be almost 100% polarized. Additional contributions from flavour-changing neutral currents [368] and other BSM-induced effects [369] are other aspects that are uniquely probed by these processes.

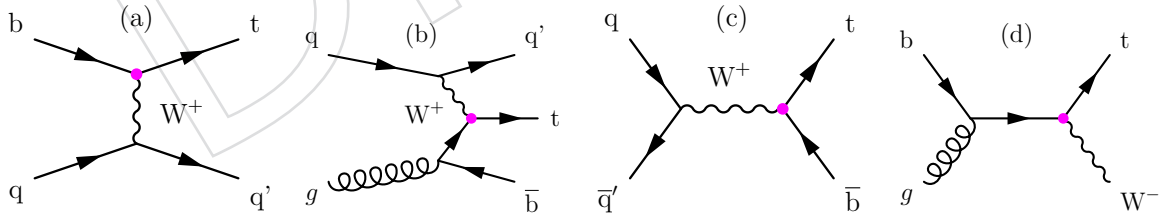

Figure 33: Feynman diagrams illustrating the pure EW contributions to single top quark production at the LHC at Born level. Charge conjugate states are implied. From left to right: the *t*-channel production, a) with and b) without a b quark in the initial state; c) the *s*-channel; and d) the tW-production. In all diagrams the tWq vertex is marked with a purple dot.

Figure 34 summarizes the measurements of EW top quark production performed by CMS at different centre-of-mass energies. At the LHC, the *t*-channel, represented in Figs. 33 (a) and (b), has the highest cross section of the EW top quark production processes. The cross section at 13 TeV, calculated at NNLO in QCD, is expected to be $\sigma_t = 214.2\,^{+2.4}_{-1.7}\,(\text{scale})\,^{+3.3}_{-2.0}\,(\text{PDF}+\alpha_S)$ pb, where "scale" refers to the contributions from the uncertainties in the QCD factorization and

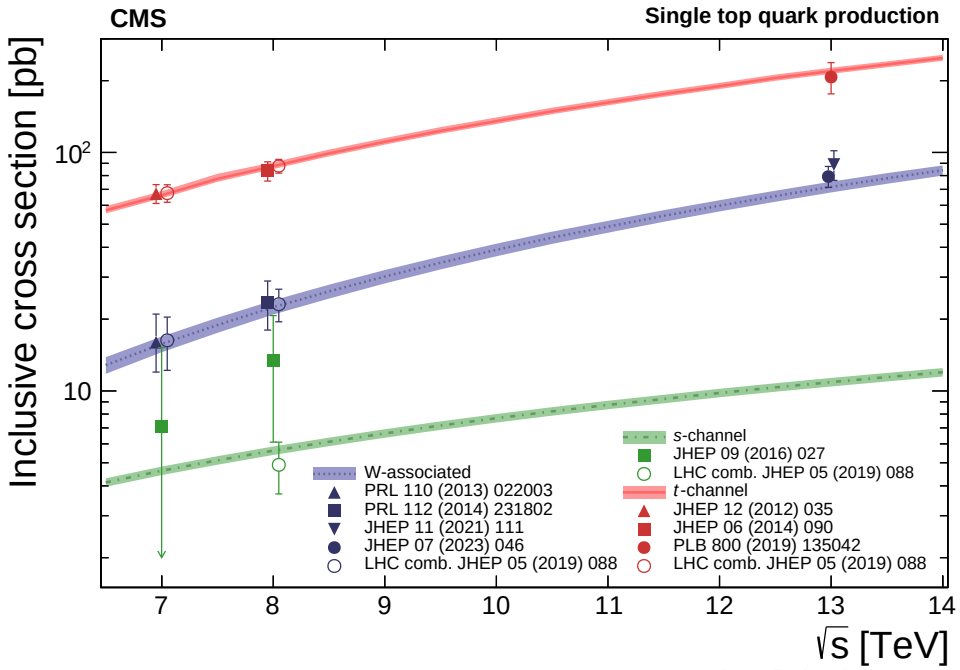

Figure 34: Single top quark cross section summary of CMS measurements as a function of the pp centre-of-mass energy. Where available the results from the full LHC combination are also overlaid for comparison. The theoretical calculations for *t*-channel, *s*-channel, and W-associated production are from Refs. [370–373].

renormalization scales [374]. The *t*-channel signature is characterized by the production of a top quark with a recoil jet that is typically produced at large rapidity. The large rapidity gap between the top quark and the forward jet is depleted in additional QCD emissions. In cross section measurements, this signature is exploited to separate the *t*-channel signal from the background, which is dominated by top quark pair production. Depending on whether the b quarks are considered part of the proton or not, measurements in the *t*-channel can be compared with predictions in the 5-flavour (udscb) scheme (5FS), or in the 4-flavour (udsc) scheme (4FS) [375].

CMS has measured the *t*-channel cross section at 7 TeV [376], 8 TeV [377], and 13 TeV [378], as depicted in the upper curve of Fig. 34. In general, the measurements indicate that the 5FS predicts the rate more accurately, as expected from the resummation of initial-state large logs in the b quark PDF, improving the stability of the calculations [379]. On the other hand, the 4FS yields a more precise description of the kinematic distributions. These conclusions are supported by additional measurements of the differential *t*-channel cross sections [380].

The selections and background estimations used in the measurement of the *t*-channel reflect the evolution of the data-taking conditions and event reconstruction techniques in CMS and of the theoretical (MC) predictions. Analyses make use of the single-lepton final states. To discriminate the signal from the main backgrounds ($t\bar{t}$, W+jets, and multijets), the events are categorized according to the jet and b jet multiplicity. The region of two jets and one b jet is expected to be enriched in signal events. Backgrounds arise from multijet events, typically estimated from data, W+jets events, and top quark pair production. Two different approaches have been explored for the signal-to-background separation: a simple robust variable (the pseudorapidity of the forward jet, $\eta_{j'}$), or a multivariate-analysis (MVA) approach. Already the experience with the 7 TeV data recorded in 2011 showed that both approaches lead to accurate measurements

of the t-channel cross section. The MVA approach improves the statistical precision by up to 40% with respect to $\eta_{j'}$ but suffers slightly more from signal-modelling uncertainties.

The relative uncertainty achieved in the measurements varies from 15% to 9%, after fitting the variable of interest in different categories. In the latest measurements the dominant uncertainties are related to the signal modelling, most notably the variation of the PS and the matching PS-ME matching algorithm. The most precise measurement of this process is attained in combination with results from the ATLAS Collaboration, yielding a 6.6% relative uncertainty [381], where the dominant contribution is still related to modelling uncertainties. Additional mitigation of this uncertainty is expected from using higher-order accuracy predictions, employing better reconstruction algorithms, and, in general, using larger data sets. Fiducial and ratio measurements, are also expected to have reduced extrapolation uncertainties [374].

The flavour of the initial light quark defines the charge of the produced top quark: $\mathrm{u}(\mathrm{d})$ quarks in the initial state result in $\mathrm{t}(\bar{\mathrm{t}})$ quarks in the final state. Given this simple property, the cross section inherits a charge asymmetry from the proton PDF of the quarks involved in the production. This asymmetry is typically quantified by the ratio of cross sections $R_\mathrm{t} = \sigma_\mathrm{t}/\sigma_{\bar{\mathrm{t}}}$, which is predicted to be about 1.7 at 13 TeV [374, 382]. In the measurement of the ratio, most systematic uncertainties cancel or are significantly reduced, resulting in a significantly more precise test of the PDF than the absolute cross section measurement. Figure 35 summarizes the different R_t measurements compared with the predictions. Overall a good agreement is found for various PDFs.

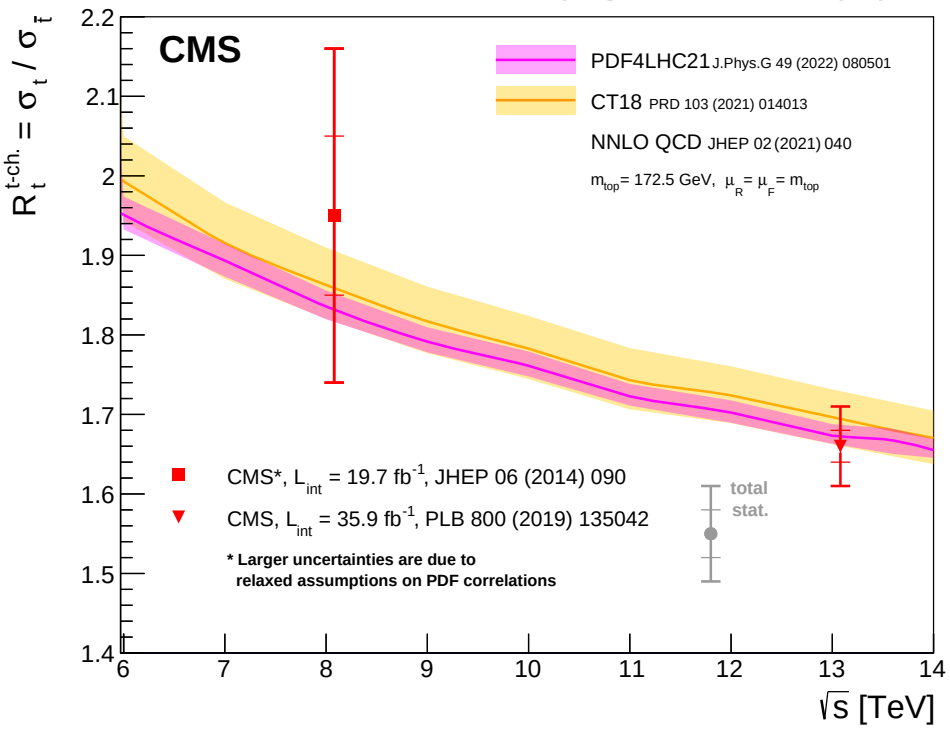

Figure 35: Summary of the CMS measurements of $R_\mathrm{t} = \sigma_\mathrm{t}/\sigma_{\bar{\mathrm{t}}}$, the cross section ratio between t-channel top quark and t-channel top antiquark production. The measurements are compared with NNLO QCD calculations using the PDF sets CT18 and PDF4LHC21. The coloured bands represent the uncertainties in the theoretical predictions (scale and PDF uncertainties). The PDF uncertainties are estimated using the PDF4LHC21 prescription [383].

From the experimental point of view, the s-channel production, shown in Fig. 33(c), is the most challenging of the purely EW processes at the LHC. This is due to the large backgrounds from $\mathrm{t\bar{t}}$, t-channel, and W boson production in association with heavy-flavour quarks, with respect to the small expected s-channel signal cross section of $10.32\,^{+0.29}_{-0.24}\,(\text{scale})\,^{+0.27}_{-0.26}\,(\text{PDF}+\alpha_\text{S})$ pb, as calculated at NLO in QCD for 13 TeV [370, 371]. The CMS Collaboration has searched for the s-channel top quark production at both 7 and 8 TeV [384], and the result is included in Fig. 34.

The analysis relies on MVAs for discriminating the signal process from the backgrounds. A combined fit to the MVA output distributions in the categories of different jet and b jet multiplicities yields a measurement with an uncertainty of about 45% in the signal strength, corresponding to an observed significance of 2.5 s.d. with 1.1 s.d. expected. Although the measurement has a significant statistical uncertainty (11%), its total uncertainty is dominated by the choice of the factorization and normalization scales, the matching scale in the modelling of the backgrounds (33%), as well as by the jet energy scale and b tagging uncertainties (25%). An experimental observation of this channel is expected with improvements in the higher-order predictions, state-of-the art b tagging, jet-energy scale uncertainties, as well as machine-learning based algorithms.

Finally we discuss the associated tW production, shown in Fig. 33(d), which can be interpreted as a more global set of double, single, and nonresonant $\mathrm{W^+W^-b\bar{b}}$ diagrams including both the tW and the $\mathrm{t\bar{t}}$ processes described in the next Section 6.2. Establishing the single-resonant tW process is interesting in itself, as it is well defined at Born level and sensitive to CKM matrix elements and possible BSM effects. Most measurements in Run 1 and Run 2 have focused on isolating this process from the double-resonant ($\mathrm{t\bar{t}}$) production by using distinctive features, such as lower jet multiplicity and the balance in the transverse plane between the top quark and the W boson decay products. The predicted cross section of tW production in pp collisions at 13 TeV is $\sigma(\mathrm{tW}) = 79.3\,^{+1.9}_{-1.8}\,(\text{scale}) \pm 2.2\,(\text{PDF}+\alpha_\text{S})$ pb at NLO+NNLL in QCD [382], and thus about 10% of the cross section for $\mathrm{t\bar{t}}$.

Evidence for tW production was attained at 7 TeV [385] and observation at 8 TeV [386]. Measurements with improved precision were made at 13 TeV [387, 388]. With the exception of Ref. [388], the measurements have focused on dilepton final states with one b jet. A fit to the output of the MVA discriminator (or ancillary variables such as the subleading jet p_T in the two-jet-two-b-tag bin) in the different categories resulted in improved precision from 31% (7 TeV) to 11% (13 TeV). Run 1 measurements were combined with those performed by the ATLAS Collaboration, and the final result is in agreement with the SM prediction with a total uncertainty of 16.5% [381]. The improvements obtained in Run 2 were due to the increased sample size and accuracy in the predictions, improved identification algorithms, and a better calibration of the CMS detector [13, 15, 16, 20, 28, 30, 389].

CMS has also measured the tW process in the single-lepton channel at 13 TeV [388]. Although this channel offers the advantages of larger branching fractions and the possibility to fully reconstruct the top-quark system, it suffers from more numerous and larger backgrounds. The result, shown in the middle curve of Fig. 34, is in agreement with that obtained in the dilepton channel.

6.2 Top quark pair production

The LO Feynman diagrams, depicted in Fig. 36, illustrate the main $\mathrm{t\bar{t}}$ production modes at the LHC, where the gluon fusion (diagrams b, c, and d) are dominant contributions to the cross section (about 85% at 13 TeV). At the lowest order in perturbation theory, the partonic cross section is proportional to $(\alpha_\text{S}/m_\mathrm{t})^2$ and it is dominated by the region where the rapidity difference of

DRAFT

the pair is relatively small. Parton distribution functions are sensitive to the determination of $\sigma_{t\bar{t}}$: the formation of a $t\bar{t}$ pair requires high energy transfer ($Q > 2m_t$) and thus a relatively high momentum fraction of the incoming partons $x > 0.03\,(0.07)$ at 13 (7) TeV; the rapidity of the $t\bar{t}$ system $y(t\bar{t})$ is related to the momentum fraction via $y(t\bar{t}) \sim 1/2 \log(x'/x)$, where x and x' are the fractional momenta of the initial-state partons. Precise cross section measurements of $\sigma_{t\bar{t}}$ have the potential to improve the knowledge of the gluon PDF, of α_S, and of the top quark pole mass m_t^{pole} [366], which are crucial ingredients to predictions for LHC physics such as the Higgs boson production cross section, and hence the Higgs boson couplings. In addition, $t\bar{t}$ is a background for many BSM searches and in some cases a final state.

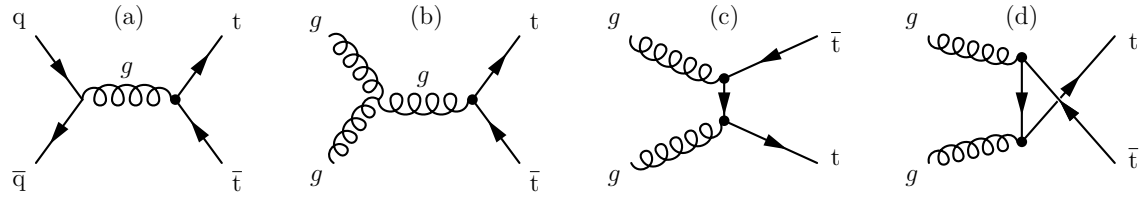

Figure 36: Leading order Feynman diagrams for $t\bar{t}$ production.

Within the top quark sector the prediction for $\sigma_{t\bar{t}}$ is currently amongst the most precise; it is calculated at NNLO and includes the resummation of soft gluon terms at NNLL. The expected cross section at 13 TeV is $\sigma_{t\bar{t}} = 833.9\,^{+20.5}_{-30.0}\,(\text{scale}) \pm 21\,(\text{PDF} + \alpha_S)\,\text{pb}$ computed with TOP++2.0 [390–396].

The CMS Collaboration made early measurements of $\sigma_{t\bar{t}}$, in pp collisions at each centre-of-mass energy, and in pPb and PbPb collisions. These were milestones in the extensive programme of precision measurements and searches for new physics. Examples are: the very first measurement which inaugurated the top quark physics programme at the LHC using as few as 11 events collected in $3\,\text{pb}^{-1}$ of 7 TeV data [397]; the first measurements at the various $\sqrt{s}$ [398–400]; and the first and so far only measurements of top quark pair cross sections in pPb [401] and PbPb [402] collisions. High precision measurements, employing larger data samples and more accurate calibrations of the detector, have been performed, such as Refs. [192, 403, 404], or in combination with the ATLAS Collaboration [405], reaching uncertainties as small as 2–3%.

In the CMS detector, top quark events can be identified with high purity and their rich final state comprising b jets and leptons also makes them standard candles for calibration purposes. The measurements have made use of all the various $t\bar{t}$ final states, which are generically classified according to the number of leptonically decaying W bosons. Among the dileptonic final states that have been exploited to measure $\sigma_{t\bar{t}}$, the channel with one electron and one muon in the final state is particularly clean, whereas the channels containing τ leptons are particularly challenging, as they require dedicated trigger and reconstruction algorithms.

The top quark programme has benefitted from the increasingly large data samples and it heavily draws on experimental techniques such as b tagging [406], missing transverse energy [407], reconstruction of boosted topologies [408], kinematics-based selections (from likelihoods to MVA-based approaches) [409, 410], fitting techniques using several control regions and variables [407], profiling of systematic uncertainties [409], and, not least, the combination of results [403].

A summary of the $\sigma_{t\bar{t}}$ measurements performed by CMS is shown in Fig. 37. In this figure, the most precise results at each centre-of-mass energy are shown. Overall, all the results are compatible with each other and with the predictions. While consistent within the uncertainties, the data tend to be somewhat lower than most NNLO+NNLL predictions obtained for $m_t =$

172.5 GeV and $\alpha_S = 0.118$. Summaries of all the individual $t\bar{t}$ measurements are shown in Fig. 38.

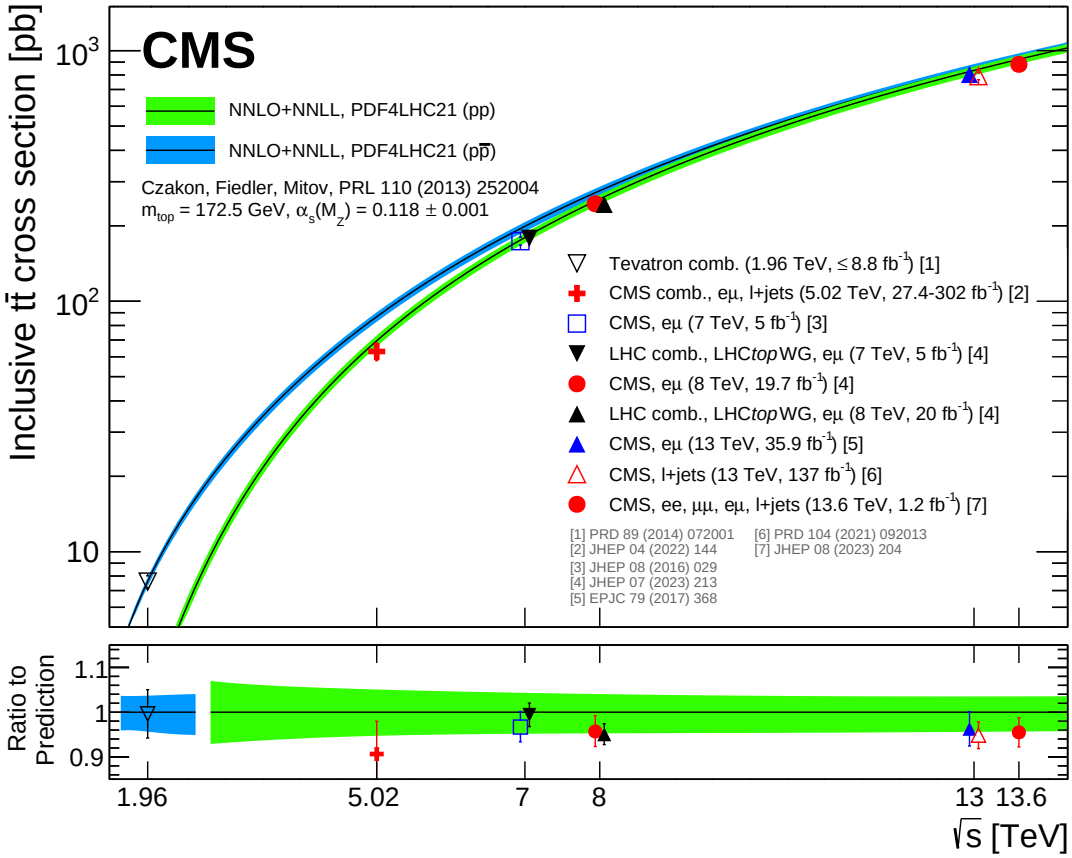

Figure 37: Summary of top quark-antiquark pair cross section measurements by the CMS Collaboration in comparison with the theory calculation at NNLO+NNLL accuracy. The Tevatron measurements are also shown. The lower panel displays the ratio between the different measurements and the theory prediction. The coloured bands represent the theory uncertainty, while the error bars represent the uncertainty on the measurements.

The precision of most top quark cross section measurements is limited by systematic uncertainties. While the initial measurements at 7 TeV were limited by the trigger and selection uncertainties (≈4%), jet energy scale and b tagging uncertainties (ranging from 7% to 20%), and the signal modelling, namely the choice of factorization and renormalization scales in the LO MC used, the most precise CMS measurements to date achieve a total relative uncertainty of 3.7% (Run 1) [403] and 3.9% (Run 2) [192]. The latter measurements are performed in the eμ final state in which a pure selection of events can be achieved with relatively loose lepton selection requirements. The analysis requires up to two b jets (from the $t\bar{t}$ decays) and counts the additional jets in the events. Categories are thus defined from the multiplicity of selected b and extra jets.

The categorization by b-tagged jet multiplicity facilitates a fit procedure in which the $t\bar{t}$ cross section and the b-tagging efficiency are measured simultaneously, exploiting the binomial dependency of the b-tagged jet multiplicity distribution on the b-tagging efficiency. With this approach, the dominant uncertainties remain in the trigger and lepton selections, as well as the integrated luminosity (≈2.2%). In the 13 TeV measurement, the signal was modelled using the NLO POWHEG v2 MC generator [79–81]. Although this change had reduced uncertainties

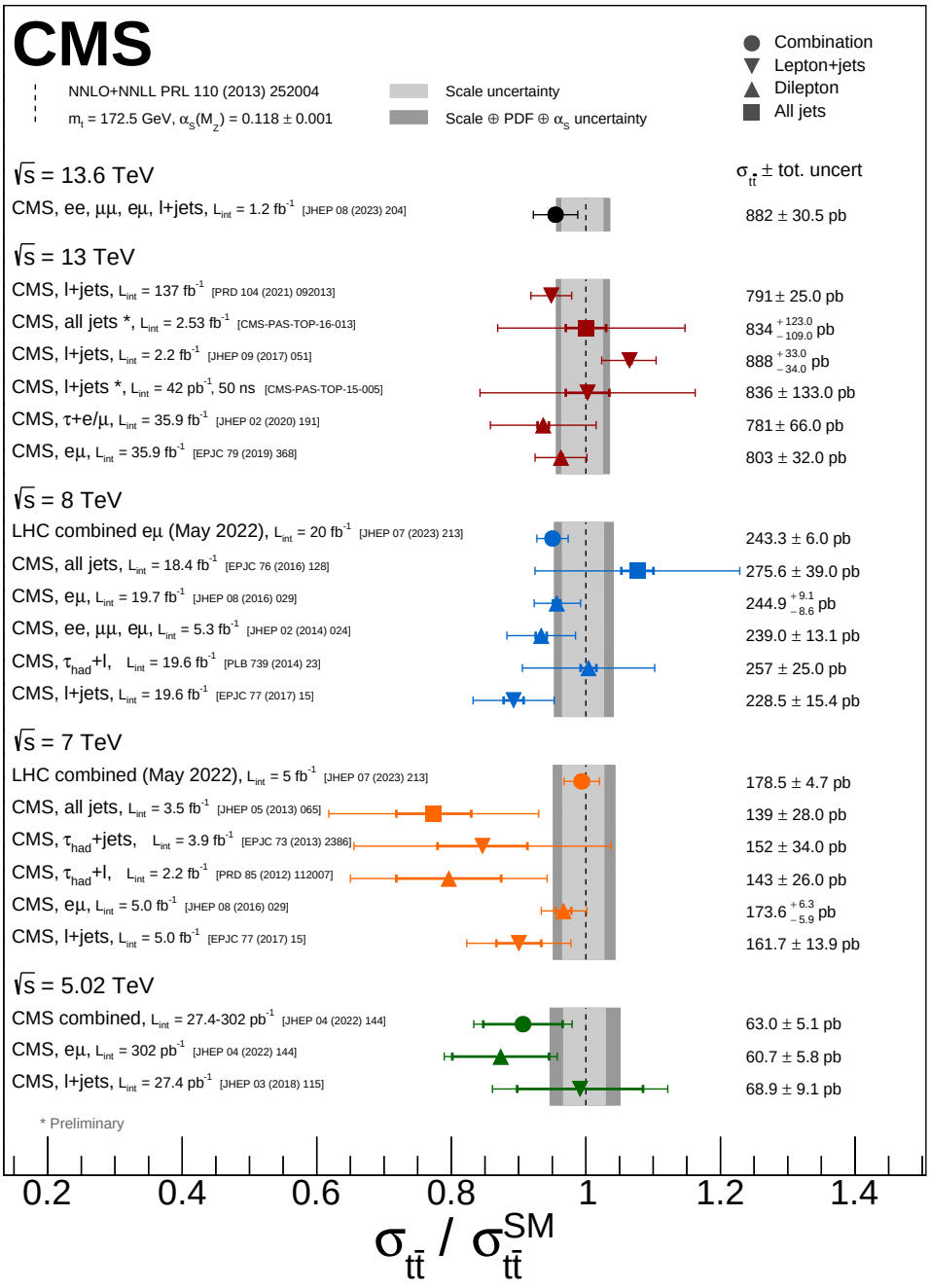

Figure 38: Summary of CMS top quark-antiquark pair cross section measurements at different $\sqrt{s}$, normalized to the theory calculation at NNLO+NNLL accuracy. The different final states and $\sqrt{s}$ are respectively represented by various markers and colours. The total (statistical) uncertainty associated with the measurements is represented by the outer (inner) error bars.

from the theoretical point of view, it had no significant impact on the total uncertainty of the measurement since the experimental method effectively decreases uncertainties related to the ME-PS matching.

Variants of this approach have also been used with the ℓ+jets final states at $\sqrt{s} = 5.02\,\text{TeV}$ [411] and 13 TeV [399], and more recently at 13.6 TeV, by combining both the dilepton and ℓ+jets final states [400]. The relative uncertainties attained in these measurements are 12%, 3.8%, and 4%, respectively. In the 5.02 TeV analysis, the uncertainty is larger because of the low integrated luminosity of that data set. These analyses have successfully applied the extra-jets categorization technique simply counting events in the different categories, or using variables such as $\Delta R(j, j')$, the distance between the two jets from the decays of W bosons ($\text{W} \to jj'$), and $m(\ell\text{b})$, the invariant mass of the lepton-b jet system.

In Ref. [404], a total of 22 different measurements of $\sigma_{\text{t}\bar{\text{t}}}$ are performed, each based on the integration of a differential cross section measurement described below. The results are in general agreement with the SM and attain a total uncertainty of 3.2%. The integrated luminosity is the dominant uncertainty (1.8%) followed by lepton-selection uncertainties (1%), b tagging (0.9%) and jet energy scale (1.4%).

Further improvements in the measurement of $\sigma_{\text{t}\bar{\text{t}}}$ require reduced uncertainties in the integrated luminosity, in the trigger, and in the lepton identification efficiencies. Luminosity measurements with an uncertainty of 1.2% have been achieved for the CMS data recorded in 2015 and 2016 [412]. Improved uncertainties are expected for the later data sets. In addition, the use of new luminosity detectors and novel techniques, such as Z boson rates, can further improve the luminosity calibrations and their extrapolation uncertainties at high beam intensities [413, 414]. Better measurements of the trigger and lepton identification efficiencies are expected from novel approaches. With larger sample sizes, efficiencies can be measured in finer categories, in turn leading to reduced uncertainties.

6.3 Differential top quark cross sections

Precise measurements of differential cross sections provide important information about the production process; the results have been used for detailed comparisons with theory predictions and to measure various SM and modelling parameters. In Fig. 39, a recent differential measurement of the $\text{t}\bar{\text{t}}$ cross section is shown as a function of the top quark transverse momentum $p_{\text{T}}(\text{t})$ and the $\text{t}\bar{\text{t}}$ invariant mass $m_{\text{t}\bar{\text{t}}}$ [404]. These are only two of 22 differential distributions, which were also used to determine the inclusive cross section, as described in Section 6.2 above.

The p_{T} distribution of the top quark, shown in Fig. 39 (left), shows a clear trend of most theory predictions to be somewhat harder than the data. Already early measurements of the top quark p_{T} in Run 1 identified this trend, as reported in Refs [353, 356, 408, 415, 416]. Although it was found that the discrepancy is reduced by higher-order QCD and EW corrections [417, 418], it still has a significant impact on precision measurements, most notably those where an extrapolation to the full phase space is needed to measure top quark properties. The uncertainty in the top quark p_{T} modelling is also relevant to searches in which the top quark is a background.

An underlying challenge of differential measurements is the wide range of energy transfer at the LHC; although the $\text{t}\bar{\text{t}}$ system is most often produced at rest, it is possible that it will also be produced at a large mass scale $Q \gg 2m_{\text{t}}$, yielding boosted topologies in which the final state objects, jets and leptons, are merged. Experimentally, special techniques are used to retain high efficiency for boosted top quark jets [408, 419]. On the theory side, additional mod-

DRAFT

elling uncertainties arise. The most recent calculations achieve NNLO accuracy in perturbative QCD [417, 420], and include NNLL corrections [390–396], and NLO EW corrections [418, 421].

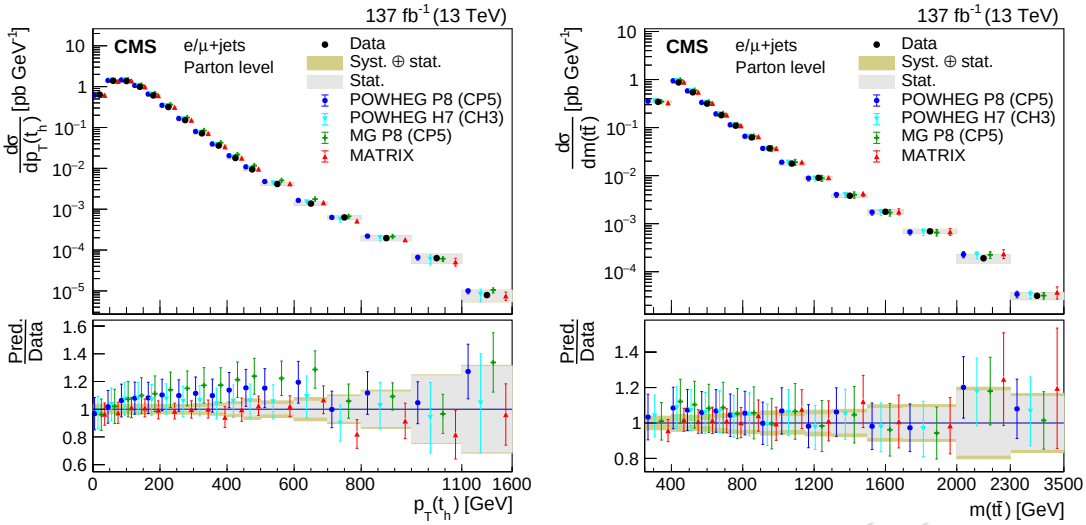

Figure 39: Differential cross sections at the parton level as a function of the hadronically decaying top quark p_T (left) and of the $t\bar{t}$ invariant mass (right). The analysis was performed using $t\bar{t}$ events in the ℓ+jets final state. The data are shown as points with grey (yellow) bands indicating the statistical (statistical and systematic) uncertainties. The cross sections are compared with the predictions of POWHEG combined with PYTHIA (P8) or HERWIG (H7), the multiparton simulation MADGRAPH5_aMC@NLO (MG)+PYTHIA FxFx, and the NNLO QCD calculations obtained with MATRIX. The error bars represent the theory uncertainty in the predictions. The ratios of the various predictions to the measured cross sections are shown in the lower panels. Figure from Ref. [404].

CMS has also published a wealth of multidifferential distributions, such as those shown in Fig. 40 for the dilepton channel [422]. Detailed comparisons are performed between the data and predictions up to approximate N^{3}LO. In Fig. 40 (upper), especially in the bin of large $m(t\bar{t})$, a clear improvement can be seen in the description of the data by the NNLO calculations MATRIX [46], STRIPPER [418] and MiNNLOPS [423]. In Fig. 40 (lower), the data are compared with predictions from POWHEG+PYTHIA (P8) for various PDF sets. The differences between the PDF illustrate the sensitivity of the data to the parton distribution functions. In the region $300 < m(t\bar{t}) < 400\,\text{GeV}$, the data are consistently higher than the NLO predictions for all PDFs.

In Fig. 41, the difference in azimuthal angle between the two charged leptons, $\Delta\phi(\ell, \ell')$ is presented as an illustration of how differential cross sections give access to the fundamental properties of the top quark. The SM predicts a correlation between the spins of the top quark and antiquark [424]. As the figure shows, the data are compatible with the standard model expectation, while a scenario without spin correlations is excluded. More recent measurements of spin correlations also show overall good agreement with the SM [425].

6.4 Top quark production in heavy ion collisions

The set of $\sigma_{t\bar{t}}$ measurements performed by CMS is augmented with the first measurements of $t\bar{t}$ production in pPb and PbPb collisions [401, 402]. These measurements bridge the SM and heavy ion physics programmes of the LHC with the potential to contribute to a better knowledge of the nuclear PDFs (nPDF) and the quark-gluon plasma (QGP) [427, 428]. Top quarks are a theoretically precise probe of the nuclear gluon density at high virtualities ($Q \sim m_t$) and in a

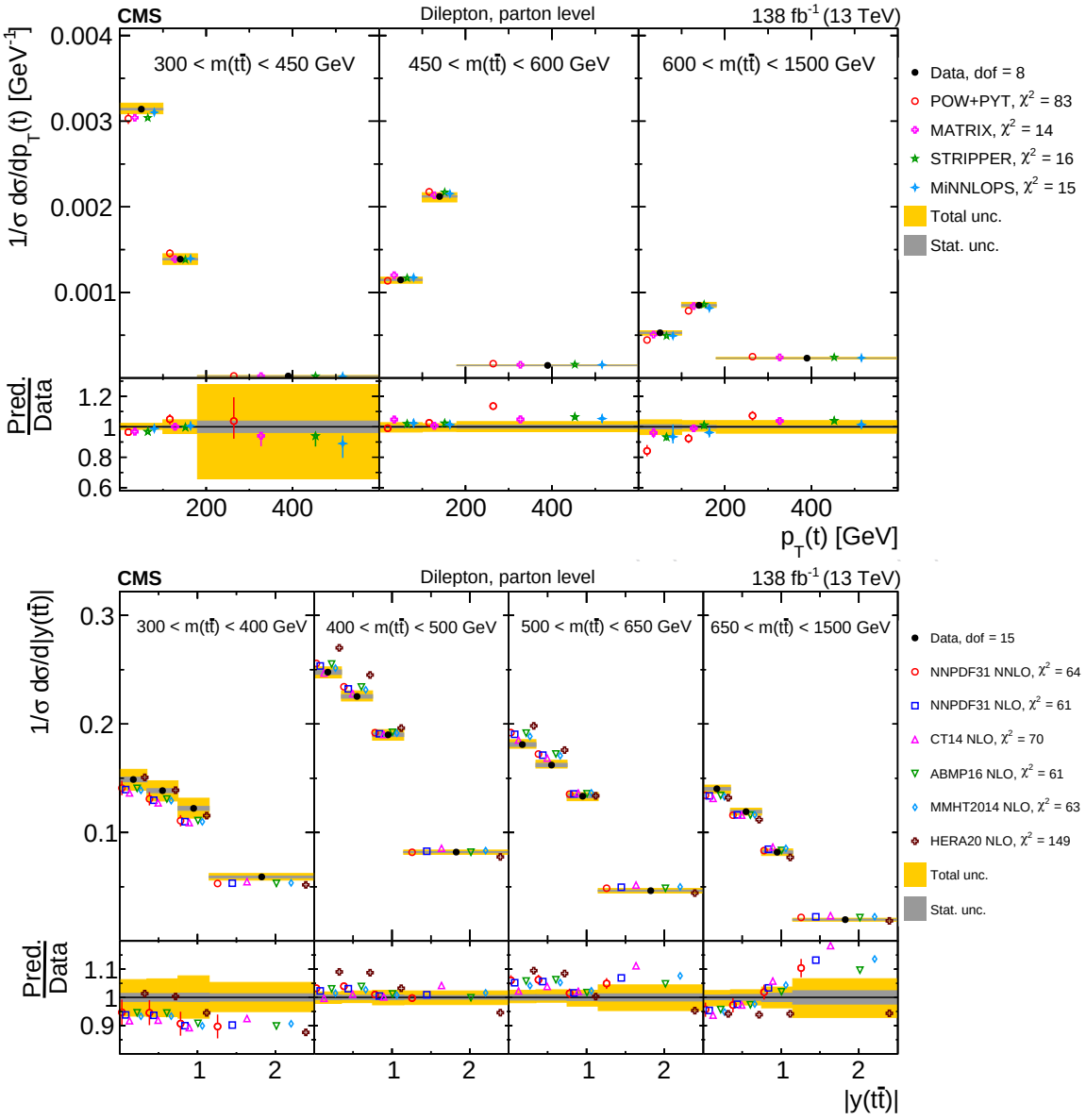

Figure 40: Normalized differential cross sections as a function of $p_T(t)$ in bins of $m(t\bar{t})$ (upper), and as a function of $y(t\bar{t})$ in bins of $m(t\bar{t})$ (lower). The data, shown as bullets with grey and yellow bands indicating the statistical and total uncertainties, are compared with the prediction from POWHEG +PYTHIA 8 and various theoretical predictions (see text). The error bars represent the theory uncertainty in some of the predictions. The lower panel in each figure shows the ratios of the predictions to the data. Figure from Ref. [422].

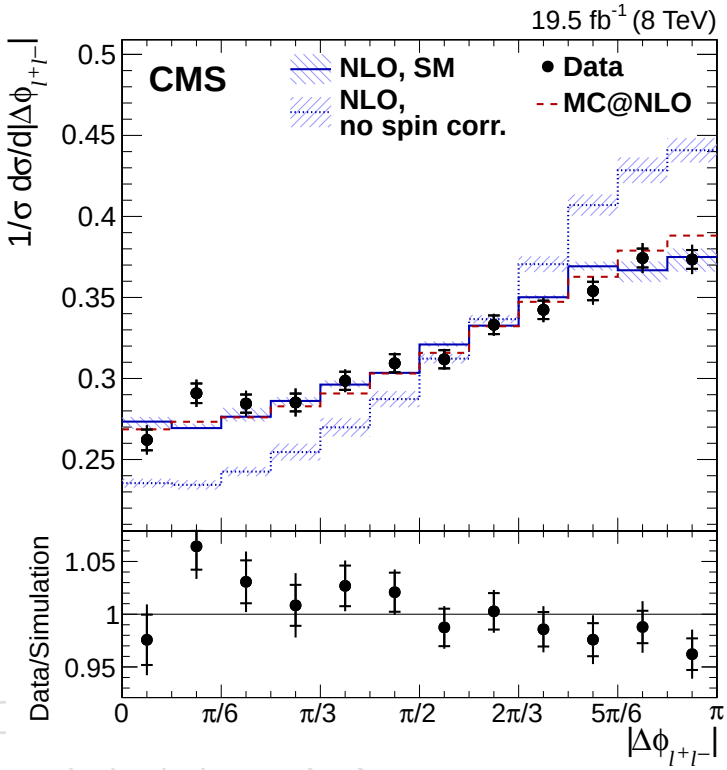

Figure 41: Normalized differential cross section as a function of the azimuthal opening angle between the two charged leptons in a $t\bar{t}$ dilepton final state ($|\Delta\phi_{\ell^+\ell^-}|$ from data (points); parton-level predictions from MC@NLO (dashed histograms); and theoretical predictions at NLO with (SM) and without (no spin corr.) spin correlations (solid and dotted histograms, respectively). The ratio of the data to the MC@NLO prediction is shown in the lower panel. The inner and outer vertical bars on the data points represent the statistical and total uncertainties, respectively. The hatched bands represent variations of μ_R and μ_F simultaneously up and down by a factor of 2. Figure from Ref. [426].

region of relatively unexplored Bjorken x ($x > 2m_t/\sqrt{s_{NN}} \approx 0.05$), where enhancement with respect to the free-proton PDF case (antishadowing) and "EMC" [429] effects are expected [430]. In both the pPb [401] and the PbPb [402] data, the CMS analyses are limited by the small size of the data sets of 174 nb^{-1} and 1.7 nb^{-1}, respectively. The $t\bar{t}$ production has been observed with a significance above 5 standard deviations (s.d.) in pPb collisions and the cross section was measured with a relative uncertainty of 18%, whereas in PbPb collisions the significance was 4 s.d. and the cross section was measured with a relative uncertainty of 33%. Both results are somewhat lower than the corresponding SM expectations, albeit compatible within 1–2 s.d., and are still largely dominated by statistical effects. The relevance of the top quark as a hard probe for nuclear PDFs (nPDFs) and the QGP is expected to gain relevance with larger data samples, as explored in Refs. [413, 428, 431].

6.5 Top quark production in association with vector bosons

Rare processes, such as the associated production of the top quark with vector bosons, have become accessible with the larger data samples of Run 2. Such processes offer the possibility to directly probe the EW couplings of the top quark and explore the sensitivity of the data to several BSM extensions. The production cross sections are typically small (<1 pb) owing to both the high mass of the state produced and the weaker couplings of the vector bosons with respect to QCD. The CMS Collaboration has either observed or found experimental evidence for all processes in which either $t\bar{t}$ or single top quarks are produced in association with vector bosons (Z,W,γ) or the Higgs boson (setting aside tHq). The measurements of associated production with the Higgs boson are later discussed in Section 7, whereas associated tW was already discussed in Section 6.1.

Processes with neutral bosons V^0 in the final state ($V^0 = \gamma, Z$) share similar diagrams that can be studied to examine the different EW dipole operators of the top quark [432], or in background estimations [433]. Examples of these Feynman diagrams are shown in Fig. 42 where the V^0 is pictured as arising either from initial state radiation (ISR) or from a direct coupling to the top quark. Figure 42(a) depicts the possibility of a W boson being produced by ISR only. Some additional differences between γ and Z bosons arise from an enhanced probability that the γ may be radiated from a final-state charged particle, because it is massless. Conversely, the dilepton states typically explored in the Z boson analysis, can be produced by additional off-shell and $\gamma^* \to \ell\ell$ contributions. In the data analyses, such additional contributions are typically suppressed by the requirement that the dilepton invariant mass $m(\ell\ell)$ is reconstructed in the vicinity of the Z boson pole mass. These differences are also present in single top quark associated production with V^0, illustrated in Fig. 43, where contributions from WWZ and WWγ TGCs may be present, as well as nonresonant dilepton contributions (Fig. 43(c)). Therefore, single top quark associated production has the potential of providing additional handles for EW fits of aTGCs. Besides the obvious interest in the couplings of the top quark and the EW sector, the presence of the V^0 introduces an additional intrinsic asymmetry in the $t\bar{t}$ system at LO level, which is a clean probe of BSM effects. The asymmetry arises from the increase of the relative contribution of $q\bar{q}$-initiated processes [434]. The $t\bar{t}V^0$ processes receive background contributions from tWV^0 processes, and at NLO, interference terms between $t\bar{t}V^0$ and tWV^0 arise, in analogy to the inclusive case of tW and $t\bar{t}$ described in Section 6.1 above. The cross section for tWZ is expected to be about 15% of that for $t\bar{t}Z$ [435]. CMS obtained evidence for the tWZ process with an observed 3.4σ statistical significance [435]. The result is in agreement with the SM expectation within one standard deviation.

The CMS Collaboration has carried out several measurements of the $t\bar{t}V^0$ and tV^0q processes; the results are summarized in Figs. 44 and 45. Table 17 summarizes the final states explored

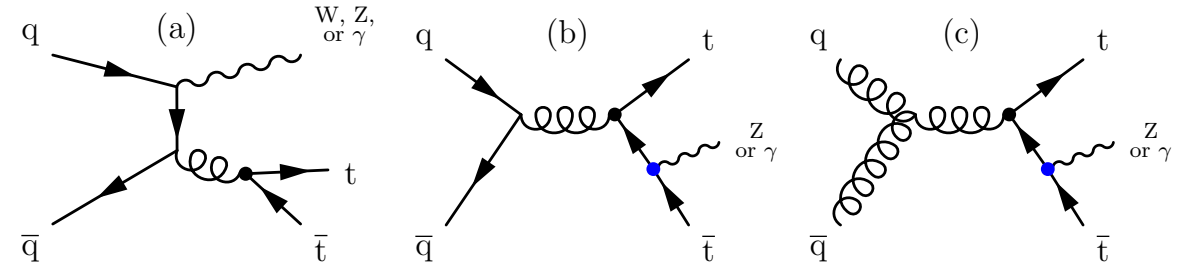

Figure 42: Example Feynman diagrams for the production of $t\bar{t}$ with a vector boson through initial state radiation (a) or a direct coupling to the top quark (b and c). The latter is only possible for neutral bosons $V^0 = \gamma, Z$.

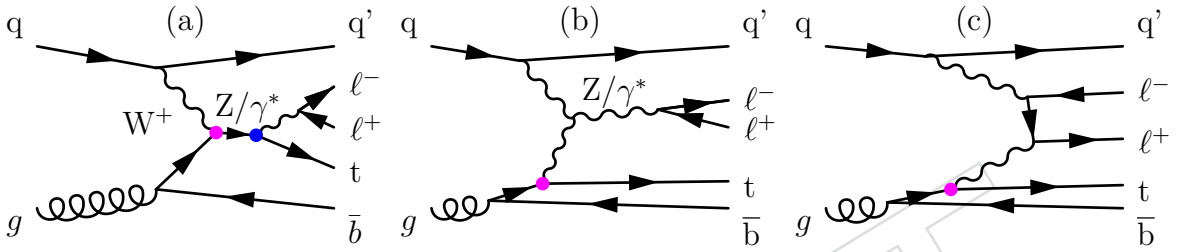

Figure 43: Example Feynman diagrams for the production of tZq.

in these measurements, the corresponding references, and the NLO predictions. Overall, good agreement between theory predictions and data is attained in these measurements.

The current uncertainties are about 8% for the $t\bar{t}Z$ cross section, dominated by statistical and lepton-selection efficiency uncertainties [436]. In this analysis, the main background is from nonprompt leptons and WZ boson production, modelled from dedicated control regions, and other associated top quark production $t(\bar{t})X$, modelled from simulation. The measurements of the tZq production cross section are mostly limited by the statistical uncertainty (≈12%) followed by systematic uncertainties related to backgrounds from WZ and $t\bar{t}Z$ processes, from misidentified lepton candidates, jet energy scale, and lepton selection efficiencies [437].

In the context of associated processes with photons, a total uncertainty of 3.5% is achieved for the $t\bar{t}\gamma$ process using all the available data at $\sqrt{s} = 13\,\text{TeV}$, whereas the $t\gamma q$ process has been measured with 10% total uncertainty (4.4 s.d. significance) [438] with an initial subset of the 13 TeV data. Both are in agreement with the SM predictions at NLO.

The $t\bar{t}W$ process, depicted in Fig. 42(a), is particularly interesting because the $t\bar{t}$ pair is produced via gluon splitting from a $q\bar{q}$ initial state. Because of the proton PDFs, it is expected that $\sigma(t\bar{t}W^+) \approx 1.9\sigma(t\bar{t}W^-)$ at LO, i.e. it is a charge-asymmetric process. With the inclusion of higher orders in perturbation theory new production channels open up, and hence new colour-flow and flavour structures, and this results in a significant increase of the cross section. The PS predictions used to model this process have NLO accuracy in QCD for the production and are limited to on-shell decays, with the top quark decay modelled at LO [442–444]. More advanced fixed-order calculations, including off-shell effects, emission of extra partons, and NNLL contributions, are available but not employed yet. Some effects, such as EW corrections, are larger in $t\bar{t}W$ than in $t\bar{t}Z$ production, making the $t\bar{t}W$ process especially interesting. In Ref. [454], it is estimated that NLO+PS cross sections, such as the one quoted in Table 17, fall short by 10–35% with respect to a calculation at the same order, including the missing full off-shell effects. The experimental measurements of $t\bar{t}W$ production are currently about 20% higher than the SM prediction and thus provide important input in a phase-space region where theory is actively

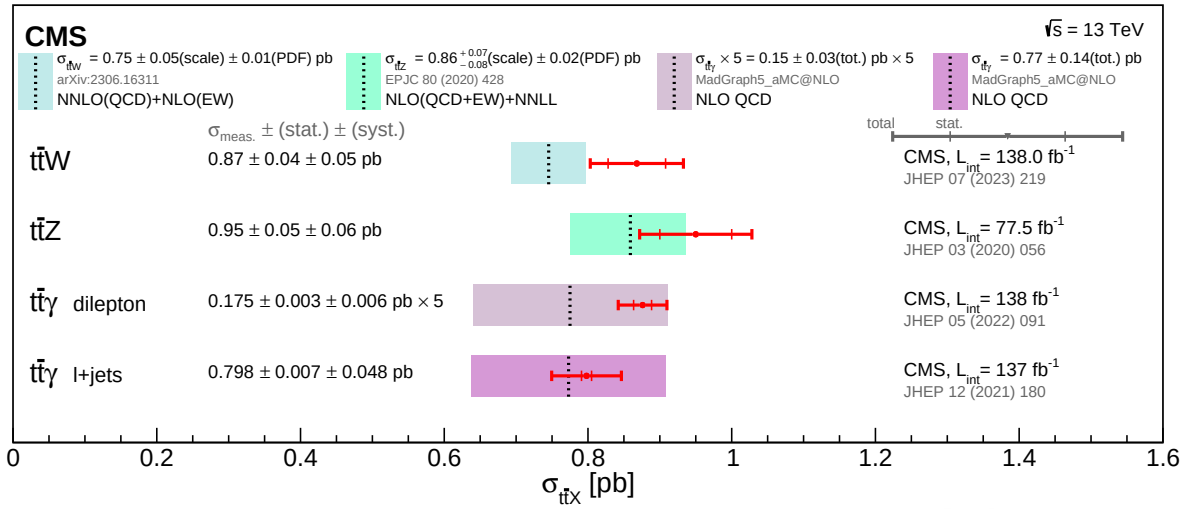

Figure 44: Summary of CMS $t\bar{t}W$ and $t\bar{t}V^0$ cross section measurements with respect to the SM prediction. The horizontal bars display separately the statistical and the total uncertainties of the experimental measurements. The uncertainty associated to the theory predictions is represented by shaded bands and includes the variations of the renormalization and factorization scales and parton density functions.

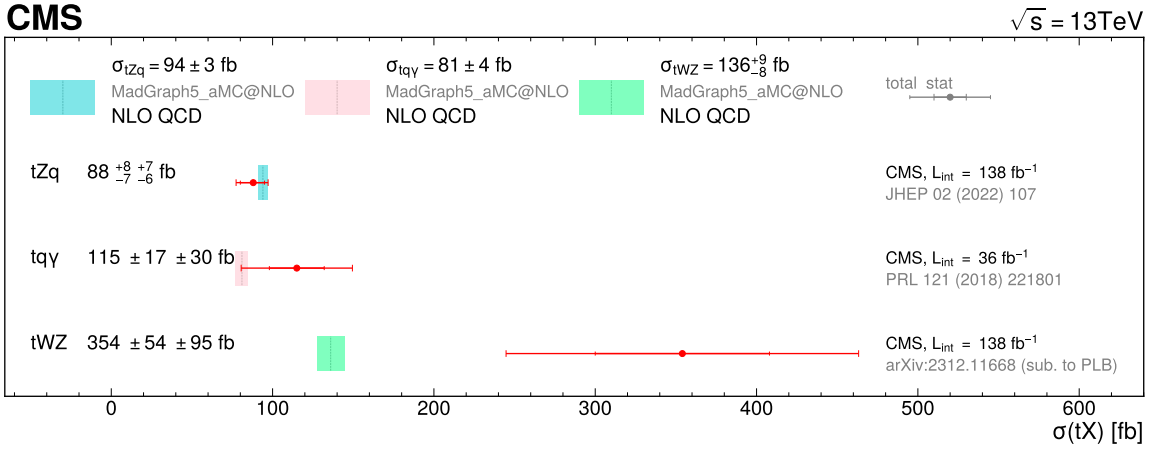

Figure 45: Summary of CMS measurements of tV^0q ($V^0 = Z, \gamma$) cross sections at 13 TeV. The cross section measurements are compared with the NLO QCD theoretical calculation. The horizontal bars display separately the statistical and the total uncertainties. The uncertainty associated to the theory predictions is represented by shaded bands and includes the variations of the renormalization and factorization scales and parton density functions.

Table 17: Summary of final states covered experimentally in associated top quark and neutral boson production by CMS. For each process listed in column (a), column (b) quotes the theoretical prediction at 13 TeV. Columns (c) and (d) summarize the different final states generated by the top quark(s) and boson decays with the corresponding branching fraction (B) listed in column (f). The combined results for the W and Z boson Bs include the propagation of τ-leptonic decays. The nomenclature assigned to these channels is shown in column (e) with SS (OS) used as a shorthand for same- (opposite-) charge lepton pairs. The CMS measurements of these channels are listed in column (g). The theoretical uncertainties include the PDF+α_S and scale choice. Symbols provide additional information: (†) predicted at NLO accuracy using MADGRAPH5_aMC@NLO v2.6.5, and corresponding to the fiducial region [439]; (•) the quoted fiducial $t\gamma$ cross section is predicted at NLO QCD accuracy [440] corresponding to the selection of Ref. [438]; ($*$) - computed at NLO including QCD+EW effects and NNLL QCD effects [441]; ($\star$) - computed at NLO QCD and EW accuracy [442–444]; ($\diamond$) - computed at NLO QCD accuracy in the 5FS [440], in the phase space of [445]. (δ) - computed at NLO QCD accuracy [243, 443].

(a)	(b)	(c)	(d)	(e)	(f)	(g)
process	σ or σ_{fid} (fb)	$t\bar{t}$ decay	boson decay	channel	B	measurements
$t\bar{t}\gamma$	$773 \pm 135^{\dagger}$	$(\ell^{\pm}\nu b)(q\bar{q}b)$	-	1ℓ	34.4%	[439, 446]
	$63 \pm 9^{\dagger}$	$(\ell^{\pm}\nu b)(\ell^{\mp}\nu b)$	-	2ℓOS	6.5%	[447]
$t\gamma(q)$	$81 \pm 4^{\bullet}$	$(\ell^{\pm}\nu b)$	-	1ℓ	25.6%	[438]
$t\bar{t}Z$	$840 \pm 100^{\star}$	$(\ell^{\pm}\nu b)(q\bar{q}b)$	$q\bar{q}$	1ℓ	24.1%	[448]
		$(\ell^{\pm}\nu b)(\ell^{\mp}\nu b)$	$q\bar{q}$	2ℓOS	4.6%	[361]
		$(\ell^{\pm}\nu b)(q\bar{q}b)$	$\ell^{\pm}\ell^{\mp}$	3ℓ	2.3%	[361, 436, 445, 449–451]
		$(\ell^{\pm}\nu b)(\ell^{\mp}\nu b)$	$\ell^{\pm}\ell^{\mp}$	4ℓ	0.4%	[361, 436, 445, 450, 451]
$tZ(q)$	$94 \pm 3.1^{\diamond}$	$(\ell^{\pm}\nu b)$	$\ell^{\pm}\ell^{\mp}$	3ℓ	1.7%	[437, 445, 452, 453]
tWZ	$136^{+9}_{-8}{}^{\delta}$	$(\ell^{\pm}\nu b)$ $(q\bar{q}b)$	$(q\bar{q})(\ell^{\pm}\ell^{\mp})$ $(\ell^{\pm}\nu)(\ell^{\pm}\ell^{\mp})$	3ℓ	1.4%	[435]

evolving.

In CMS, the measurements of the $t\bar{t}W$ process have mostly focused on multilepton final states, in particular those comprising either a same-sign dilepton pair or three leptons. A multitude of different competing processes constitute the background ranging from $t\bar{t}$, dibosons, non-prompt leptons, and rare $t\bar{t}$ associated production processes, but also conversions of photons into electron pairs, and incorrect lepton charge measurements. These need to be estimated from data themselves. The events are analysed in different categories that enhance the different contributions, typically using jet or b jet multiplicities, total lepton charge, Z bosons reconstructed with same-sign lepton candidates, or leptons with loosened identification criteria. To reduce the uncertainties in lepton selection and background contamination, dedicated MVA methods have been employed. The most precise measurement of the $t\bar{t}W$ cross section has a relative uncertainty of 7.5%, dominated by the statistical component and the modelling of signal and backgrounds, specifically $t\bar{t}H$. The interplay between the $t\bar{t}W$ and $t\bar{t}H$ processes is discussed in Section 7. The measured charge asymmetry, $\sigma_{t\bar{t}W^+}/\sigma_{t\bar{t}W^-} = 1.61^{+0.17}_{-0.16}$, is slightly below the SM prediction. Table 18 summarizes the $t\bar{t}W$ measurements performed so far by the CMS Collaboration, and Fig. 44 includes a comparison of the most precise $t\bar{t}W$ measurement with the theory prediction.

Table 18: Summary of final states covered experimentally in associated $t\bar{t}W$ production. The structure of the table is similar to that of Table 17. The cross section column cites the prediction at 13 TeV computed at NLO including QCD (up to two jets) and EW contributions [455].

Process	σ (fb)	$t\bar{t}$ decay	boson decay	channel	B	measurements
$t\bar{t}W$	722^{+71}_{-78}	$(\ell^{\pm}\nu b)(q\bar{q}b)$	$\ell^{\pm}\nu$	$2\ell SS$	4.4%	[361, 449–451, 456]
		$(\ell^{\pm}\nu b)(\ell^{\mp}\nu b)$	$\ell^{\pm}\nu$	3ℓ	1.7%	[361, 456]

6.6 Associated production of $t\bar{t}$ with jets

Measurements of $t\bar{t}$ with jets are typically performed as differential cross section measurements and interpreted as tests of perturbative QCD. The CMS Collaboration has produced several such measurements at different $\sqrt{s}$, using different final states and exploring the correlation with the kinematics of the top quark, the $t\bar{t}$ system, and other event variables, as outlined in Refs. [404, 457–462]. The sensitivity of these distributions to the UE, PS modelling, and the ME-PS matching is explored in conjunction with ancillary measurements to improve the theoretical modelling and to validate new models. Recent examples are available in Ref. [37], where the best agreement with data is found for the MADGRAPH5_aMC@NLO matrix element generator and the FXFX matching scheme using PYTHIA 8, and in Ref. [463] where good agreement is found between data and the POWHEG+HERWIG 7 setup.

When the additional jets are heavy-flavoured, these processes are particularly important to understand, since they constitute backgrounds to the measurements of processes such as $t\bar{t}H(\rightarrow b\bar{b})$ and $t\bar{t}t\bar{t}$. The final states of $t\bar{t}b\bar{b}$ and $t\bar{t}c\bar{c}$ are complex, as they comprise many jets. The additional heavy-flavour quark pair arises typically from gluon splitting and the jets in the final state end up being soft in p_T and close in the η–ϕ plane. A gluon splitting Feynman diagram is shown in Fig. 46(a). With the exception of the $t\bar{t}H$ measurements, described in Section 7, the analyses do not distinguish whether the origin of a jet is from gluon splitting, boson decay or another multiparton interaction. Two of these cases are represented in Figs. 46(b) and (c).

A summary of the $t\bar{t}b\bar{b}$ measurements by CMS is given in Fig. 47. The latest $t\bar{t}b\bar{b}$ [462, 464, 465]

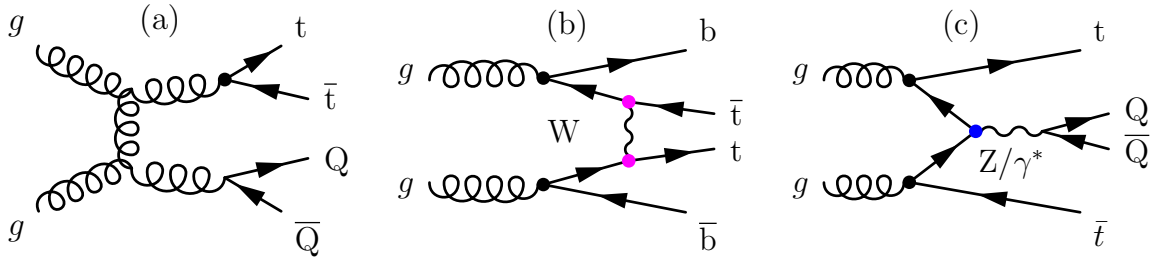

Figure 46: Feynman diagrams contributing to the associated production of top quarks with heavy-flavoured jets.

and $\mathrm{t\bar{t}c\bar{c}}$ [466] measurements improve significantly over previous results because of higher statistics and better identification of heavy-flavoured jets. The achievement was made possible by the improved tracking capabilities of the upgraded pixel detector in the second part of Run 2 and the usage of more modern machine learning (ML) algorithms such as DEEPJET [35, 36].

The measured cross sections are generally somewhat higher than the predictions. Models that rely on parton showers for high jet multiplicities tend to underestimate the rate of events with three or more b jets, indicating that either additional tuning or higher-order accuracy is needed. From the theoretical point of view, the calculations of these multiscale processes come with large NLO corrections, up to a factor of 2, and a relatively large final uncertainty of typically 20% [467, 468]. Because of the still large theoretical uncertainties, the difference of the experimental data with respect to theory has a reduced significance (1–2 s.d.). Similar to previous discussions in Section 6.1, the 5FS generally describes the observed rates better than the 4FS. The dominant experimental uncertainties are related to the efficiency of the flavour-tagging algorithms and to the modelling of the parton shower.

Additional measurements, with larger data samples and exploring new jet algorithms which can probe the phase space typically vetoed by the hard jet selection constraints, will help to improve the description of these important processes.

6.7 Four top quark production

With a cross section that is five orders of magnitude lower than that of $\mathrm{t\bar{t}}$ production, four top quark production ($\mathrm{t\bar{t}t\bar{t}}$) is among the rarest QCD processes established by the CMS experiment. At NLO plus next-to-leading logarithmic accuracy (NLO+NLL' QCD+EW), the expected cross section is $\sigma_{\mathrm{t\bar{t}t\bar{t}}}(13\,\mathrm{TeV}) = 13.4^{+1.0}_{-1.8}\,\mathrm{fb}$ [469]. The large number of permutations of decay modes of the four W bosons leads to a large number of different final states, all of which also contain four b jets. Besides the dominant strong production mode, $\mathrm{t\bar{t}t\bar{t}}$ receives contributions from EW vertices, such as the ones involving the top quark Yukawa coupling as shown in Fig. 48(b). In addition, several BSM scenarios, such as supersymmetry, simplified dark matter models, and Type II Higgs doublet models, predict modifications to the SM $\mathrm{t\bar{t}t\bar{t}}$ production [470, 471].

The CMS Collaboration has analysed a large number of decay channels, including the fully hadronic [472], 1ℓ [472–475], 2ℓOS [472, 474, 475], 2ℓSS, and multilepton [476–478] final states. Various backgrounds contribute to each of these final states, some of them being common with the backgrounds of $\mathrm{t\bar{t}}$+V associated production or $\mathrm{t\bar{t}}$+jets. The correct modelling of $\mathrm{t\bar{t}}$ in association with vector bosons and with heavy flavours plays a crucial role, and control regions are established in data to validate the background estimations.

Among all these final states, the multilepton final states, specifically the 2ℓSS and 3ℓ channels, achieve the highest significance, owing to their purity. In both Ref. [477] and Ref. [478] MVA discriminators are trained to separate the $\mathrm{t\bar{t}t\bar{t}}$ signal from the backgrounds. The cross section

DRAFT

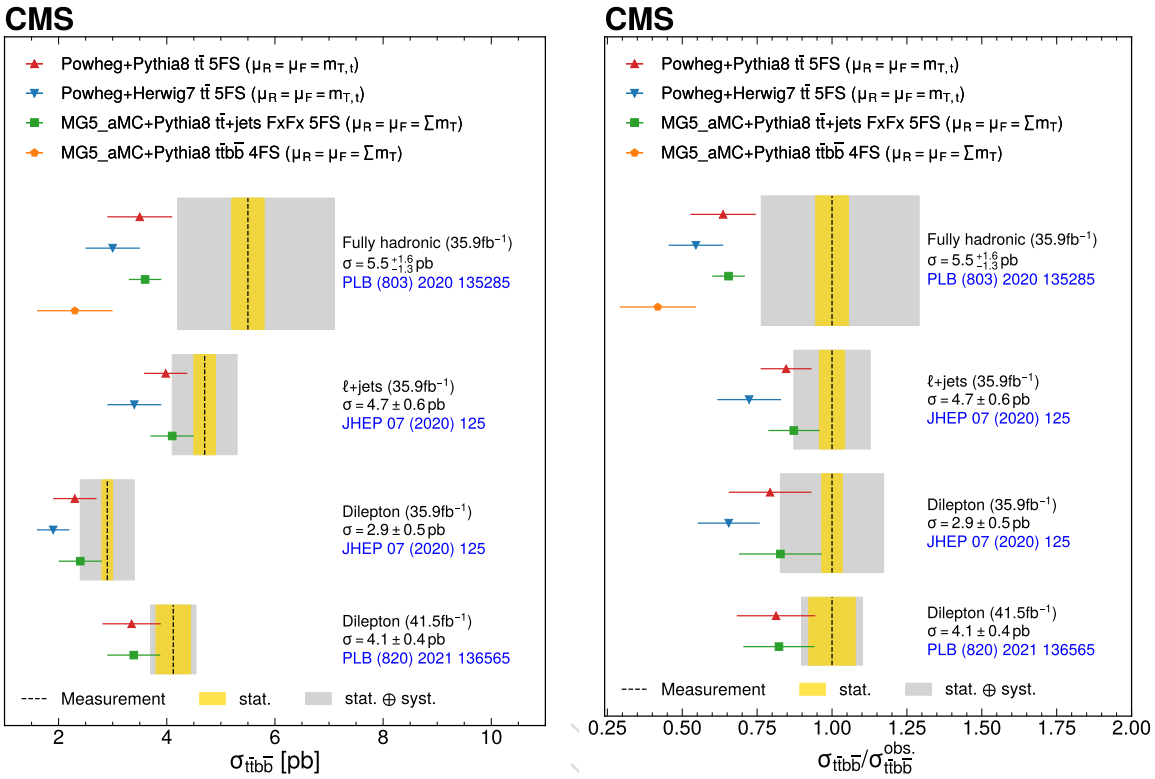

Figure 47: Summary of $t\bar{t}b\bar{b}$ cross section measurements. The left plot depicts the measurements performed in the full phase space using different final states and data sets, compared with different MC predictions. The right plot shows the ratio between the theoretical and measured cross. The statistical and total uncertainties on the measurements are represented by different shaded bands, while the uncertainty on the predictions are represented by error bars.

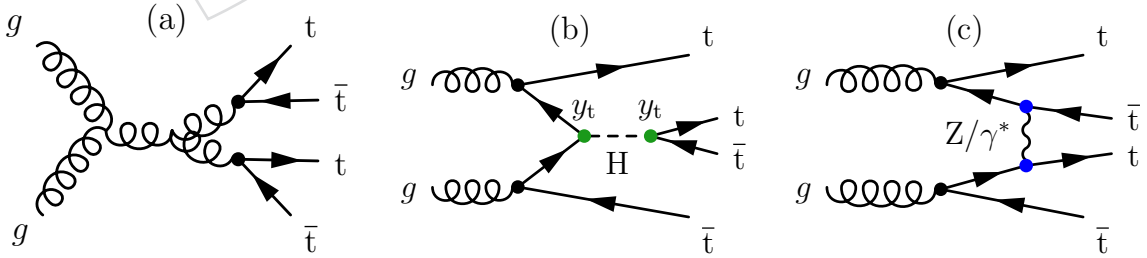

Figure 48: Representation of different Feynman diagrams contributing to $t\bar{t}t\bar{t}$ production at the LHC. Diagrams that involve strong coupling vertices, shown in (a), are expected to dominate.

is measured from a combined fit using several categories. Although using the same data set, Ref. [478] improves over the results obtained in Ref. [477] because of the improved lepton and b jet identification techniques. Observation-level significance above the background-only hypothesis is attained in Ref. [478]: 5.6 s.d. with 4.9 s.d. expected. The measured cross section $\sigma_{t\bar{t}t\bar{t}}(13\,\text{TeV})$ is 17.9 ± 4.1 fb, in agreement with the SM. The result is still statistically limited, and the main systematic uncertainties arise from the b tagging efficiency (about 5%) and the jet energy scale uncertainty (about 3%).

The all-hadronic channel has also been explored by the CMS experiment for the first time [472], making use of both resolved and boosted top quark reconstruction. A custom BDT and minimum η–ϕ separation is used in the resolved regime, whereas the boosted regime makes use of CMS's DEEPAK8 algorithm [419]. The combination of the ℓ+jets, 2ℓOS, and all hadronic channels using full Run 2 data yield a significance of 3.9 s.d. with 1.5 s.d. expected; the excess is attributed to the full hadronic channel. After combination with the 2ℓSS and multilepton analysis from Ref. [477] and the 2ℓOS analysis from Ref. [475] the observed significance becomes 4.0 s.d. with 3.2 s.d. expected.

Figure 49 summarizes all the $t\bar{t}t\bar{t}$ searches and measurements performed so far by CMS. They are consistent with the SM within the uncertainties. The most precise combination [478] shows a slightly larger measured cross section value and achieves observation of $t\bar{t}t\bar{t}$ production.

Larger data sets will be used by CMS to further explore this process, to constrain fundamental parameters such as y_t and to look for BSM effects [413]. Related analyses of the production of three top quarks in association with a jet or a W boson will require data sets of higher integrated luminosity because of their small expected cross sections of about 0.47 and 0.73 fb, respectively [480, 481]. This is analogous to the history of top quark cross section measurements in which the tW process was established long after that of $t\bar{t}$. The three-top quark processes share similar overlapping issues, albeit at a higher energy scale and top quark multiplicity.

6.8 Extraction of fundamental theory parameters from top quark cross sections

One of the main aims of inclusive cross section measurements is to extract information about fundamental SM parameters. Top quark production cross sections allow measurements of α_S, y_t and V_{tb}. A short description of the precision achieved so far by CMS is given below. Direct measurements of $t\bar{t}H$ and the combined Higgs boson results to extract y_t are described later in Section 7.

As noted in Section 6.2, the $\sigma_{t\bar{t}}$ cross section is sensitive to both α_S and m_t^{pole}, thus its measurement can be used to extract one of the two parameters while fixing the other. In addition, a choice has to be made related to the PDF set, and the corresponding fixed order and mass scheme. In differential cross section measurements, e.g. of the mass and rapidity of the $t\bar{t}$ system, the three quantities (α_S, m_t^{pole} and PDF) can be extracted simultaneously, as demonstrated in Ref. [181].

For the extraction of α_S, the inclusive $t\bar{t}$ cross section is used, and hence, residual uncertainties related to the extrapolation of the cross section from the fiducial phase space to the full phase space enter the measurement and cannot be constrained from data since they impact a region that is not accessible experimentally. The uncertainties include scale choices, PDF uncertainties, and the uncertainty in the LHC beam energy. Nonperturbative (NP) contributions related to the intrinsic k_T, but also to the modelling of the QCD colour charge carried by the top quark or antiquark (i.e. colour reconnection [482]) may contribute as well. Even though NP effects occur at a scale Λ_{QCD} and in most cross section measurements $Q^2 \gg \Lambda_{QCD}$ (and $\sigma > \sigma_{NP}$),

DRAFT

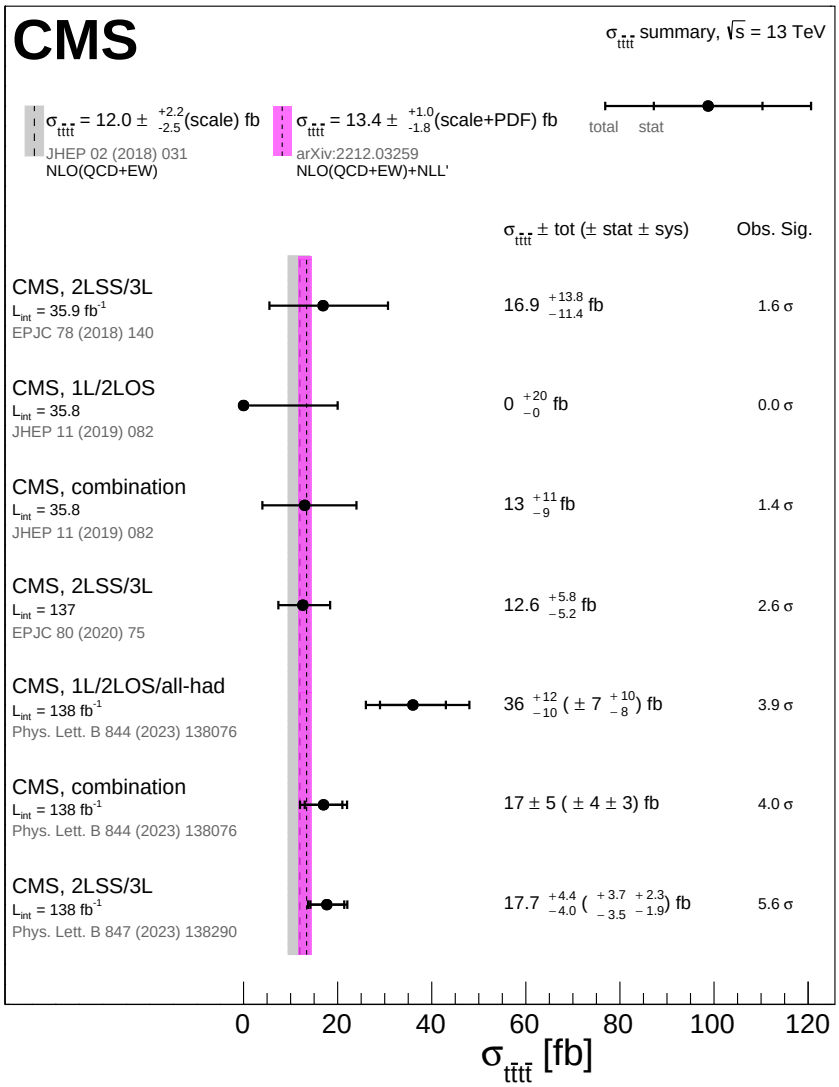

Figure 49: Summary of CMS measurements of the $t\bar{t}t\bar{t}$ production cross section at 13 TeV in various channels. The total (statistical) uncertainty associated with the measurements is represented by the outer (inner) error bars. The cross section measurements are compared with the NLO QCD and EW theoretical calculation. The theoretical band represents uncertainties due to renormalization and factorization scales. Complementary theory predictions are also available in Ref. [479].

NP effects may still be relevant if the selection is strict or involves a large extrapolation. The p_T distribution of the top quarks, discussed in the previous section, is also relevant. In most cases, cross section measurements using dilepton final states have been used in the determination of α_S since they involve smaller extrapolations to the full phase space and have overall the best precision achieved so far. In the most precise measurements of α_S from $\sigma_{t\bar{t}}$, summarized in the next paragraph, the dominant uncertainties turn out to be related to the QCD scale choice and the PDF.

The strong coupling α_S is technically measured at the $t\bar{t}$ scale, and one relies on the running of α_S to translate the results to the m_Z scale. The measurement of $\alpha_S(m_Z)$ from $\sigma_{t\bar{t}}$ with the 7 TeV data has a total uncertainty of 2.4% [190] and with 13 TeV data a total uncertainty of 3.4% [483]. Data sets at smaller centre-of-mass energy are more sensitive owing to the larger correlation between α_S and $\sigma_{t\bar{t}}$. The most precise result to date comes from the combination of the CMS and ATLAS measurements at 7 and 8 TeV and achieves a total uncertainty of 1.8%, as the main uncertainties in the individual measurements ($t\bar{t}$ signal modelling and lepton identification and energy) are largely complementary between CMS and ATLAS [405]. The measurements are in agreement with the world average, as summarized in Fig. 50.

Another fundamental standard model parameter is V_{tb}. Since V_{tb} is related to the EW coupling of the top quark, the measurement is carried out using the single top quark t-channel (Figs. 33 (a) and (b)). As noted in Section 6.1, in t-channel processes, the tWb vertices contribute twice, in the production and in the decay, giving rise to terms of order V_{tb}^2. This results in an increased sensitivity with respect to the analysis of the top quark decays alone. In practice, from the signal strength of the t-channel, i.e. the ratio between observed and theoretical cross section, one extracts $|f_{LV}V_{tb}| = \sqrt{\frac{\sigma_{obs}}{\sigma_{theo}}}$, where in the SM the form factor $f_{LV} = 1$. For simplicity, we assume $f_{LV} = 1$ in the following. The CMS Collaboration has made several measurements at different $\sqrt{s}$, the most precise result is achieved by combination of the results using this method on the 7 TeV and 8 TeV data: $|V_{tb}| = 0.998 \pm 0.038\,(\text{exp}) \pm 0.016\,(\text{theo})$ [377]. The experimental uncertainty is dominated by the signal modelling and jet energy scale, as summarized in Section 6.1. The combination with ATLAS results achieves a total uncertainty of 4.4% [381]. More recently, by performing a fit which includes the parameterized contributions of the different CKM matrix elements to the production and decay of single top quarks [484], a more precise measurement of $|V_{tb}| = 0.988 \pm 0.024$ has been obtained. The uncertainty is limited by jet energy scale and PS scale uncertainties. The result is promising since it relaxes the SM-based assumptions used in the most precise measurement of V_{tb} to date, based on the measurement $R_b = B(t \to Wb)/B(t \to Wq)$ in $t\bar{t}$ events in which a limit of $V_{tb} > 0.975$ at 95% confidence level was determined [485]. A direct measurement of $|V_{td}|^2 + |V_{ts}|^2 = 0.06 \pm 0.06$ is also made in [484]. Figure 51 summarizes the various measurements of $|V_{tb}|$ performed by the CMS Collaboration. The combinations with ATLAS results are also included. All measurements are consistent with each other.

Finally, the top quark Yukawa coupling can be extracted from the $t\bar{t}t\bar{t}$ cross section as an almost independent measurement in which no other Higgs boson couplings intervene, given that at LO $\sigma_{t\bar{t}t\bar{t}} \propto |y_t/y_t^{SM}|^4$, neglecting interference terms [488]. There is, however, a contamination from the $t\bar{t}H$ background in the final sample. Its contribution (about 5%) must also be taken into account for the final limit. The resulting upper limit is $|y_t/y_t^{SM}| < 1.7$ at 95% confidence level [477]. The value of y_t can also be extracted from the differential measurement of $m_{t\bar{t}}$ and $y_{t\bar{t}}$, attaining uncertainties of 20 to 40% with 13 TeV data. This is possible owing to the contribution of diagrams where a virtual Higgs boson is exchanged between the $t\bar{t}$ pair, giving sensitivity to y_t independently of other H couplings. More details about the CMS measure-

DRAFT

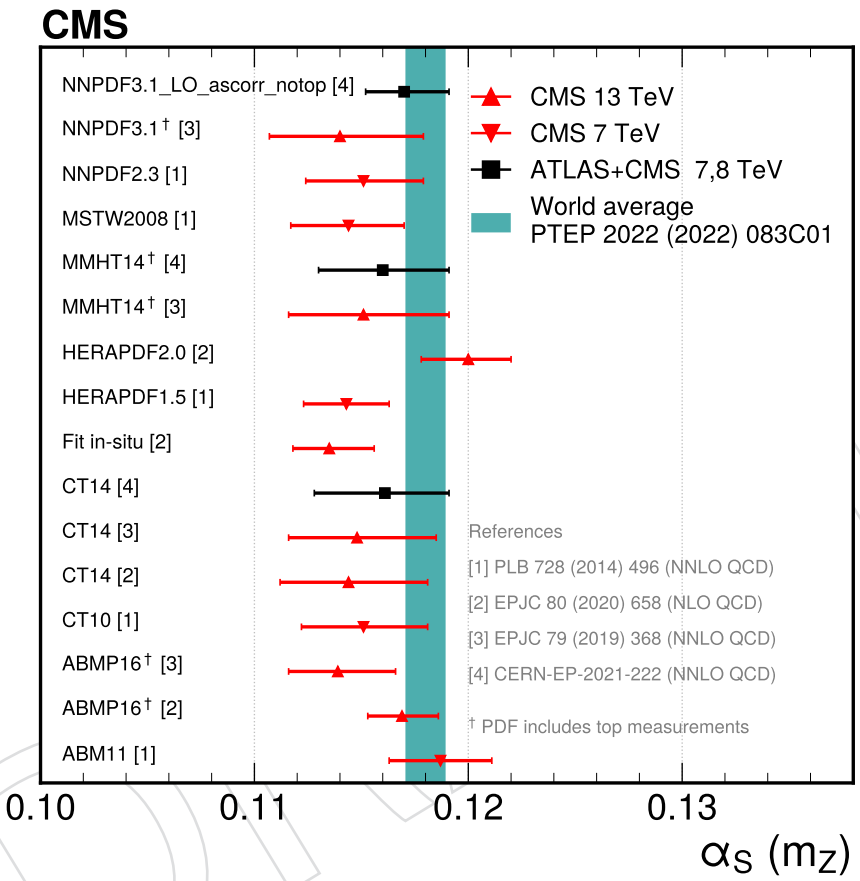

Figure 50: Summary of α_S determinations from inclusive and differential top quark cross section measurements. The error bars represent the total uncertainty of the measurements. The results obtained with different PDF sets are compared with the world average [123] and the reference α_S in the corresponding PDF set. The 68% confidence intervals are represented by the error bars and the coloured ranges. The PDFs marked with a † include LHC top quark data in their fits.

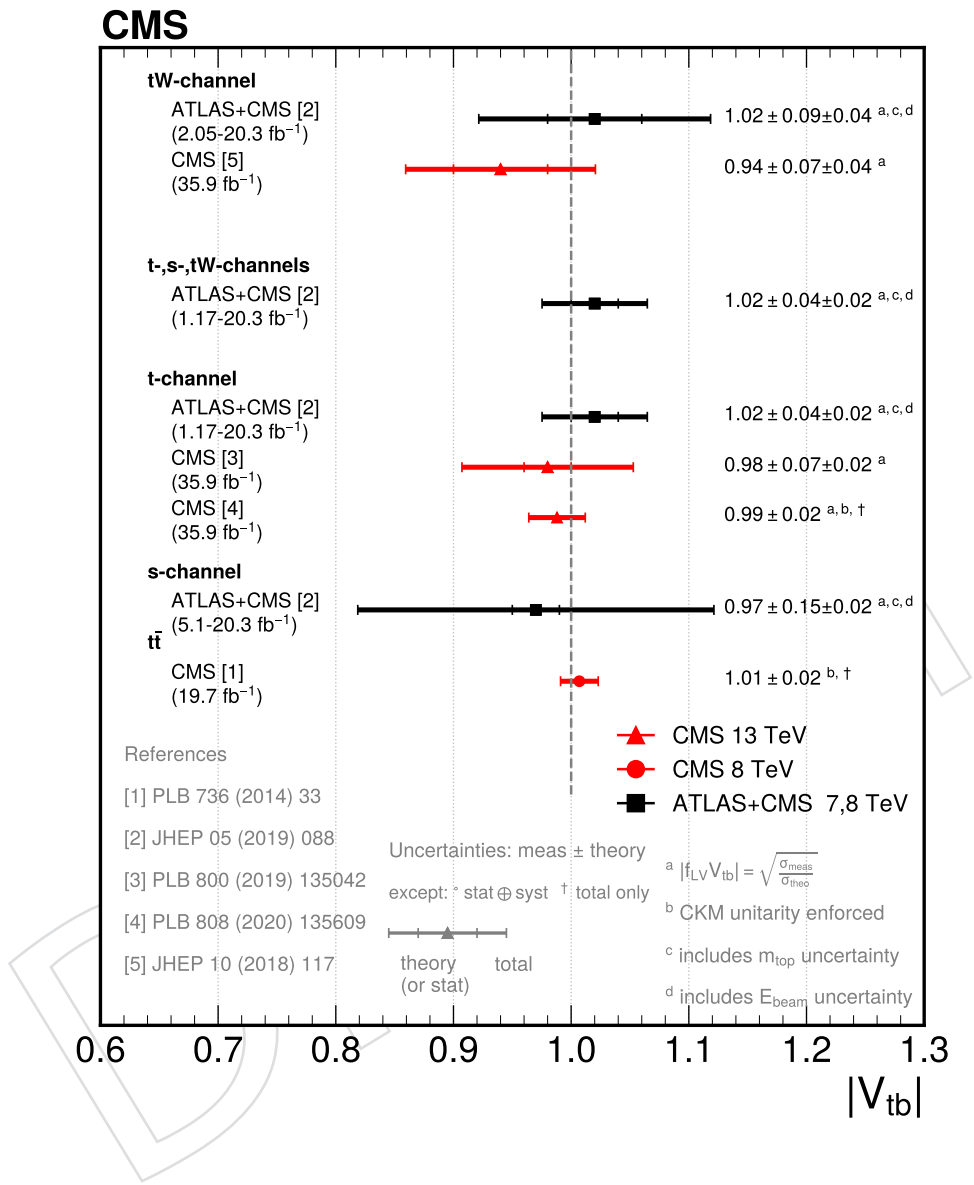

Figure 51: Summary of $|V_{tb}|$ determinations from top quark events using different techniques. The values measured and the corresponding references are given in the figures. The error bars represent separately different uncertainties, as described in the legend. In the LHC combinations, the reference theory cross section used in the t- and s-channel measurements is computed at NLO QCD accuracy [371] with the PDF4LHC prescription for the PDF uncertainty using CT10nlo, MCSTW2008nlo, and NNPDF2.3nlo [486], whereas in the tW channel the theory reference is computed at NNLO+NNLL QCD accuracy [487] using the MSTW2008 NNLO PDF [109]. A line at $|V_{tb}| = 1$ is used as a common reference.

ments can be found in Refs. [358, 489].

Additional constraints on the Higgs boson propagator can be obtained from $\mathrm{t\bar{t}t\bar{t}}$ production. The constraints are obtained after quantifying the modifications to $\sigma_{\mathrm{t\bar{t}t\bar{t}}}$ with an effective field theory approach where additional contributions are added to the SM Lagrangian. These BSM contributions can be modelled with new operators proportional to m_H/Λ^2, where Λ is the energy scale of new physics. The so-called oblique $\hat{H}$-parameter falls in this category and modifies the Higgs boson propagator [490] inducing a parabolic variation of $\sigma_{\mathrm{t\bar{t}t\bar{t}}}$ as a function of $\hat{H}$. This dependency is used to obtain $\hat{H} < 0.12$ at 95% confidence level [475]. Even though it does not use the most precise $\sigma_{\mathrm{t\bar{t}t\bar{t}}}$ measurement, this limit is better than that originally expected for the end of the HL-LHC [490].

6.9 Top quark summary

The CMS experiment has observed or measured the majority of the expected production processes involving top quarks at the LHC. The results are in good agreement with the SM predictions and, in some cases such as $\mathrm{t\bar{t}t\bar{t}}$, are still dominated by statistical uncertainties. The inclusive cross section measurements have been used to extract or set independent constraints on fundamental parameters of the theory such as α_S, V_{tb}, or y_t. Furthermore, measurements of $\sigma_{\mathrm{t\bar{t}}}$ and t-channel single top quark production provide important inputs for the determination of PDFs.

An overview of the main top quark cross section measurements at CMS is provided in Fig. 52. Good overall agreement with the SM is observed. Future measurements with increased statistics, improved experimental methodologies, and theoretical models are expected to contribute to finer tests of the SM along with the final goal to discover new physics.

7 Measurements of Higgs boson production

The discovery of the Higgs boson in 2012 by the CMS and ATLAS Collaborations [210, 491, 492] was a milestone in particle physics, leading to the experimental confirmation of the BEH EW symmetry-breaking mechanism and the first measurement of a fundamental parameter of the SM: the Higgs boson mass. The production of Higgs bosons at the LHC is dominated by gluon-gluon fusion (ggF) proceeding via a virtual top quark loop. Over the past decade, many studies have been performed in the form of precise measurements in order to characterize the nature of the Higgs boson. These started with the verification of the BEH mechanism through the observation of the direct Higgs boson decays to pairs of W or Z bosons [210, 491, 493–496], and the indirect decay to photon pairs through fermion and W boson loops [210, 491, 497, 498]. An additional feature of this mechanism is that it grants masses to fermions through the Yukawa interaction, confirmed by the measurement of the Yukawa couplings of the Higgs boson to b quarks and τ leptons [499–502] and tree-level ttH production [503]. There is also evidence for other decay channels with smaller branching fractions, such as $\mathrm{H} \to \mu\mu$ [504] and $\mathrm{H} \to \mathrm{Z}\gamma$ [505, 506]. The Higgs boson mass is now known to the permille level ($125.38 \pm 0.14\,\mathrm{GeV}$ [18]). The total Higgs boson width has been measured to be $\Gamma_\mathrm{H} = 3.2^{+2.4}_{-1.7}\,\mathrm{MeV}$, in agreement with the SM expectation of 4.1 MeV [507]. The spin (J) and parity (P) were also found to be compatible with the SM prediction ($J^P = 0^+$), already during Run 1 [508, 509]. Further measurements have explored the Higgs boson spin and tensor structure [510–514] of its couplings to bosons and fermions [515]. Limits on the production cross section of pairs of Higgs bosons in a variety of final states and constraints on the Higgs boson self-coupling have also been derived [515–521]. A large number of direct and indirect searches for BSM physics

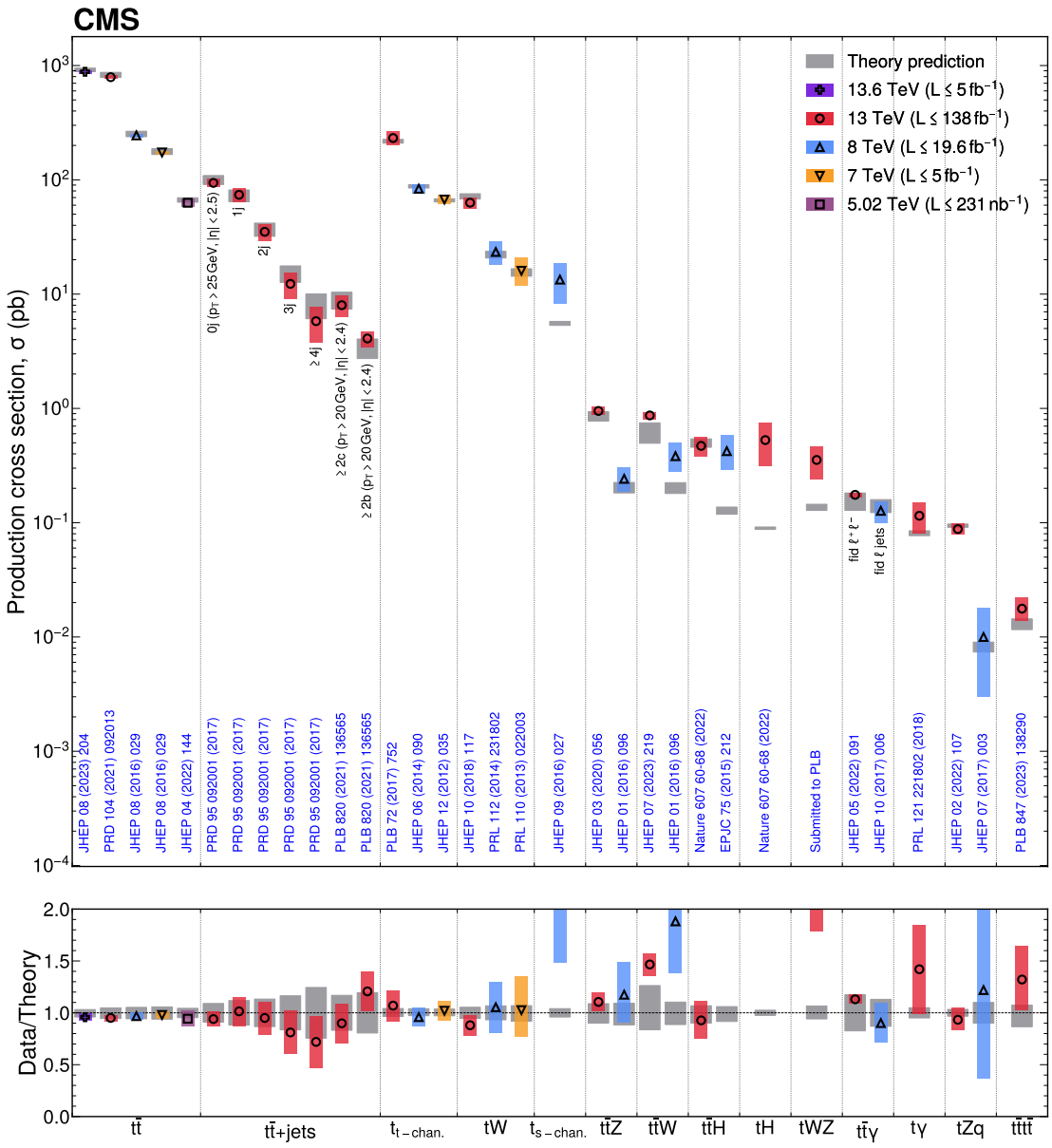

Figure 52: Summary of production cross section measurements involving top quarks. Measurements performed at different LHC pp collision energies are marked by unique symbols and the coloured bands indicate the combined statistical and systematic uncertainty of the measurement. Grey bands indicate the uncertainty of the corresponding SM theory predictions. Shaded hashed bars indicate the excluded cross section region for a production process with the measured 95% C.L. upper limit on the process indicated by the solid line of the same colour.

connected to the Higgs sector have also probed the frontiers of the SM. With the current level of precision, the results are in agreement with the SM predictions.

The study of the cross section of the Higgs boson production at the LHC provides valuable insights into its underlying production mechanisms and kinematics, a stringent test of the SM predictions. These cross section measurements are not only performed inclusively, but also have been expanded to focus on obtaining a thorough description of the Higgs boson kinematics with the measurement of fiducial, differential, and double-differential cross sections.

A detailed discussion of recent CMS measurements of Higgs boson production and decay is presented in Ref. [515]. In the next sections, the status of inclusive and differential cross sections of single Higgs boson production is reported, followed by a discussion of the current constraints on the production of pairs of Higgs bosons. These results are based on the pp collision data collected by the CMS experiment during the Run 2 of the LHC, at a centre-of-mass energy of 13 TeV. When useful, comparisons to the corresponding 7 and 8 TeV results are made.

7.1 Inclusive cross sections for single Higgs boson production

The main Feynman diagrams for the production and decay of the Higgs boson are shown in Fig. 53. For a Higgs boson mass of 125.38 GeV, the total predicted cross section for its production within the SM in pp collisions at a centre-of-mass energy of 13 TeV is 55.4 ± 2.6 pb [522]. In the dominant production mode, gluon-gluon fusion (ggF, Fig. 53 a), the Higgs boson is produced by the fusion of a pair of gluons, one from each of the colliding protons. With a cross section in the SM of 48.3 ± 2.4 pb, the ggF dominates over the other production modes. The next in relevance is vector boson fusion (VBF, Fig. 53 b), with a SM cross section of 3.77 ± 0.80 pb, where two quarks radiate virtual vector bosons (W or Z), which then combine to produce a Higgs boson. As discussed in Section 5.3, a distinctive feature of VBF production is the presence of forward- and backward-scattered quarks that produce jets with large separation in rapidity. Other processes where the Higgs boson is produced in association with other SM particles have smaller cross sections. These include the associated production with vector bosons (WH and ZH, Fig. 53 c, 1.359 ± 0.028 pb and 0.877 ± 0.036 pb in the SM, respectively), the associated production with pairs of top quarks (ttH, Fig. 53 d, 0.503 ± 0.028 pb in the SM) or single top quarks (tH, Fig. 53 e and f, 0.092 ± 0.008 pb in the SM), and the associated production with bottom quarks (bbH, Fig. 53 d, 0.482 ± 0.097 pb in the SM). The leading Higgs boson production modes (ggF, VBF, VH, tH+ttH) have been observed independently, with the measurements of the cross sections with precision at the 10–20% level. The sensitivity of the LHC to the bbH SM production is limited and this mode has not been extensively studied yet.

These production cross sections have been measured with dedicated analyses targeting the decay to a pair of b quarks (with the branching fraction in the SM [522] of $\mathcal{B}(\mathrm{H} \to \mathrm{b\bar{b}} = 57.63 \pm 0.70\%)$, W bosons ($\mathcal{B}(\mathrm{H} \to \mathrm{WW}) = 22.00 \pm 0.33\%$), τ leptons, ($\mathcal{B}(\mathrm{H} \to \tau\tau) = 6.21 \pm 0.09\%$), Z bosons ($\mathcal{B}(\mathrm{H} \to \mathrm{ZZ}) = 2.71 \pm 0.04\%$), and photons ($\mathcal{B}(\mathrm{H} \to \gamma\gamma) = 0.2\%$). These decay modes have all been measured [495, 496, 498, 501, 502] and their branching fractions are in good agreement with the SM predictions in Ref. [522]. Other decay modes, which are rarer or more challenging to observe experimentally, also have been studied. Examples include $\mathrm{H} \to \mu\mu$ [504], $\mathrm{H} \to \mathrm{c\bar{c}}$ [523], and $\mathrm{H} \to \mathrm{Z}\gamma$ [505, 506].

Specific signatures associated with each decay mode and production mechanism are used to categorize the events. The reconstruction of Higgs boson candidates is based on the identification of pairs of photons, oppositely charged leptons (e, μ, τ), or b jets. Kinematic variables and their correlations are needed to discriminate against other SM processes with similar decay products that are produced more abundantly, such as the Z boson. Production modes other

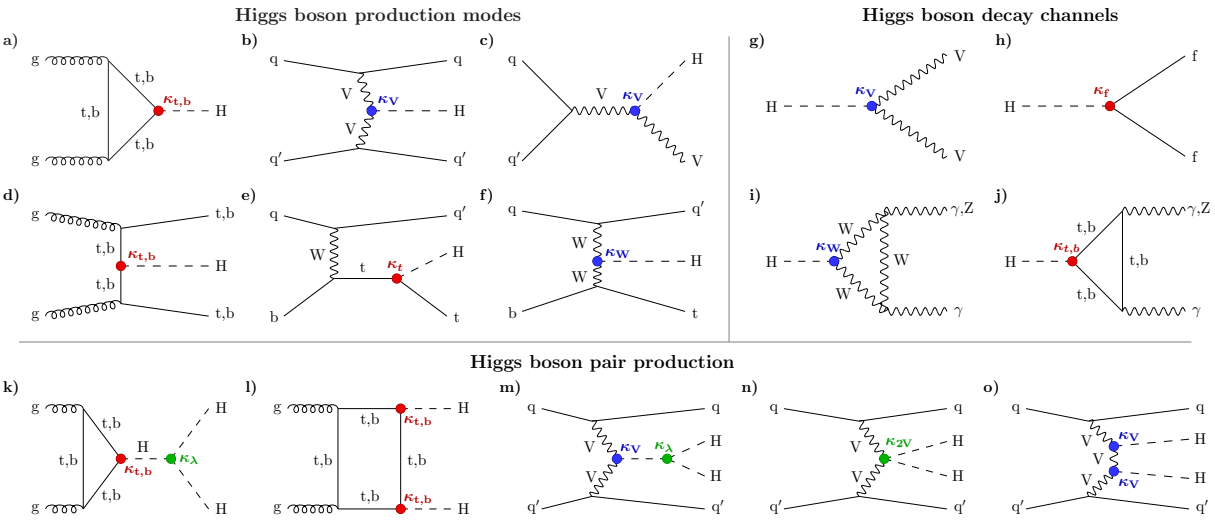

Figure 53: Higgs boson production in (a) gluon-gluon fusion (ggH), (b) vector boson fusion (VBF), (c) associated production with a W or Z (V) boson (VH), (d) associated production with a top or bottom quark pair (ttH or bbH), (e, f) associated production with a single top quark (tH); with Higgs boson decays into (g) heavy vector boson pairs, (h) fermion-antifermion pairs, and (i, j) photon pairs or $Z\gamma$; Higgs boson pair production: (k, l) via gluon-gluon fusion, and (m, n, o) via vector boson fusion. The corresponding Higgs boson interactions are labelled with the coupling modifiers κ , and highlighted in different colours for Higgs-fermion interactions (red), Higgs-gauge-boson interactions (blue), and multiple Higgs boson interactions (green). The distinction between a particle and its antiparticle is dropped. Figure taken from Ref. [515].

than ggF are distinguishable because of the additional objects in the event. The VBF events are characterized by the presence of two high-p_{T} jets with a large separation in rapidity, and VH events by the identification of the V decay through high-p_{T} charged leptons, jets, and/or $p_{\mathrm{T}}^{\mathrm{miss}}$. The ttH and tH signatures involve the decay of both the top quark and the Higgs boson, resulting in a rich variety of final states with the distinctive presence of multiple b jets. Detailed descriptions of the event selection for each final state and production mode are presented in the references cited above. A brief summary was included in Ref. [515].

Measurements are compared with the predictions of the production and decay of the Higgs boson obtained using MC generators such as POWHEG 2.0 [79–81], MADGRAPH5_aMC@NLO [69, 70], JHUGEN [61–65], or HJ-MINLO [58–60]. Events produced via the ggF mechanism are simulated at NLO with POWHEG 2.0 and reweighted to match the predictions at NNLO in the strong coupling, including matching to the parton shower (NNLOPS [71–73]) as a function of the $p_{\mathrm{T}}^{\mathrm{H}}$ and of the number of jets in the event.

The individual results featuring specific production and decay modes are combined for a global picture of Higgs boson production. The overall statistical methodology used in this combination is described in Refs. [524, 525].

As a first step towards quantifying the agreement of the observed Higgs boson signal with the expectation of the SM, the data from the various production modes and decay channels discussed are combined through a model that introduces signal strength parameters (μ). These parameters scale the observed signal yields relative to the SM predictions, while preserving the shape of the distributions. For specific initial and final states $i \to f$, the corresponding signal strength is denoted as μ_i^f. Signal strengths for individual production channels and decay modes are defined as functions of the cross section σ_i and the branching fraction $\mathcal{B}_f$ as $\mu_i =$

$\sigma_i/\sigma_i^{\mathrm{SM}}$ and $\mu^f = \mathcal{B}_f/\mathcal{B}_f^{\mathrm{SM}}$, respectively. A result in total agreement with the SM would be characterized by all signal strengths μ_i^f being equal to 1.

We introduce different scenarios in which we incrementally increase the freedom allowed in the model, from considering a single signal strength parameter (μ) that connects all the production and decay modes to allowing individual parameters (μ_i^f) that modify individual channels independently. Figure 54 summarizes the signal strength parameters per individual production mode and decay channel μ_i^f, and combined per production mode μ_i and decay channel μ^f. This result was obtained with the data collected at 13 TeV, corresponding to an integrated luminosity of 138 fb^{-1}. Here the ttH and tH production modes are considered together. This global picture, including details of the production and decay of the Higgs boson, shows good agreement with the SM expectation.

The measurements [515, 526] of a common signal strength parameter are in excellent agreement with the SM:

$$\mu_{\mathrm{H}}(7 \text{ and } 8\,\mathrm{TeV}) = 1.00 \pm 0.008\,(\mathrm{theo}) \pm 0.09\,(\mathrm{stat}) \pm 0.07\,(\mathrm{syst}),$$

$$\mu_{\mathrm{H}}(13\,\mathrm{TeV}) = 1.002 \pm 0.036\,(\mathrm{theo}) \pm 0.029\,(\mathrm{stat}) \pm 0.033\,(\mathrm{syst}).$$

For the 13 TeV measurement, the theoretical uncertainties in the signal prediction, as well as the experimental statistical and systematic uncertainties, are of comparable size.

The theoretical uncertainties in the prediction of the production cross section impact the rate of events being produced and the kinematics of the Higgs boson and its decays. The signal strength parameters are relative measurements of the agreement with the SM, $\mu = \sigma/\sigma_{\mathrm{SM}}$, and therefore fold in the total theoretical uncertainty in the prediction. In contrast, a cross section measurement is only subject to theoretical uncertainties in the acceptance, as discussed in Section 1. As a result, production cross sections are less affected by theoretical uncertainties than the signal strength parameters.

The signal strength model with six μ_i parameters presented in Ref. [515] has been modified to obtain cross sections per production mode. The measurements of the inclusive cross sections at 13 TeV obtained deploying this method are represented graphically in Table 19 and Fig. 55. Table 19 also lists the available measurements of inclusive cross section at 7 and 8 TeV. These have been derived by scaling the theoretical cross sections of Ref. [527] by the signal strengths published in Ref. [526]. The table also shows the corresponding SM prediction for the cross sections, taken from Ref. [527] and computed for $m_{\mathrm{H}} = 125\,\mathrm{GeV}$ for the 7 and 8 TeV results, and from Ref. [526] and for $m_{\mathrm{H}} = 125.38\,\mathrm{GeV}$ for 13 TeV results, following the comparison done in the original publications. Overall, there is good agreement with the SM prediction in Ref. [522].

In addition to this global view of Higgs boson production, fiducial production cross sections for specific decay modes have also been measured individually [528–533]. These fiducial cross sections correspond to well-defined regions of the phase space, and avoid the extrapolation to the full phase space necessary for the determination of total inclusive cross sections. Minimizing the differences in selection between the reconstructed- and particle-level objects facilitates a more model-independent comparison to theoretical calculations. Table 20 summarizes the available measurements at a centre-of-mass energy of 13 TeV, with an integrated luminosity of 138 fb^{-1}. The table also lists the variables and the selection criteria that delineate the fiducial phase space. The variables used to define it follow closely the event selection criteria of each

DRAFT

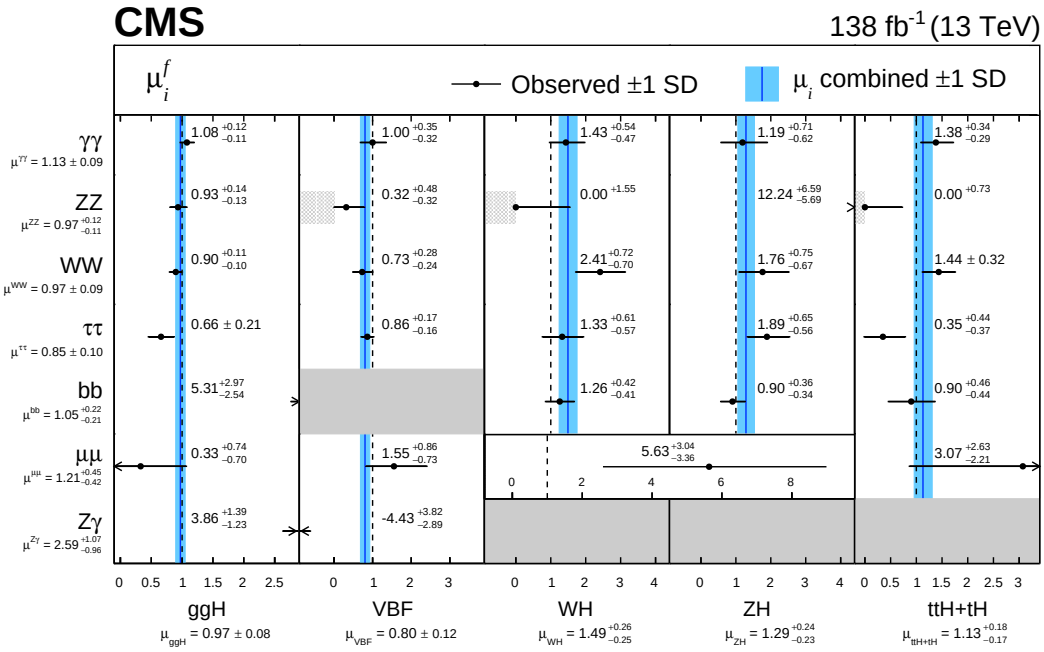

Figure 54: Signal strength parameters per individual production mode and decay channel μ_i^f, and combined per production mode μ_i and decay channel μ^f . The SM expectation at 1 (dashed vertical lines) is shown as a reference. Light-grey shading indicates that μ is constrained to be positive. Dark-grey shading indicates the absence of a measurement. The measured value for each production cross section modifier obtained from the combination across the decay channels, μ_i, is indicated by the blue vertical line. The corresponding 68% CL interval is indicated by the blue bands. The arrows indicate cases where the confidence intervals exceed the scale of the horizontal axis. Figure taken from Ref. [515].

Table 19: Measured inclusive cross sections for the main Higgs boson production modes. At 7 and 8 TeV, the measured cross sections are derived by scaling the theoretical cross sections of Ref. [527] by the signal strengths published in Ref. [526]. At $\sqrt{s} = 13$ TeV, the cross sections are obtained from a global fit, as described in the text. The results are in good agreement with the predictions from Ref. [527] and Ref. [522], respectively.

$\sqrt{s}$	Production Mode	$\sigma(\mathrm{H})$ (pb)	$\sigma^{\mathrm{SM}}(\mathrm{H})$ (pb)
7 TeV	ggF	$15.6^{+5.6}_{-5.0}$	15.13 ± 1.58
	VBF	$2.2^{+1.2}_{-1.1}$	1.222 ± 0.038
8 TeV	ggF	$15.2^{+3.7}_{-3.3}$	19.27 ± 2.01
	VBF	$1.61^{+0.62}_{-0.57}$	1.578 ± 0.035
	VH	$1.08^{+0.46}_{-0.44}$	1.120 ± 0.034
	ttH	$0.42^{+0.16}_{-0.13}$	0.1293 ± 0.0078
13 TeV	ggF+bbH	$47.6^{+1.8}_{-1.8}\,(\mathrm{stat})^{+2.3}_{-2.0}\,(\mathrm{syst})$	48.80 ± 2.46
	VBF	$2.94^{+0.37}_{-0.36}\,(\mathrm{stat})^{+0.27}_{-0.25}\,(\mathrm{syst})$	3.77 ± 0.81
	WH	$1.95^{+0.28}_{-0.28}\,(\mathrm{stat})^{+0.21}_{-0.19}\,(\mathrm{syst})$	1.359 ± 0.028
	ZH	$1.13^{+0.18}_{-0.18}\,(\mathrm{stat})^{+0.11}_{-0.10}\,(\mathrm{syst})$	0.877 ± 0.036
	ttH	$0.467^{+0.074}_{-0.072}\,(\mathrm{stat})^{0.054}_{-0.052}\,(\mathrm{syst})$	0.503 ± 0.035
	tH	$0.54^{+0.19}_{-0.18}\,(\mathrm{stat})^{+0.14}_{-0.12}\,(\mathrm{syst})$	0.092 ± 0.008

DRAFT

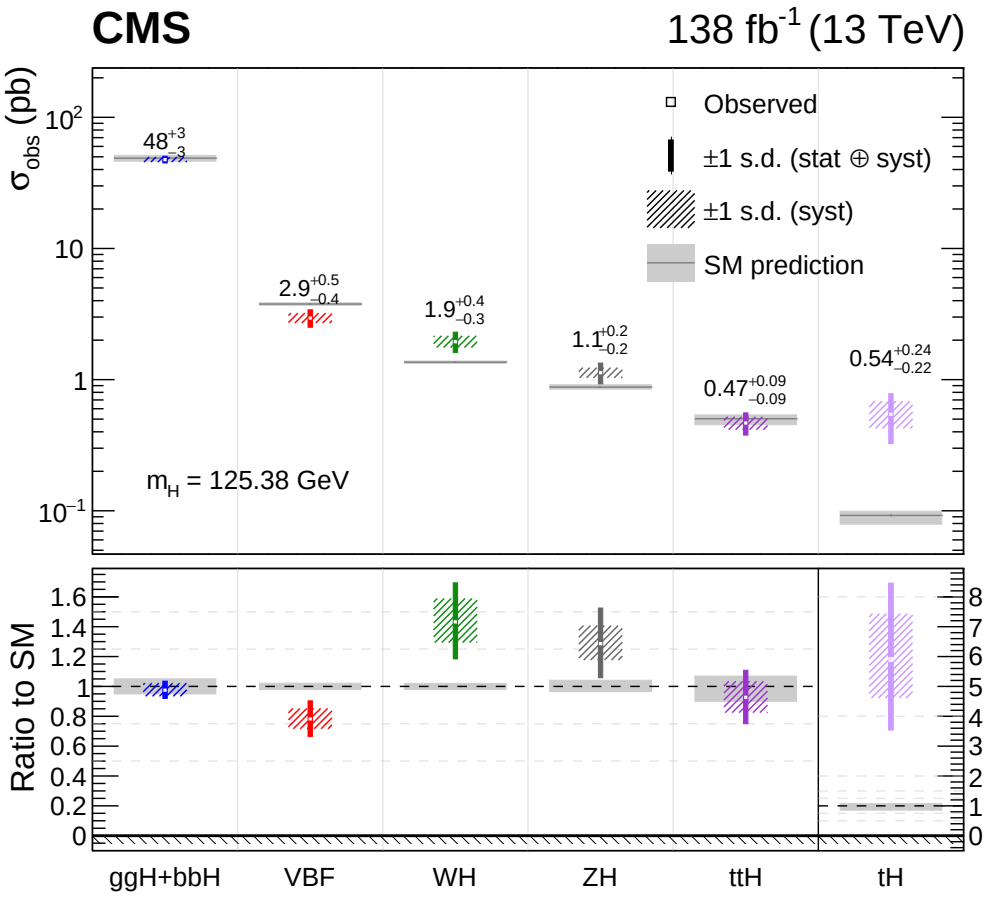

Figure 55: Measured cross sections for the main Higgs boson production modes. The best fit cross sections are plotted together with the respective 68% confidence level intervals. The systematic components of the uncertainty in each parameter are shown by the coloured boxes. The grey boxes indicate the theoretical uncertainties in the SM predictions. The lower panel shows the ratio of the fitted values to the SM predictions.

analysis. These variables include the p_T and (pseudo)rapidities of the reconstructed Higgs boson and its visible decay products, the reconstructed invariant and transverse masses of the system, or the jet multiplicity. They are calculated at the MC generator level after parton showering and hadronization. The lepton momentum includes the momenta of photons radiated within a cone of $\Delta R < 0.1$ in the WW and $\tau\tau$ analyses or $\Delta R < 0.3$ in the ZZ case. Lepton or photon isolation ($\mathcal{I}^{\gamma}_{\text{gen}}$, $\mathcal{I}^{\ell}_{\text{gen}}$) is defined at the generator level as the sum of the energy of all stable hadrons produced in a cone of radius $\Delta R = 0.3$ around the object. Additional details on the definition of the fiducial cross section are presented in the original references. Overall, there is remarkable agreement with the SM prediction. Figure 56 shows the evolution of the fiducial cross section for $H \to ZZ \to 4\ell$ from 7 and 8 TeV [529] to 13 TeV [531].

Table 20: Measurements of the fiducial cross sections of Higgs boson production in various decay modes published by CMS using pp data at a centre-of-mass energy of 13 TeV and an integrated luminosity of 138 fb^{-1}. The reference Higgs boson mass is 125.38 GeV. Isolation ($\mathcal{I}$) represents the sum of scalar p_T of all stable particles within $\Delta R = 0.3$ of the lepton or photon. Additional details on the fiducial phase space variables and on the calculation of the reference SM cross section are presented in the original references.

Decay mode	Fiducial phase space	$\sigma_{\text{fid}}(\text{H})$ (fb)	$\sigma^{\text{SM}}_{\text{fid}}(\text{H})$ (fb)
$H \to \gamma\gamma$ [530]	$p_T^{\gamma_1}/m_{\gamma\gamma} > 1/3$, $p_T^{\gamma_2}/m_{\gamma\gamma} > 1/4$, $\mathcal{I}^{\gamma}_{\text{gen}} < 10\,\text{GeV}$, $\lvert\eta^{\gamma}\rvert < 2.5$	$73.4^{+5.4}_{-5.3}\,(\text{stat})^{+2.4}_{-2.2}\,(\text{syst})$	75.4 ± 4.1
$H \to ZZ \to 4\ell$ [531]	$p_T^{\text{lead}} > 20\,\text{GeV}$, $p_T^{\text{sublead}} > 10\,\text{GeV}$, $p_T^{\ell} > 5(57\,\text{GeV for } \mu\text{ (e)})$, $\lvert\eta^{\ell}\rvert < 2.4\,(2.5)$ for μ (e), $\mathcal{I}^{\ell}_{\text{gen}} < 0.35 p_T$, $40 < m_{Z1} < 120\,\text{GeV}$, $12 < m_{Z2} < 120\,\text{GeV}$, $\Delta R(\ell_i, \ell_j) > 0.02$ for $i \neq j$, $m_{\ell^+\ell^-} > 4\,\text{GeV}$, $105 < m_{4\ell} < 160\,\text{GeV}$	$2.73 \pm 0.22\,(\text{stat}) \pm 0.15\,(\text{syst})$	2.86 ± 0.15
$H \to \tau\tau$ [532]	$\mu\tau_h$ ($e\tau_h$): $p_T^{\ell} > 20\,(25)\,\text{GeV}$, $p_{T,\text{vis}}^{\tau_h} > 30\,\text{GeV}$, $\lvert\eta^{\ell}\rvert < 2.1$, $\lvert\eta^{\tau_h}\rvert < 2.3$, $m_T(\ell, p_T^{\text{miss}}) < 50\,\text{GeV}$, $\tau_h\tau_h$: $p_{T,\text{vis}}^{\tau_h} > 40\,\text{GeV}$, $\lvert\eta^{\tau_h}\rvert < 2.1$, $n_{j\,30\,\text{GeV}} \geq 1$ $e\mu$: $p_T^{\text{lead}} > 24\,\text{GeV}$, $p_T^{\text{sublead}} > 15\,\text{GeV}$, $\lvert\eta^{\ell}\rvert < 2.4$, $m_T(e\mu, \vec{p}_T^{\text{miss}}) < 60\,\text{GeV}$	426 ± 102	408 ± 27
$H \to WW$ [533]	$e\mu$, $p_T^{\text{lead}} > 25\,\text{GeV}$, $p_T^{\text{sublead}} > 13\,\text{GeV}$, $\lvert\eta_{\ell}\rvert < 2.5$, $m_{\ell\ell} > 12\,\text{GeV}$, $p_T^{\ell\ell} > 30\,\text{GeV}$, $m_T^{\ell 2} > 30\,\text{GeV}$, $m_T^{\text{H}} > 60\,\text{GeV}$	86.5 ± 9.5	82.5 ± 4.2

DRAFT

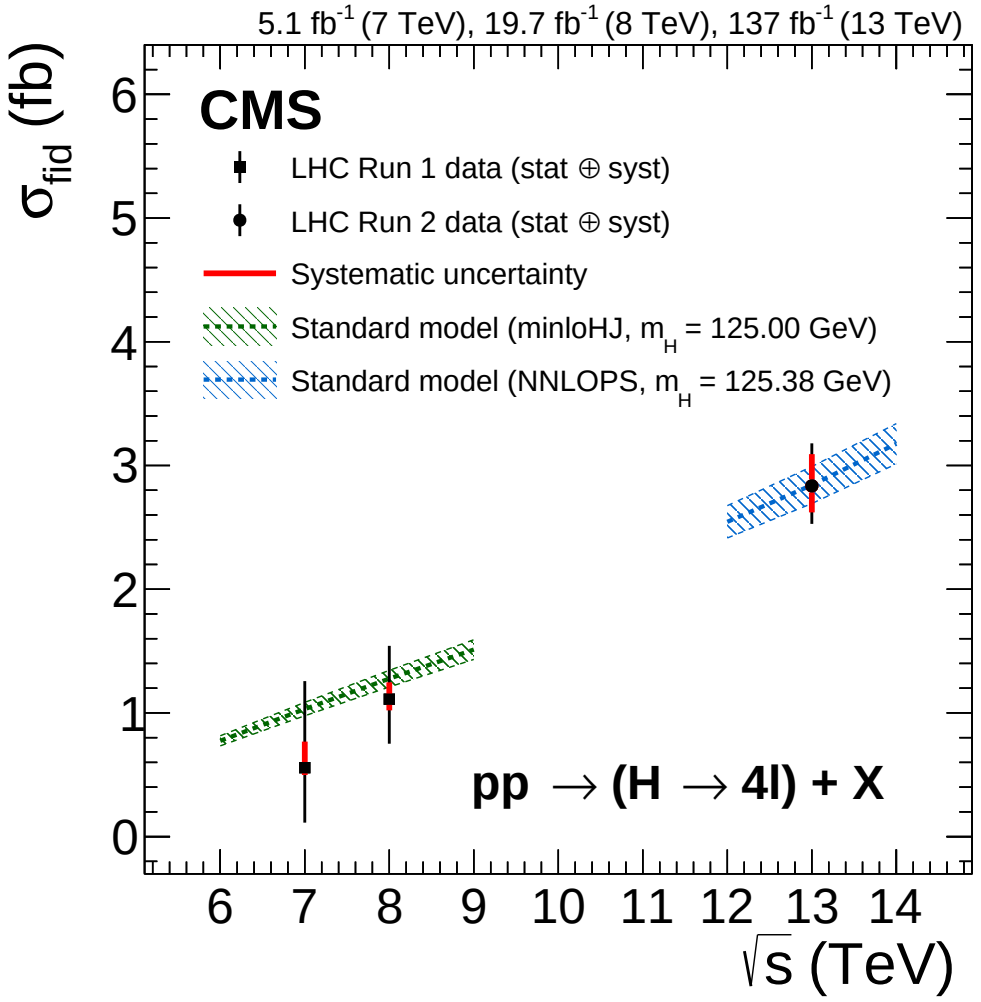

Figure 56: The measured inclusive fiducial cross section for $H \to ZZ \to 4\ell$ as a function of $\sqrt{s}$. The acceptance is calculated using HRES [534, 535] at 7 and 8 TeV, and POWHEG at 13 TeV, and the total gluon fusion cross section and uncertainty are taken from Ref. [536]. The SM predictions and measurements are calculated at $m_H = 125.0$ GeV for $\sqrt{s} = 6$–9 TeV, and at $m_H = 125.38$ GeV for 12–14 TeV. Figure taken from Ref. [495].

7.2 Differential cross sections for single Higgs boson production

The characterization of Higgs boson production cannot rely solely on measuring inclusive production cross sections. For a more complete picture of the nature of the boson, a detailed mapping is needed of its production as a function of different observables, such as its transverse momentum, $p_{\mathrm{T}}^{\mathrm{H}}$. The measurement of differential production cross sections with respect to key kinematic variables, compared with the corresponding theoretical expectations, provides a useful probe of the effects from higher-order corrections in perturbation theory or any deviation from the SM expectations.

The CMS experiment has measured Higgs boson differential production cross sections in the principal decay modes: $\mathrm{H} \to \gamma\gamma$ [528, 530, 537], $\mathrm{H} \to \mathrm{ZZ} \to 4\ell$ [529, 531, 538], $\mathrm{H} \to \tau\tau$ [532], $\mathrm{H} \to \mathrm{WW}$ [533, 539], Lorentz-boosted $\mathrm{H} \to \mathrm{b\bar{b}}$ [540, 541]. These measurements are complementary, as they probe different aspects of the Higgs boson production. As previously discussed, in the SM, the branching fraction for the Higgs boson decaying to a pair of photons or to four leptons is remarkably small. Nevertheless, because of the high precision of the invariant mass reconstruction and the fully reconstructed final state, the $\mathrm{H} \to \gamma\gamma$ and $\mathrm{H} \to \mathrm{ZZ} \to 4\ell$ decay channels provide the most comprehensive measurements of the Higgs boson differential production cross sections. These analyses probe a large number of observables, related to the measurement of the diphoton or four-lepton system, but also to the accompanying jets and event topology. These include the kinematics of the Higgs boson (e.g. $p_{\mathrm{T}}^{\mathrm{H}}$ or $|y_{\mathrm{H}}|$) and the accompanying jets (e.g. m_{jj} or the rapidity-weighted jet veto, $\mathcal{T}^{\max}$, which provides a complementary way to divide the phase space into exclusive jet bins, allowing for an accurate comparison to theory predictions [542]). In the case of the four-lepton analysis, the measurements can also be performed as a function of matrix element discriminators targeting anomalous couplings (D^{dec}). Double-differential cross sections are also possible to measure for a selected number of variables.

The larger branching fractions of the $\mathrm{H} \to \mathrm{b\bar{b}}$, $\mathrm{H} \to \mathrm{WW}$, and $\mathrm{H} \to \tau\tau$ decay modes allow studies in the areas of the phase space with smaller production cross sections. This is the case for high jet multiplicities (n_j) and large Lorentz boosts of the Higgs boson. There is considerable interest in the measurement of Higgs bosons produced with very high p_{T} in the more dominant decay modes (particularly in $\mathrm{H} \to \mathrm{b\bar{b}}$) since they yield significantly better sensitivity than in $\mathrm{H} \to \gamma\gamma$ and $\mathrm{H} \to \mathrm{ZZ} \to 4\ell$ final states. At the highest p_{T}, this measurement can resolve loop-induced contributions to the ggH process from BSM particles, which would be described by an effective ggH vertex at low p_{T}. Advances in the identification of large-radius jets [419] resulting from massive colour-singlet particles with high p_{T} and decaying to $\mathrm{b\bar{b}}$ pairs have been fundamental for these measurements.

These measurements of the differential cross sections in the different decay modes can be combined, as shown in Ref. [543], which incorporated the first measurements at 13 TeV, with 36 fb^{-1} of $\mathrm{H} \to \gamma\gamma$, $\mathrm{H} \to ZZ$ and $\mathrm{H} \to \mathrm{b\bar{b}}$ into a global measurement of the differential cross section as a function of observables, such as $p_{\mathrm{T}}^{\mathrm{H}}$ or n_j. The $\mathrm{H} \to \mathrm{ZZ}$, $\mathrm{H} \to \gamma\gamma$, $\mathrm{H} \to \mathrm{WW}$, and $\mathrm{H} \to \tau\tau$ measurements have been updated using the full data sample collected during the second data-taking period of the LHC, 138 fb^{-1}, and are summarized in Table 21. Additional details of the observables targeted in each case are presented in the original references [530–533, 541]. Overall, they are in agreement with the SM predictions within uncertainties.

Figures 57 and 58 show the fiducial differential distributions as functions of the p_{T} of the Higgs boson and the number of jets in the event for the various decay modes, respectively. Figure 59 is an example of a double-differential cross section; it shows the differential cross sections in

bins of the absolute rapidity of the Higgs boson $|y_{\mathrm{H}}|$ as functions of the Higgs boson transverse momentum $p_{\mathrm{T}}^{\mathrm{H}}$ in the $\mathrm{H} \to \mathrm{ZZ} \to 4\ell$ decay channel. The measurements are compared with the predictions of the production and decay of the Higgs boson obtained using MC generators mentioned in the previous section.

An alternative approach to characterize the production of the Higgs boson is the "simplified template cross sections", STXS [544]. In this approach, fiducial cross sections are measured per production mode and in specific regions of phase space ("bins"), defined in terms of specific kinematic variables ($p_{\mathrm{T}}^{\mathrm{H}}$, m_{jj}, $p_{\mathrm{T}}^{\mathrm{H}jj}$, $p_{\mathrm{T}}^{\mathrm{V}}$). Their purpose is to reduce the theoretical uncertainties, that are directly folded into the measurements, as much as possible, while at the same time allowing for the combination of the measurements of different decay channels. The STXS approach offers convenient benchmarks for comparing theoretical predictions with experimental data to probe and understand the properties and interactions of the Higgs boson, while providing a well-defined platform to test for BSM deviations in kinematic distributions.

The CMS experiment has measured STXS in the principal Higgs boson decay modes at 13 TeV: $\mathrm{H} \to \gamma\gamma$ [498], $\mathrm{H} \to \mathrm{ZZ} \to 4\ell$ [495], $\mathrm{H} \to \tau\tau$ [502], $\mathrm{H} \to WW$ [496], and $\mathrm{H} \to \mathrm{b\bar{b}}$ [545]. Figure 60 shows the STXS measurement for the $\mathrm{H} \to \gamma\gamma$ process as an illustration.

Table 21: Measurements of the various fiducial cross sections of the Higgs boson for different decay modes published by CMS using proton-proton data at a centre-of-mass energy of 13 TeV. Previous results at 7 and 8 TeV or with a partial data sample are not included in the table. The list of Higgs boson kinematic variables targeted in each case are listed.

Decay mode	Observables	Data set
$\mathrm{H} \to \gamma\gamma$ [530]	$p_{\mathrm{T}}^{\gamma\gamma}$,$n_j$,$\lvert y^{\gamma\gamma}\rvert$,$\lvert\cos(\theta^*)\rvert$, ϕ_η, $n_{\mathrm{b\ jet}}$, n_ℓ, $p_{\mathrm{T}}^{\mathrm{miss}}$, p_{T}^{j1}, $\lvert y_{j1}\rvert$, $\lvert\Delta\phi_{\gamma\gamma,j1}\rvert$, $\lvert\Delta y_{\gamma\gamma,j1}\rvert$, $\mathcal{T}_C^j$, p_{T}^{j2}, $\lvert y_{j2}\rvert$,$\lvert\Delta\Phi_{j1,j2}\rvert$, $\lvert\Delta\Phi_{\gamma\gamma,j1j2}\rvert$, $\lvert\overline{\eta}_{j1j2} - \eta_{\gamma\gamma}\rvert$, m_{jj}, $\lvert\Delta\eta_{j1j2}\rvert$	$137\,\mathrm{fb}^{-1}$
$\mathrm{H} \to \mathrm{ZZ} \to 4\ell$ [531]	$p_{\mathrm{T}}^{\mathrm{H}}$,$\lvert y_{\mathrm{H}}\rvert$, n_j , p_{T}^{j1}, p_{T}^{j2}, m_{jj}, $\Delta\Phi_{jj}$, $\lvert\Delta\eta_{jj}\rvert$, $m_{\mathrm{H}j}$, $p_{\mathrm{T}}^{\mathrm{H}j}$, $p_{\mathrm{T}}^{\mathrm{H}jj}$, $\mathcal{T}_C^{\max}$,$\mathcal{T}_B^{\max}$, m_{Z1},m_{Z2},$\cos\theta^*$,$\cos\theta_1$, $\cos\theta_2$, Φ, Φ_1, D_{0-}^{dec}, $D_{0\mathrm{h}+}^{\mathrm{dec}}$, D_{CP}^{dec}, $D_{\mathrm{int}}^{\mathrm{dec}}$, $D_{\Lambda 1}^{\mathrm{dec}}$, $D_{\Lambda 1}^{\mathrm{Z}\gamma,\mathrm{dec}}$	$138\,\mathrm{fb}^{-1}$
$\mathrm{H} \to \tau\tau$ [532]	$p_{\mathrm{T}}^{\mathrm{H}}$, n_j, p_{T}^{j1}	$137\,\mathrm{fb}^{-1}$
$\mathrm{H} \to \mathrm{WW}$ [533]	$p_{\mathrm{T}}^{\mathrm{H}}$, n_j	$137\,\mathrm{fb}^{-1}$
Boosted $\mathrm{H} \to \mathrm{b\bar{b}}$ [541]	$p_{\mathrm{T}}^{\mathrm{H}}$ ($p_{\mathrm{T}}^{\mathrm{H}} > 450\,\mathrm{GeV}$)	$137\,\mathrm{fb}^{-1}$
Combination $\mathrm{H} \to \gamma\gamma$ $\mathrm{H} \to \mathrm{ZZ}^*$, $\mathrm{H} \to \mathrm{b\bar{b}}$ [543]	$p_{\mathrm{T}}^{\mathrm{H}}$,$n_j$,$y_{\mathrm{H}}$, p_{T}^{j}	$36\,\mathrm{fb}^{-1}$

7.3 Pair production of Higgs bosons

The main mechanisms for Higgs boson pair production at the LHC were shown in Fig. 53. This process has not been observed yet at the LHC because of its very small production cross section. In the SM, Higgs boson pairs are produced at the LHC mainly via ggF, involving either couplings to a loop of virtual fermions, or the λ_{HHH} coupling itself. The LO ggF Feynman diagrams shown in Fig. 53 have approximately the same amplitude but interfere destructively. This yields a very small SM cross section: $\sigma_{\mathrm{ggF}}^{\mathrm{HH}} = 31.05^{+2.1}_{-7.2}$ fb at NNLO precision for a centre-of-mass energy of $\sqrt{s} = 13\,\mathrm{TeV}$ and an m_{H} of 125 GeV [546–553]. The CMS experiment has

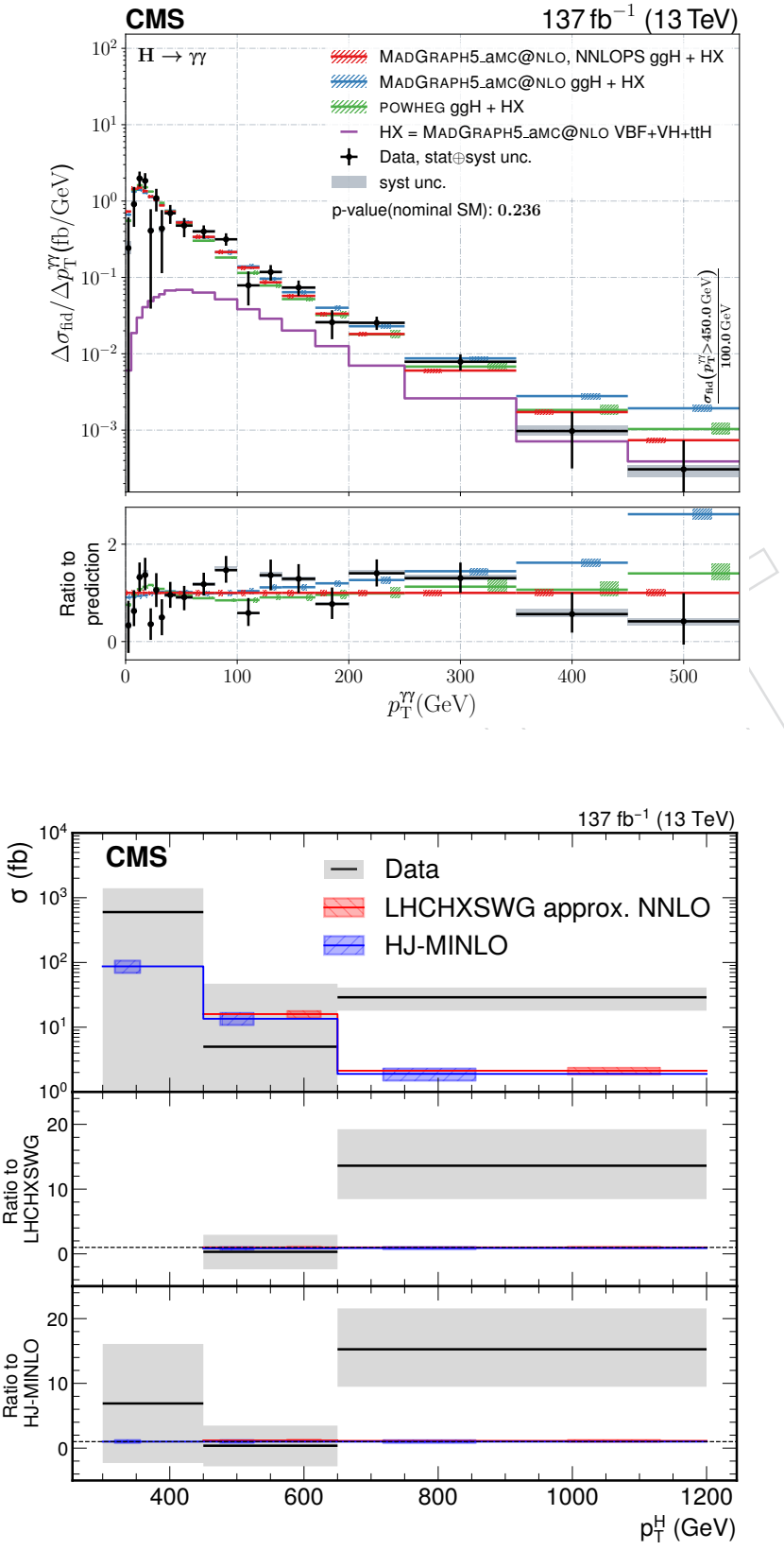

Figure 57: Differential fiducial cross sections for Higgs boson production in the $\mathrm{H} \to \gamma\gamma$ [530] (upper) and $\mathrm{H} \to \mathrm{b\bar{b}}$ [541] (lower) decay channels as functions of the transverse momentum of the Higgs boson $p_{\mathrm{T}}^{\mathrm{H}}$. Figure compiled from Refs. [530, 541].

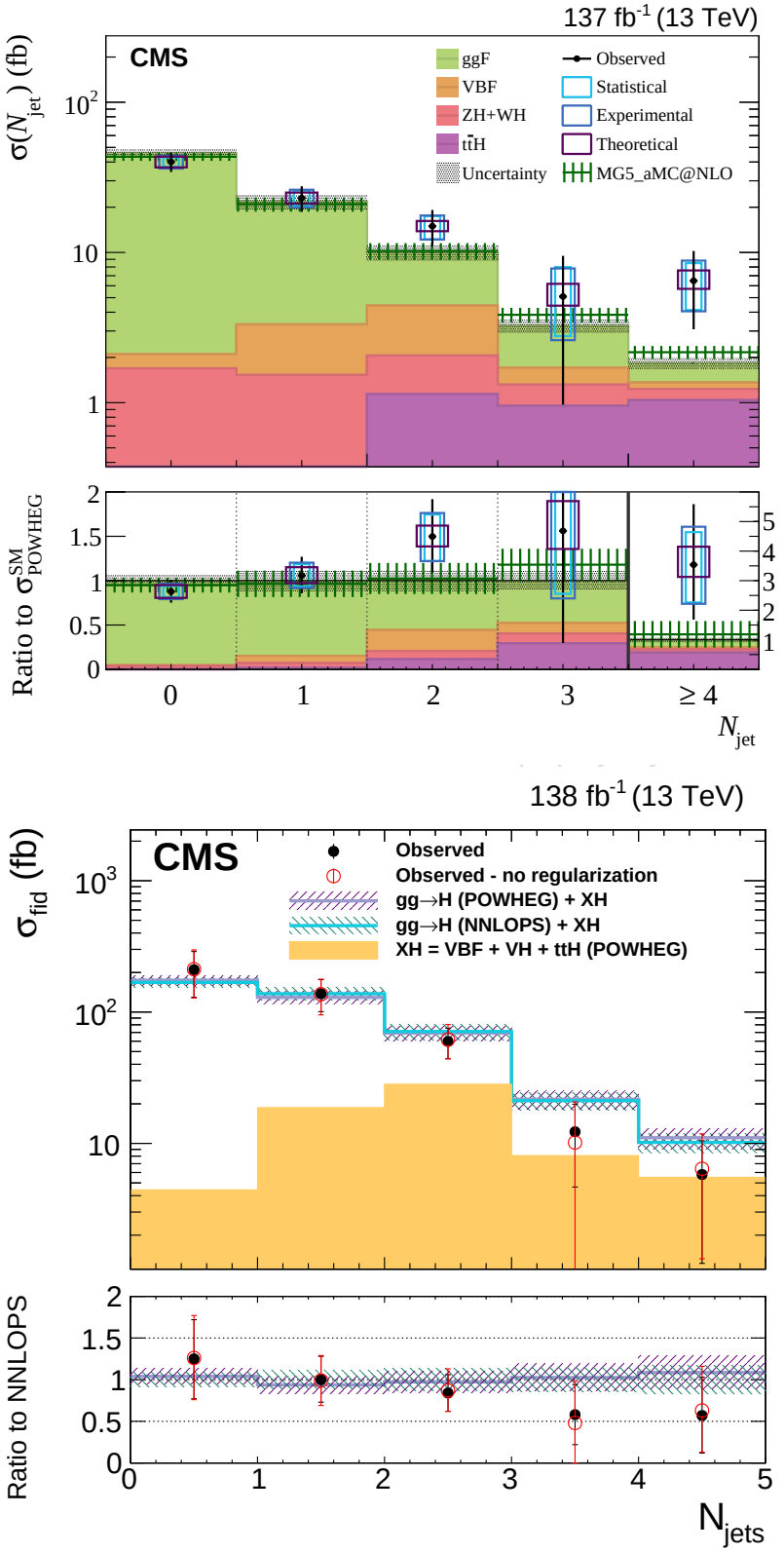

Figure 58: Differential fiducial cross sections for Higgs boson production as functions of the number of jets in the event, for the H $\rightarrow$ WW [533] (upper) and H $\rightarrow \tau\tau$ [532] (lower) decay modes. Figure compiled from Refs. [530, 541].

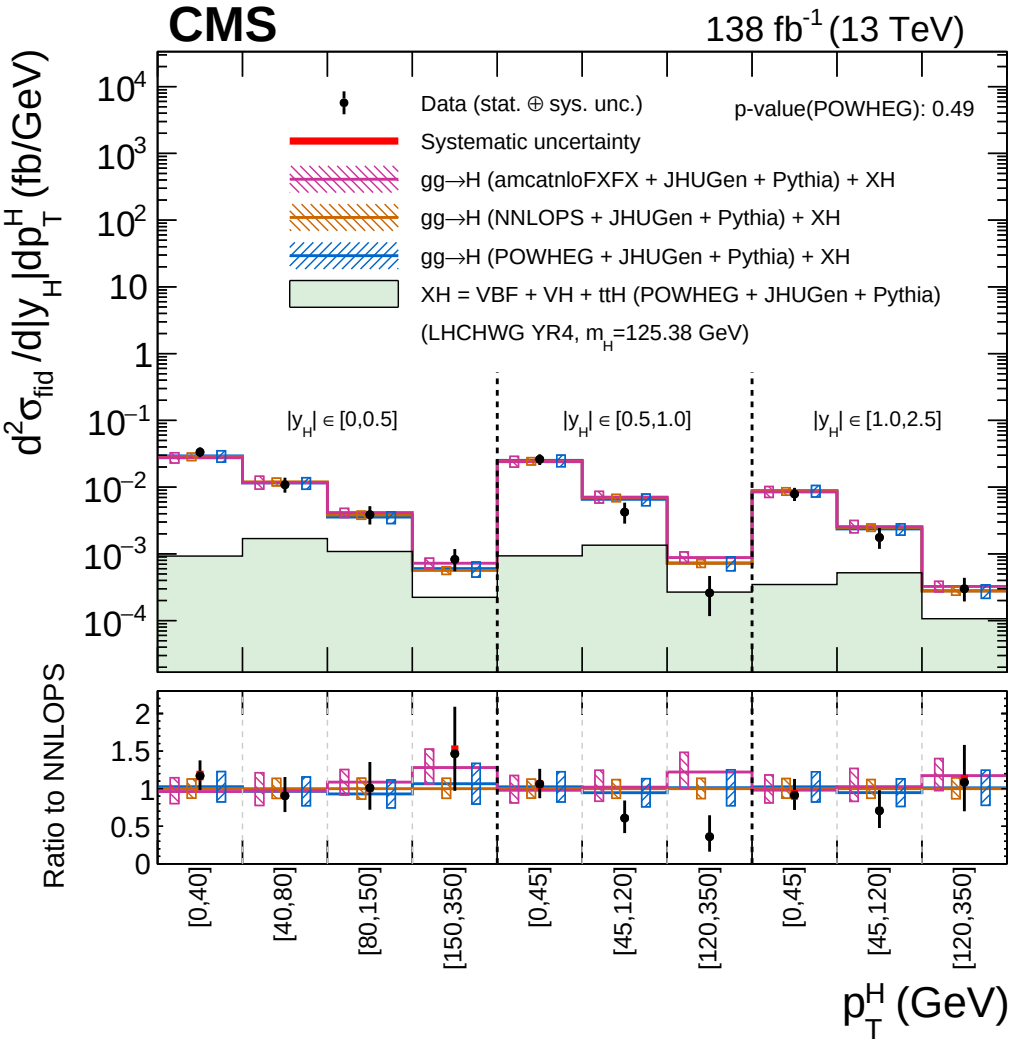

Figure 59: Double-differential cross sections for Higgs boson production in the $H \to ZZ \to 4\ell$ decay channel. The cross section is measured in bins of the rapidity of the Higgs boson $|y_H|$, as a function of the Higgs boosn transverse momentum p_T^H. Figure taken from Ref. [531].

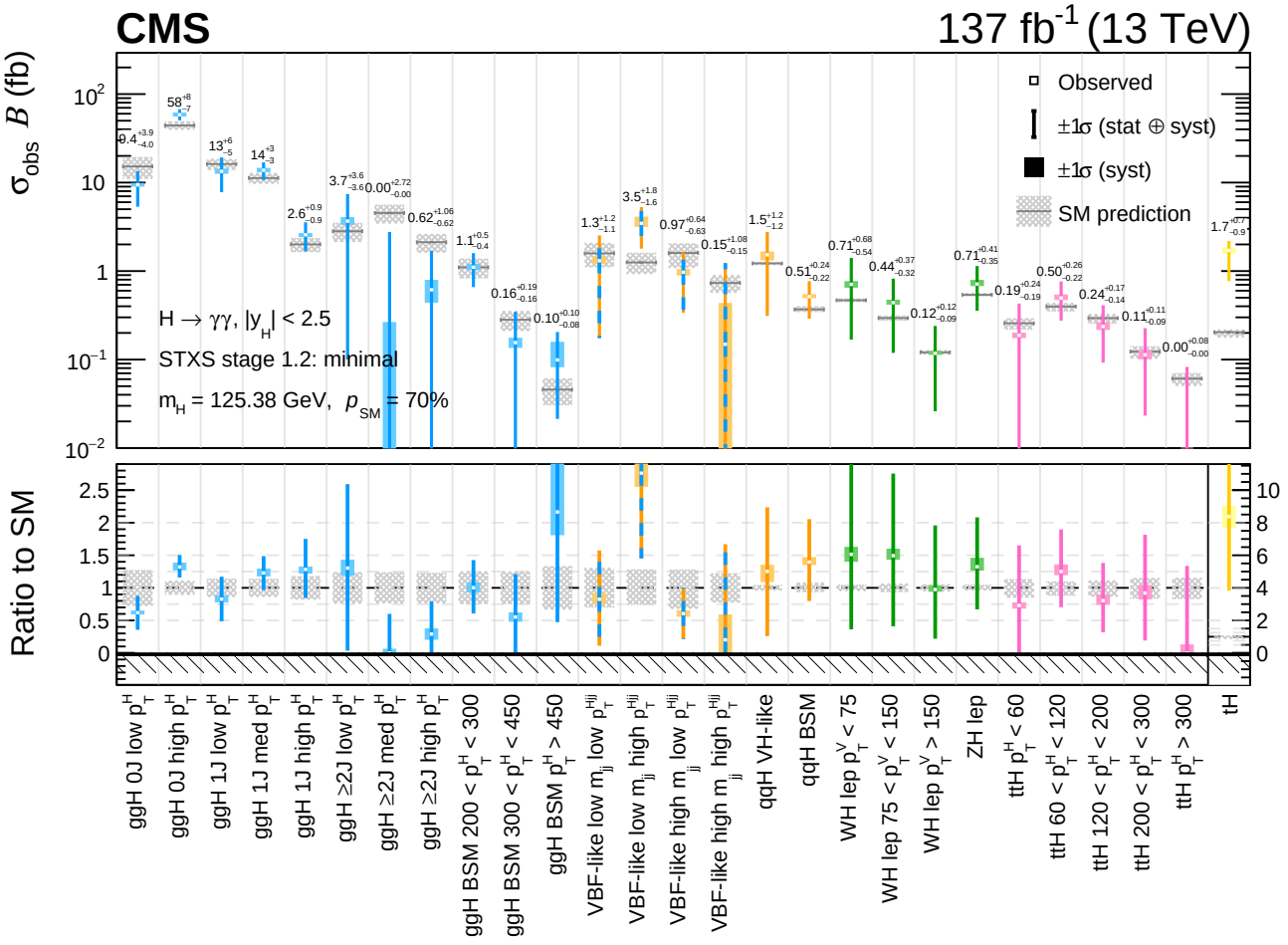

Figure 60: Observed results of the minimal merging scheme STXS fit for H $\rightarrow \gamma\gamma$ at 13 TeV. The best fit cross sections are plotted together with the respective 68% confidence level intervals. Figure taken from Ref. [498].

searched for this production in a variety of final states [515–521] and placed limits at 95% CL on the production cross section and the self-coupling. The most sensitive final states are $HH \to \gamma\gamma b\bar{b}$, $HH \to \tau\tau b\bar{b}$, $HH \to b\bar{b}b\bar{b}$, which benefit from the larger branching fraction of $b\bar{b}$ decays and the identification of the diphoton or ditau pair.

Figure 61 shows the expected and observed limits on Higgs boson pair production, expressed as ratios to the SM expectation, in searches using the different final states and their combination. With the current data set, and combining data from all currently studied modes and channels, the Higgs boson pair production cross section is less than 3.4 times the SM expectation at 95% CL [515].

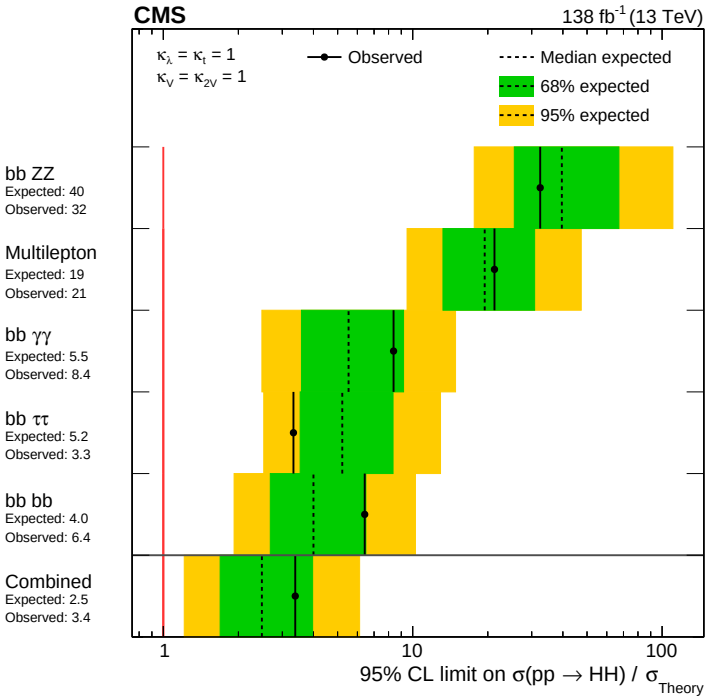

Figure 61: The expected and observed upper limits on the production of Higgs boson pairs. The results are expressed as a ratio to the SM prediction for the cross section ($\sigma(\mathrm{pp} \to \mathrm{HH})/\sigma_{\mathrm{SM}}$). A vertical red line at $\sigma(\mathrm{pp} \to \mathrm{HH})/\sigma_{\mathrm{SM}} = 1$ is drawn to guide the eye. The search modes are ordered, from upper to lower, by their expected sensitivities from the least to the most sensitive. The overall combination of all searches is shown by the lowest entry. Figure taken from Ref. [515].

8 Prospects

The upgraded High-Luminosity LHC machine (HL-LHC), scheduled to start running in 2029, is planned to deliver, over its operational life, an integrated luminosity of 3000 fb^{-1} at a collision energy of $\sqrt{s} = 14$ TeV. This will make available a data sample some 30 times larger than that used in this paper, making possible measurements offering interesting and exciting prospects. In addition, the CMS detector, with its trigger and readout, will be substantially upgraded for HL-LHC running, resulting in important improvements in performance. The larger data set will improve the cross section measurement of processes, where they are currently statistically limited. Constraints on PDFs at high values of x will be improved, providing reduced PDF uncertainties in cross section measurements. The precision to which α_S is known will also be improved. The larger data set will allow more detailed studies of backgrounds and allow

tighter selection to reduce them, increasing the precision of the measurements of processes, where dealing with background contributes significantly to the uncertainty. It will enable a search of BSM particles some 200 GeV beyond their current mass limits in numerous suggested models. A discussion of the physics potential of CMS during the HL-LHC can be found in Refs. [413, 554]. This section presents some of the highlights in terms of future measurements of cross sections and SM parameters.

The remaining unobserved SM EW processes, such as production of ZZZ and VBS ZZ are expected to be observed during LHC Run 3, but during the HL-LHC era the cross section of some VBS final states will be measured with a precision similar to that of current measurements of diboson final states [554]. An interesting prospect for the full HL-LHC data set is the measurement of longitudinal VBS, a key process in establishing the mathematical consistency of the SM, because of the role played by the Higgs boson in regulating its calculated cross section (resulting in its being finite). Projection of the sensitivity for the full HL-LHC data set using simulation of the upgraded CMS Phase-2 detector indicates that a significance greater than 5σ can be expected for longitudinal VBS of $W^{\pm}W^{\pm}$ [555]. The uncertainty in the SM parameters, such as $\sin^2\theta^{\text{eff}}_{\text{lept}}$ will be reduced by a factor which may be as large as 4, due to improved statistical precision and improved constraints on PDFs. More details are reported in Section 6.1.1 of Ref. [554].

The HL-LHC will enable better measurement of rare top quark processes, such as $t\bar{t}t\bar{t}$ production, as discussed in Section 4.1.3 of Ref. [554]. With increased integrated luminosity for heavy ion collisions, the top quark is expected to produce significant results when used as a hard probe for nuclear PDFs, and for exploring the quark-gluon plasma [413, 428, 431].

The HL-LHC will see the reduction of the uncertainties in the cross sections of all Higgs boson production modes, ranging from $< 2\%$ for ggH to about 6% for WH when both ATLAS and CMS results are combined [413]. A factor of 5 reduction is anticipated in the uncertainties in the measurements published so far of Higgs boson couplings to other SM particles. This will enable testing of BSM theories that predict only subtle differences in these couplings from the SM expectation.

The observation of Higgs boson pair production will be a landmark result. This process provides information on the exact shape of the BEH potential and is crucial for the understanding of the EW phase transition that occurred in the early universe, and its consequences [556]. Projection of the $36\,\text{fb}^{-1}$ analyses to $3000\,\text{fb}^{-1}$ has shown that the combination of the CMS and ATLAS data sets could provide a signal significance in excess of 4 standard deviations for HH production [413]. The corresponding precision obtained on the Higgs boson self-coupling would be approximately 50%. The projections do not include all improvements expected from future detector upgrades. With the addition of future analysis developments, it can be hoped that the observation and first measurement of this process will take place during the HL-LHC era.

9 Summary

A wide selection of cross section measurements has been presented from the CMS programme of the quantum chromodynamics, electroweak, top quark, and Higgs physics. Summary plots of electroweak (Fig. 62), electroweak with jets (Fig. 63), top quark (Fig. 64), and Higgs boson (Fig. 65) production cross sections are shown below. No significant deviations from the standard-model (SM) predictions have been found in total or fiducial cross section measurements. Some deviations from the best predictions based on SM physics are found in differential

measurements of difficult-to-model areas of phase space in events where multiple SM particles are produced including both light-flavour QCD jets and massive SM bosons or quarks. There is an expectation that improvements in the modelling of QCD and electroweak physics would result in better agreement in these measurements. These discrepancies present a challenge to improve our ability to model SM physics, rather than a sign of beyond-the-SM physics. Of particular note among the CMS cross section measurements are: the SM single W boson production cross section determined with 1.9% uncertainty; the ratios of W to Z production cross sections measured with 0.35% accuracy; the measurement of the WZ diboson cross section with 3.4% precision; the measurement of the top quark pair production cross section with 3.2% uncertainty; and the measurement of the inclusive Higgs boson production cross section with an uncertainty of 5.7%. The achievement of sub-2% level accuracy in production cross section measurements of massive SM particles is unprecedented at hadron colliders. The exploration of the Higgs boson through cross section measurements with high precision is one of the CMS physics programme's most exciting aspects, and the study of the Higgs boson, currently unique to the LHC, is one of our best prospects for finding signs of new physics. These CMS cross section measurements are an enduring legacy in particle physics.

DRAFT

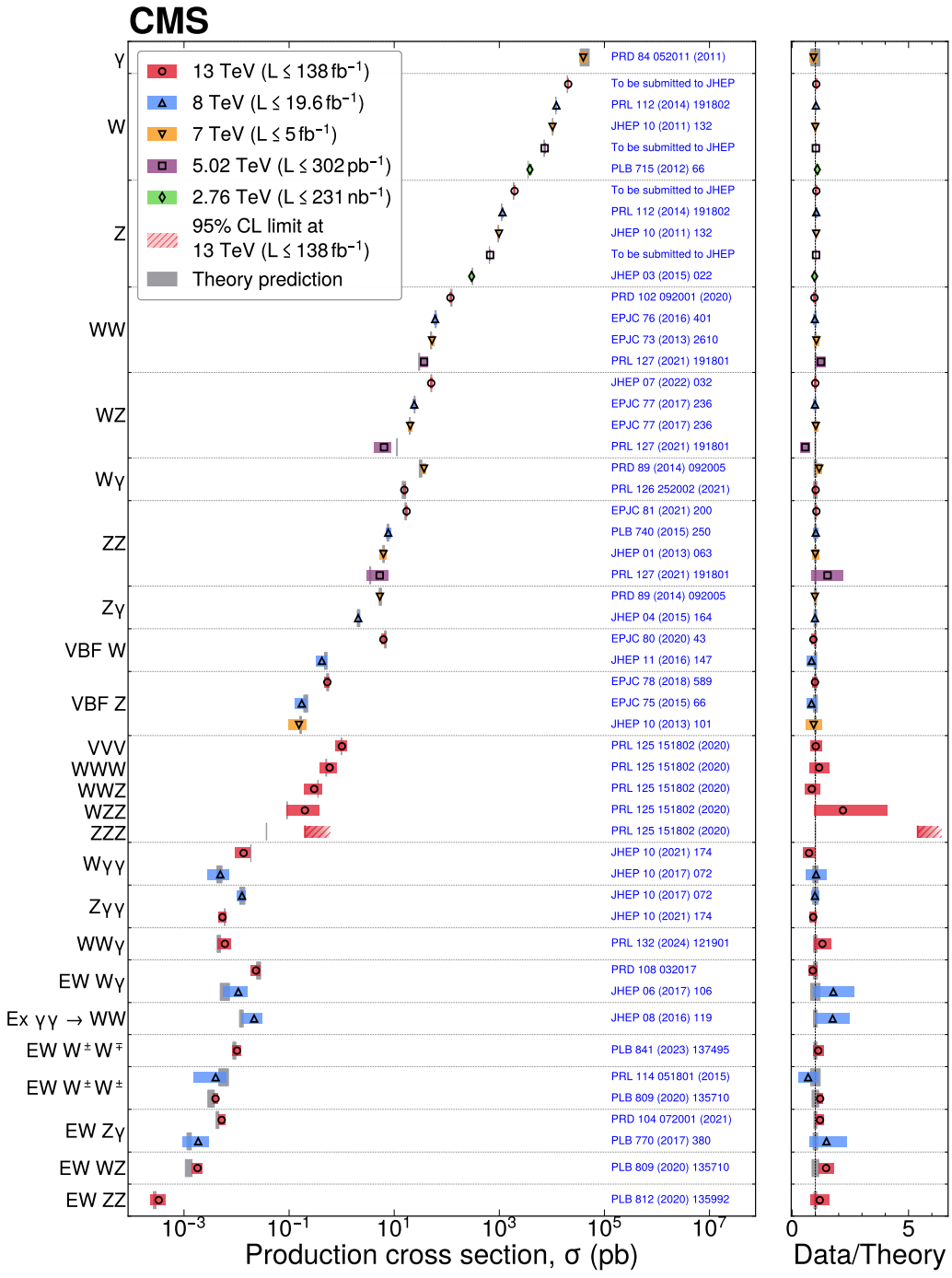

Figure 62: Summary of electroweak cross section measurements. Measurements performed at different LHC pp collision energies are marked by unique symbols and the coloured bands indicate the combined statistical and systematic uncertainty of the measurement. Grey bands indicate the uncertainty of the corresponding SM theory predictions. Shaded hashed bars indicate the excluded cross section region for a production process with the measured 95% C.L. upper limit on the process indicated by the solid line of the same colour.

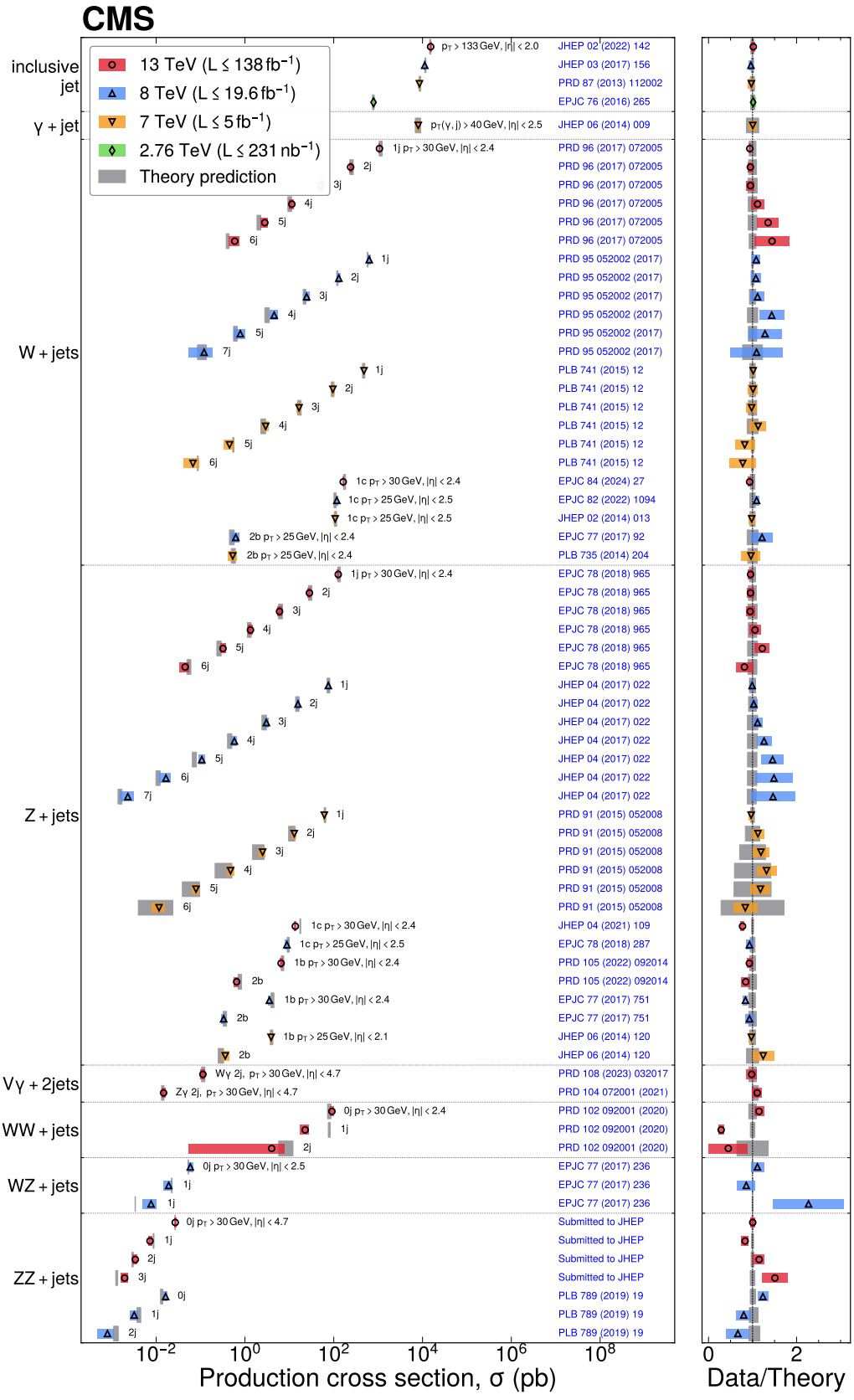

Figure 63: Summary of measurements of jet cross sections and electroweak processes in association with jets.

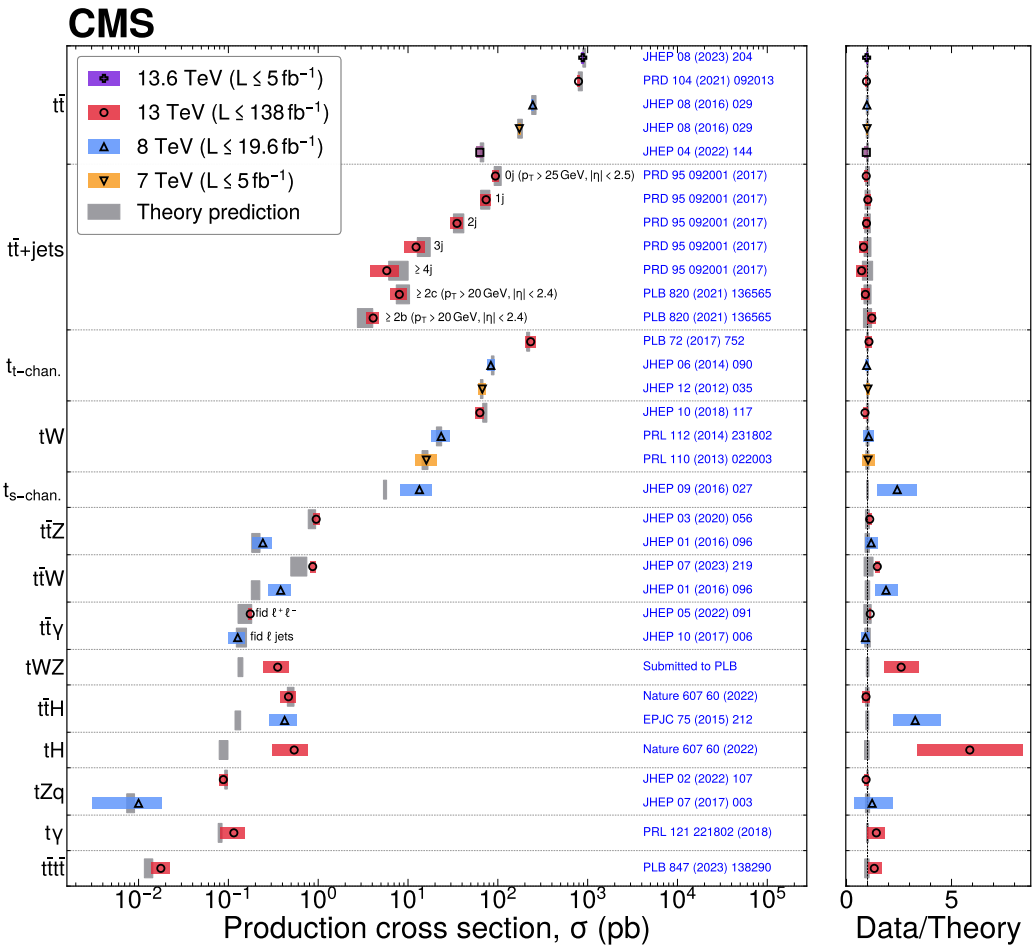

Figure 64: Summary of top quark production cross section measurements.

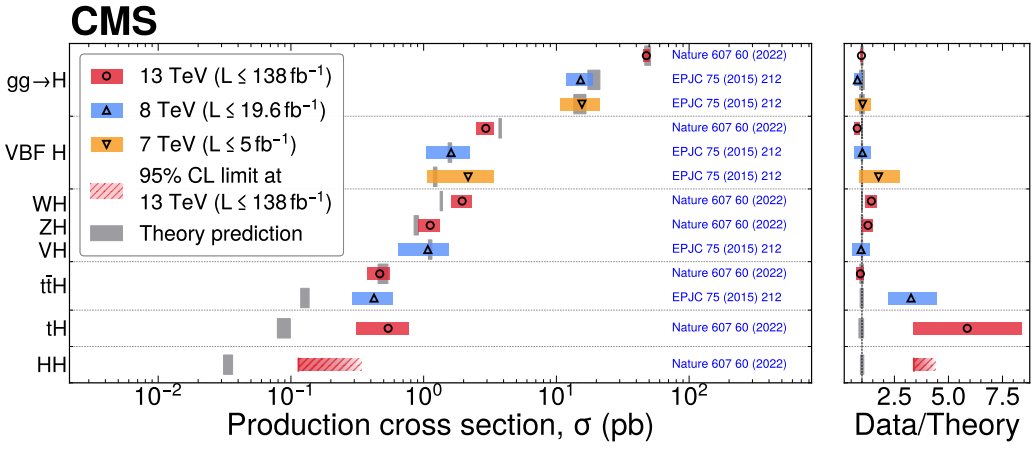

Figure 65: Summary of Higgs boson production cross section measurements.

A Glossary of terms

Abbreviations:

- 4FS: four-flavour scheme (udcs)
- 5FS: five-flavour scheme (udcsb)
- α_S: the strong coupling
- aNNLL: approximate next-to-next-to-leading logarithmic (approximation)
- aQGC: anomalous quartic gauge boson couplings
- aTGC: anomalous triple gauge boson coupling
- BDT: boosted decision tree
- BSM: beyond the standard model
- CA: Cambridge–Aachen jet clustering algorithm
- CERN: Conseil Européen pour la Recherche Nucléaire (English: European Council for Nuclear Research)
- CKM: Cabibbo–Kobayashi–Maskawa
- CMS: Compact Muon Solenoid
- CSV: Combined secondary vertex, a secondary vertex tagger used in CMS analyses
- DEEPCSV: Deep learning based secondary vertex tagger used in CMS analyses
- DIS: deep inelastic scattering
- DPS: double-parton scattering
- DY: Drell–Yan quark-antiquark annihilation forming a virtual photon or Z boson which decays to a charged lepton-antilepton pair. Sometimes also used to refer to the similar process forming a W boson decaying to a lepton-antineutrino pair
- ECAL: electromagnetic calorimeter
- EW: electroweak
- FS: flavour schemes
- FSR: final-state radiation
- ggF: gluon-gluon fusion
- ggH: gluon-gluon fusion Higgs production
- ISR: initial-state radiation
- IVF: inclusive vertex finder, secondary vertex tagger used in CMS analyses
- IP: interaction point
- IP5: interaction point 5, where the CMS experiment is located
- HCAL: hadron calorimeter
- HF: hadron forward calorimeter
- HL LHC: High-Luminosity LHC upgrade
- j: jet, also jj for two jets and jjj for three jets
- JES: jet energy scale
- JER: jet energy resolution
- ℓ: charged lepton, typically an electron or a muon
- LHC: Large Hadron Collider

DRAFT

- LO: leading order, as in calculation in QCD or EW theory
- MC: Monte Carlo
- ME: matrix element
- ML: Machine learning
- MPI: Multiparton interactions
- MVA: Multivariate analysis
- NLL: next-to-leading logarithmic all-order resummation calculations in QCD theory. Typically used with an NLO calculation after matching the calculations to remove any overlaps.
- NLO: next-to-leading order, as in calculation in QCD or EW theory
- NNLL: next-to-next-to-leading logarithmic all order resummation calculations in QCD theory. In principle for use with an NNLO calculation but more often used as an addition to a NLO+NLL calculation.
- NNLO: next-to-next-to-leading order, as in calculation in QCD theory
- nNNLO: NNLO QCD calculations matched to PS showers using the MiNNLO method
- N^3LO: next-to-next-to-next-to-leading order, as in calculation in QCD theory
- NP: Nonperturbative, including underlying event, hadronization, and multiparton interactions
- nPDF: nuclear parton distribution functions
- os or OS: opposite-sign
- PB: Parton branching, as used in parton branching method transverse momentum dependent parton distribution functions PB-TMD PDFs
- PDF: parton (typically quark and gluon) distribution functions
- PF: particle flow, CMS global event reconstruction
- pp: proton-proton
- $p\overline{p}$: proton-antiproton
- pQDC: perturbative quantum chromodynamics
- PS: parton shower
- PU: pileup
- PUPPI: pileup-per-particle identification algorithm
- PV: primary vertex
- Q: momentum or energy transfer between partons in a collision
- QGC: Quartic gauge boson coupling
- QCD: quantum chromodynamics
- QED: quantum electrodynamics
- QGP: quark-gluon plasma
- RGE: renormalization group equation
- RP: Roman pot particle detectors
- sd: standard deviations
- SM: standard model
- SPS: single-parton scattering

DRAFT

- SSV: Simple secondary vertex, a secondary vertex tagger used in CMS analyses
- SV: Secondary vertex where a b or c hadron decays
- ss or SS: same-sign
- SU: special unitary, as in the special unitary groups $SU(2)$ and $SU(3)$
- TGC: triple gauge boson coupling
- TMD: transverse momentum dependent, as used in parton branching method transverse momentum dependent parton distribution functions PB-TMD PDFs
- TPS: triple-parton scattering
- U; unitary, as in the unitary group $U(1)$
- UE: underlying event
- VBF: vector boson fusion
- VBS: vector boson scattering
- x: Bjorken x, momentum fraction of the proton carried by a parton

Units:

- b: barn $= 1 \times 10^{-24}\,\text{cm}^2$
- mb: millibarn $= 1 \times 10^{-3}\,\text{b}$
- μb: microbarn $= 1 \times 10^{-6}\,\text{b}$
- nb: nanobarn $= 1 \times 10^{-9}\,\text{b}$
- pb: picobarn $= 1 \times 10^{-12}\,\text{b}$
- fb: femtobarn $= 1 \times 10^{-15}\,\text{b}$
- eV: electronvolt $= 1.60218 \times 10^{-19}\,\text{J}$; energy gained by an electron traversing a potential difference of 1 V
- keV: kiloelectronvolt $= 1 \times 10^{3}\,\text{eV}$
- MeV: megaelectronvolt $= 1 \times 10^{6}\,\text{eV}$
- GeV: gigaelectronvolt $= 1 \times 10^{9}\,\text{eV}$
- TeV: teraelectronvolt $= 1 \times 10^{12}\,\text{eV}$
- Energy: typically given in GeV
- Momentum: typically given in GeV, which should be understood as GeV/c
- Mass: typically given in GeV, which should be understood as GeV/c^2

Types of uncertainties in cross sections and other measurements:

- (α_S): uncertainties associated with the uncertainty in the strong coupling (α_S) (in this Report types of uncertainties are listed with parenthesis around the type)
- (exp): uncertainties associated with experimental sources
- (fit): fit uncertainty
- (lumi): integrated luminosity uncertainty
- (model) uncertainties associated with a model or comparisons between different models
- (num) numerical uncertainties
- (param): parameter uncertainty

DRAFT

- (PDF): parton distribution function uncertainties
- (scale): factorization and renormalization scale uncertainties
- (stat): statistical uncertainty
- (syst): systematic uncertainty
- (theo): theoretical uncertainty
- (tot): total uncertainty

Monte Carlo simulation programmes and production cross section and related process calculators. More details on the use of simulations for generating physics samples, on detector simulation, and the use of PDFs are given in Section 3.

- 2γNNLO [283]: NNLO diphoton production calculation
- BFG [216]: Bourhis, Fontannazand, Guillet fragmentation functions for quarks and gluons into photons
- BLACKHAT [56]: Monte Carlo programme for automatic calculation of one-loop amplitudes for QCD cross sections
- CA3: CASCADE [85]: Monte Carlo event generator based on transverse momentum dependent (TMD) parton distribution functions
- COMIX [93]: matrix element generator typically used with SHERPA
- COMPHEP [57]: automatic calculation in high-energy physics from Lagrangians to collision events or particle decays
- CSSHOWER [94]: parton shower programme based on the Catani–Seymour dipole factorization, typically used with SHERPA
- DGLAP: Dokshitzer–Gribov–Lipatov–Altarelli–Parisi [167–174] QCD evolution equations that describe the variation of PDFs with the energy scale
- DYTURBO [38]: fast predictions for Drell–Yan processes at NNLO and N^3LO
- FEWZ [39–41]: Fully Exclusive W and Z production generator
- γ + jet [42, 43]: NLL calculation of photon plus jet cross sections
- GEANT4 [97]: toolkit for simulation of the passage of particles through matter used for full detector simulations
- GENEVA [244, 245]: Monte Carlo programme that combines NNLO matrix element calculations with NNLL-accuracy resummation
- HATHOR [370, 371]: HAdronic Top and Heavy quarks crOss section calculatoR Monte Carlo programme
- HELAC-ONIA [44, 45]: onia production Monte Carlo generator
- HERWIG and HERWIG++ [86, 87]: general-purpose Monte Carlo generator
- HJ-MINLO [58–60]: programme for precise predictions for Lorentz-boosted Higgs boson production
- JETPHOX [215]: NLO photon production programme
- JHUGEN [61–65]: programme for simulating Higgs boson decays with full angular correlations
- MADGRAPH 5 or MG5 and MADGRAPH5_aMC@NLO or MG5_aMC [70, 440]: automated computation of tree-level and NLO differential cross sections, matched to parton shower simulations

DRAFT

- MATRIX [46]: Munich Automates qT-subtraction and Resummation to Integrate X-sections, fully automated NNLO QCD and NLO EW calculator
- MCFM [66]: parton-level Monte Carlo programme at NLO, NNLO, and N^{3}LO in QCD
- MiNNLO [309]: nNNLO Monte Carlo simulation with NNLO QCD calculations matched to parton showers using the MiNNLO method
- NLOJET++ [48, 49] and FASTNLO [50, 51]: 3-jet NLO QCD calculator
- NLLJET [47]: next-to-leading logarthmic cross section calculator for jet production
- NNLOJET [52–54]: NNLO QCD calcualtor for single jet inclusive production
- NNLOPS [71–73]: NNLO matched to parton shower simulation of Higgs boson production
- OPENLOOPS [74–77]: matrix element calculator, typically used with SHERPA for NLO+EW accuracy simulations
- PHOJET [88]: Monte Carlo programme for generating processes with large rapidity gaps
- PHOTOS [78]: Monte Carlo programme for precision simulation of QED radiation in decays. Used for description of final-state radiation
- POWHEG and POWHEG BPX [79–81]: matching NLO QCD computations with parton shower simulations
- PYTHIA 6.4 [89], 8.1 [90], 8.2 [91], Py: general-purpose LO Monte Carlo generator with simulation of parton showers, underlying event, and hadronization [91]
- SHERPA versions 1 and 2 [92]: general-purpose Monte Carlo generator
- PB-TMD PDFs: transverse momentum dependent parton distribution functions [120] based on the parton branching method [121, 122]
- VBFNL0 VBFNL0 2.7 [82–84]: NLO vector boson fusion and vector boson scattering cross section Monte Carlo calculator

Acknowledgments

References

[1] CMS Collaboration, "Precision luminosity measurement in proton-proton collisions at $\sqrt{s} = 13$ TeV in 2015 and 2016 at CMS", *Eur. Phys. J. C* **81** (2021) 800, doi:10.1140/epjc/s10052-021-09538-2, arXiv:2104.01927.

[2] CMS Collaboration, "CMS luminosity measurement for the 2017 data-taking period at $\sqrt{s} = 13$ TeV", CMS Physics Analysis Summary CMS-PAS-LUM-17-004, 2018.

[3] CMS Collaboration, "CMS luminosity measurement for the 2018 data-taking period at $\sqrt{s} = 13$ TeV", CMS Physics Analysis Summary CMS-PAS-LUM-18-002, 2019.

[4] CMS Collaboration, "Absolute calibration of the luminosity measurement at CMS: winter 2012 update", CMS Physics Analysis Summary CMS-PAS-SMP-12-008, 2012.

[5] CMS Collaboration, "CMS luminosity based on pixel cluster counting - summer 2013 update", CMS Physics Analysis Summary CMS-PAS-LUM-13-001, 2013.

DRAFT

[6] CMS Collaboration, "Luminosity measurement in proton-proton collisions at 13.6 TeV in 2022 at CMS", CMS Physics Analysis Summary CMS-PAS-LUM-22-001, 2024.

[7] V. Andreev et al., "Performance studies of a full-length prototype for the CASTOR forward calorimeter at the CMS experiment", *Eur. Phys. J. C* **67** (2010) 601, doi:10.1140/epjc/s10052-010-1316-4.

[8] M. Albrow et al., "CMS-TOTEM precision proton spectrometer", technical report, 2014.

[9] CMS Collaboration, "The CMS experiment at the CERN LHC", *JINST* **3** (2008) S08004, doi:10.1088/1748-0221/3/08/S08004.

[10] CMS Collaboration, "Development of the CMS detector for the CERN LHC Run 3", 2023. arXiv:2309.05466. Accepted by *JINST*.

[11] CMS Collaboration, "Performance of the CMS Level-1 trigger in proton-proton collisions at $\sqrt{s} = 13$ TeV", *JINST* **15** (2020) P10017, doi:10.1088/1748-0221/15/10/P10017, arXiv:2006.10165.

[12] CMS Collaboration, "The CMS trigger system", *JINST* **12** (2017) P01020, doi:10.1088/1748-0221/12/01/P01020, arXiv:1609.02366.

[13] CMS Collaboration, "Particle-flow reconstruction and global event description with the CMS detector", *JINST* **12** (2017) P10003, doi:10.1088/1748-0221/12/10/P10003, arXiv:1706.04965.

[14] CMS Collaboration, "Performance of electron reconstruction and selection with the CMS detector in proton-proton collisions at $\sqrt{s} = 8$ TeV", *JINST* **10** (2015) P06005, doi:10.1088/1748-0221/10/06/P06005, arXiv:1502.02701.

[15] CMS Collaboration, "Electron and photon reconstruction and identification with the CMS experiment at the CERN LHC", *JINST* **16** (2021) P05014, doi:10.1088/1748-0221/16/05/P05014, arXiv:2012.06888.

[16] CMS Collaboration, "ECAL 2016 refined calibration and Run 2 summary plots", CMS Detector Performance Note CMS-DP-2020-021, 2020.

[17] CMS Collaboration, "Performance of photon reconstruction and identification with the CMS detector in proton-proton collisions at $\sqrt{s} = 8$ TeV", *JINST* **10** (2015) P08010, doi:10.1088/1748-0221/10/08/P08010, arXiv:1502.02702.

[18] CMS Collaboration, "A measurement of the Higgs boson mass in the diphoton decay channel", *Phys. Lett. B* **805** (2020) 135425, doi:10.1016/j.physletb.2020.135425, arXiv:2002.06398.

[19] CMS Collaboration, "Performance of CMS muon reconstruction in pp collision events at $\sqrt{s} = 7$ TeV", *JINST* **7** (2012) P10002, doi:10.1088/1748-0221/7/10/P10002, arXiv:1206.4071.

[20] CMS Collaboration, "Performance of the CMS muon detector and muon reconstruction with proton-proton collisions at $\sqrt{s} = 13$ TeV", *JINST* **13** (2018) P06015, doi:10.1088/1748-0221/13/06/P06015, arXiv:1804.04528.

[21] CMS Collaboration, "Performance of reconstruction and identification of τ leptons decaying to hadrons and ν_τ in pp collisions at $\sqrt{s} = 13$ TeV", *JINST* **13** (2018) P10005, doi:10.1088/1748-0221/13/10/P10005, arXiv:1809.02816.

DRAFT

[22] CMS Collaboration, "Identification of hadronic tau lepton decays using a deep neural network", *JINST* **17** (2022) P07023, doi:10.1088/1748-0221/17/07/P07023, arXiv:2201.08458.

[23] CMS Collaboration, "Technical proposal for the Phase II upgrade of the Compact Muon Solenoid", CMS Technical Proposal CERN-LHCC-2015-010, CMS-TDR-15-02, 2015.

[24] M. Cacciari, G. P. Salam, and G. Soyez, "The anti-k_{T} jet clustering algorithm", *JHEP* **04** (2008) 063, doi:10.1088/1126-6708/2008/04/063, arXiv:0802.1189.

[25] M. Cacciari, G. P. Salam, and G. Soyez, "FastJet user manual", *Eur. Phys. J. C* **72** (2012) 1896, doi:10.1140/epjc/s10052-012-1896-2, arXiv:1111.6097.

[26] CMS Collaboration, "Jet energy scale and resolution in the CMS experiment in pp collisions at 8 TeV", *JINST* **12** (2017) P02014, doi:10.1088/1748-0221/12/02/P02014, arXiv:1607.03663.

[27] CMS Collaboration, "Jet algorithms performance in 13 TeV data", CMS Physics Analysis Summary CMS-PAS-JME-16-003, 2017.

[28] CMS Collaboration, "Pileup mitigation at CMS in 13 TeV data", *JINST* **15** (2020) P09018, doi:10.1088/1748-0221/15/09/P09018, arXiv:2003.00503.

[29] D. Bertolini, P. Harris, M. Low, and N. Tran, "Pileup per particle identification", *JHEP* **10** (2014) 059, doi:10.1007/JHEP10(2014)059, arXiv:1407.6013.

[30] CMS Collaboration, "Performance of missing transverse momentum reconstruction in proton-proton collisions at $\sqrt{s} = 13$ TeV using the CMS detector", *JINST* **14** (2019) P07004, doi:10.1088/1748-0221/14/07/P07004, arXiv:1903.06078.

[31] CMS Collaboration, "Identification of b-quark jets with the CMS experiment", *JINST* **8** (2013) P04013, doi:10.1088/1748-0221/8/04/P04013, arXiv:1211.4462.

[32] CMS Collaboration, "Measurement of the cross section and angular correlations for associated production of a Z boson with b hadrons in pp collisions at $\sqrt{s} = 7$ TeV", *JHEP* **12** (2013) 039, doi:10.1007/JHEP12(2013)039, arXiv:1310.1349.

[33] CMS Collaboration, "Measurement of $\mathrm{B\overline{B}}$ angular correlations based on secondary vertex reconstruction at $\sqrt{s} = 7$ TeV", *JHEP* **03** (2011) 136, doi:10.1007/JHEP03(2011)136, arXiv:1102.3194.

[34] CMS Collaboration, "Performance of b tagging at $\sqrt{s} = 8$ TeV in multijet, $\mathrm{t\bar{t}}$ and boosted topology events", technical report, 2013.

[35] CMS Collaboration, "Identification of heavy-flavour jets with the CMS detector in pp collisions at 13 TeV", *JINST* **13** (2018) P05011, doi:10.1088/1748-0221/13/05/P05011, arXiv:1712.07158.

[36] CMS Collaboration, "A new calibration method for charm jet identification validated with proton-proton collision events at $\sqrt{s}$ =13 TeV", *JINST* **17** (2022) P03014, doi:10.1088/1748-0221/17/03/P03014, arXiv:2111.03027.

[37] CMS Collaboration, "Extraction and validation of a new set of CMS PYTHIA8 tunes from underlying-event measurements", *Eur. Phys. J. C* **80** (2020) 4, doi:10.1140/epjc/s10052-019-7499-4, arXiv:1903.12179.

DRAFT

[38] S. Camarda et al., "DYTurbo: Fast predictions for Drell-Yan processes", *Eur. Phys. J. C* **80** (2020) 251, doi:10.1140/epjc/s10052-020-7757-5, arXiv:1910.07049. [Erratum: Eur.Phys.J.C 80 (2020) 440].

[39] K. Melnikov and F. Petriello, "The W boson production cross section at the LHC through $O(\alpha_s^2)$", *Phys. Rev. Lett.* **96** (2006) 231803, doi:10.1103/PhysRevLett.96.231803, arXiv:hep-ph/0603182.

[40] K. Melnikov and F. Petriello, "Electroweak gauge boson production at hadron colliders through $O(\alpha_s^2)$", *Phys. Rev. D* **74** (2006) 114017, doi:10.1103/PhysRevD.74.114017, arXiv:hep-ph/0609070.

[41] R. Gavin, Y. Li, F. Petriello, and S. Quackenbush, "FEWZ 2.0: A code for hadronic Z production at next-to-next-to-leading order", *Comput. Phys. Commun.* **182** (2011) 2388, doi:10.1016/j.cpc.2011.06.008, arXiv:1011.3540.

[42] H. Baer, J. Ohnemus, and J. F. Owens, "A calculation of the direct photon plus jet cross-section in the next-to-leading logarithm approximation", *Phys. Lett. B* **234** (1990) 127, doi:10.1016/0370-2693(90)92015-B.

[43] H. Baer, J. Ohnemus, and J. F. Owens, "A next-to-leading logarithm calculation of direct photon production", *Phys. Rev. D* **42** (1990) 61, doi:10.1103/PhysRevD.42.61.

[44] H.-S. Shao, "HELAC-Onia: An automatic matrix element generator for heavy quarkonium physics", *Comput. Phys. Commun.* **184** (2013) 2562, doi:10.1016/j.cpc.2013.05.023, arXiv:1212.5293.

[45] H.-S. Shao, "HELAC-Onia 2.0: an upgraded matrix-element and event generator for heavy quarkonium physics", *Comput. Phys. Commun.* **198** (2016) 238, doi:10.1016/j.cpc.2015.09.011, arXiv:1507.03435.

[46] M. Grazzini, S. Kallweit, and M. Wiesemann, "Fully differential NNLO computations with MATRIX", *Eur. Phys. J. C* **78** (2018) 537, doi:10.1140/epjc/s10052-018-5771-7, arXiv:1711.06631.

[47] X. Liu, S.-O. Moch, and F. Ringer, "Phenomenology of single-inclusive jet production with jet radius and threshold resummation", *Phys. Rev. D* **97** (2018) 056026, doi:10.1103/PhysRevD.97.056026, arXiv:1801.07284.

[48] Z. Nagy, "Three jet cross-sections in hadron hadron collisions at next-to-leading order", *Phys. Rev. Lett.* **88** (2002) 122003, doi:10.1103/PhysRevLett.88.122003, arXiv:hep-ph/0110315.

[49] Z. Nagy, "Next-to-leading order calculation of three jet observables in hadron hadron collision", *Phys. Rev. D* **68** (2003) 094002, doi:10.1103/PhysRevD.68.094002, arXiv:hep-ph/0307268.

[50] T. Kluge, K. Rabbertz, and M. Wobisch, "FastNLO: Fast pQCD calculations for PDF fits", in *14th International Workshop on Deep Inelastic Scattering*, p. 483. 2006. arXiv:hep-ph/0609285. doi:10.1142/9789812706706_0110.

[51] fastNLO Collaboration, D. Britzger, K. Rabbertz, F. Stober, and M. Wobisch, "New features in version 2 of the fastNLO project", in *20th International Workshop on Deep-Inelastic Scattering and Related Subjects*, p. 217. 2012. arXiv:1208.3641. doi:10.3204/DESY-PROC-2012-02/165.

DRAFT

[52] J. Currie, E. W. N. Glover, and J. Pires, "Next-to-next-to leading order QCD predictions for single jet inclusive production at the LHC", *Phys. Rev. Lett.* **118** (2017) 072002, doi:10.1103/PhysRevLett.118.072002, arXiv:1611.01460.

[53] J. Currie et al., "Infrared sensitivity of single jet inclusive production at hadron colliders", *JHEP* **10** (2018) 155, doi:10.1007/JHEP10(2018)155, arXiv:1807.03692.

[54] T. Gehrmann et al., "Jet cross sections and transverse momentum distributions with NNLOJET", *PoS* **RADCOR2017** (2018) 074, doi:10.22323/1.290.0074, arXiv:1801.06415.

[55] M. Schönherr et al., "NLO QCD+EW for V+jets", *PoS* **LHCP2016** (2016) 058, doi:10.22323/1.276.0058, arXiv:1609.01445.

[56] C. F. Berger et al., "One-loop calculations with BlackHat", *Nucl. Phys. B Proc. Suppl.* **183** (2008) 313, doi:10.1016/j.nuclphysbps.2008.09.123, arXiv:0807.3705.

[57] E. E. Boos et al., "Automatic calculation in high-energy physics by Grace/Chanel and CompHEP", *Int. J. Mod. Phys. C* **5** (1994) 615, doi:10.1142/S0129183194000787.

[58] G. Luisoni, P. Nason, C. Oleari, and F. Tramontano, "$HW^{\pm}$/HZ + 0 and 1 jet at NLO with the POWHEG BOX interfaced to GoSam and their merging within MiNLO", *JHEP* **10** (2013) 1, doi:10.1007/JHEP10(2013)083, arXiv:1306.2542.

[59] K. Hamilton, P. Nason, C. Oleari, and G. Zanderighi, "Merging H/W/Z + 0 and 1 jet at NLO with no merging scale: a path to parton shower + NNLO matching", *JHEP* **05** (2013) 082, doi:10.1007/JHEP05(2013)082, arXiv:1212.4504.

[60] K. Becker et al., "Precise predictions for boosted Higgs production", CERN theory report CERN-TH-2020-074, 2020. arXiv:2005.07762.

[61] Y. Gao et al., "Spin determination of single-produced resonances at hadron colliders", *Phys. Rev. D* **81** (2010) 075022, doi:10.1103/PhysRevD.81.075022, arXiv:1001.3396. [Erratum: doi:10.1103/PhysRevD.81.079905].

[62] S. Bolognesi et al., "On the spin and parity of a single-produced resonance at the LHC", *Phys. Rev. D* **86** (2012) 095031, doi:10.1103/PhysRevD.86.095031, arXiv:1208.4018.

[63] I. Anderson et al., "Constraining anomalous *HVV* interactions at proton and lepton colliders", *Phys. Rev. D* **89** (2014) 035007, doi:10.1103/PhysRevD.89.035007, arXiv:1309.4819.

[64] A. V. Gritsan, R. Röntsch, M. Schulze, and M. Xiao, "Constraining anomalous Higgs boson couplings to the heavy flavor fermions using matrix element techniques", *Phys. Rev. D* **94** (2016) 055023, doi:10.1103/PhysRevD.94.055023, arXiv:1606.03107.

[65] A. V. Gritsan et al., "New features in the JHU generator framework: constraining Higgs boson properties from on-shell and off-shell production", *Phys. Rev. D* **102** (2020) 056022, doi:10.1103/PhysRevD.102.056022, arXiv:2002.09888.

DRAFT

[66] J. M. Campbell and R. K. Ellis, "MCFM for the Tevatron and the LHC", *Nucl. Phys. B Proc. Suppl.* **205-206** (2010) 10, doi:10.1016/j.nuclphysbps.2010.08.011, arXiv:1007.3492.

[67] J. M. Campbell, R. K. Ellis, and C. Williams, "Vector boson pair production at the LHC", *JHEP* **07** (2011) 018, doi:10.1007/JHEP07(2011)018, arXiv:1105.0020.

[68] J. Alwall et al., "MadGraph 5: going beyond", *JHEP* **06** (2011) 128, doi:10.1007/JHEP06(2011)128, arXiv:1106.0522.

[69] M. Wiesemann et al., "Higgs production in association with bottom quarks", *JHEP* **02** (2015) 132, doi:10.1007/JHEP02(2015)132, arXiv:1409.5301.

[70] J. Alwall et al., "The automated computation of tree-level and next-to-leading order differential cross sections, and their matching to parton shower simulations", *JHEP* **07** (2014) 079, doi:10.1007/JHEP07(2014)079, arXiv:1405.0301.

[71] K. Hamilton, P. Nason, E. Re, and G. Zanderighi, "NNLOPS simulation of Higgs boson production", *JHEP* **10** (2013) 222, doi:10.1007/JHEP10(2013)222, arXiv:1309.0017.

[72] K. Hamilton, P. Nason, and G. Zanderighi, "MINLO: Multi scale improved NLO", *JHEP* **10** (2012) 155, doi:10.1007/JHEP10(2012)155, arXiv:1206.3572.

[73] A. Kardos, P. Nason, and C. Oleari, "Three-jet production in POWHEG", *JHEP* **04** (2014) 043, doi:10.1007/JHEP04(2014)043, arXiv:1402.4001.

[74] F. Buccioni et al., "OpenLoops 2", *Eur. Phys. J. C* **79** (2019) 866, doi:10.1140/epjc/s10052-019-7306-2, arXiv:1907.13071.

[75] A. Denner, S. Dittmaier, and L. Hofer, "Collier: a Fortran-based complex one-loop library in extended regularizations", *Comput. Phys. Commun.* **212** (2017) 220, doi:10.1016/j.cpc.2016.10.013, arXiv:1604.06792.

[76] G. Ossola, C. G. Papadopoulos, and R. Pittau, "CutTools: A program implementing the OPP reduction method to compute one-loop amplitudes", *JHEP* **03** (2008) 042, doi:10.1088/1126-6708/2008/03/042, arXiv:0711.3596.

[77] A. van Hameren, "OneLOop: For the evaluation of one-loop scalar functions", *Comput. Phys. Commun.* **182** (2011) 2427, doi:10.1016/j.cpc.2011.06.011, arXiv:1007.4716.

[78] P. Golonka and Z. Was, "PHOTOS Monte Carlo: A precision tool for QED corrections in Z and W decays", *Eur. Phys. J. C* **45** (2006) 97, doi:10.1140/epjc/s2005-02396-4, arXiv:hep-ph/0506026.

[79] P. Nason, "A new method for combining NLO QCD with shower Monte Carlo algorithms", *JHEP* **11** (2004) 040, doi:10.1088/1126-6708/2004/11/040, arXiv:hep-ph/0409146.

[80] S. Frixione, P. Nason, and C. Oleari, "Matching NLO QCD computations with parton shower simulations: the POWHEG method", *JHEP* **11** (2007) 070, doi:10.1088/1126-6708/2007/11/070, arXiv:0709.2092.

DRAFT

[81] S. Alioli, P. Nason, C. Oleari, and E. Re, "A general framework for implementing NLO calculations in shower Monte Carlo programs: the POWHEG BOX", *JHEP* **06** (2010) 043, doi:10.1007/JHEP06(2010)043, arXiv:1002.2581.

[82] K. Arnold et al., "VBFNLO: A parton level Monte Carlo for processes with electroweak bosons", *Comput. Phys. Commun.* **180** (2009) 1661, doi:10.1016/j.cpc.2009.03.006, arXiv:0811.4559.

[83] J. Baglio et al., "Release note – VBFNLO 2.7.0", (2014) arXiv:1404.3940.

[84] J. Baglio et al., "VBFNLO: A parton level Monte Carlo for processes with electroweak bosons – Manual for version 2.7.0", arXiv:1107.4038.

[85] CASCADE Collaboration, "CASCADE3 A Monte Carlo event generator based on TMDs", *Eur. Phys. J. C* **81** (2021) 425, doi:10.1140/epjc/s10052-021-09203-8, arXiv:2101.10221.

[86] M. Bahr et al., "Herwig++ physics and manual", *Eur. Phys. J. C* **58** (2008) 639, doi:10.1140/epjc/s10052-008-0798-9, arXiv:0803.0883.

[87] J. Bellm et al., "Herwig 7.0/Herwig++ 3.0 release note", *Eur. Phys. J. C* **76** (2016) 196, doi:10.1140/epjc/s10052-016-4018-8, arXiv:1512.01178.

[88] F. W. Bopp, R. Engel, and J. Ranft, "Rapidity gaps and the PHOJET Monte Carlo", in *LAFEX International School on High-Energy Physics (LISHEP 98) Session A: Particle Physics for High School Teachers - Session B: Advanced School in HEP - Session C: Workshop on Diffractive Physics*, p. 729. 1998. arXiv:hep-ph/9803437.

[89] T. Sjöstrand, S. Mrenna, and P. Z. Skands, "PYTHIA 6.4 physics and manual", *JHEP* **05** (2006) 026, doi:10.1088/1126-6708/2006/05/026, arXiv:hep-ph/0603175.

[90] T. Sjöstrand, S. Mrenna, and P. Z. Skands, "A brief introduction to PYTHIA 8.1", *Comput. Phys. Commun.* **178** (2008) 852, doi:10.1016/j.cpc.2008.01.036, arXiv:0710.3820.

[91] T. Sjöstrand et al., "An introduction to PYTHIA 8.2", *Comput. Phys. Commun.* **191** (2015) 159, doi:10.1016/j.cpc.2015.01.024, arXiv:1410.3012.

[92] T. Gleisberg et al., "Event generation with SHERPA 1.1", *JHEP* **02** (2009) 007, doi:10.1088/1126-6708/2009/02/007, arXiv:0811.4622.

[93] T. Gleisberg and S. Hoeche, "Comix, a new matrix element generator", *JHEP* **12** (2008) 039, doi:10.1088/1126-6708/2008/12/039, arXiv:0808.3674.

[94] S. Schumann and F. Krauss, "A parton shower algorithm based on Catani-Seymour dipole factorisation", *JHEP* **03** (2008) 038, doi:10.1088/1126-6708/2008/03/038, arXiv:0709.1027.

[95] S. Hoeche, F. Krauss, S. Schumann, and F. Siegert, "QCD matrix elements and truncated showers", *JHEP* **05** (2009) 053, doi:10.1088/1126-6708/2009/05/053, arXiv:0903.1219.

[96] Sherpa Collaboration, "Event generation with Sherpa 2.2", *SciPost Phys.* **7** (2019) 034, doi:10.21468/SciPostPhys.7.3.034, arXiv:1905.09127.

DRAFT

[97] GEANT4 Collaboration, "GEANT4 – a simulation toolkit", *Nucl. Instrum. Meth. A* **506** (2003) 250, doi:10.1016/S0168-9002(03)01368-8.

[98] S. Alekhin, J. Blumlein, S. Klein, and S. Moch, "The 3, 4, and 5-flavor NNLO parton from deep-inelastic-scattering data and at hadron colliders", *Phys. Rev. D* **81** (2010) 014032, doi:10.1103/PhysRevD.81.014032, arXiv:0908.2766.

[99] S. Alekhin, J. Blumlein, and S. Moch, "Parton distribution functions and benchmark cross sections at NNLO", *Phys. Rev. D* **86** (2012) 054009, doi:10.1103/PhysRevD.86.054009, arXiv:1202.2281.

[100] S. Alekhin, J. Blümlein, S. Moch, and R. Placakyte, "Parton distribution functions, α_s, and heavy-quark masses for LHC Run II", *Phys. Rev. D* **96** (2017) 014011, doi:10.1103/PhysRevD.96.014011, arXiv:1701.05838.

[101] S. Alekhin, J. Blümlein, and S. Moch, "NLO PDFs from the ABMP16 fit", *Eur. Phys. J. C* **78** (2018) 477, doi:10.1140/epjc/s10052-018-5947-1, arXiv:1803.07537.

[102] A. Accardi et al., "Constraints on large-x parton distributions from new weak boson production and deep-inelastic scattering data", *Phys. Rev. D* **93** (2016) 114017, doi:10.1103/PhysRevD.93.114017, arXiv:1602.03154.

[103] H.-L. Lai et al., "New parton distributions for collider physics", *Phys. Rev. D* **82** (2010) 074024, doi:10.1103/PhysRevD.82.074024, arXiv:1007.2241.

[104] J. Gao et al., "CT10 next-to-next-to-leading order global analysis of QCD", *Phys. Rev. D* **89** (2014) 033009, doi:10.1103/PhysRevD.89.033009, arXiv:1302.6246.

[105] S. Dulat et al., "New parton distribution functions from a global analysis of quantum chromodynamics", *Phys. Rev. D* **93** (2016) 033006, doi:10.1103/PhysRevD.93.033006, arXiv:1506.07443.

[106] T.-J. Hou et al., "New CTEQ global analysis of quantum chromodynamics with high-precision data from the LHC", *Phys. Rev. D* **103** (2021) 014013, doi:10.1103/PhysRevD.103.014013, arXiv:1912.10053.

[107] H1 and ZEUS Collaboration, "Combined measurement and QCD analysis of the inclusive $e^{\pm}p$ scattering sross sections at HERA", *JHEP* **01** (2010) 109, doi:10.1007/JHEP01(2010)109, arXiv:0911.0884.

[108] H1 and ZEUS Collaboration, "Combination of measurements of inclusive deep inelastic $e^{\pm}p$ scattering cross sections and QCD analysis of HERA data", *Eur. Phys. J. C* **75** (2015) 580, doi:10.1140/epjc/s10052-015-3710-4, arXiv:1506.06042.

[109] A. D. Martin, W. J. Stirling, R. S. Thorne, and G. Watt, "Parton distributions for the LHC", *Eur. Phys. J. C* **63** (2009) 189, doi:10.1140/epjc/s10052-009-1072-5, arXiv:0901.0002.

[110] L. A. Harland-Lang, A. D. Martin, P. Motylinski, and R. S. Thorne, "Parton distributions in the LHC era: MMHT 2014 PDFs", *Eur. Phys. J. C* **75** (2015) 204, doi:10.1140/epjc/s10052-015-3397-6, arXiv:1412.3989.

[111] S. Bailey et al., "Parton distributions from LHC, HERA, Tevatron and fixed target data: MSHT20 PDFs", *Eur. Phys. J. C* **81** (2021) 341, doi:10.1140/epjc/s10052-021-09057-0, arXiv:2012.04684.

DRAFT

[112] J. McGowan, T. Cridge, L. A. Harland-Lang, and R. S. Thorne, "Approximate N^{3}LO parton distribution functions with theoretical uncertainties: MSHT20aN^{3}LO PDFs", *Eur. Phys. J. C* **83** (2023) 185, doi:10.1140/epjc/s10052-023-11236-0, arXiv:2207.04739. [Erratum: Eur.Phys.J.C 83 (2023) 302].

[113] R. D. Ball et al., "A first unbiased global NLO determination of parton distributions and their uncertainties", *Nucl. Phys. B* **838** (2010) 136, doi:10.1016/j.nuclphysb.2010.05.008, arXiv:1002.4407.

[114] R. D. Ball et al., "Impact of heavy quark masses on parton distributions and LHC phenomenology", *Nucl. Phys. B* **849** (2011) 296, doi:10.1016/j.nuclphysb.2011.03.021, arXiv:1101.1300.

[115] R. D. Ball et al., "Parton distributions with LHC data", *Nucl. Phys. B* **867** (2013) 244, doi:10.1016/j.nuclphysb.2012.10.003, arXiv:1207.1303.

[116] NNPDF Collaboration, "Parton distributions for the LHC run II", *JHEP* **04** (2015) 040, doi:10.1007/JHEP04(2015)040, arXiv:1410.8849.

[117] NNPDF Collaboration, "Parton distributions from high-precision collider data", *Eur. Phys. J. C* **77** (2017) 663, doi:10.1140/epjc/s10052-017-5199-5, arXiv:1706.00428.

[118] NNPDF Collaboration, "Illuminating the photon content of the proton within a global PDF analysis", *SciPost Phys.* **5** (2018) 008, doi:10.21468/SciPostPhys.5.1.008, arXiv:1712.07053.

[119] NNPDF Collaboration, "The path to proton structure at 1% accuracy", *Eur. Phys. J. C* **82** (2022) 428, doi:10.1140/epjc/s10052-022-10328-7, arXiv:2109.02653.

[120] A. Bermudez Martinez et al., "Collinear and TMD parton densities from fits to precision DIS measurements in the parton branching method", *Phys. Rev. D* **99** (2019) 074008, doi:10.1103/PhysRevD.99.074008, arXiv:1804.11152.

[121] F. Hautmann et al., "Soft-gluon resolution scale in QCD evolution equations", *Phys. Lett. B* **772** (2017) 446, doi:10.1016/j.physletb.2017.07.005, arXiv:1704.01757.

[122] F. Hautmann et al., "Collinear and TMD quark and gluon densities from parton branching solution of QCD evolution equations", *JHEP* **01** (2018) 070, doi:10.1007/JHEP01(2018)070, arXiv:1708.03279.

[123] Particle Data Group Collaboration, "Review of Particle Physics", *PTEP* **2022** (2022) 083C01, doi:10.1093/ptep/ptac097.

[124] V. Barone and E. Predazzi, "High-energy particle diffraction", volume v.565 of *Texts and Monographs in Physics*. Springer-Verlag, Berlin Heidelberg, 2002. ISBN 978-3-540-42107-8.

[125] CMS Collaboration, "Measurement of the inelastic proton-proton cross section at $\sqrt{s} = 7$ TeV", *Phys. Lett. B* **722** (2013) 5, doi:10.1016/j.physletb.2013.03.024, arXiv:1210.6718.

[126] CMS Collaboration, "Measurement of the inelastic proton-proton cross section at $\sqrt{s} = 13$ TeV", *JHEP* **07** (2018) 161, doi:10.1007/JHEP07(2018)161, arXiv:1802.02613.

DRAFT

[127] S. Ostapchenko, "QGSJET-II: Towards reliable description of very high energy hadronic interactions", *Nucl. Phys. B Proc. Suppl.* **151** (2006) 143, doi:10.1016/j.nuclphysbps.2005.07.026, arXiv:hep-ph/0412332.

[128] S. Ostapchenko, "Monte Carlo treatment of hadronic interactions in enhanced Pomeron scheme: I. QGSJET-II model", *Phys. Rev. D* **83** (2011) 014018, doi:10.1103/PhysRevD.83.014018, arXiv:1010.1869.

[129] R. S. Fletcher, T. K. Gaisser, P. Lipari, and T. Stanev, "Sibyll: An event generator for simulation of high energy cosmic ray cascades", *Phys. Rev. D* **50** (1994) 5710, doi:10.1103/PhysRevD.50.5710.

[130] K. Werner, F.-M. Liu, and T. Pierog, "Parton ladder splitting and the rapidity dependence of transverse momentum spectra in deuteron-gold collisions at RHIC", *Phys. Rev. C* **74** (2006) 044902, doi:10.1103/PhysRevC.74.044902, arXiv:hep-ph/0506232.

[131] G. Antchev et al., "First measurement of the total proton-proton cross section at the LHC energy of $\sqrt{s}$ =7 TeV", *EPL* **96** (2011) 21002, doi:10.1209/0295-5075/96/21002, arXiv:1110.1395.

[132] TOTEM Collaboration, "Luminosity-independent measurements of total, elastic and inelastic cross sections at $\sqrt{s} = 7$ TeV", *EPL* **101** (2013) 21004, doi:10.1209/0295-5075/101/21004.

[133] TOTEM Collaboration, "Luminosity-independent measurement of the proton-proton total cross section at $\sqrt{s} = 8$ TeV", *Phys. Rev. Lett.* **111** (2013) 012001, doi:10.1103/PhysRevLett.111.012001.

[134] TOTEM Collaboration, "First measurement of elastic, inelastic and total cross section at $\sqrt{s} = 13$ TeV by TOTEM and overview of cross section data at LHC energies", *Eur. Phys. J. C* **79** (2019) 103, doi:10.1140/epjc/s10052-019-6567-0, arXiv:1712.06153.

[135] Particle Data Group, K. Nakamura et al., "Review of particle physics", *J. Phys. G* **37** (2010) 075021, doi:10.1088/0954-3899/37/7A/075021.

[136] COMPETE Collaboration, "Benchmarks for the forward observables at RHIC, the Tevatron Run II and the LHC", *Phys. Rev. Lett.* **89** (2002) 201801, doi:10.1103/PhysRevLett.89.201801, arXiv:hep-ph/0206172.

[137] Pierre Auger Collaboration, "Measurement of the proton-air cross section at $\sqrt{s} = 57$ TeV with the Pierre Auger Observatory", *Phys. Rev. Lett.* **109** (2012) 062002, doi:10.1103/PhysRevLett.109.062002, arXiv:1208.1520.

[138] CMS Collaboration, "Measurement of the inclusive jet cross section in pp collisions at $\sqrt{s} = 2.76$ TeV", *Eur. Phys. J. C* **76** (2016) 265, doi:10.1140/epjc/s10052-016-4083-z, arXiv:1512.06212.

[139] CMS Collaboration, "Measurement and QCD analysis of double-differential inclusive jet cross sections in pp collisions at $\sqrt{s} = 8$ TeV and cross section ratios to 2.76 and 7 TeV", *JHEP* **03** (2017) 156, doi:10.1007/JHEP03(2017)156, arXiv:1609.05331.

DRAFT

[140] CMS Collaboration, "Measurement of the double-differential inclusive jet cross section in proton-proton collisions at $\sqrt{s}$ = 5.02 TeV", *submitted to JHEP* (2024) arXiv:2401.11355.

[141] CMS Collaboration, "Measurement of the inclusive jet cross section in pp collisions at $\sqrt{s} = 7$ TeV", *Phys. Rev. Lett.* **107** (2011) 132001, doi:10.1103/PhysRevLett.107.132001, arXiv:1106.0208.

[142] CMS Collaboration, "Measurements of differential jet cross sections in proton-proton collisions at $\sqrt{s} = 7$ TeV with the CMS detector", *Phys. Rev. D* **87** (2013) 112002, doi:10.1103/PhysRevD.87.112002, arXiv:1212.6660. [Erratum: Phys.Rev.D 87 (2013) 119902].

[143] CMS Collaboration, "Measurement of the ratio of inclusive jet cross sections using the anti-k_T algorithm with radius parameters R=0.5 and 0.7 in pp collisions at $\sqrt{s} = 7$ TeV", *Phys. Rev. D* **90** (2014) 072006, doi:10.1103/PhysRevD.90.072006, arXiv:1406.0324.

[144] CMS Collaboration, "Constraints on parton distribution functions and extraction of the strong coupling constant from the inclusive jet cross section in pp collisions at $\sqrt{s} = 7$ TeV", *Eur. Phys. J. C* **75** (2015) 288, doi:10.1140/epjc/s10052-015-3499-1, arXiv:1410.6765.

[145] CMS Collaboration, "Measurement of the double-differential inclusive jet cross section in proton–proton collisions at $\sqrt{s} = 13$ TeV", *Eur. Phys. J. C* **76** (2016) 451, doi:10.1140/epjc/s10052-016-4286-3, arXiv:1605.04436.

[146] CMS Collaboration, "Measurement and QCD analysis of double-differential inclusive jet cross sections in proton-proton collisions at $\sqrt{s}$ = 13 TeV", *JHEP* **02** (2022) 142, doi:10.1007/JHEP02(2022)142, arXiv:2111.10431. [Addendum: JHEP 12, 035 (2022)].

[147] S. Dittmaier, A. Huss, and C. Speckner, "Weak radiative corrections to dijet production at hadron colliders", *JHEP* **11** (2012) 095, doi:10.1007/JHEP11(2012)095, arXiv:1210.0438.

[148] CMS Collaboration, "Event generator tunes obtained from underlying event and multiparton scattering measurements", *Eur. Phys. J. C* **76** (2016) 155, doi:10.1140/epjc/s10052-016-3988-x, arXiv:1512.00815.

[149] CMS Collaboration, "Measurements of jet multiplicity and jet transverse momentum in multijet events in proton–proton collisions at $\sqrt{s} = 13$ TeV", *Eur. Phys. J. C* **83** (2023) 742, doi:10.1140/epjc/s10052-023-11753-y, arXiv:2210.13557.

[150] CMS Collaboration, "Measurement of the differential dijet production cross section in proton-proton collisions at $\sqrt{s} = 7$ TeV", *Phys. Lett. B* **700** (2011) 187, doi:10.1016/j.physletb.2011.05.027, arXiv:1104.1693.

[151] CMS Collaboration, "Dijet azimuthal decorrelations in pp collisions at $\sqrt{s} = 7$~TeV", *Phys. Rev. Lett.* **106** (2011) 122003, doi:10.1103/PhysRevLett.106.122003, arXiv:1101.5029.

[152] CMS Collaboration, "Measurement of dijet azimuthal decorrelation in pp collisions at $\sqrt{s} = 8$ TeV", *Eur. Phys. J. C* **76** (2016) 536, doi:10.1140/epjc/s10052-016-4346-8, arXiv:1602.04384.

DRAFT

[153] CMS Collaboration, "Azimuthal correlations for inclusive 2-jet, 3-jet, and 4-jet events in pp collisions at $\sqrt{s} = 13$ TeV", *Eur. Phys. J. C* **78** (2018) 566, doi:10.1140/epjc/s10052-018-6033-4, arXiv:1712.05471.

[154] CMS Collaboration, "Measurement of the ratio of the 3-jet to 2-jet cross sections in pp collisions at $\sqrt{s} = 7$ TeV", *Phys. Lett. B* **702** (2011) 336, doi:10.1016/j.physletb.2011.07.067, arXiv:1106.0647.

[155] CMS Collaboration, "Shape, transverse size, and charged hadron multiplicity of jets in pp collisions at 7 TeV", *JHEP* **06** (2012) 160, doi:10.1007/JHEP06(2012)160, arXiv:1204.3170.

[156] CMS Collaboration, "Studies of jet mass in dijet and W/Z + jet events", *JHEP* **05** (2013) 090, doi:10.1007/JHEP05(2013)090, arXiv:1303.4811.

[157] CMS Collaboration, "Measurements of the differential jet cross section as a function of the jet mass in dijet events from proton-proton collisions at $\sqrt{s} = 13$ TeV", *JHEP* **11** (2018) 113, doi:10.1007/JHEP11(2018)113, arXiv:1807.05974.

[158] CMS Collaboration, "Probing color coherence effects in pp collisions at $\sqrt{s} = 7$ TeV", *Eur. Phys. J. C* **74** (2014) 2901, doi:10.1140/epjc/s10052-014-2901-8, arXiv:1311.5815.

[159] CMS Collaboration, "Study of hadronic event-shape variables in multijet final states in pp collisions at $\sqrt{s}$ = 7 TeV", *JHEP* **10** (2014) 087, doi:10.1007/JHEP10(2014)087, arXiv:1407.2856.

[160] CMS Collaboration, "Event shape variables measured using multijet final states in proton-proton collisions at $\sqrt{s} = 13$ TeV", *JHEP* **12** (2018) 117, doi:10.1007/JHEP12(2018)117, arXiv:1811.00588.

[161] CMS Collaboration, "Distributions of topological observables in inclusive three- and four-jet events in pp collisions at sqrt(s) = 7 TeV", *Eur. Phys. J. C* **75** (2015) 302, doi:10.1140/epjc/s10052-015-3491-9, arXiv:1502.04785.

[162] CMS Collaboration, "Measurements of jet charge with dijet events in pp collisions at $\sqrt{s} = 8$ TeV", *JHEP* **10** (2017) 131, doi:10.1007/JHEP10(2017)131, arXiv:1706.05868.

[163] CMS Collaboration, "Azimuthal separation in nearly back-to-back jet topologies in inclusive 2- and 3-jet events in pp collisions at $\sqrt{s} = 13$ TeV", *Eur. Phys. J. C* **79** (2019) 773, doi:10.1140/epjc/s10052-019-7276-4, arXiv:1902.04374.

[164] CMS Collaboration, "Dependence of inclusive jet production on the anti-k_T distance parameter in pp collisions at $\sqrt{s}$ = 13 TeV", *JHEP* **12** (2020) 082, doi:10.1007/JHEP12(2020)082, arXiv:2005.05159.

[165] CMS Collaboration, "Study of quark and gluon jet substructure in Z+jet and dijet events from pp collisions", *JHEP* **01** (2022) 188, doi:10.1007/JHEP01(2022)188, arXiv:2109.03340.

[166] J. C. Collins, D. E. Soper, and G. F. Sterman, "Factorization of hard processes in QCD", *Adv. Ser. Direct. High Energy Phys.* **5** (1989) 1, doi:10.1142/9789814503266_0001, arXiv:hep-ph/0409313.

DRAFT

[167] V. N. Gribov and L. N. Lipatov, "Deep inelastic ep scattering in perturbation theory", *Sov. J. Nucl. Phys.* **15** (1972) 438.

[168] L. N. Lipatov, "The parton model and perturbation theory", *Sov. J. Nucl. Phys.* **20** (1975) 94.

[169] Y. L. Dokshitzer, "Calculation of the structure functions for deep inelastic scattering and e^+e^- annihilation by perturbation theory in quantum chromodynamics.", *Sov. Phys. JETP* **46** (1977) 641.

[170] G. Altarelli and G. Parisi, "Asymptotic freedom in parton language", *Nucl. Phys. B* **126** (1977) 298, doi:10.1016/0550-3213(77)90384-4.

[171] G. Curci, W. Furmanski, and R. Petronzio, "Evolution of parton densities beyond leading order: The non-singlet case", *Nucl. Phys. B* **175** (1980) 27, doi:10.1016/0550-3213(80)90003-6.

[172] W. Furmanski and R. Petronzio, "Singlet parton densities beyond leading order", *Phys. Lett. B* **97** (1980) 437, doi:10.1016/0370-2693(80)90636-X.

[173] S. Moch, J. A. M. Vermaseren, and A. Vogt, "The three-loop splitting functions in QCD: the non-singlet case", *Nucl. Phys. B* **688** (2004) 101, doi:10.1016/j.nuclphysb.2004.03.030, arXiv:hep-ph/0403192.

[174] A. Vogt, S. Moch, and J. A. M. Vermaseren, "The three-loop splitting functions in QCD: the singlet case", *Nucl. Phys. B* **691** (2004) 129, doi:10.1016/j.nuclphysb.2004.04.024, arXiv:hep-ph/0404111.

[175] S. Alekhin et al., "HERAFitter", *Eur. Phys. J. C* **75** (2015) 304, doi:10.1140/epjc/s10052-015-3480-z, arXiv:1410.4412.

[176] xFitter Collaboration, H. Abdolmaleki et al., "xFitter: An open source QCD analysis framework. A resource and reference document for the Snowmass study", 2022. arXiv:2206.12465.

[177] CMS Collaboration, "Measurement of the muon charge asymmetry in inclusive $pp \to W^+X$ Production at $\sqrt{s} = 7$ TeV and an improved determination of light parton distribution functions", *Phys. Rev. D* **90** (2014) 032004, doi:10.1103/PhysRevD.90.032004, arXiv:1312.6283.

[178] CMS Collaboration, "Measurement of associated W + charm production in pp collisions at $\sqrt{s} = 7$ TeV", *JHEP* **02** (2014) 013, doi:10.1007/JHEP02(2014)013, arXiv:1310.1138.

[179] CMS Collaboration, "Measurement of the differential cross section and charge asymmetry for inclusive $pp \to W^{\pm} + X$ production at $\sqrt{s} = 8$ TeV", *Eur. Phys. J. C* **76** (2016) 469, doi:10.1140/epjc/s10052-016-4293-4, arXiv:1603.01803.

[180] CMS Collaboration, "Measurement of the triple-differential dijet cross section in proton-proton collisions at $\sqrt{s} = 8$ TeV and constraints on parton distribution functions", *Eur. Phys. J. C* **77** (2017) 746, doi:10.1140/epjc/s10052-017-5286-7, arXiv:1705.02628.

DRAFT

[181] CMS Collaboration, "Measurement of $\mathrm{t\bar{t}}$ normalised multi-differential cross sections in pp collisions at $\sqrt{s} = 13$ TeV, and simultaneous determination of the strong coupling strength, top quark pole mass, and parton distribution functions", *Eur. Phys. J. C* **80** (2020) 658, doi:10.1140/epjc/s10052-020-7917-7, arXiv:1904.05237.

[182] CMS Collaboration, "Measurement of multidifferential cross sections for dijet production in proton-proton collisions at $\sqrt{s} = 13$ TeV", *submitted to EPJC*, (2023) arXiv:2312.16669.

[183] A. Deur, S. J. Brodsky, and G. F. de Teramond, "The QCD running coupling", *Nucl. Phys.* **90** (2016) 1, doi:10.1016/j.ppnp.2016.04.003, arXiv:1604.08082.

[184] CMS Collaboration, "Measurement of the ratio of the inclusive 3-jet cross section to the inclusive 2-jet cross section in pp collisions at $\sqrt{s} = 7$ TeV and first determination of the strong coupling constant in the TeV range", *Eur. Phys. J. C* **73** (2013) 2604, doi:10.1140/epjc/s10052-013-2604-6, arXiv:1304.7498.

[185] CMS Collaboration, "Measurement of energy correlators inside jets and determination of the strong coupling $\alpha_S(m_Z)$", *submitted to PRL*, (2024) arXiv:2402.13864.

[186] L. J. Dixon, I. Moult, and H. X. Zhu, "Collinear limit of the energy-energy correlator", *Phys. Rev. D* **100** (2019) 014009, doi:10.1103/PhysRevD.100.014009, arXiv:1905.01310.

[187] K. Lee, B. Meçaj, and I. Moult, "Conformal colliders meet the LHC", (2022) arXiv:2205.03414.

[188] W. Chen et al., "NNLL resummation for projected three-point energy correlator", (2023) arXiv:2307.07510.

[189] CMS Collaboration, "Measurement of the inclusive 3-jet production differential cross section in proton–proton collisions at 7 TeV and determination of the strong coupling constant in the TeV range", *Eur. Phys. J. C* **75** (2015) 186, doi:10.1140/epjc/s10052-015-3376-y, arXiv:1412.1633.

[190] CMS Collaboration, "Determination of the top quark pole mass and strong coupling constant from the $t\bar{t}$ production cross section in pp Collisions at $\sqrt{s} = 7$ TeV", *Phys. Lett. B* **728** (2014) 496, doi:10.1016/j.physletb.2013.12.009, arXiv:1307.1907. [Erratum: Phys.Lett.B 738 (2014) 526].

[191] CMS Collaboration, "Determination of the strong coupling constant $\alpha_S(m_Z)$ from measurements of inclusive $\mathrm{W}^{\pm}$ and Z boson production cross sections in proton-proton collisions at $\sqrt{\mathrm{s}} = 7$ and 8 TeV", *JHEP* **06** (2020) 018, doi:10.1007/JHEP06(2020)018, arXiv:1912.04387.

[192] CMS Collaboration, "Measurement of the $\mathrm{t\bar{t}}$ production cross section, the top quark mass, and the strong coupling constant using dilepton events in pp collisions at $\sqrt{s} = 13$ TeV", *Eur. Phys. J. C* **79** (2019) 368, doi:10.1140/epjc/s10052-019-6863-8, arXiv:1812.10505.

[193] CMS Collaboration, "Measurement of multijet azimuthal correlations and determination of the strong coupling in proton-proton collisions at $\sqrt{s} = 13$ TeV", *submitted to EPJC*, (2024) arXiv:2404.16082.

DRAFT

[194] ATLAS Collaboration, "Determination of the strong coupling constant α_s from transverse energy–energy correlations in multijet events at $\sqrt{s} = 8$ TeV using the ATLAS detector", *Eur. Phys. J. C* **77** (2017) 872, doi:10.1140/epjc/s10052-017-5442-0, arXiv:1707.02562.

[195] ATLAS Collaboration, "Measurement of dijet azimuthal decorrelations in pp collisions at $\sqrt{s} = 8$ TeV with the ATLAS detector and determination of the strong coupling", *Phys. Rev. D* **98** (2018) 092004, doi:10.1103/PhysRevD.98.092004, arXiv:1805.04691.

[196] D0 Collaboration, "Determination of the strong coupling constant from the inclusive jet cross section in $p\bar{p}$ collisions at $\sqrt{s} = 1.96$ TeV", *Phys. Rev. D* **80** (2009) 111107, doi:10.1103/PhysRevD.80.111107, arXiv:0911.2710.

[197] D0 Collaboration, "Measurement of angular correlations of jets at $\sqrt{s} = 1.96$ TeV and determination of the strong coupling at high momentum transfers", *Phys. Lett. B* **718** (2012) 56, doi:10.1016/j.physletb.2012.10.003, arXiv:1207.4957.

[198] H1 Collaboration, "Jet production in ep collisions at low Q^2 and determination of α_s", *Eur. Phys. J. C* **67** (2010) 1, doi:10.1140/epjc/s10052-010-1282-x, arXiv:0911.5678.

[199] ZEUS Collaboration, "Inclusive-jet photoproduction at HERA and determination of α_s", *Nucl. Phys. B* **864** (2012) 1, doi:10.1016/j.nuclphysb.2012.06.006, arXiv:1205.6153.

[200] CDF Collaboration, "Measurement of double parton scattering in $\bar{p}p$ collisions at $\sqrt{s} = 1.8$ TeV", *Phys. Rev. Lett.* **79** (1997) 584, doi:10.1103/PhysRevLett.79.584.

[201] D0 Collaboration, "Observation and studies of double J/ψ production at the Tevatron", *Phys. Rev. D* **90** (2014) 111101, doi:10.1103/PhysRevD.90.111101, arXiv:1406.2380.

[202] D0 Collaboration, "Evidence for simultaneous production of J/ψ and Y mesons", *Phys. Rev. Lett.* **116** (2016) 082002, doi:10.1103/PhysRevLett.116.082002, arXiv:1511.02428.

[203] D0 Collaboration, "Double parton interactions in $\gamma + 3$ jet and $\gamma +$ b/c jet + 2 jet events in $p\bar{p}$ collisions at $\sqrt{s} = 1.96$ TeV", *Phys. Rev. D* **89** (2014) 072006, doi:10.1103/PhysRevD.89.072006, arXiv:1402.1550.

[204] D0 Collaboration, "Study of double parton interactions in diphoton + dijet events in $p\bar{p}$ collisions at $\sqrt{s} = 1.96$ TeV", *Phys. Rev. D* **93** (2016) 052008, doi:10.1103/PhysRevD.93.052008, arXiv:1512.05291.

[205] CMS Collaboration, "Observation of triple J/ψ meson production in proton-proton collisions", *Nature Phys.* **19** (2023) 338, doi:10.1038/s41567-022-01838-y, arXiv:2111.05370. [Erratum: Nature Phys. 19 (2023)].

[206] CMS Collaboration, "Study of double parton scattering Using W + 2-Jet events in proton-proton collisions at $\sqrt{s} = 7$ TeV", *JHEP* **03** (2014) 032, doi:10.1007/JHEP03(2014)032, arXiv:1312.5729.

DRAFT

[207] CMS Collaboration, "Evidence for WW production from double-parton interactions in proton-proton collisions at $\sqrt{s} = 13$ TeV", *Eur. Phys. J. C* **80** (2020) 41, doi:10.1140/epjc/s10052-019-7541-6, arXiv:1909.06265.

[208] CMS Collaboration, "Observation of same-sign WW production from double parton scattering in proton-proton collisions at $\sqrt{s}$ = 13 TeV", *Phys. Rev. Lett.* **131** (2023) 091803, doi:10.1103/PhysRevLett.131.091803, arXiv:2206.02681.

[209] S. D. Drell and T.-M. Yan, "Massive lepton-pair production in hadron-hadron collisions at high energies", *Phys. Rev. Lett.* **25** (1970) 316, doi:10.1103/PhysRevLett.25.316.

[210] CMS Collaboration, "Observation of a new boson at a mass of 125 GeV with the CMS experiment at the LHC", *Phys. Lett. B* **716** (2012) 30, doi:10.1016/j.physletb.2012.08.021, arXiv:1207.7235.

[211] CMS Collaboration, "Search for new physics in the monophoton final state in proton-proton collisions at $\sqrt{s} = 13$ TeV", *JHEP* **10** (2017) 073, doi:10.1007/JHEP10(2017)073, arXiv:1706.03794.

[212] CMS Collaboration, "Measurement of the differential cross section for isolated prompt photon production in pp collisions at 7 TeV", *Phys. Rev. D* **84** (2011) 052011, doi:10.1103/PhysRevD.84.052011, arXiv:1108.2044.

[213] CMS Collaboration, "Measurement of the isolated prompt photon production cross section in pp collisions at $\sqrt{s} = 7$˜TeV", *Phys. Rev. Lett.* **106** (2011) 082001, doi:10.1103/PhysRevLett.106.082001, arXiv:1012.0799.

[214] CMS Collaboration, "Measurement of differential cross sections for inclusive isolated-photon and photon+jets production in proton-proton collisions at $\sqrt{s} = 13$ TeV", *Eur. Phys. J. C* **79** (2019) 20, doi:10.1140/epjc/s10052-018-6482-9, arXiv:1807.00782.

[215] S. Catani, M. Fontannaz, J. P. Guillet, and E. Pilon, "Cross-section of isolated prompt photons in hadron hadron collisions", *JHEP* **05** (2002) 028, doi:10.1088/1126-6708/2002/05/028, arXiv:hep-ph/0204023.

[216] L. Bourhis, M. Fontannaz, and J. P. Guillet, "Quarks and gluon fragmentation functions into photons", *Eur. Phys. J. C* **2** (1998) 529, doi:10.1007/s100520050158, arXiv:hep-ph/9704447.

[217] CMS Collaboration, "Study of W boson production in PbPb and pp collisions at $\sqrt{s_{NN}} = 2.76$ TeV", *Phys. Lett. B* **715** (2012) 66, doi:10.1016/j.physletb.2012.07.025, arXiv:1205.6334.

[218] CMS Collaboration, "Study of Z production in PbPb and pp collisions at $\sqrt{s_{\mathrm{NN}}} = 2.76$ TeV in the dimuon and dielectron decay channels", *JHEP* **03** (2015) 022, doi:10.1007/JHEP03(2015)022, arXiv:1410.4825.

[219] CMS Collaboration, "Measurement of W and Z boson inclusive cross sections in pp collisions at 5.02 and 13 TeV", CMS Physics Analysis Summary CMS-PAS-SMP-20-004, 2023.

DRAFT

[220] CMS Collaboration, "Measurement of the inclusive W and Z production cross sections in pp collisions at $\sqrt{s} = 7$ TeV", *JHEP* **10** (2011) 132, doi:10.1007/JHEP10(2011)132, arXiv:1107.4789.

[221] CMS Collaboration, "Measurement of the differential and double-differential Drell-Yan cross sections in proton-proton collisions at $\sqrt{s} = 7$ TeV", *JHEP* **12** (2013) 030, doi:10.1007/JHEP12(2013)030, arXiv:1310.7291.

[222] CMS Collaboration, "Measurement of inclusive W and Z boson production cross sections in pp collisions at $\sqrt{s}$ = 8 TeV", *Phys. Rev. Lett.* **112** (2014) 191802, doi:10.1103/PhysRevLett.112.191802, arXiv:1402.0923.

[223] CMS Collaboration, "Measurements of differential and double-differential Drell-Yan cross sections in proton-proton collisions at 8 TeV", *Eur. Phys. J. C* **75** (2015) 147, doi:10.1140/epjc/s10052-015-3364-2, arXiv:1412.1115.

[224] J. Baglio, C. Duhr, B. Mistlberger, and R. Szafron, "Inclusive production cross sections at N^{3}LO", *JHEP* **12** (2022) 066, doi:10.1007/JHEP12(2022)066, arXiv:2209.06138.

[225] C. Albajar et al., "Intermediate vector boson cross sections at the CERN super proton synchrotron collider and the number of neutrino types", *Phys. Lett. B* **198** (1987) 271, doi:https://doi.org/10.1016/0370-2693(87)91510-3.

[226] UA2 Collaboration, "Measurement of W and Z production cross sections at the CERN pp collider", *Z. Phys C* **47** (1990) 11.

[227] CDF Collaboration, "First measurements of inclusive W and Z cross sections from Run II of the Tevatron collider", *Phys. Rev. Lett.* **94** (2005) 091803, doi:10.1103/PhysRevLett.94.091803, arXiv:hep-ex/0406078.

[228] D0 Collaboration, "Extraction of the width of the W boson from measurements of $\sigma(p\overline{p} \to W + X) \times B(W \to ev)$ and $\sigma(p\overline{p} \to Z + X) \times B(Z \to ee)$ and their ratio", *Phys. Rev. D* **61** (2000) 072001, doi:10.1103/PhysRevD.61.072001, arXiv:hep-ex/9906025.

[229] S. Camarda, L. Cieri, and G. Ferrera, "Drell–Yan lepton-pair production: q_T resummation at N^{3}LL accuracy and fiducial cross sections at N^{3}LO", *Phys. Rev. D* **104** (2021) L111503, doi:10.1103/PhysRevD.104.L111503, arXiv:2103.04974.

[230] S. Camarda, L. Cieri, and G. Ferrera, "Fiducial perturbative power corrections within the $\mathbf{q}_T$ subtraction formalism", *Eur. Phys. J. C* **82** (2022) 575, doi:10.1140/epjc/s10052-022-10510-x, arXiv:2111.14509.

[231] C. Balazs, J.-w. Qiu, and C. P. Yuan, "Effects of QCD resummation on distributions of leptons from the decay of electroweak vector bosons", *Phys. Lett. B* **355** (1995) 548, doi:10.1016/0370-2693(95)00726-2, arXiv:hep-ph/9505203.

[232] S. Catani, D. de Florian, G. Ferrera, and M. Grazzini, "Vector boson production at hadron colliders: transverse-momentum resummation and leptonic decay", *JHEP* **12** (2015) 047, doi:10.1007/JHEP12(2015)047, arXiv:1507.06937.

[233] CMS Collaboration, "Measurement of the lepton charge asymmetry in inclusive W production in pp collisions at $\sqrt{s} = 7$ TeV", *JHEP* **04** (2011) 050, doi:10.1007/JHEP04(2011)050, arXiv:1103.3470.

DRAFT

[234] CMS Collaboration, "Measurement of the electron charge asymmetry in inclusive W Production in pp collisions at $\sqrt{s} = 7$ TeV", *Phys. Rev. Lett.* **109** (2012) 111806, doi:10.1103/PhysRevLett.109.111806, arXiv:1206.2598.

[235] CMS Collaboration, "Measurements of the W boson rapidity, helicity, double-differential cross sections, and charge asymmetry in pp collisions at $\sqrt{s}$ = 13 TeV", *Phys. Rev. D* **102** (2020) 092012, doi:10.1103/PhysRevD.102.092012, arXiv:2008.04174.

[236] CMS Collaboration, "Measurement of the weak mixing angle with the Drell-Yan process in proton-proton collisions at the LHC", *Phys. Rev. D* **84** (2011) 112002, doi:10.1103/PhysRevD.84.112002, arXiv:1110.2682.

[237] CMS Collaboration, "Forward-backward asymmetry of Drell-Yan lepton pairs in pp collisions at $\sqrt{s} = 7$ TeV", *Phys. Lett. B* **718** (2013) 752, doi:10.1016/j.physletb.2012.10.082, arXiv:1207.3973.

[238] CMS Collaboration, "Forward–backward asymmetry of Drell–Yan lepton pairs in pp collisions at $\sqrt{s} = 8$ TeV", *Eur. Phys. J. C* **76** (2016) 325, doi:10.1140/epjc/s10052-016-4156-z, arXiv:1601.04768.

[239] CMS Collaboration, "Measurement of the weak mixing angle using the forward-backward asymmetry of Drell-Yan events in pp collisions at 8 TeV", *Eur. Phys. J. C* **78** (2018) 701, doi:10.1140/epjc/s10052-018-6148-7, arXiv:1806.00863.

[240] CMS Collaboration, "Measurement of differential cross sections for the production of a Z boson in association with jets in proton-proton collisions at $\sqrt{s}$ = 13 TeV", *Phys. Rev. D* **108** (2023) 052004, doi:10.1103/PhysRevD.108.052004, arXiv:2205.02872.

[241] J. Alwall et al., "Comparative study of various algorithms for the merging of parton showers and matrix elements in hadronic collisions", *Eur. Phys. J. C* **53** (2008) 473, doi:10.1140/epjc/s10052-007-0490-5, arXiv:0706.2569.

[242] J. Alwall, S. de Visscher, and F. Maltoni, "QCD radiation in the production of heavy colored particles at the LHC", *JHEP* **02** (2009) 017, doi:10.1088/1126-6708/2009/02/017, arXiv:0810.5350.

[243] R. Frederix and S. Frixione, "Merging meets matching in MC@NLO", *JHEP* **12** (2012) 061, doi:10.1007/JHEP12(2012)061, arXiv:1209.6215.

[244] S. Alioli et al., "Drell-Yan production at NNLL'+NNLO matched to parton showers", *Phys. Rev. D* **92** (2015) 094020, doi:10.1103/PhysRevD.92.094020, arXiv:1508.01475.

[245] S. Alioli et al., "Combining higher-order resummation with multiple NLO calculations and parton showers in GENEVA", *JHEP* **09** (2013) 120, doi:10.1007/JHEP09(2013)120, arXiv:1211.7049.

[246] I. W. Stewart, F. J. Tackmann, and W. J. Waalewijn, "N-Jettiness: An inclusive event shape to veto jets", *Phys. Rev. Lett.* **105** (2010) 092002, doi:10.1103/PhysRevLett.105.092002, arXiv:1004.2489.

DRAFT

[247] P. Skands, S. Carrazza, and J. Rojo, "Tuning PYTHIA 8.1: the Monash 2013 tune", *Eur. Phys. J. C* **74** (2014) 3024, doi:10.1140/epjc/s10052-014-3024-y, arXiv:1404.5630.

[248] CMS Collaboration, "Measurements of differential production cross sections for a Z boson in association with jets in pp collisions at $\sqrt{s} = 8$ TeV", *JHEP* **04** (2017) 022, doi:10.1007/JHEP04(2017)022, arXiv:1611.03844.

[249] CMS Collaboration, "Differential cross section measurements for the production of a W boson in association with jets in proton–proton collisions at $\sqrt{s} = 7$ TeV", *Phys. Lett. B* **741** (2015) 12, doi:10.1016/j.physletb.2014.12.003, arXiv:1406.7533.

[250] CMS Collaboration, "Measurements of differential cross sections for associated production of a W boson and jets in proton-proton collisions at $\sqrt{s} = 8$ TeV", *Phys. Rev. D* **95** (2017) 052002, doi:10.1103/PhysRevD.95.052002, arXiv:1610.04222.

[251] CMS Collaboration, "Measurement of the differential cross sections for the associated production of a W boson and jets in proton-proton collisions at $\sqrt{s} = 13$ TeV", *Phys. Rev. D* **96** (2017) 072005, doi:10.1103/PhysRevD.96.072005, arXiv:1707.05979.

[252] CMS Collaboration, "Measurements of jet multiplicity and differential production cross sections of Z+ jets events in proton-proton collisions at $\sqrt{s} = 7$ TeV", *Phys. Rev. D* **91** (2015) 052008, doi:10.1103/PhysRevD.91.052008, arXiv:1408.3104.

[253] CMS Collaboration, "Measurement of differential cross sections for Z boson production in association with jets in proton-proton collisions at $\sqrt{s} = 13$ TeV", *Eur. Phys. J. C* **78** (2018) 965, doi:10.1140/epjc/s10052-018-6373-0, arXiv:1804.05252.

[254] CMS Collaboration, "Study of the underlying event at forward rapidity in pp collisions at $\sqrt{s}$ = 0.9, 2.76, and 7 TeV", *JHEP* **04** (2013) 072, doi:10.1007/JHEP04(2013)072, arXiv:1302.2394.

[255] C. F. Berger et al., "Vector boson + jets with BlackHat and Sherpa", *Nucl. Phys. B Proc. Suppl.* **205-206** (2010) 92, doi:10.1016/j.nuclphysbps.2010.08.025, arXiv:1005.3728.

[256] S. Hoeche, F. Krauss, M. Schonherr, and F. Siegert, "QCD matrix elements + parton showers: The NLO case", *JHEP* **04** (2013) 027, doi:10.1007/JHEP04(2013)027, arXiv:1207.5030.

[257] CMS Collaboration, "Measurement of the triple-differential cross section for photon+jets production in proton-proton collisions at $\sqrt{s}$=7 TeV", *JHEP* **06** (2014) 009, doi:10.1007/JHEP06(2014)009, arXiv:1311.6141.

[258] CMS Collaboration, "Measurements of triple-differential cross sections for inclusive isolated-photon+jet events in pp collisions at $\sqrt{s} = 8$ TeV", *Eur. Phys. J. C* **79** (2019) 969, doi:10.1140/epjc/s10052-019-7451-7, arXiv:1907.08155.

[259] CMS Collaboration, "Rapidity distributions in exclusive Z + jet and γ + jet events in pp collisions at $\sqrt{s}$ = 7 TeV", *Phys. Rev. D* **88** (2013) 112009, doi:10.1103/PhysRevD.88.112009, arXiv:1310.3082.

[260] CMS Collaboration, "Comparison of the Z/γ^* + jets to γ + jets cross sections in pp collisions at $\sqrt{s} = 8$ TeV", *JHEP* **10** (2015) 128, doi:10.1007/JHEP04(2016)010, arXiv:1505.06520. [Erratum: JHEP 04 (2016) 010].

DRAFT

[261] CMS Collaboration, "Measurements of the differential cross sections of the production of Z + jets and γ + jets and of Z boson emission collinear with a jet in pp collisions at $\sqrt{s}$ = 13 TeV", *JHEP* **05** (2021) 285, doi:10.1007/JHEP05(2021)285, arXiv:2102.02238.

[262] S. Hoeche, F. Krauss, M. Schonherr, and F. Siegert, "A critical appraisal of NLO+PS matching methods", *JHEP* **09** (2012) 049, doi:10.1007/JHEP09(2012)049, arXiv:1111.1220.

[263] S. Frixione and B. R. Webber, "Matching NLO QCD computations and parton shower simulations", *JHEP* **06** (2002) 029, doi:10.1088/1126-6708/2002/06/029, arXiv:hep-ph/0204244.

[264] CMS Collaboration, "Measurement of WZ and ZZ production in pp collisions at $\sqrt{s} = 8$ TeV in final states with b-tagged jets", *Eur. Phys. J. C* **74** (2014) 2973, doi:10.1140/epjc/s10052-014-2973-5, arXiv:1403.3047.

[265] CMS Collaboration, "Measurement of associated Z + charm production in proton-proton collisions at $\sqrt{s} = 8$ TeV", *Eur. Phys. J. C* **78** (2018) 287, doi:10.1140/epjc/s10052-018-5752-x, arXiv:1711.02143.

[266] M. Czakon, A. Mitov, M. Pellen, and R. Poncelet, "NNLO QCD predictions for W+c-jet production at the LHC", *JHEP* **06** (2021) 100, doi:10.1007/JHEP06(2021)100, arXiv:2011.01011.

[267] M. Czakon, A. Mitov, M. Pellen, and R. Poncelet, "A detailed investigation of W+c-jet at the LHC", *JHEP* **02** (2023) 241, doi:10.1007/JHEP02(2023)241, arXiv:2212.00467.

[268] CMS Collaboration, "Measurements of the associated production of a W boson and a charm quark in proton–proton collisions at $\sqrt{s} = 8$ TeV", *Eur. Phys. J. C* **82** (2022) 1094, doi:10.1140/epjc/s10052-022-10897-7, arXiv:2112.00895.

[269] CMS Collaboration, "Measurement of associated production of a W boson and a charm quark in proton-proton collisions at $\sqrt{s} = 13$ TeV", *Eur. Phys. J. C* **79** (2019) 269, doi:10.1140/epjc/s10052-019-6752-1, arXiv:1811.10021.

[270] CMS Collaboration, "Measurement of the production cross section for a W boson in association with a charm quark in proton–proton collisions at $\sqrt{s} = 13$ TeV", *Eur. Phys. J. C* **84** (2024) 27, doi:10.1140/epjc/s10052-023-12258-4, arXiv:2308.02285.

[271] CMS Collaboration, "Measurement of the production cross section for a W boson and two b jets in pp collisions at $\sqrt{s}$=7 TeV", *Phys. Lett. B* **735** (2014) 204, doi:10.1016/j.physletb.2014.06.041, arXiv:1312.6608.

[272] CMS Collaboration, "Measurement of the production cross section of a W boson in association with two b jets in pp collisions at $\sqrt{s} = 8$ TeV", *Eur. Phys. J. C* **77** (2017) 92, doi:10.1140/epjc/s10052-016-4573-z, arXiv:1608.07561.

[273] CMS Collaboration, "Measurement of differential cross sections for Z bosons produced in association with charm jets in pp collisions at $\sqrt{s} = 13$ TeV", *JHEP* **04** (2021) 109, doi:10.1007/JHEP04(2021)109, arXiv:2012.04119.

DRAFT

[274] CMS Collaboration, "Measurement of the production cross sections for a Z boson and one or more b jets in pp collisions at $\sqrt{s} = 7$ TeV", *JHEP* **06** (2014) 120, doi:10.1007/JHEP06(2014)120, arXiv:1402.1521.

[275] CMS Collaboration, "Measurements of the associated production of a Z boson and b jets in pp collisions at $\sqrt{s} = 8$ TeV", *Eur. Phys. J. C* **77** (2017) 751, doi:10.1140/epjc/s10052-017-5140-y, arXiv:1611.06507.

[276] CMS Collaboration, "Measurement of the production cross section for Z+b jets in proton-proton collisions at $\sqrt{s} = 13$ TeV", *Phys. Rev. D* **105** (2022) 092014, doi:10.1103/PhysRevD.105.092014, arXiv:2112.09659.

[277] CMS Collaboration, "Evidence for electroweak production of four charged leptons and two jets in proton-proton collisions at $\sqrt{s} = 13$ TeV", *Phys. Lett. B* **812** (2021) 135992, doi:10.1016/j.physletb.2020.135992, arXiv:2008.07013.

[278] CMS Collaboration, "Measurement of differential cross sections for the production of a pair of isolated photons in pp collisions at $\sqrt{s} = 7$ TeV", *Eur. Phys. J. C* **74** (2014) 3129, doi:10.1140/epjc/s10052-014-3129-3, arXiv:1405.7225.

[279] CMS Collaboration, "Measurement of the Wγ and Zγ inclusive cross sections in pp collisions at $\sqrt{s} = 7$ TeV and limits on anomalous triple gauge boson couplings", *Phys. Rev. D* **89** (2014) 092005, doi:10.1103/PhysRevD.89.092005, arXiv:1308.6832.

[280] CMS Collaboration, "Measurement of the W^+W^- cross section in pp collisions at $\sqrt{s} = 7$ TeV and limits on anomalous WWγ and WWZ couplings", *Eur. Phys. J. C* **73** (2013) 2610, doi:10.1140/epjc/s10052-013-2610-8, arXiv:1306.1126.

[281] CMS Collaboration, "Measurement of the WZ production cross section in pp collisions at $\sqrt{s} = 7$ and 8 TeV and search for anomalous triple gauge couplings at $\sqrt{s} = 8$ TeV", *Eur. Phys. J. C* **77** (2017) 236, doi:10.1140/epjc/s10052-017-4730-z, arXiv:1609.05721.

[282] CMS Collaboration, "Measurement of the ZZ production cross section and search for anomalous couplings in $2\ell 2\ell'$ final states in pp collisions at $\sqrt{s} = 7$ TeV", *JHEP* **01** (2013) 063, doi:10.1007/JHEP01(2013)063, arXiv:1211.4890.

[283] S. Catani et al., "Diphoton production at hadron colliders: a fully-differential QCD calculation at NNLO", *Phys. Rev. Lett.* **108** (2012) 072001, doi:10.1103/PhysRevLett.108.072001, arXiv:1110.2375. [Erratum: Phys.Rev.Lett. 117 (2016) 089901].

[284] M. Grazzini, S. Kallweit, D. Rathlev, and A. Torre, "$Z\gamma$ production at hadron colliders in NNLO QCD", *Phys. Lett. B* **731** (2014) 204, doi:10.1016/j.physletb.2014.02.037, arXiv:1309.7000.

[285] CMS Collaboration, "Measurement of the Wγ production cross section in proton-proton collisions at $\sqrt{s} = 13$ TeV and constraints on effective field theory coefficients", *Phys. Rev. Lett.* **126** (2021) 252002, doi:10.1103/PhysRevLett.126.252002, arXiv:2102.02283.

[286] CMS Collaboration, "Measurement of the Zγ production cross section in pp collisions at 8 TeV and search for anomalous triple gauge boson couplings", *JHEP* **04** (2015) 164, doi:10.1007/JHEP04(2015)164, arXiv:1502.05664.

DRAFT

[287] CMS Collaboration, "Measurements of the electroweak diboson production cross sections in proton-proton collisions at $\sqrt{s} = 5.02$ TeV using leptonic decays", *Phys. Rev. Lett.* **127** (2021) 191801, doi:10.1103/PhysRevLett.127.191801, arXiv:2107.01137.

[288] CMS Collaboration, "Measurement of the W^+W^- cross section in pp collisions at $\sqrt{s} =$ 8 TeV and limits on anomalous gauge couplings", *Eur. Phys. J. C* **76** (2016) 401, doi:10.1140/epjc/s10052-016-4219-1, arXiv:1507.03268.

[289] CMS Collaboration, "W^+W^- boson pair production in proton-proton collisions at $\sqrt{s} =$ 13 TeV", *Phys. Rev. D* **102** (2020) 092001, doi:10.1103/PhysRevD.102.092001, arXiv:2009.00119.

[290] CMS Collaboration, "Measurement of the inclusive and differential WZ production cross sections, polarization angles, and triple gauge couplings in pp collisions at $\sqrt{s}$ = 13 TeV", *JHEP* **07** (2022) 032, doi:10.1007/JHEP07(2022)032, arXiv:2110.11231.

[291] CMS Collaboration, "Measurement of the pp $\to$ ZZ production cross section and constraints on anomalous triple gauge couplings in four-lepton final states at $\sqrt{s}$ = 8 TeV", *Phys. Lett. B* **740** (2015) 250, doi:10.1016/j.physletb.2016.04.010, arXiv:1406.0113. [Erratum: Phys.Lett.B 757 (2016) 569].

[292] CMS Collaboration, "Measurements of pp $\to$ ZZ production cross sections and constraints on anomalous triple gauge couplings at $\sqrt{s} = 13$ TeV", *Eur. Phys. J. C* **81** (2021) 200, doi:10.1140/epjc/s10052-020-08817-8, arXiv:2009.01186.

[293] ATLAS Collaboration, "Measurement of W^+W^- production in pp collisions at $\sqrt{s}$=7 TeV with the ATLAS detector and limits on anomalous WWZ and WWγ couplings", *Phys. Rev. D* **87** (2013) 112001, doi:10.1103/PhysRevD.87.112001, arXiv:1210.2979. [Erratum: Phys.Rev.D 88 (2013) 079906].

[294] ATLAS Collaboration, "Measurement of total and differential W^+W^- production cross sections in proton-proton collisions at $\sqrt{s} = 8$ TeV with the ATLAS detector and limits on anomalous triple-gauge-boson couplings", *JHEP* **09** (2016) 029, doi:10.1007/JHEP09(2016)029, arXiv:1603.01702.

[295] ATLAS Collaboration, "Measurement of the W^+W^- production cross section in pp collisions at a centre-of-mass energy of $\sqrt{s}$ = 13 TeV with the ATLAS experiment", *Phys. Lett. B* **773** (2017) 354, doi:10.1016/j.physletb.2017.08.047, arXiv:1702.04519.

[296] ATLAS Collaboration, "Measurement of WZ production in proton-proton collisions at $\sqrt{s} = 7$ TeV with the ATLAS detector", *Eur. Phys. J. C* **72** (2012) 2173, doi:10.1140/epjc/s10052-012-2173-0, arXiv:1208.1390.

[297] ATLAS Collaboration, "Measurements of $W^\pm Z$ production cross sections in pp collisions at $\sqrt{s} = 8$ TeV with the ATLAS detector and limits on anomalous gauge boson self-couplings", *Phys. Rev. D* **93** (2016) 092004, doi:10.1103/PhysRevD.93.092004, arXiv:1603.02151.

[298] ATLAS Collaboration, "Measurement of $W^\pm Z$ production cross sections and gauge boson polarisation in pp collisions at $\sqrt{s} = 13$ TeV with the ATLAS detector", *Eur. Phys. J. C* **79** (2019) 535, doi:10.1140/epjc/s10052-019-7027-6, arXiv:1902.05759.

DRAFT

[299] ATLAS Collaboration, "Measurement of ZZ production in pp collisions at $\sqrt{s} = 7$ TeV and limits on anomalous ZZZ and ZZγ couplings with the ATLAS detector", *JHEP* **03** (2013) 128, doi:10.1007/JHEP03(2013)128, arXiv:1211.6096.

[300] ATLAS Collaboration, "Measurement of the ZZ production cross section in proton-proton collisions at $\sqrt{s} = 8$ TeV using the ZZ$\to \ell^-\ell^+\ell'^-\ell'^+$ and ZZ$\to \ell^-\ell^+\nu\overline{\nu}$ channels with the ATLAS detector", *JHEP* **01** (2017) 099, doi:10.1007/JHEP01(2017)099, arXiv:1610.07585.

[301] ATLAS Collaboration, "ZZ$\to \ell^+\ell^-\ell'^+\ell'^-$ cross section measurements and search for anomalous triple gauge couplings in 13 TeV pp collisions with the ATLAS detector", *Phys. Rev. D* **97** (2018) 032005, doi:10.1103/PhysRevD.97.032005, arXiv:1709.07703.

[302] CDF Collaboration, "Measurement of the WW and WZ production cross section using final states with a charged lepton and heavy-flavor jets in the full CDF Run II data set", *Phys. Rev. D* **94** (2016) 032008, doi:10.1103/PhysRevD.94.032008, arXiv:1606.06823.

[303] CDF Collaboration, "Measurement of the ZZ production cross section using the full CDF II data set", *Phys. Rev. D* **89** (2014) 112001, doi:10.1103/PhysRevD.89.112001, arXiv:1403.2300.

[304] D0 Collaboration, "Measurements of WW and WZ production in W + jets final states in $p\overline{p}$ collisions", *Phys. Rev. Lett.* **108** (2012) 181803, doi:10.1103/PhysRevLett.108.181803, arXiv:1112.0536.

[305] D0 Collaboration, "A measurement of the WZ and ZZ production cross sections using leptonic final states in 8.6 fb^{-1} of $p\overline{p}$ collisions", *Phys. Rev. D* **85** (2012) 112005, doi:10.1103/PhysRevD.85.112005, arXiv:1201.5652.

[306] D0 Collaboration, "Measurement of the ZZ production cross section and search for the standard model Higgs boson in the four-lepton final state in $p\overline{p}$ collisions", *Phys. Rev. D* **88** (2013) 032008, doi:10.1103/PhysRevD.88.032008, arXiv:1304.5422.

[307] M. Grazzini, S. Kallweit, M. Wiesemann, and J. Y. Yook, "ZZ production at the LHC: NLO QCD corrections to the loop-induced gluon fusion channel", *JHEP* **03** (2019) 070, doi:10.1007/JHEP03(2019)070, arXiv:1811.09593.

[308] CMS Collaboration, "Measurement of differential Z+jets production cross sections in pp collisions at $\sqrt{s}$ = 13 TeV", *submitted to JHEP*, (2024) arXiv:2404.02711.

[309] L. Buonocore et al., "ZZ production at nNNLO+PS with MiNNLO$_{PS}$", *JHEP* **01** (2022) 072, doi:10.1007/JHEP01(2022)072, arXiv:2108.05337.

[310] CDF Collaboration, "Measurement of the production and differential cross sections of W^+W^- bosons in association with jets in $p\overline{p}$ collisions at $\sqrt{s} = 1.96$ TeV", *Phys. Rev. D* **91** (2015) 111101, doi:10.1103/PhysRevD.91.111101, arXiv:1505.00801. [Addendum: Phys.Rev.D 92, 039901 (2015)].

[311] CMS Collaboration, "Measurement of the electroweak production of Wγ in association with two jets in proton-proton collisions at $\sqrt{s}$ = 13 TeV", *Phys. Rev. D* **108** (2023) 032017, doi:10.1103/PhysRevD.108.032017, arXiv:2212.12592.

DRAFT

[312] CMS Collaboration, "Measurement of the electroweak production of $Z\gamma$ and two jets in proton-proton collisions at $\sqrt{s} = 13$ TeV and constraints on anomalous quartic gauge couplings", *Phys. Rev. D* **104** (2021) 072001, doi:10.1103/PhysRevD.104.072001, arXiv:2106.11082.

[313] CMS Collaboration, "Measurement of differential cross sections for Z boson pair production in association with jets at $\sqrt{s} = 8$ and 13 TeV", *Phys. Lett. B* **789** (2019) 19, doi:10.1016/j.physletb.2018.11.007, arXiv:1806.11073.

[314] T. Gehrmann et al., "W^+W^- production at hadron colliders in next to next to leading order QCD", *Phys. Rev. Lett.* **113** (2014) 212001, doi:10.1103/PhysRevLett.113.212001, arXiv:1408.5243.

[315] CMS Collaboration, "Measurement of the differential ZZ+jets production cross sections in pp collisions at $\sqrt{s} = 13$ TeV", CMS Physics Analysis Summary CMS-PAS-SMP-22-001, 2023.

[316] CMS Collaboration, "Observation of the production of three massive gauge bosons at $\sqrt{s}$ =13 TeV", *Phys. Rev. Lett.* **125** (2020) 151802, doi:10.1103/PhysRevLett.125.151802, arXiv:2006.11191.

[317] CMS Collaboration, "Measurements of the pp $\to W\gamma\gamma$ and pp $\to Z\gamma\gamma$ cross sections and limits on anomalous quartic gauge couplings at $\sqrt{s} = 8$ TeV", *JHEP* **10** (2017) 072, doi:10.1007/JHEP10(2017)072, arXiv:1704.00366.

[318] CMS Collaboration, "Measurements of the pp $\to W^{\pm}\gamma\gamma$ and pp $\to Z\gamma\gamma$ cross sections at $\sqrt{s} = 13$ TeV and limits on anomalous quartic gauge couplings", *JHEP* **10** (2021) 174, doi:10.1007/JHEP10(2021)174, arXiv:2105.12780.

[319] CMS Collaboration, "Search for WWγ and WZγ production and constraints on anomalous quartic gauge couplings in pp collisions at $\sqrt{s} = 8$ TeV", *Phys. Rev. D* **90** (2014) 032008, doi:10.1103/PhysRevD.90.032008, arXiv:1404.4619.

[320] CMS Collaboration, "Observation of WWγ production and search for Hγ production in proton-proton collisions at $\sqrt{s}$ = 13 TeV", *Phys. Rev. Lett.* **132** (2024) 121901, doi:10.1103/PhysRevLett.132.121901, arXiv:2310.05164.

[321] A. Lazopoulos, K. Melnikov, and F. Petriello, "QCD corrections to tri-boson production", *Phys. Rev. D* **76** (2007) 014001, doi:10.1103/PhysRevD.76.014001, arXiv:hep-ph/0703273.

[322] T. Binoth, G. Ossola, C. G. Papadopoulos, and R. Pittau, "NLO QCD corrections to tri-boson production", *JHEP* **06** (2008) 082, doi:10.1088/1126-6708/2008/06/082, arXiv:0804.0350.

[323] V. Hankele and D. Zeppenfeld, "QCD corrections to hadronic WWZ production with leptonic decays", *Phys. Lett. B* **661** (2008) 103, doi:10.1016/j.physletb.2008.02.014, arXiv:0712.3544.

[324] CMS Collaboration, "Measurement of the hadronic activity in events with a Z and two Jets and extraction of the cross section for the electroweak production of a Z with two jets in pp Collisions at $\sqrt{s}$ = 7 TeV", *JHEP* **10** (2013) 062, doi:10.1007/JHEP10(2013)062, arXiv:1305.7389.

DRAFT

[325] CMS Collaboration, "Measurement of electroweak production of a W boson and two forward jets in proton-proton collisions at $\sqrt{s} = 8$ TeV", *JHEP* **11** (2016) 147, doi:10.1007/JHEP11(2016)147, arXiv:1607.06975.

[326] CMS Collaboration, "Measurement of electroweak production of two jets in association with a Z boson in proton-proton collisions at $\sqrt{s} = 8$ TeV", *Eur. Phys. J. C* **75** (2015) 66, doi:10.1140/epjc/s10052-014-3232-5, arXiv:1410.3153.

[327] CMS Collaboration, "Measurement of electroweak production of a W boson in association with two jets in proton–proton collisions at $\sqrt{s} = 13$ TeV", *Eur. Phys. J. C* **80** (2020) 43, doi:10.1140/epjc/s10052-019-7585-7, arXiv:1903.04040.

[328] CMS Collaboration, "Electroweak production of two jets in association with a Z boson in proton–proton collisions at $\sqrt{s} = 13$ TeV", *Eur. Phys. J. C* **78** (2018) 589, doi:10.1140/epjc/s10052-018-6049-9, arXiv:1712.09814.

[329] CMS Collaboration, "Evidence for WW/WZ vector boson scattering in the decay channel $\ell\nu$qq produced in association with two jets in proton-proton collisions at $\sqrt{s} =$ 13 TeV", *Phys. Lett. B* **834** (2022) 137438, doi:10.1016/j.physletb.2022.137438, arXiv:2112.05259.

[330] CMS Collaboration, "Evidence for exclusive $\gamma\gamma \to W^+W^-$ production and constraints on anomalous quartic gauge couplings in pp collisions at $\sqrt{s} = 7$ and 8 TeV", *JHEP* **08** (2016) 119, doi:10.1007/JHEP08(2016)119, arXiv:1604.04464.

[331] CMS Collaboration, "Measurement of electroweak-induced production of Wγ with two jets in pp collisions at $\sqrt{s} = 8$ TeV and constraints on anomalous quartic gauge couplings", *JHEP* **06** (2017) 106, doi:10.1007/JHEP06(2017)106, arXiv:1612.09256.

[332] CMS Collaboration, "Measurement of the cross section for electroweak production of $Z\gamma$ in association with two jets and constraints on anomalous quartic gauge couplings in proton–proton collisions at $\sqrt{s} = 8$ TeV", *Phys. Lett. B* **770** (2017) 380, doi:10.1016/j.physletb.2017.04.071, arXiv:1702.03025.

[333] CMS Collaboration, "Study of vector boson scattering and search for new physics in events with two same-sign leptons and two jets", *Phys. Rev. Lett.* **114** (2015) 051801, doi:10.1103/PhysRevLett.114.051801, arXiv:1410.6315.

[334] CMS Collaboration, "Observation of electroweak production of same-sign W boson pairs in the two jet and two same-sign lepton final state in proton-proton collisions at $\sqrt{s} = 13$ TeV", *Phys. Rev. Lett.* **120** (2018) 081801, doi:10.1103/PhysRevLett.120.081801, arXiv:1709.05822.

[335] B. Biedermann, A. Denner, and M. Pellen, "Large electroweak corrections to vector-boson scattering at the Large Hadron Collider", *Phys. Rev. Lett.* **118** (2017) 261801, doi:10.1103/PhysRevLett.118.261801, arXiv:1611.02951.

[336] B. Biedermann, A. Denner, and M. Pellen, "Complete NLO corrections to W^+W^+ scattering and its irreducible background at the LHC", *JHEP* **10** (2017) 124, doi:10.1007/JHEP10(2017)124, arXiv:1708.00268.

[337] CMS Collaboration, "Observation of electroweak W^+W^- pair production in association with two jets in proton-proton collisions at $\sqrt{s} = 13$ TeV", *Phys. Lett. B* **841** (2023) 137495, doi:10.1016/j.physletb.2022.137495, arXiv:2205.05711.

DRAFT

[338] CMS Collaboration, "Measurements of production cross sections of WZ and same-sign WW boson pairs in association with two jets in proton-proton collisions at $\sqrt{s} = 13$ TeV", *Phys. Lett. B* **809** (2020) 135710, doi:10.1016/j.physletb.2020.135710, arXiv:2005.01173.

[339] A. Denner et al., "QCD and electroweak corrections to WZ scattering at the LHC", *JHEP* **06** (2019) 067, doi:10.1007/JHEP06(2019)067, arXiv:1904.00882.

[340] B. Jäger, A. Karlberg, and G. Zanderighi, "Electroweak $ZZjj$ production in the Standard Model and beyond in the POWHEG-BOX V2", *JHEP* **03** (2014) 141, doi:10.1007/JHEP03(2014)141, arXiv:1312.3252.

[341] CMS Collaboration, "Measurements of production cross sections of polarized same-sign W boson pairs in association with two jets in proton-proton collisions at $\sqrt{s} = 13$ TeV", *Phys. Lett. B* **812** (2021) 136018, doi:10.1016/j.physletb.2020.136018, arXiv:2009.09429.

[342] V. M. Budnev, I. F. Ginzburg, G. V. Meledin, and V. G. Serbo, "The two-photon particle production mechanism. Physical problems. Applications. Equivalent photon approximation", *Phys. Rept.* **15** (1975) 181, doi:10.1016/0370-1573(75)90009-5.

[343] J. A. M. Vermaseren, "Two-photon processes at very high energies", *Nucl. Phys. B* **229** (1983) 347, doi:10.1016/0550-3213(83)90336-X.

[344] S. P. Baranov, O. Duenger, H. Shooshtari, and J. A. M. Vermaseren, "LPAIR: A generator for lepton pair production", in *Proceedings of Physics at HERA*, volume 3, p. 1478. 1991.

[345] CMS and TOTEM Collaboration, "Search for high-mass exclusive $\gamma\gamma \to WW$ and $\gamma\gamma \to ZZ$ production in proton-proton collisions at $\sqrt{s}$ = 13 TeV", *JHEP* **07** (2023) 229, doi:10.1007/JHEP07(2023)229, arXiv:2211.16320.

[346] ATLAS and CMS Collaborations, "Combination of measurements of the top quark mass from data collected by the ATLAS and CMS experiments at $\sqrt{s} = 7$ and 8 TeV", *submitted to PRL*, (2023) arXiv:2402.08713.

[347] I. Bigi et al., "Production and decay properties of ultraheavy quarks", *Phys. Lett. B* **181** (1986) 157, doi:10.1016/0370-2693(86)91275-X.

[348] C. T. Hill, "Topcolor: Top quark condensation in a gauge extension of the standard model", *Phys. Lett. B* **266** (1991) 419, doi:10.1016/0370-2693(91)91061-Y.

[349] S. Weinberg, "Implications of dynamical symmetry breaking", *Phys. Rev. D* **13** (1976) 974, doi:10.1103/PhysRevD.19.1277. [Addendum: Phys.Rev.D 19, 1277 (1979)].

[350] C. T. Hill, "Topcolor assisted technicolor", *Phys. Lett. B* **345** (1995) 483, doi:10.1016/0370-2693(94)01660-5, arXiv:hep-ph/9411426.

[351] M. E. Peskin and T. Takeuchi, "Estimation of oblique electroweak corrections", *Phys. Rev. D* **46** (1992) 381, doi:10.1103/PhysRevD.46.381.

[352] R. Franceschini, "Physics Beyond the Standard Model Associated with the Top Quark", *Ann. Rev. Nucl. Part. Sci.* **73** (2023) 397, doi:10.1146/annurev-nucl-102020-011427, arXiv:2301.04407.

DRAFT

[353] CMS Collaboration, "Measurement of the $\mathrm{t\bar{t}}$ production cross section in the all-jets final state in pp collisions at $\sqrt{s} = 8$ TeV", *Eur. Phys. J. C* **76** (2016) 128, doi:10.1140/epjc/s10052-016-3956-5, arXiv:1509.06076.

[354] CMS Collaboration, "Measurement of the top-quark mass in all-jets $\mathrm{t\bar{t}}$ events in pp collisions at $\sqrt{s}$=7 TeV", *Eur. Phys. J. C* **74** (2014) 2758, doi:10.1140/epjc/s10052-014-2758-x, arXiv:1307.4617.

[355] CMS Collaboration, "Measurement of the top-quark mass in $\mathrm{t\bar{t}}$ events with lepton+jets final states in pp collisions at $\sqrt{s} = 7$ TeV", *JHEP* **12** (2012) 105, doi:10.1007/JHEP12(2012)105, arXiv:1209.2319.

[356] CMS Collaboration, "Measurement of the differential cross section for top quark pair production in pp collisions at $\sqrt{s} = 8$ TeV", *Eur. Phys. J. C* **75** (2015) 542, doi:10.1140/epjc/s10052-015-3709-x, arXiv:1505.04480.

[357] CMS Collaboration, "Measurement of the top-quark mass in $\mathrm{t\bar{t}}$ events with dilepton final states in pp collisions at $\sqrt{s} = 7$ TeV", *Eur. Phys. J. C* **72** (2012) 2202, doi:10.1140/epjc/s10052-012-2202-z, arXiv:1209.2393.

[358] CMS Collaboration, "Measurement of the top quark Yukawa coupling from $\mathrm{t\bar{t}}$ kinematic distributions in the dilepton final state in proton-proton collisions at $\sqrt{s} = 13$ TeV", *Phys. Rev. D* **102** (2020) 092013, doi:10.1103/PhysRevD.102.092013, arXiv:2009.07123.

[359] CMS Collaboration, "Measurement of differential $\mathrm{t\bar{t}}$ production cross sections using top quarks at large transverse momenta in pp collisions at $\sqrt{s} = 13$ TeV", *Phys. Rev. D* **103** (2021) 052008, doi:10.1103/PhysRevD.103.052008, arXiv:2008.07860.

[360] CMS Collaboration, "Measurement of the differential $\mathrm{t\bar{t}}$ production cross section as a function of the jet mass and extraction of the top quark mass in hadronic decays of boosted top quarks", *Eur. Phys. J. C* **83** (2023) 560, doi:10.1140/epjc/s10052-023-11587-8, arXiv:2211.01456.

[361] CMS Collaboration, "Observation of top quark pairs produced in association with a vector boson in pp collisions at $\sqrt{s} = 8$ TeV", *JHEP* **01** (2016) 096, doi:10.1007/JHEP01(2016)096, arXiv:1510.01131.

[362] J. S. Conway, "Nuisance parameters in likelihoods for multisource spectra", in *Proceedings of PHYSTAT 2011 Workshop on Statistical Issues Related to Discovery Claims in Search Experiments and Unfolding*, H. Propser and L. Lyons, eds., p. 115. CERN, 2011. doi:10.5170/CERN-2011-006.115.

[363] T. Adye, "Unfolding algorithms and tests using RooUnfold", in *PHYSTAT 2011 Workshop on Statistical Issues Related to Discovery Claims in Search Experiments and Unfolding*, H. Prosper and L. Lyons, eds., p. 313. Geneva, Switzerland, 2011. arXiv:1105.1160. doi:10.5170/CERN-2011-006.313.

[364] S. Schmitt, "TUnfold: an algorithm for correcting migration effects in high energy physics", *JINST* **7** (2012) T10003, doi:10.1088/1748-0221/7/10/T10003, arXiv:1205.6201.

[365] ATLAS and CMS Collaborations, "LHCTopWG - LHC top physics working group". https://twiki.cern.ch/twiki/bin/view/LHCPhysics/LHCTopWG.

DRAFT

[366] CMS Collaboration, "Review of top quark mass measurements in CMS", *submitted to Phys. Rep.*, (2024) arXiv:2403.01313.

[367] CMS Collaboration, "Object definitions for top quark analyses at the particle level", Technical Report CMS-NOTE-2017-004, 2017.

[368] J. Gao, C. S. Li, L. L. Yang, and H. Zhang, "Searching for anomalous top quark production at the early lhc", *Phys. Rev. Lett.* **107** (2011) 092002, doi:10.1103/PhysRevLett.107.092002.

[369] J. A. Aguilar-Saavedra, "Single top quark production at LHC with anomalous Wtb couplings", *Nucl. Phys. B* **804** (2008) 160, doi:10.1016/j.nuclphysb.2008.06.013, arXiv:0803.3810.

[370] M. Aliev et al., "HATHOR: Hadronic top and heavy quarks cross section calculator", *Comput. Phys. Commun.* **182** (2011) 1034, doi:10.1016/j.cpc.2010.12.040, arXiv:1007.1327.

[371] P. Kant et al., "HatHor for single top-quark production: Updated predictions and uncertainty estimates for single top-quark production in hadronic collisions", *Comput. Phys. Commun.* **191** (2015) 74, doi:10.1016/j.cpc.2015.02.001, arXiv:1406.4403.

[372] N. Kidonakis, "Two-loop soft anomalous dimensions for single top quark associated production with a W^- or H^-", *Phys. Rev. D* **82** (2010) 054018, doi:10.1103/PhysRevD.82.054018, arXiv:1005.4451.

[373] N. Kidonakis, "Top quark production", in *Helmholtz International Summer School on Physics of Heavy Quarks and Hadrons*, p. 139. 2014. arXiv:1311.0283. doi:10.3204/DESY-PROC-2013-03/Kidonakis.

[374] J. Campbell, T. Neumann, and Z. Sullivan, "Single top quark production in the t-channel at NNLO", *JHEP* **02** (2021) 040, doi:10.1007/JHEP02(2021)040, arXiv:2012.01574.

[375] R. Frederix, E. Re, and P. Torrielli, "Single-top t-channel hadroproduction in the four-flavour scheme with POWHEG and aMC@NLO", *JHEP* **09** (2012) 130, doi:10.1007/JHEP09(2012)130, arXiv:1207.5391.

[376] CMS Collaboration, "Measurement of the single top quark t-channel cross section in pp collisions at $\sqrt{s} = 7$ TeV", *JHEP* **12** (2012) 035, doi:10.1007/JHEP12(2012)035, arXiv:1209.4533.

[377] CMS Collaboration, "Measurement of the t-channel single top quark production cross section and of the $|V_{tb}|$ CKM matrix element in pp collisions at $\sqrt{s}$= 8 TeV", *JHEP* **06** (2014) 090, doi:10.1007/JHEP06(2014)090, arXiv:1403.7366.

[378] CMS Collaboration, "Measurement of the single top quark and antiquark production cross sections in the t-channel and their ratio in proton-proton collisions at $\sqrt{s} = 13$ TeV", *Phys. Lett. B* **800** (2020) 135042, doi:10.1016/j.physletb.2019.135042, arXiv:1812.10514.

[379] F. Maltoni, G. Ridolfi, and M. Ubiali, "b-initiated processes at the LHC: a reappraisal", *JHEP* **07** (2012) 022, doi:10.1007/JHEP04(2013)095, arXiv:1203.6393. [Erratum: JHEP 04 (2013) 095].

DRAFT

[380] CMS Collaboration, "Measurement of differential cross sections and charge ratios for t-channel single top quark production in proton–proton collisions at $\sqrt{s} = 13\,\text{TeV}$", *Eur. Phys. J. C* **80** (2020) 370, doi:10.1140/epjc/s10052-020-7858-1, arXiv:1907.08330.

[381] ATLAS and CMS Collaborations, "Combinations of single top quark production cross-section measurements and $|f_{LV}V_{tb}|$ determinations at $\sqrt{s} = 7$ and 8 TeV with the ATLAS and CMS experiments", *JHEP* **05** (2019) 088, doi:10.1007/JHEP05(2019)088, arXiv:1902.07158.

[382] N. Kidonakis and N. Yamanaka, "Higher-order corrections for tW production at high-energy hadron colliders", *JHEP* **05** (2021) 278, doi:10.1007/JHEP05(2021)278, arXiv:2102.11300.

[383] PDF4LHC Working Group Collaboration, "The PDF4LHC21 combination of global PDF fits for the LHC Run III", *J. Phys. G* **49** (2022) 080501, doi:10.1088/1361-6471/ac7216, arXiv:2203.05506.

[384] CMS Collaboration, "Search for s-channel single top quark production in pp collisions at $\sqrt{s} = 7$ and 8 TeV", *JHEP* **09** (2016) 027, doi:10.1007/JHEP09(2016)027, arXiv:1603.02555.

[385] CMS Collaboration, "Evidence for associated production of a single top quark and W boson in pp Collisions at $\sqrt{s} = 7$ TeV", *Phys. Rev. Lett.* **110** (2013) 022003, doi:10.1103/PhysRevLett.110.022003, arXiv:1209.3489.

[386] CMS Collaboration, "Observation of the associated production of a single top quark and a W boson in pp collisions at $\sqrt{s} = 8$ TeV", *Phys. Rev. Lett.* **112** (2014) 231802, doi:10.1103/PhysRevLett.112.231802, arXiv:1401.2942.

[387] CMS Collaboration, "Measurement of the production cross section for single top quarks in association with W bosons in proton-proton collisions at $\sqrt{s} = 13$ TeV", *JHEP* **10** (2018) 117, doi:10.1007/JHEP10(2018)117, arXiv:1805.07399.

[388] CMS Collaboration, "Observation of tW production in the single-lepton channel in pp collisions at $\sqrt{s} = 13$ TeV", *JHEP* **11** (2021) 111, doi:10.1007/JHEP11(2021)111, arXiv:2109.01706.

[389] CMS Collaboration, "Identification of heavy-flavour jets with the CMS detector in pp collisions at 13 TeV", *JINST* **13** (2018) P05011, doi:10.1088/1748-0221/13/05/P05011, arXiv:1712.07158.

[390] M. Beneke, P. Falgari, S. Klein, and C. Schwinn, "Hadronic top-quark pair production with NNLL threshold resummation", *Nucl. Phys. B* **855** (2012) 695, doi:10.1016/j.nuclphysb.2011.10.021, arXiv:1109.1536.

[391] M. Cacciari et al., "Top-pair production at hadron colliders with next-to-next-to-leading logarithmic soft-gluon resummation", *Phys. Lett. B* **710** (2012) 612, doi:10.1016/j.physletb.2012.03.013, arXiv:1111.5869.

[392] P. Bärnreuther, M. Czakon, and A. Mitov, "Percent level precision physics at the Tevatron: First genuine NNLO QCD corrections to $q\bar{q} \to t\bar{t} + X$", *Phys. Rev. Lett.* **109** (2012) 132001, doi:10.1103/PhysRevLett.109.132001, arXiv:1204.5201.

DRAFT

[393] M. Czakon and A. Mitov, "NNLO corrections to top-pair production at hadron colliders: the all-fermionic scattering channels", *JHEP* **12** (2012) 054, doi:10.1007/JHEP12(2012)054, arXiv:1207.0236.

[394] M. Czakon and A. Mitov, "NNLO corrections to top pair production at hadron colliders: the quark-gluon reaction", *JHEP* **01** (2013) 080, doi:10.1007/JHEP01(2013)080, arXiv:1210.6832.

[395] M. Czakon, P. Fiedler, and A. Mitov, "Total top-quark pair-production cross section at hadron colliders through $O(\alpha_S^4)$", *Phys. Rev. Lett.* **110** (2013) 252004, doi:10.1103/PhysRevLett.110.252004, arXiv:1303.6254.

[396] M. Czakon and A. Mitov, "Top++: A program for the calculation of the top-pair cross-section at hadron colliders", *Comput. Phys. Commun.* **185** (2014) 2930, doi:10.1016/j.cpc.2014.06.021, arXiv:1112.5675.

[397] CMS Collaboration, "First measurement of the cross section for top-quark pair production in proton-proton collisions at $\sqrt{s} = 7$ TeV", *Phys. Lett. B* **695** (2011) 424, doi:10.1016/j.physletb.2010.11.058, arXiv:1010.5994.

[398] CMS Collaboration, "Measurement of the top quark pair production cross section in proton-proton collisions at $\sqrt{s} = 13$ TeV", *Phys. Rev. Lett.* **116** (2016) 052002, doi:10.1103/PhysRevLett.116.052002, arXiv:1510.05302.

[399] CMS Collaboration, "Measurement of the $t\bar{t}$ production cross section using events with one lepton and at least one jet in pp collisions at $\sqrt{s} = 13$ TeV", *JHEP* **09** (2017) 051, doi:10.1007/JHEP09(2017)051, arXiv:1701.06228.

[400] CMS Collaboration, "First measurement of the top quark pair production cross section in proton-proton collisions at $\sqrt{s} = 13.6$ TeV", *JHEP* **08** (2023) 204, doi:10.1007/JHEP08(2023)204, arXiv:2303.10680.

[401] CMS Collaboration, "Observation of top quark production in proton-nucleus collisions", *Phys. Rev. Lett.* **119** (2017) 242001, doi:10.1103/PhysRevLett.119.242001, arXiv:1709.07411.

[402] CMS Collaboration, "Evidence for top quark production in nucleus-nucleus collisions", *Phys. Rev. Lett.* **125** (2020) 222001, doi:10.1103/PhysRevLett.125.222001, arXiv:2006.11110.

[403] CMS Collaboration, "Measurement of the t-tbar production cross section in the e-mu channel in proton-proton collisions at $\sqrt{s} = 7$ and 8 TeV", *JHEP* **08** (2016) 029, doi:10.1007/JHEP08(2016)029, arXiv:1603.02303.

[404] CMS Collaboration, "Measurement of differential $t\bar{t}$ production cross sections in the full kinematic range using lepton+jets events from proton-proton collisions at $\sqrt{s} = 13$ TeV", *Phys. Rev. D* **104** (2021) 092013, doi:10.1103/PhysRevD.104.092013, arXiv:2108.02803.

[405] ATLAS and CMS Collaborations, "Combination of inclusive top-quark pair production cross-section measurements using ATLAS and CMS data at $\sqrt{s} = 7$ and 8 TeV", *JHEP* **07** (2023) 213, doi:10.1007/JHEP07(2023)213, arXiv:2205.13830.

DRAFT

[406] CMS Collaboration, "Measurement of the $\mathrm{t\bar{t}}$ production cross section and the top quark mass in the dilepton channel in pp collisions at $\sqrt{s} = 7$ TeV", *JHEP* **07** (2011) 049, doi:10.1007/JHEP07(2011)049, arXiv:1105.5661.

[407] CMS Collaboration, "Measurement of the top-antitop production cross section in pp collisions at $\sqrt{s} = 7$ TeV using the kinematic properties of events with leptons and jets", *Eur. Phys. J. C* **71** (2011) 1721, doi:10.1140/epjc/s10052-011-1721-3, arXiv:1106.0902.

[408] CMS Collaboration, "Measurement of the integrated and differential $\mathrm{t\bar{t}}$ production cross sections for high-p_{T} top quarks in pp collisions at $\sqrt{s} = 8$ TeV", *Phys. Rev. D* **94** (2016) 072002, doi:10.1103/PhysRevD.94.072002, arXiv:1605.00116.

[409] CMS Collaboration, "Measurement of the $t\bar{t}$ production cross section in pp collisions at 7 TeV in lepton + jets events using b-quark jet identification", *Phys. Rev. D* **84** (2011) 092004, doi:10.1103/PhysRevD.84.092004, arXiv:1108.3773.

[410] CMS Collaboration, "Measurement of the $\mathrm{t\bar{t}}$ production cross section in the τ + jets channel in pp collisions at $\sqrt{s} = 7$ TeV", *Eur. Phys. J. C* **73** (2013) 2386, doi:10.1140/epjc/s10052-013-2386-x, arXiv:1301.5755.

[411] CMS Collaboration, "Measurement of the inclusive $\mathrm{t\bar{t}}$ cross section in pp collisions at $\sqrt{s} = 5.02$ TeV using final states with at least one charged lepton", *JHEP* **03** (2018) 115, doi:10.1007/JHEP03(2018)115, arXiv:1711.03143.

[412] CMS Collaboration, "Precision luminosity measurement in proton-proton collisions at $\sqrt{s} = 13$ TeV in 2015 and 2016 at CMS", *Eur. Phys. J. C* **81** (2021) 800, doi:10.1140/epjc/s10052-021-09538-2, arXiv:2104.01927.

[413] A. Dainese et al., eds., "Report on the physics at the HL-LHC,and perspectives for the HE-LHC", volume 7/2019 of *CERN Yellow Reports: Monographs*. CERN, Geneva, Switzerland, 2019. doi:10.23731/CYRM-2019-007, ISBN 978-92-9083-549-3.

[414] CMS Collaboration, "Luminosity determination using Z boson production at the CMS experiment", *Eur. Phys. J. C* **84** (2024) 26, doi:10.1140/epjc/s10052-023-12268-2, arXiv:2309.01008.

[415] CMS Collaboration, "Measurement of differential top-quark pair production cross sections in pp collisions at $\sqrt{s} = 7$ TeV", *Eur. Phys. J. C* **73** (2013) 2339, doi:10.1140/epjc/s10052-013-2339-4, arXiv:1211.2220.

[416] CMS Collaboration, "Measurement of double-differential cross sections for top quark pair production in pp collisions at $\sqrt{s} = 8$ TeV and impact on parton distribution functions", *Eur. Phys. J. C* **77** (2017) 459, doi:10.1140/epjc/s10052-017-4984-5, arXiv:1703.01630.

[417] S. Catani et al., "Top-quark pair production at the LHC: Fully differential QCD predictions at NNLO", *JHEP* **07** (2019) 100, doi:10.1007/JHEP07(2019)100, arXiv:1906.06535.

[418] M. Czakon et al., "Top-pair production at the LHC through NNLO QCD and NLO EW", *JHEP* **10** (2017) 186, doi:10.1007/JHEP10(2017)186, arXiv:1705.04105.

DRAFT

[419] CMS Collaboration, "Identification of heavy, energetic, hadronically decaying particles using machine-learning techniques", *JINST* **15** (2020) P06005, doi:10.1088/1748-0221/15/06/P06005, arXiv:2004.08262.

[420] S. Catani et al., "Top-quark pair hadroproduction at next-to-next-to-leading order in QCD", *Phys. Rev. D* **99** (2019) 051501, doi:10.1103/PhysRevD.99.051501, arXiv:1901.04005.

[421] M. Czakon et al., "Top-quark charge asymmetry at the LHC and Tevatron through NNLO QCD and NLO EW", *Phys. Rev. D* **98** (2018) 014003, doi:10.1103/PhysRevD.98.014003, arXiv:1711.03945.

[422] CMS Collaboration, "Differential cross section measurements for the production of top quark pairs and of additional jets using dilepton events from pp collisions at $\sqrt{s}$ = 13 TeV", *submitted to JHEP* (2024) doi:10.48550/arXiv.2402.08486, arXiv:2402.08486.

[423] J. Mazzitelli et al., "Top-pair production at the LHC with MINNLO$_{PS}$", *JHEP* **04** (2022) 079, doi:10.1007/JHEP04(2022)079, arXiv:2112.12135.

[424] W. Bernreuther, D. Heisler, and Z.-G. Si, "A set of top quark spin correlation and polarization observables for the LHC: Standard Model predictions and new physics contributions", *JHEP* **12** (2015) 026, doi:10.1007/JHEP12(2015)026, arXiv:1508.05271.

[425] CMS Collaboration, "Measurement of the top quark polarization and $\mathrm{t\bar{t}}$ spin correlations using dilepton final states in proton-proton collisions at $\sqrt{s} = 13$ TeV", *Phys. Rev. D* **100** (2019) 072002, doi:10.1103/PhysRevD.100.072002, arXiv:1907.03729.

[426] CMS Collaboration, "Measurements of $\mathrm{t\bar{t}}$ spin correlations and top quark polarization using dilepton final states in pp collisions at $\sqrt{s} = 8$ TeV", *Phys. Rev. D* **93** (2016) 052007, doi:10.1103/PhysRevD.93.052007, arXiv:1601.01107.

[427] D. d'Enterria, K. Krajczár, and H. Paukkunen, "Top-quark production in proton–nucleus and nucleus–nucleus collisions at LHC energies and beyond", *Phys. Lett. B* **746** (2015) 64, doi:10.1016/j.physletb.2015.04.044, arXiv:1501.05879.

[428] L. Apolinário, J. G. Milhano, G. P. Salam, and C. A. Salgado, "Probing the time structure of the quark-gluon plasma with top quarks", *Phys. Rev. Lett.* **120** (2018) 232301, doi:10.1103/PhysRevLett.120.232301, arXiv:1711.03105.

[429] European Muon Collaboration, "The ratio of the nucleon structure functions $F2_n$ for iron and deuterium", *Phys. Lett. B* **123** (1983) 275, doi:10.1016/0370-2693(83)90437-9.

[430] K. J. Eskola, P. Paakkinen, H. Paukkunen, and C. A. Salgado, "EPPS16: Nuclear parton distributions with LHC data", *Eur. Phys. J. C* **77** (2017) 163, doi:10.1140/epjc/s10052-017-4725-9, arXiv:1612.05741.

[431] CMS Collaboration, "Constraining nuclear parton distributions with heavy ion collisions at the HL-LHC with the CMS experiment", CMS Physics Analysis Summary CMS-PAS-FTR-18-027, 2018.

DRAFT

[432] M. Schulze and Y. Soreq, "Pinning down electroweak dipole operators of the top quark", *Eur. Phys. J. C* **76** (2016) 466, doi:10.1140/epjc/s10052-016-4263-x, arXiv:1603.08911.

[433] CMS Collaboration, "Search for top squarks and dark matter particles in opposite-charge dilepton final states at $\sqrt{s} = 13$ TeV", *Phys. Rev. D* **97** (2018) 032009, doi:10.1103/PhysRevD.97.032009, arXiv:1711.00752.

[434] J. A. Aguilar-Saavedra, E. Álvarez, A. Juste, and F. Rubbo, "Shedding light on the $t\bar{t}$ asymmetry: the photon handle", *JHEP* **04** (2014) 188, doi:10.1007/JHEP04(2014)188, arXiv:1402.3598.

[435] CMS Collaboration, "Evidence for tWZ production in proton-proton collisions at $\sqrt{s}$ = 13 TeV in multilepton final states", *submitted to PLB*, (2023) arXiv:2312.11668.

[436] CMS Collaboration, "Measurement of top quark pair production in association with a Z boson in proton-proton collisions at $\sqrt{s} = 13$ TeV", *JHEP* **03** (2020) 056, doi:10.1007/JHEP03(2020)056, arXiv:1907.11270.

[437] CMS Collaboration, "Inclusive and differential cross section measurements of single top quark production in association with a Z boson in proton-proton collisions at $\sqrt{s}$ = 13 TeV", *JHEP* **02** (2022) 107, doi:10.1007/JHEP02(2022)107, arXiv:2111.02860.

[438] CMS Collaboration, "Evidence for the associated production of a single top quark and a photon in proton-proton collisions at $\sqrt{s} = 13$ TeV", *Phys. Rev. Lett.* **121** (2018) 221802, doi:10.1103/PhysRevLett.121.221802, arXiv:1808.02913.

[439] CMS Collaboration, "Measurement of the inclusive and differential $\mathrm{t\bar{t}}\gamma$ cross sections in the single-lepton channel and EFT interpretation at $\sqrt{s}$ = 13 TeV", *JHEP* **12** (2021) 180, doi:10.1007/JHEP12(2021)180, arXiv:2107.01508.

[440] J. Alwall et al., "The automated computation of tree-level and next-to-leading order differential cross sections, and their matching to parton shower simulations", *JHEP* **07** (2014) 079, doi:10.1007/JHEP07(2014)079, arXiv:1405.0301.

[441] A. Kulesza et al., "Associated top quark pair production with a heavy boson: differential cross sections at NLO+NNLL accuracy", *Eur. Phys. J. C* **80** (2020) 428, doi:10.1140/epjc/s10052-020-7987-6, arXiv:2001.03031.

[442] LHC Higgs Cross Section Working Group Collaboration, "Handbook of LHC Higgs cross sections: 4. Deciphering the nature of the Higgs sector", doi:10.23731/CYRM-2017-002, arXiv:1610.07922.

[443] S. Frixione et al., "Electroweak and QCD corrections to top-pair hadroproduction in association with heavy bosons", *JHEP* **06** (2015) 184, doi:10.1007/JHEP06(2015)184, arXiv:1504.03446.

[444] R. Frederix et al., "The automation of next-to-leading order electroweak calculations", *JHEP* **07** (2018) 185, doi:10.1007/JHEP11(2021)085, arXiv:1804.10017. [Erratum: JHEP 11 (2021) 085].

[445] CMS Collaboration, "Probing effective field theory operators in the associated production of top quarks with a Z boson in multilepton final states at $\sqrt{s}$ = 13 TeV", *JHEP* **12** (2021) 083, doi:10.1007/JHEP12(2021)083, arXiv:2107.13896.

DRAFT

[446] CMS Collaboration, "Measurement of the semileptonic $t\bar{t}$ + γ production cross section in pp collisions at $\sqrt{s} = 8$ TeV", *JHEP* **10** (2017) 006, doi:10.1007/JHEP10(2017)006, arXiv:1706.08128.

[447] CMS Collaboration, "Measurement of the inclusive and differential $t\bar{t}\gamma$ cross sections in the dilepton channel and effective field theory interpretation in proton-proton collisions at $\sqrt{s}$ =13 TeV", *JHEP* **05** (2022) 091, doi:10.1007/JHEP05(2022)091, arXiv:2201.07301.

[448] CMS Collaboration, "Search for new physics using effective field theory in 13 TeV pp collision events that contain a top quark pair and a boosted Z or Higgs boson", *Phys. Rev. D* **108** (2023) 032008, doi:10.1103/PhysRevD.108.032008, arXiv:2208.12837.

[449] CMS Collaboration, "Measurement of associated production of vector bosons and top quark-antiquark pairs at $\sqrt{s} = 7$ TeV", *Phys. Rev. Lett.* **110** (2013) 172002, doi:10.1103/PhysRevLett.110.172002, arXiv:1303.3239.

[450] CMS Collaboration, "Measurement of top quark-antiquark pair production in association with a W or Z boson in pp collisions at $\sqrt{s} = 8$ TeV", *Eur. Phys. J. C* **74** (2014) 3060, doi:10.1140/epjc/s10052-014-3060-7, arXiv:1406.7830.

[451] CMS Collaboration, "Measurement of the cross section for top quark pair production in association with a W or Z boson in proton-proton collisions at $\sqrt{s} = 13$ TeV", *JHEP* **08** (2018) 011, doi:10.1007/JHEP08(2018)011, arXiv:1711.02547.

[452] CMS Collaboration, "Measurement of the associated production of a single top quark and a Z boson in pp collisions at $\sqrt{s} = 13$ TeV", *Phys. Lett. B* **779** (2018) 358, doi:10.1016/j.physletb.2018.02.025, arXiv:1712.02825.

[453] CMS Collaboration, "Observation of single top quark production in association with a Z boson in proton-proton collisions at $\sqrt{s}$ =13 TeV", *Phys. Rev. Lett.* **122** (2019) 132003, doi:10.1103/PhysRevLett.122.132003, arXiv:1812.05900.

[454] G. Bevilacqua et al., "Modeling uncertainties of $t\bar{t}W^{\pm}$ multilepton signatures", *Phys. Rev. D* **105** (2022) 014018, doi:10.1103/PhysRevD.105.014018, arXiv:2109.15181.

[455] R. Frederix and I. Tsinikos, "On improving NLO merging for $t\bar{t}$W production", *JHEP* **11** (2021) 029, doi:10.1007/JHEP11(2021)029, arXiv:2108.07826.

[456] CMS Collaboration, "Measurement of the cross section of top quark-antiquark pair production in association with a W boson in proton-proton collisions at $\sqrt{s}$ = 13 TeV", *JHEP* **07** (2023) 219, doi:10.1007/JHEP07(2023)219, arXiv:2208.06485.

[457] CMS Collaboration, "Measurement of jet multiplicity distributions in $t\bar{t}$ production in pp collisions at $\sqrt{s} = 7$ TeV", *Eur. Phys. J. C* **74** (2015) 3014, doi:10.1140/epjc/s10052-014-3014-0, arXiv:1404.3171. [Erratum: Eur.Phys.J.C 75 (2015) 216].

[458] CMS Collaboration, "Measurement of $t\bar{t}$ production with additional jet activity, including b quark jets, in the dilepton decay channel using pp collisions at $\sqrt{s} = 8$ TeV", *Eur. Phys. J. C* **76** (2016) 379, doi:10.1140/epjc/s10052-016-4105-x, arXiv:1510.03072.

DRAFT

[459] CMS Collaboration, "Measurement of differential cross sections for the production of top quark pairs and of additional jets in lepton+jets events from pp collisions at $\sqrt{s} = 13$ TeV", *Phys. Rev. D* **97** (2018) 112003, doi:10.1103/PhysRevD.97.112003, arXiv:1803.08856.

[460] CMS Collaboration, "Study of the underlying event in top quark pair production in pp collisions at 13 TeV", *Eur. Phys. J. C* **79** (2019) 123, doi:10.1140/epjc/s10052-019-6620-z, arXiv:1807.02810.

[461] CMS Collaboration, "Measurement of jet substructure observables in $\mathrm{t\bar{t}}$ events from proton-proton collisions at $\sqrt{s} = 13$ TeV", *Phys. Rev. D* **98** (2018) 092014, doi:10.1103/PhysRevD.98.092014, arXiv:1808.07340.

[462] CMS Collaboration, "Measurement of the cross section for $\mathrm{t\bar{t}}$ production with additional jets and b jets in pp collisions at $\sqrt{s} = 13$ TeV", *JHEP* **07** (2020) 125, doi:10.1007/JHEP07(2020)125, arXiv:2003.06467.

[463] CMS Collaboration, "Development and validation of HERWIG 7 tunes from CMS underlying-event measurements", *Eur. Phys. J. C* **81** (2021) 312, doi:10.1140/epjc/s10052-021-08949-5, arXiv:2011.03422.

[464] CMS Collaboration, "Measurement of the $\mathrm{t\bar{t}b\bar{b}}$ production cross section in the all-jet final state in pp collisions at $\sqrt{s} = 13$ TeV", *Phys. Lett. B* **803** (2020) 135285, doi:10.1016/j.physletb.2020.135285, arXiv:1909.05306.

[465] CMS Collaboration, "Inclusive and differential cross section measurements of $\mathrm{t\bar{t}b\bar{b}}$ production in the lepton+jets channel at $\sqrt{s}$ = 13 TeV", *submitted to JHEP* (2023) arXiv:2309.14442.

[466] CMS Collaboration, "First measurement of the cross section for top quark pair production with additional charm jets using dileptonic final states in pp collisions at $\sqrt{s} = 13$ TeV", *Phys. Lett. B* **820** (2021) 136565, doi:10.1016/j.physletb.2021.136565, arXiv:2012.09225.

[467] A. Denner, J.-N. Lang, and M. Pellen, "Full NLO QCD corrections to off-shell $\mathrm{t\bar{t}b\bar{b}}$ production", *Phys. Rev. D* **104** (2021) 056018, doi:10.1103/PhysRevD.104.056018, arXiv:2008.00918.

[468] G. Bevilacqua et al., "ttbb at the LHC: On the size of off-shell effects and prompt b-jet identification", *Phys. Rev. D* **107** (2023) 014028, doi:10.1103/PhysRevD.107.014028, arXiv:2202.11186.

[469] M. van Beekveld, A. Kulesza, and L. M. Valero, "Threshold resummation for the production of four top quarks at the LHC", *Phys. Rev. Lett.* **131** (2023) 211901, doi:10.1103/PhysRevLett.131.211901, arXiv:2212.03259.

[470] L. Darmé, B. Fuks, and M. Goodsell, "Cornering sgluons with four-top-quark events", *Phys. Lett. B* **784** (2018) 223, doi:10.1016/j.physletb.2018.08.001, arXiv:1805.10835.

[471] M. Bauer, U. Haisch, and F. Kahlhoefer, "Simplified dark matter models with two Higgs doublets: I. Pseudoscalar mediators", *JHEP* **05** (2017) 138, doi:10.1007/JHEP05(2017)138, arXiv:1701.07427.

DRAFT

[472] CMS Collaboration, "Evidence for four-top quark production in proton-proton collisions at $\sqrt{s}$ = 13 TeV", *Phys. Lett. B* **844** (2023) 138076, doi:10.1016/j.physletb.2023.138076, arXiv:2303.03864.

[473] CMS Collaboration, "Search for standard model production of four top quarks in the lepton + jets channel in pp collisions at $\sqrt{s}$ = 8 TeV", *JHEP* **11** (2014) 154, doi:10.1007/JHEP11(2014)154, arXiv:1409.7339.

[474] CMS Collaboration, "Search for standard model production of four top quarks in proton-proton collisions at $\sqrt{s}$ = 13 TeV", *Phys. Lett. B* **772** (2017) 336, doi:10.1016/j.physletb.2017.06.064, arXiv:1702.06164.

[475] CMS Collaboration, "Search for the production of four top quarks in the single-lepton and opposite-sign dilepton final states in proton-proton collisions at $\sqrt{s}$ = 13 TeV", *JHEP* **11** (2019) 082, doi:10.1007/JHEP11(2019)082, arXiv:1906.02805.

[476] CMS Collaboration, "Search for standard model production of four top quarks with same-sign and multilepton final states in proton–proton collisions at $\sqrt{s} = 13\,\text{TeV}$", *Eur. Phys. J. C* **78** (2018) 140, doi:10.1140/epjc/s10052-018-5607-5, arXiv:1710.10614.

[477] CMS Collaboration, "Search for production of four top quarks in final states with same-sign or multiple leptons in proton-proton collisions at $\sqrt{s} = 13\,\text{TeV}$", *Eur. Phys. J. C* **80** (2020) 75, doi:10.1140/epjc/s10052-019-7593-7, arXiv:1908.06463.

[478] CMS Collaboration, "Observation of four top quark production in proton-proton collisions at $\sqrt{s} = 13$ TeV", *Phys. Lett. B* **847** (2023) 138290, doi:10.1016/j.physletb.2023.138290, arXiv:2305.13439.

[479] R. Frederix, D. Pagani, and M. Zaro, "Large NLO corrections in $\mathrm{t\bar{t}W^{\pm}}$ and $\mathrm{t\bar{t}t\bar{t}}$ hadroproduction from supposedly subleading EW contributions", *JHEP* **02** (2018) 031, doi:10.1007/JHEP02(2018)031, arXiv:1711.02116.

[480] V. Barger, W.-Y. Keung, and B. Yencho, "Triple-top signal of new physics at the LHC", *Phys. Lett. B* **687** (2010) 70, doi:10.1016/j.physletb.2010.03.001, arXiv:1001.0221.

[481] E. Boos and L. Dudko, "Triple top quark production in standard model", *Int. J. Mod. Phys. A* **37** (2022) 2250023, doi:10.1142/S0217751X22500233, arXiv:2107.07629.

[482] CMS Collaboration, "CMS PYTHIA 8 colour reconnection tunes based on underlying-event data", *Eur. Phys. J. C* **83** (2023) 587, doi:10.1140/epjc/s10052-023-11630-8, arXiv:2205.02905.

[483] CMS Collaboration, "Measurement of the $\mathrm{t\bar{t}}$ production cross section using events in the eμ final state in pp collisions at $\sqrt{s} = 13$ TeV", *Eur. Phys. J. C* **77** (2017) 172, doi:10.1140/epjc/s10052-017-4718-8, arXiv:1611.04040.

[484] CMS Collaboration, "Measurement of CKM matrix elements in single top quark t-channel production in proton-proton collisions at $\sqrt{s} = 13$ TeV", *Phys. Lett. B* **808** (2020) 135609, doi:10.1016/j.physletb.2020.135609, arXiv:2004.12181.

DRAFT

[485] CMS Collaboration, "Measurement of the ratio $\mathcal{B}(\mathrm{t} \to \mathrm{Wb})/\mathcal{B}(\mathrm{t} \to \mathrm{Wq})$ in pp collisions at $\sqrt{s} = 8$ TeV", *Phys. Lett. B* **736** (2014) 33, doi:10.1016/j.physletb.2014.06.076, arXiv:1404.2292.

[486] S. Alekhin et al., "The PDF4LHC working group interim report", (2011) arXiv:1101.0536.

[487] N. Kidonakis, "NNLL threshold resummation for top-pair and single-top production", *Phys. Part. Nucl.* **45** (2014) 714, doi:10.1134/S1063779614040091, arXiv:1210.7813.

[488] Q.-H. Cao, S.-L. Chen, and Y. Liu, "Probing Higgs width and top quark Yukawa coupling from $\mathrm{t\bar{t}H}$ and $\mathrm{t\bar{t}t\bar{t}}$ productions", *Phys. Rev. D* **95** (2017) 053004, doi:10.1103/PhysRevD.95.053004, arXiv:1602.01934.

[489] CMS Collaboration, "Measurement of the top quark Yukawa coupling from $\mathrm{t\bar{t}}$ kinematic distributions in the lepton+jets final state in proton-proton collisions at $\sqrt{s} = 13$ TeV", *Phys. Rev. D* **100** (2019) 072007, doi:10.1103/PhysRevD.100.072007, arXiv:1907.01590.

[490] C. Englert, G. F. Giudice, A. Greljo, and M. Mccullough, "The $\hat{H}$-parameter: An oblique Higgs view", *JHEP* **09** (2019) 041, doi:10.1007/JHEP09(2019)041, arXiv:1903.07725.

[491] CMS Collaboration, "Observation of a new boson with mass near 125 GeV in pp collisions at $\sqrt{s} = 7$ and 8 TeV", *JHEP* **06** (2013) 081, doi:10.1007/JHEP06(2013)081, arXiv:1303.4571.

[492] ATLAS Collaboration, "Observation of a new particle in the search for the standard model Higgs boson with the ATLAS detector at the LHC", *Phys. Lett. B* **716** (2012) 1, doi:10.1016/j.physletb.2012.08.020, arXiv:1207.7214.

[493] CMS Collaboration, "Measurement of Higgs boson production and properties in the WW decay channel with leptonic final states", *JHEP* **01** (2014) 096, doi:10.1007/JHEP01(2014)096, arXiv:1312.1129.

[494] CMS Collaboration, "Measurement of the properties of a Higgs boson in the four-lepton final state", *Phys. Rev. D* **89** (2014) 092007, doi:10.1103/PhysRevD.89.092007, arXiv:1312.5353.

[495] CMS Collaboration, "Measurements of production cross sections of the Higgs boson in the four lepton final-state in proton–proton collisions at $\sqrt{s} = 13\,\mathrm{TeV}$", *Eur. Phys. J. C* **81** (2021) 488, doi:10.1140/epjc/s10052-021-09200-x, arXiv:2103.04956.

[496] CMS Collaboration, "Measurements of the Higgs boson production cross section and couplings in the W boson pair decay channel in proton-proton collisions at $\sqrt{s} = 13\,\mathrm{TeV}$", *Eur. Phys. J. C* **83** (2023) 667, doi:10.1140/epjc/s10052-023-11632-6, arXiv:2206.09466.

[497] CMS Collaboration, "Observation of the diphoton decay of the Higgs boson and measurement of its properties", *Eur. Phys. J. C* **74** (2014) 3076, doi:10.1140/epjc/s10052-014-3076-z, arXiv:1407.0558.

DRAFT

[498] CMS Collaboration, "Measurements of Higgs boson production cross sections and couplings in the diphoton decay channel at $\sqrt{s}$ = 13 TeV", *JHEP* **07** (2021) 027, doi:10.1007/JHEP07(2021)027, arXiv:2103.06956.

[499] CMS Collaboration, "Evidence for the direct decay of the 125 GeV Higgs boson to fermions", *Nature Phys.* **10** (2014) 557, doi:10.1038/nphys3005, arXiv:1401.6527.

[500] CMS Collaboration, "Observation of the Higgs boson decay to a pair of τ leptons with the CMS detector", *Phys. Lett. B* **779** (2018) 283, doi:10.1016/j.physletb.2018.02.004, arXiv:1708.00373.

[501] CMS Collaboration, "Observation of Higgs boson decay to bottom quarks", *Phys. Rev. Lett.* **121** (2018) 121801, doi:10.1103/PhysRevLett.121.121801, arXiv:1808.08242.

[502] CMS Collaboration, "Measurements of Higgs boson production in the decay channel with a pair of τ leptons in proton–proton collisions at $\sqrt{s} = 13$ TeV", *Eur. Phys. J. C* **83** (2023) 562, doi:10.1140/epjc/s10052-023-11452-8, arXiv:2204.12957.

[503] CMS Collaboration, "Observation of $t\bar{t}H$ production", *Phys. Rev. Lett.* **120** (2018) 231801, doi:10.1103/PhysRevLett.120.231801, arXiv:1804.02610.

[504] CMS Collaboration, "Evidence for Higgs boson decay to a pair of muons", *JHEP* **01** (2021) 148, doi:10.1007/JHEP01(2021)148, arXiv:2009.04363.

[505] CMS Collaboration, "Search for Higgs boson decays to a Z boson and a photon in proton-proton collisions at $\sqrt{s}$ = 13 TeV", *JHEP* **05** (2023) 233, doi:10.1007/JHEP05(2023)233, arXiv:2204.12945.

[506] ATLAS and CMS Collaboration, "Evidence for the Higgs boson decay to a Z boson and a photon at the LHC", *Phys. Rev. Lett.* **132** (2024) 021803, doi:10.1103/PhysRevLett.132.021803, arXiv:2309.03501.

[507] CMS Collaboration, "Measurement of the Higgs boson width and evidence of its off-shell contributions to ZZ production", *Nature Phys.* **18** (2022) 1329, doi:10.1038/s41567-022-01682-0, arXiv:2202.06923.

[508] CMS Collaboration, "Study of the mass and spin-parity of the Higgs boson candidate via its decays to Z boson pairs", *Phys. Rev. Lett.* **110** (2013) 081803, doi:10.1103/PhysRevLett.110.081803, arXiv:1212.6639.

[509] CMS Collaboration, "Constraints on the spin-parity and anomalous HVV couplings of the Higgs boson in proton collisions at 7 and 8 TeV", *Phys. Rev. D* **92** (2015) 012004, doi:10.1103/PhysRevD.92.012004, arXiv:1411.3441.

[510] CMS Collaboration, "Search for *CP* violation in ttH and tH production in multilepton channels in proton-proton collisions at $\sqrt{s}$ = 13 TeV", *JHEP* **07** (2023) 092, doi:10.1007/JHEP07(2023)092, arXiv:2208.02686.

[511] CMS Collaboration, "Constraints on anomalous Higgs boson couplings to vector bosons and fermions from the production of Higgs bosons using the $\tau\tau$ final-state", *Phys. Rev. D* **108** (2023) 032013, doi:10.1103/PhysRevD.108.032013, arXiv:2205.05120.

DRAFT

[512] CMS Collaboration, "Analysis of the *CP* structure of the Yukawa coupling between the Higgs boson and τ leptons in proton-proton collisions at $\sqrt{s}$ = 13 TeV", *JHEP* **06** (2022) 012, doi:10.1007/JHEP06(2022)012, arXiv:2110.04836.

[513] CMS Collaboration, "Constraints on anomalous Higgs boson couplings to vector bosons and fermions in its production and decay using the four lepton final-state", *Phys. Rev. D* **104** (2021) 052004, doi:10.1103/PhysRevD.104.052004, arXiv:2104.12152.

[514] CMS Collaboration, "Measurements of H production and the CP structure of the Yukawa interaction between the Higgs boson and top quark in the diphoton decay channel", *Phys. Rev. Lett.* **125** (2020) 061801, doi:10.1103/PhysRevLett.125.061801, arXiv:2003.10866.

[515] CMS Collaboration, "A portrait of the Higgs boson by the CMS experiment ten years after the discovery", *Nature* **607** (2022) 60, doi:10.1038/s41586-022-04892-x, arXiv:2207.00043.

[516] CMS Collaboration, "Search for nonresonant Higgs boson pair production in final state with two bottom quarks and two tau leptons in proton-proton collisions at $\sqrt{s} = 13$ TeV", *Phys. Lett. B* **842** (2023) 137531, doi:10.1016/j.physletb.2022.137531, arXiv:2206.09401.

[517] CMS Collaboration, "Search for Higgs boson pair production in the four b quark final-state in proton-proton collisions at $\sqrt{s} = 13$ TeV", *Phys. Rev. Lett.* **129** (2022) 081802, doi:10.1103/PhysRevLett.129.081802, arXiv:2202.09617.

[518] CMS Collaboration, "Search for nonresonant Higgs boson pair production in final states with two bottom quarks and two photons in proton-proton collisions at $\sqrt{s}$ = 13 TeV", *JHEP* **03** (2021) 257, doi:10.1007/JHEP03(2021)257, arXiv:2011.12373.

[519] CMS Collaboration, "Search for nonresonant Higgs boson pair production in the four leptons plus two b jets final-state in proton-proton collisions at $\sqrt{s}$ = 13 TeV", *JHEP* **06** (2023) 130, doi:10.1007/JHEP06(2023)130, arXiv:2206.10657.

[520] CMS Collaboration, "Search for Higgs boson pairs decaying to WW*WW*, WW*$\tau\tau$, and $\tau\tau\tau\tau$ in proton-proton collisions at $\sqrt{s}$ = 13 TeV", *JHEP* **07** (2023) 095, doi:10.1007/JHEP07(2023)095, arXiv:2206.10268.

[521] CMS Collaboration, "Search for nonresonant pair production of highly energetic Higgs bosons decaying to bottom quarks", *Phys. Rev. Lett.* **131** (2023) 041803, doi:10.1103/PhysRevLett.131.041803, arXiv:2205.06667.

[522] LHC Higgs Cross Section Working Group, D. de Florian et al., "Handbook of LHC Higgs cross sections: 4. Deciphering the nature of the Higgs sector". CERN Yellow Reports: Monographs. CERN, Geneva, 2017. 869 pages, 295 figures, 248 tables and 1645 citations. Working Group web page: https://twiki.cern.ch/twiki/bin/view/LHCPhysics/LHCHXSWG. doi:10.23731/CYRM-2017-002.

[523] CMS Collaboration, "Search for higgs boson decay to a charm quark-antiquark pair in proton-proton collisions at $\sqrt{s}$ = 13 TeV", *Phys. Rev. Lett.* **131** (2023) 061801, doi:10.1103/PhysRevLett.131.061801, arXiv:2205.05550.

DRAFT

[524] CMS Collaboration, "Combined measurements of Higgs boson couplings in proton–proton collisions at $\sqrt{s} = 13\,\text{TeV}$", *Eur. Phys. J. C* **79** (2019) 421, doi:10.1140/epjc/s10052-019-6909-y, arXiv:1809.10733.

[525] ATLAS and CMS Collaboration, "Measurements of the Higgs boson production and decay rates and constraints on its couplings from a combined ATLAS and CMS analysis of the LHC pp collision data at $\sqrt{s} = 7$ and 8 TeV", *JHEP* **08** (2016) 045, doi:10.1007/JHEP08(2016)045, arXiv:1606.02266.

[526] CMS Collaboration, "Precise determination of the mass of the Higgs boson and tests of compatibility of its couplings with the standard model predictions using proton collisions at 7 and 8 TeV", *Eur. Phys. J. C* **75** (2015) 212, doi:10.1140/epjc/s10052-015-3351-7, arXiv:1412.8662.

[527] LHC Higgs Cross Section Working Group Collaboration, "Handbook of LHC Higgs cross sections: 3. Higgs properties", doi:10.5170/CERN-2013-004, arXiv:1307.1347.

[528] CMS Collaboration, "Measurement of differential cross sections for Higgs boson production in the diphoton decay channel in pp collisions at $\sqrt{s} = 8\,\text{TeV}$", *Eur. Phys. J. C* **76** (2016) 13, doi:10.1140/epjc/s10052-015-3853-3, arXiv:1508.07819.

[529] CMS Collaboration, "Measurement of differential and integrated fiducial cross sections for Higgs boson production in the four-lepton decay channel in pp collisions at $\sqrt{s} = 7$ and 8 TeV", *JHEP* **04** (2016) 005, doi:10.1007/JHEP04(2016)005, arXiv:1512.08377.

[530] CMS Collaboration, "Measurement of the Higgs boson inclusive and differential fiducial production cross sections in the diphoton decay channel with pp collisions at $\sqrt{s}$ = 13 TeV", *JHEP* **07** (2023) 091, doi:10.1007/JHEP07(2023)091, arXiv:2208.12279.

[531] CMS Collaboration, "Measurements of inclusive and differential cross sections for the Higgs boson production and decay to four-leptons in proton-proton collisions at $\sqrt{s}$ = 13 TeV", *JHEP* **08** (2023) 040, doi:10.1007/JHEP08(2023)040, arXiv:2305.07532.

[532] CMS Collaboration, "Measurement of the inclusive and differential Higgs boson production cross sections in the decay mode to a pair of τ leptons in pp collisions at $\sqrt{s} = 13\,\text{TeV}$", *Phys. Rev. Lett.* **128** (2022) 081805, doi:10.1103/PhysRevLett.128.081805, arXiv:2107.11486.

[533] CMS Collaboration, "Measurement of the inclusive and differential Higgs boson production cross sections in the leptonic WW decay mode at $\sqrt{s} = 13\,\text{TeV}$", *JHEP* **03** (2021) 003, doi:10.1007/JHEP03(2021)003, arXiv:2007.01984.

[534] M. Grazzini and H. Sargsyan, "Heavy-quark mass effects in Higgs boson production at the LHC", *JHEP* **09** (2013) 129, doi:10.1007/JHEP09(2013)129, arXiv:1306.4581.

[535] D. de Florian, G. Ferrera, M. Grazzini, and D. Tommasini, "Higgs boson production at the LHC: transverse momentum resummation effects in the $H \to \gamma\gamma$, $H \to WW \to \ell\nu\ell\nu$ and $H \to ZZ \to 4\ell$ decay modes", *JHEP* **06** (2012) 132, doi:10.1007/JHEP06(2012)132, arXiv:1203.6321.

DRAFT

[536] C. Anastasiou et al., "High precision determination of the gluon fusion Higgs boson cross-section at the LHC", *JHEP* **05** (2016) 058, doi:10.1007/JHEP05(2016)058, arXiv:1602.00695.

[537] CMS Collaboration, "Measurement of inclusive and differential Higgs boson production cross sections in the diphoton decay channel in proton-proton collisions at $\sqrt{s} = 13$ TeV", *JHEP* **01** (2019) 183, doi:10.1007/JHEP01(2019)183, arXiv:1807.03825.

[538] CMS Collaboration, "Measurements of properties of the Higgs boson decaying into the four lepton final-state in pp collisions at $\sqrt{s} = 13$ TeV", *JHEP* **11** (2017) 047, doi:10.1007/JHEP11(2017)047, arXiv:1706.09936.

[539] CMS Collaboration, "Measurement of the transverse momentum spectrum of the Higgs boson produced in pp collisions at $\sqrt{s} = 8$ TeV using $H \to WW$ decays", *JHEP* **03** (2017) 032, doi:10.1007/JHEP03(2017)032, arXiv:1606.01522.

[540] CMS Collaboration, "Inclusive search for a highly boosted Higgs boson decaying to a bottom quark-antiquark pair", *Phys. Rev. Lett.* **120** (2018) 071802, doi:10.1103/PhysRevLett.120.071802, arXiv:1709.05543.

[541] CMS Collaboration, "Inclusive search for highly boosted Higgs bosons decaying to bottom quark-antiquark pairs in proton-proton collisions at $\sqrt{s} = 13$ TeV", *JHEP* **12** (2020) 085, doi:10.1007/JHEP12(2020)085, arXiv:2006.13251.

[542] S. Gangal, M. Stahlhofen, and F. J. Tackmann, "Rapidity-dependent jet vetoes", *Phys. Rev. D* **91** (2015) 054023, doi:10.1103/PhysRevD.91.054023, arXiv:1412.4792.

[543] CMS Collaboration, "Measurement and interpretation of differential cross sections for Higgs boson production at $\sqrt{s} = 13$ TeV", *Phys. Lett. B* **792** (2019) 369, doi:10.1016/j.physletb.2019.03.059, arXiv:1812.06504.

[544] N. Berger et al., "Simplified template cross sections - Stage 1.1", Technical Report LHCHXSWG-2019-003, DESY-19-070, 2019. arXiv:1906.02754.

[545] CMS Collaboration, "Measurement of simplified template cross sections of the Higgs boson produced in association with W or Z bosons in the $H \to b\bar{b}$ decay channel in proton-proton collisions at $\sqrt{s} = 13$ TeV", 2023. arXiv:2312.07562. Submitted to Phys.Rev. D.

[546] S. Dawson, S. Dittmaier, and M. Spira, "Neutral Higgs boson pair production at hadron colliders: QCD corrections", *Phys. Rev. D* **58** (1998) 115012, doi:10.1103/PhysRevD.58.115012, arXiv:hep-ph/9805244.

[547] S. Borowka et al., "Higgs boson pair production in gluon fusion at next-to-leading order with full top quark mass dependence", *Phys. Rev. Lett.* **117** (2016) 012001, doi:10.1103/PhysRevLett.117.079901, arXiv:1604.06447. [Erratum: Phys.Rev.Lett. 117 (2016) 079901].

[548] J. Baglio et al., "Gluon fusion into Higgs pairs at NLO QCD and the top mass scheme", *Eur. Phys. J. C* **79** (2019) 459, doi:10.1140/epjc/s10052-019-6973-3, arXiv:1811.05692.

[549] D. de Florian and J. Mazzitelli, "Higgs boson pair production at next-to-next-to-leading order in QCD", *Phys. Rev. Lett.* **111** (2013) 201801, doi:10.1103/PhysRevLett.111.201801, arXiv:1309.6594.

DRAFT

[550] D. Y. Shao, C. S. Li, H. T. Li, and J. Wang, "Threshold resummation effects in Higgs boson pair production at the LHC", *JHEP* **07** (2013) 169, doi:10.1007/JHEP07(2013)169, arXiv:1301.1245.

[551] D. de Florian and J. Mazzitelli, "Higgs pair production at next-to-next-to-leading logarithmic accuracy at the LHC", *JHEP* **09** (2015) 053, doi:10.1007/JHEP09(2015)053, arXiv:1505.07122.

[552] M. Grazzini et al., "Higgs boson pair production at NNLO with top quark mass effects", *JHEP* **05** (2018) 059, doi:10.1007/JHEP05(2018)059, arXiv:1803.02463.

[553] J. Baglio et al., "gg $\rightarrow$ HH : Combined uncertainties", *Phys. Rev. D* **103** (2021) 056002, doi:10.1103/PhysRevD.103.056002, arXiv:2008.11626.

[554] ATLAS and CMS Collaboration, "Snowmass white paper contribution: Physics with the Phase-2 ATLAS and CMS detectors", Technical Report ATL-PHYS-PUB-2022-018, 2022. All figures including auxiliary figures are available at https://atlas.web.cern.ch/Atlas/GROUPS/PHYSICS/PUBNOTES/ATL-PHYS-PUB-2022-018.

[555] CMS Collaboration, "Prospects for the measurement of vector boson scattering production in leptonic $W^{\pm}W^{\pm}$ and WZ diboson events at $\sqrt{s} = 14$ TeV at the High-Luminosity LHC", CMS Physics Analysis Summary CMS-PAS-FTR-21-001, 2021.

[556] G. Isidori, G. Ridolfi, and A. Strumia, "On the metastability of the standard model vacuum", *Nucl. Phys. B* **609** (2001) 387, doi:10.1016/S0550-3213(01)00302-9, arXiv:hep-ph/0104016.

DRAFT